Structure and morphology of NiO / Cu(111) and NiO /FeNi / Cu(111) ultra-thin layers and nanostructures

Stefan Stanescu

Thèse de Doctorat de l'Université Louis Pasteur – Strasbourg I

Spécialité:
Physique de la matière condensée

Présentée par:

Stefan STANESCU

Pour obtenir le grade de:
Docteur de l'Université Louis Pasteur – Strasbourg I

Structure and morphology of NiO / Cu(111) and NiO /FeNi / Cu(111) ultra-thin layers and nanostructures

---

Soutenue le 3 décembre 2002 devant la commission d'examen :

Mme.	M. GAUTIER-SOYER	*Rapporteur*
MM.	S. FERRER	*Rapporteur*
	M. ALOUANI	*Rapporteur*
	A. BARBIER	*Invité*
	J.-P. DEVILLE	*Invité*
Mme.	C. BOEGLIN	*Directeur de thèse*

TABLE OF CONTENTS

INTRODUCTION

In the last decade, a tremendous amount of work has been devoted to the study of oxide surfaces, *e.g.* single crystal surface structures, metal particles supported by oxide surfaces, oxide films on metal single crystals, micro-structural characterization of oxide compounds etc.. In particular, nickel oxide (NiO) has attracted high interest because of its fascinating chemical and magnetic properties enabling a potential successful implementation in many high impact devices of technological interest such as catalysis and high-density magnetic data storage technologies (using giant magnetoresistance (GMR) effects). A number of puzzling issues of fundamental interest are however still pending. The direct inclusion of NiO films in complex structures like spin-valves makes the characterization of the wealth of important properties critical. As a matter of fact mastering the growth of NiO remains a challenging issue. In the framework of NiO growth, because of their chemical stability, small parameter mismatched noble metals or oxide substrates have been the main subject of fundamental studies.

However, for the technologically useful GMR systems, the basic principle consists of the pinning of a ferromagnetic transition metal layer by an antiferromagnet such as NiO, the actual interfaces being thus made of NiO in direct contact with transition metals (typically Cu for the non-magnetic spacer and Ni, Fe and Co for the magnetic layers). Up to now the fine tuned description of such interfaces largely remained in its infancy, although it is obviously mandatory for the sake of a better understanding of the role of each interface when properties like “orange-peel” due to interface roughening or oscillatory exchange coupling effects are considered. Moreover these effects generally severally limit the device usefulness and deserve thus high attention with respect to device optimization.

We have thus undertaken studies aiming at tackling the important question of the description of the interfaces really involved in GMR structures, even the ones that may only occur on pin-holes *i.e.* direct contact of the spacer and the antiferromagnet. Different preparation methods were used and/or developed in order to characterize each of the possible interfaces when building “top” spin-valves (NiO is deposited on top of the transition metal layers). Since the ferromagnetic transition metals have a known large affinity to oxidation that is detrimental to the devices, it was important to develop a deposition method, excluding an oxygen partial pressure during deposition, allowing growing NiO films at low substrate temperatures. In order to understand the role of oxygen on the growth, it was in turn also important to study the growth of metallic nickel and of NiO films elaborated under partial oxygen pressure.

The two first chapters I will introduce briefly the scientific background of my thesis work and the experimental methods that I used.

In the first experimental part **(chapter 3)** I will present the study of the growth of metallic Ni films on Cu(111). The aim of this study is to introduce and compare the effects on magnetic properties for instance, observed for metallic Ni films or alloys. Indeed such configurations may also appear at the NiO/Cu(111) interface.

In the second experimental part **(chapter 4)** I will present the detailed study of the NiO growth on a Cu(111) single crystal substrate at room temperature upon evaporation from NiO nuggets without an extra additional partial oxygen pressure in the chamber. The stoichiometry and chemical evolution as a function of the NiO thickness were studied through an analysis of the Auger signal *vs.* time (As-t) curves and of the XPS Ni 2p line shapes during the first stages of growth. In the second section we shall discuss the evolution of the morphology as a function of the deposited thicknesses. The last section will be devoted to the structural description of the NiO/Cu(111) interface, obtained through the analysis of Grazing Incidence X-ray Diffraction (GIXD) data.

In the third experimental part **(chapter 5)** I will introduce the temperature effects observed with respect to the crystalline order in the ultra-thin oxide films. In this part of my work I will also focus on a different NiO films preparation method. First experimental results belonging to NiO/Cu(111) ultra-thin films elaborated under a partial pressure of oxygen gas (O_2) will be presented. The differences and the similarities between the two methods of elaboration and the influence of the temperature on the crystalline quality and homogeneity of the NiO films are discussed in this chapter.

Chapter 1:

SCIENTIFIC BACKGROUND

1.1 INTRODUCTION

While metal and semiconductor surfaces and interfaces were extensively studied since 20 years, comparatively less work has been done on oxide surfaces and thin films [Freu96, Cham00a, Good96, Kuhl97], although oxide surfaces play a major role in important industrial sectors such as catalysis, electronic devices, etc. Several physical reasons have severely hindered scientific studies of oxide surfaces, as for example: the lack of availability of high-quality oxide surfaces and difficulties due to the insulating nature of most oxide materials, preventing the use of electron based spectroscopies. Nevertheless, several studies on oxide materials exist nowadays showing that the oxides surface science is in continuous expansion. Due to the potential applicability in new technologies (catalysis [Freu02, Freu93, Capp93], nuclear waste packaging [Fuji95a], sensors [Lund96, Ulme97, Comi02], electronic devices: GMR, TMR, spin-polarized tunneling junctions, MRAMs [Baib88, Chie95, Slau02, Maek82, Suez87, Suez92]) a huge research effort has been devoted to oxides in the very recent years.

Thin-film growth techniques enabled the preparation of model oxide surfaces only recently. In this way, films a few angstroms thick can be grown. Their crystalline quality depends strongly on the lattice parameter misfit between the oxide and its substrate and on preparation conditions such as deposition rate, oxidizing temperature etc. These ultra-thin films exhibit several unusual properties which are of interest both from fundamental [Fuji96, Alde98] and technological application point of view [Freu02, Freu93, Capp93, Fuji95, Lund96, Ulme97, Comi02, Baib88, Chie95, Slau02, Maek82, Suez87, Suez92]. First, because of their small thickness, charge build-up is less efficient and electron spectroscopies can be applied successfully. Through such techniques the field is no longer limited to the less stable cleavage planes of the bulk, and may even be extended to polar surfaces [Freu93]. The substrate induced strain may also lead these epitaxial oxide layers adopting lattices different from those of the thermodynamically stable bulk.

As a matter of fact the field can be splitted in two major issues: the development of oxide materials fundamental studies seeking the complete characterization (structural, electronic structure, magnetic properties) of the mono-crystalline model oxide surfaces (reviews: [Henr94, Freu93, Freu96]), and the elaboration and the characterization of thin oxide films (reviews: [Cham00a, Fran00]).

In the following chapter we aim at providing a brief overview of the state of art of the domain of oxide materials surface science. We restrict our presentation to the oxide materials involved in the development of the future generation of electronic devices and especially to

the so-called *magnetic oxides* (transition metals oxides – TM oxides): NiO, CoO, FeO, α-Fe_2O_3, Fe_3O_4, CrO_2, α-Cr_2O_3. This section should highlight the framework of my own studies on NiO which is the major topic of my work. The interested reader can find more exhaustive presentations in several recent reviews concerning the oxides surface science [Freu93, Henr94, Freu96, Rena98, Cham00a, Fran00, Weis02].

The following section is split in four parts, following the classification of oxide materials function of their crystallographic structure (figure 1.1): rock-salt oxides (NiO, CoO, FeO), corundum oxides (α-Fe_2O_3, α-Cr_2O_3), rutile oxides (CrO_2) and spinel oxides (Fe_3O_4).

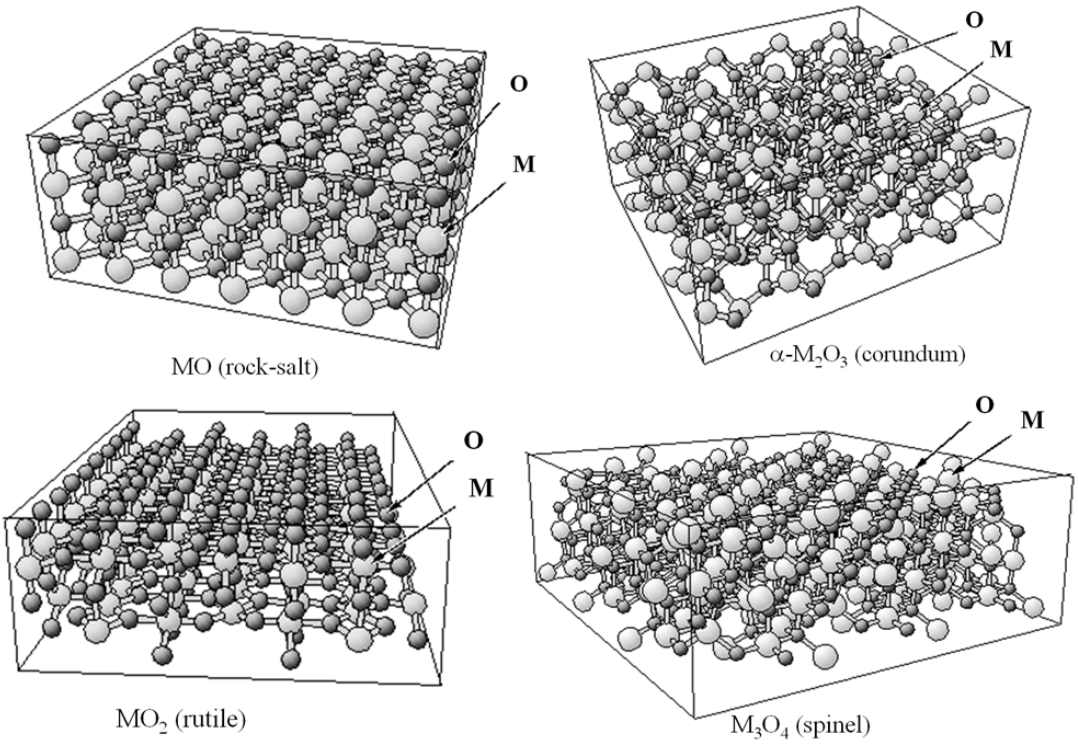

Figure 1.1: *Classification of oxides with respect to their structure*
Larger circles stand for the metal atom and smaller circles for the oxygen atoms, as indicated in each case.

We will pay a particular attention to the properties of thin epitaxial oxide films. In the case of the NiO and CoO we give also some results concerning the bulk properties (from [MocuPhD]).

1.2 STATE OF THE ART

1.2.1 Rock-salt oxides: NiO, CoO, FeO

The crystalline and magnetic structures of NiO and CoO were described in detail by Roth et al. [Roth58a]. Above the Néel temperature, the crystal structure of CoO and NiO is face centered cubic *Fm3m* and magnetically disordered (paramagnets). The lattice constants of NiO (4.177 Å) and CoO (4.26 Å) differ by only 2% at room temperature. Below the Néel temperature (523 K for NiO and 292 K for CoO), both oxides exhibit a spontaneous antiferromagnetic (AF) ordering. Figure 1.2 shows a type II AF structure, consisting of (111)

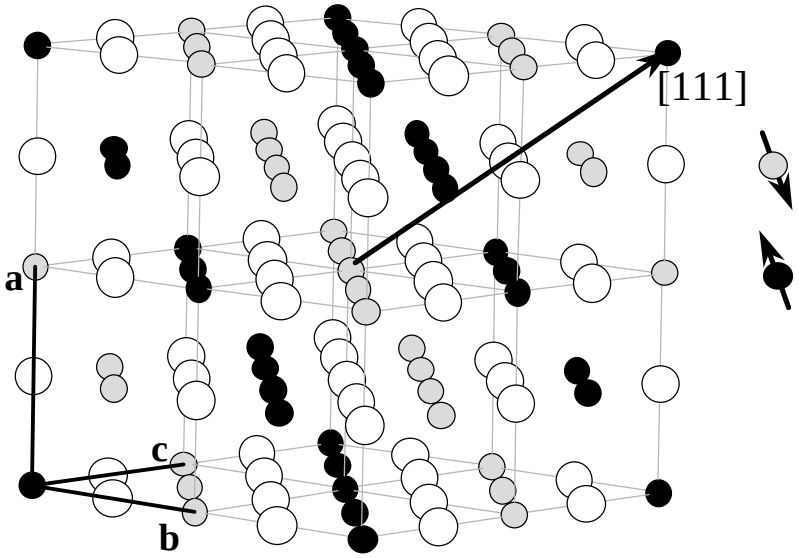

Figure 1.2: *Chemical and magnetic structure of antiferromagnetic NiO*:
The smaller filled circles stand for the magnetic metal atoms, and the larger empty ones are the oxygen atoms. The spins are ferromagnetically aligned in (111) planes. The Ni planes are super-exchange coupled antiferromagnetically through the oxygen atoms. The magnetic unit cell is twice as large as the structural one along the [111] direction.

ferromagnetically (F) aligned spins planes, with anti-parallel coupling between planes: the spins of the cations are anti-parallel to their next-nearest neighbors (along the [111] axes) due to the super-exchange through oxygen atoms. As a consequence, 8 independent magnetic sub-lattices can potentially exist. Early neutron diffraction measurements on bulk NiO and CoO support the existence of only two magnetic sub-lattices rather than a multi-spin axis configuration [Roth58b].

The AF ordering is related with crystallographic contractions along particular axes: tetragonal distortion (contraction along the [100] cubic axis) in the case of CoO, and a rhombohedral distortion (contraction along the [111] axis) for NiO. This distortion increases

linearly with decreasing temperature, and is attributed to the dipolar coupling between the ferromagnetically aligned (111) spin planes.

Unlike their similar crystalline structures, the electronic structure differences of Ni^{2+} and Co^{2+} yield to different magnetic properties (spin and magnitude of magneto-crystalline anisotropy). The anisotropy in type II AF materials has been discussed and calculated [Kapl54, Keff57, Yama66]. In NiO, the dipole-dipole interaction predominates, and the magnetization lies in the (111) plane. There is a weak in-plane anisotropy which is the result of second-order effects aligning the spins along the $[11\bar{2}]$ directions. Unlike NiO, the CoO experiences a large tetragonal distortion (1.2%) in the ordered magnetic state. The spins do not lie in the (111) plane, but are parallel to a $[\bar{1}\,\bar{1}\,7]$ direction: the spins are tilted 23.8° above the (111) plane and 11.4° from the [001] contraction axis. The resulting spin alignment is a compromise between the dipole-dipole interactions and the crystalline field that arises from the deformation which favors a direction parallel to the [100] tetragonal axis.

In summary: CoO has a high magneto-crystalline anisotropy and a low Néel temperature (T_N = 292 K), while NiO has a much lower magnetocrystalline anisotropy (quenched orbital momentum) but a considerably higher Néel temperature (T_N = 523 K). The properties of NiO and CoO can be combined in alloys ($Ni_xCo_{1-x}O$) and multilayer structures [Care92, Care93a]. The $Ni_xCo_{1-x}O$ alloy is very interesting and was extensively studied since it allows studying AF materials within a wide range of magnetocrystalline anisotropy and ordering temperatures [Taka98].

Polar surfaces

The prototype of the polar crystals is the ionic rock-salt NaCl, having a cubic closed packed crystallographic structure, in which the Na^+ and Cl^- ions alternate along the [111] direction. These crystals naturally show (100) facets. The (111) surface cannot be naturally observed, thus suggesting that it is highly unstable from an electrostatic point of view. Calculations of the surface energy for different compounds and surfaces show that the (111) surface is of high energy, and should thus not appear when crystallites are formed ([Tayl99, Wolf92, Shi88, Task79]).

Indeed, along the cubic [111] direction, pure Na^+ and Cl^- ion sheets alternate (figure 1.3-a). Each two layers (one of Na and one of Cl), form an electric dipole of dipolar moment

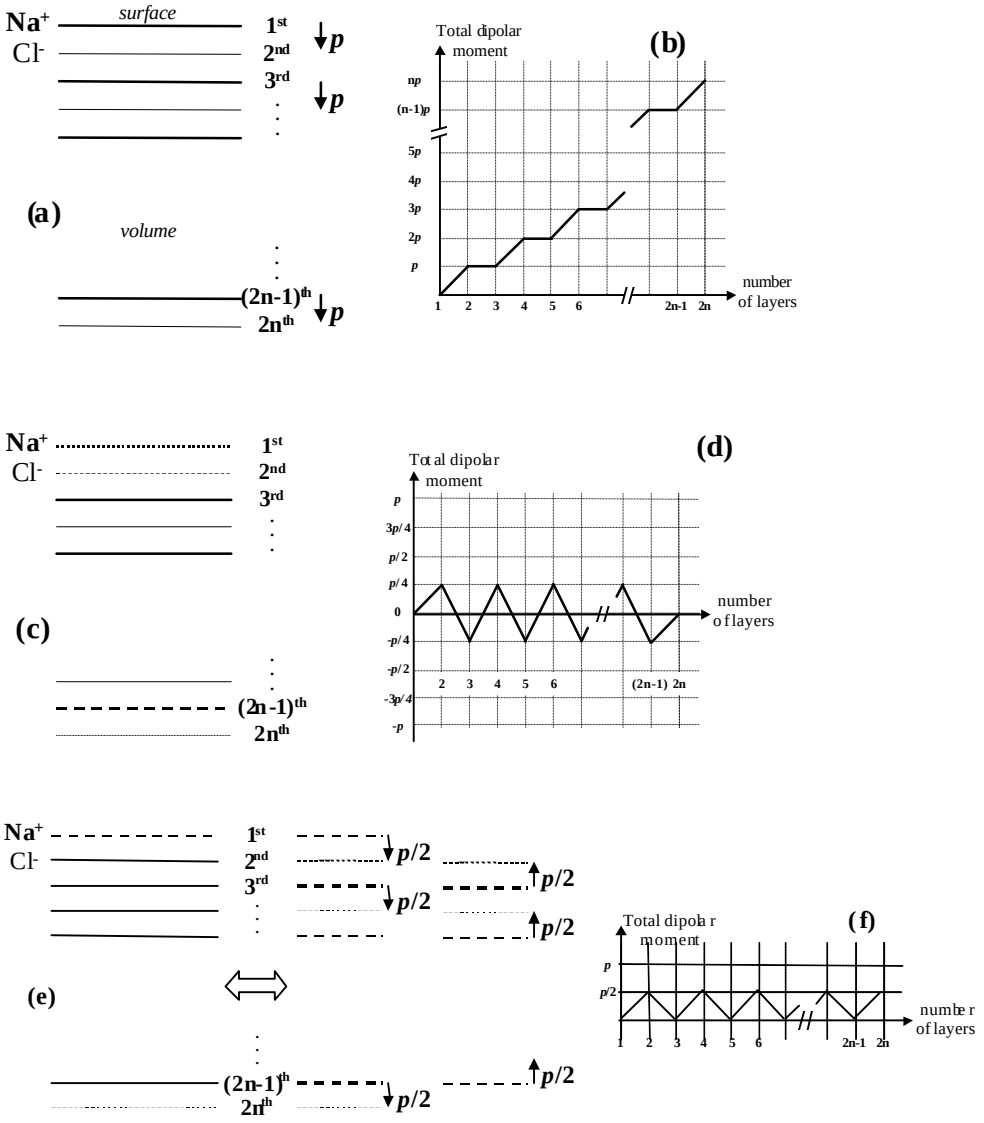

Figure 1.3:
(a) Schematic view of the alternating anionic and cationic planes for a polar surface; (b) The total dipole moment evolution (similar to the Coulomb potential), showing its divergence with increasing the number of layers. (c) Configuration stabilising the polar surface (octopolar reconstruction). Dashed and dotted lines stands for 3/4th, respectively 1/4th, occupied layers. (d) the dipolar moment is found to oscillate around zero. (e) Another configuration which can stabilise the polar surface. Dashed lines stand for half occupied layers. The total dipolar moment is calculated using the equivalent scheme showed on the right side: splitting into two polar surfaces of opposite dipolar moment, with $p/2$ dipolar moment per layer. (f) The evolution of the total dipolar moment with the number of layer (oscillations around a $p/4$ mean value).

$\boldsymbol{p}$. The total dipolar moment ($\sum_{i=1}^{n} \boldsymbol{p}$) and the resulting coulomb potential are diverging with the number of layers ($2n$) (figure 1.3-b).

A simple way to stabilise these polar surfaces is to consider an octopolar basis for the bulk unit cell [Wolf92]. Maintaining full octopolar unit cells at the surface leads to a p(2×2) surface reconstruction. This reconstruction is obtained from the standard bulk unit cell by removing atoms. The reconstruction extends over two atomic planes: 3 atoms over 4 of the

last surface plane are missing and 1 over 4 of the second plane (figure 1.3-c, 1.3-d). In this case the Coulomb potential oscillates around zero and its mean value is zero, too. In this simple way, the divergence in Coulomb potential exhibited by a polar surface is avoided. This model leads to the formation of two atomic planes high micro-pyramids on the surface. Alternatively, a reconstruction extending over one surface plane, with half of the atoms missing in the first surface plane (figure 1.3-e, 1.3-f) may stabilise polar surfaces too. The Coulomb potential is now oscillating around half the mean value of the one corresponding for two layers.

Despite their interesting properties, epitaxial NiO thin films were seldomly studied for themselves. Most of today's knowledge is related to their properties when directly implemented in complex structures such as spin-valves [Care92, Soey93, Oshi96, Soey97, Kita96]. Moreover, the sputtering elaboration technique, widely used in their fabrication, leads to formation of polycrystalline films which are not well suited for fundamental studies, i.e. the relationship between structure, morphology and magnetic behavior cannot be established easily. Thus, only relatively few results concerning the growth and the properties of the NiO, CoO and FeO thin[♣] films can be found in the literature. I will now present briefly these results.

1.2.1.1 *The growth on oxide substrates*

The crystallographic lattice and the mesh parameters of NiO and CoO are close to the MgO (1% lattice mismatch, *Fm3m* structure), making it an attractive substrate. Imaduddin and Lad [Imad96, Imad95] used OPA-MBE ("*Oxygen Plasma Assisted – Molecular Beam Epitaxy*") to grow MgO on NiO(001) as well as NiO/MgO superlattices using NiO(001) as substrate and growth temperatures in the 100 – 250°C range. High-quality crystalline layers can be grown in this temperature range. However, it does not clearly appear that the growth proceed in a layer-by-layer manner. UPS ("*Ultraviolet Photoemission Spectroscopy*") measurements performed after the completion of various layers in a superlattice structure revealed the consistency in electronic structure that can be achieved for superlattices periods as small as 10 Å.

[♣] Note that the notion of "thin" and "ultra-thin" layers vary from one author to the other. There is no necessarily a strict definition of the boundary between the two of the cases. However, the reader have to keep in mind that all the reports reviewed here concerns generally films with thicknesses larger than 10 Å.

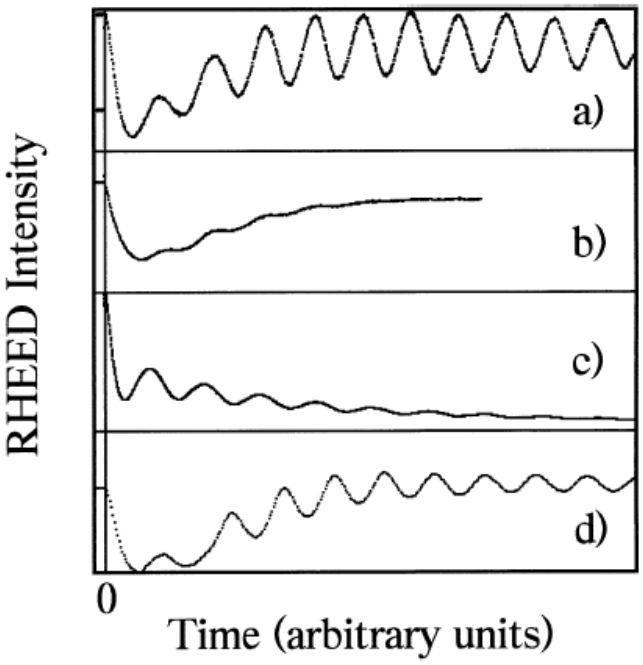

Figure 1.4: *RHEED specular beam intensity oscillations for NiO grown on*:
a) ex situ cleaved MgO (001) at 400°C;
b) in situ cleaved MgO (001) at 400°C;
c) NiO film that was previously grown on MgO (001) at 400°C, but with the latter film grown at 30°C;
d) CoO film grown on ex situ cleaved MgO (001) at 400°C. Taken from [Peac94]

Peacor and Himba [Peac94] used NO_2 – assisted MBE to grow both NiO and CoO on cleaved MgO(001) maintaining the substrate temperature at 400°C. They found that NiO can be grown in a layer-by-layer fashion when cleaved MgO(001) is used in a temperature range from 200°C up to 450°C, as suggested by RHEED ("*Reflection High Energy Electron Diffraction*") oscillations (figure 1.4, taken from [Peac94]). It is interesting to remark that in figure 1.4-c, the authors report the NiO growth at 30°C on a previously grown NiO layer at 400°C (NiO homoepitaxy). The author's main conclusion was that growth at substrate temperatures smaller than 200°C results in poorly ordered films. In the case of the CoO growth they found that the ratio between the Co and the O fluxes dramatically influences the nucleation of CoO. Increasing the oxidation favors crystalline Co_3O_4 spinel, leading to twice the MgO parameter.

Using the same method for the nickel oxide film elaboration, Alders et al. [Alde98] performed XAS ("*X-ray Absorption Spectroscopy*") and XMLD ("*X-ray Magnetic Linear Dichroism*") on NiO films for 5, 10 and 20 ML (ML = mono-layers) film thicknesses deposited on MgO(100). Temperature-dependent XMLD measurements revealed that the Néel temperatures of the thin films are strongly reduced compared to the bulk value (figure 1.5): T_N = 470, 430, and 295 K for NiO films with thicknesses of 20, 10, and 5 ML, respectively.

More recent results of the NiO films grown on different surface orientations of MgO (MgO(001), MgO(110), and MgO(111)) were reported by Warot et al. [Waro01], using the RF-sputtering deposition method in an UHV preparation chamber. The authors studied the

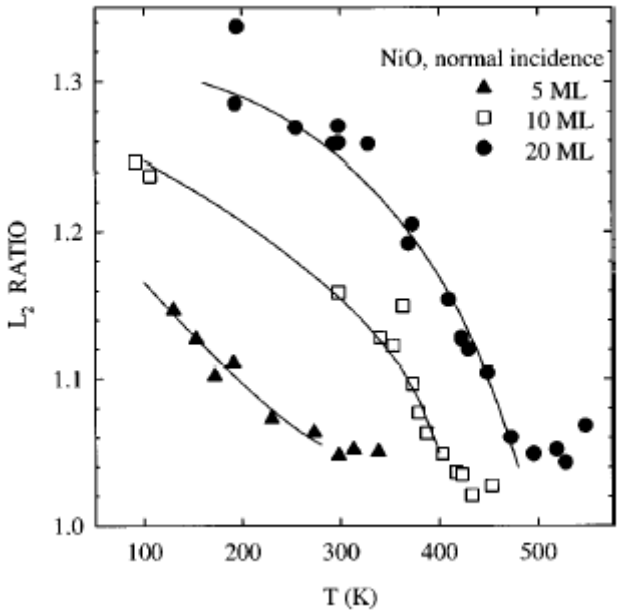

Figure 1.5:
Temperature and thickness dependence of the ratio of the two peaks in the Ni L2 – XAS of NiO(001) films, taken at normal incidence. Néel temperatures of 290, 430 and 470 K can be found for the 5, 10, and 20 monolayer films, respectively. (taken from [Alde98])

influence of the MgO substrate orientation on the surface morphology of the deposited layers. Using combined RHEED, TEM ("*Transmission Electron Microscopy*") and AFM ("*Atomic Force Microscopy*"), they evidenced a flat NiO surface on MgO(001), whereas the NiO layers on MgO(110) and MgO(111) were found to be very rough. Two different surface microstructures depending on the substrate orientation were found: wires in the case of NiO/MgO(110) and tetrahedrons for the NiO/MgO(111), both structures presenting low surface energy (100) facets. The authors explain the different morphologies using energetic considerations. We have to remark that the used deposition method (RF-sputtering) and the range of the films thickness (> 100 Å) can not give a clear and detailed picture of the NiO growth. In all cases presented above, the threshold temperature for the interdiffusion was found to be of about 750°C.

The metal/oxide interface (with oxide = NiO and CoO, and metal = Fe, Ni, and Co) was studied by high-resolution XAS by Regan et al. [Rega01]. Two series of samples were fabricated *ex-situ* and *in-situ*: Ru(20Å)/metal(10Å)/oxide(10Å)/MgO(001), and Fe(1-10Å)/NiO(5-30Å)/Si, respectively. They show, using the strong chemical selectivity of XAS, the existence of an important chemical reaction at the metal/oxide interface and describe this interface as an oxidized-metal region adjacent to a reduced-oxide region. The authors showed experimentally that the origin of the exchange anisotropy at the interface is due to the uncompensated interfacial spin moments as proposed by Takano et al. [Taka97] earlier.

Although generally very popular, sapphire α-Al_2O_3 was less used to grow NiO films because of its huge lattice mismatch of 24% with the NiO lattice parameter. Mocuta et al.

[Mocu00a] grew NiO films with thicknesses between 300 and 2000 Å on α-Al_2O_3(0001) substrates within a temperature range of 320 – 700°C. Combined surface techniques such as LEED ("*Low Energy Electron Diffraction*"), AFM and GIXD ("*Grazing Incidence X-ray Diffraction*") were used to completely determine the structure and the morphology of the NiO films. They found a structure characterized by the formation of epitaxial NiO within a twinned fcc-scheme: the NiO unit cells are rotated by 30° and 90° with respect to the Al_2O_3 one, for the fcc and twinned-fcc stacking respectively. The morphology of the NiO films is characterized by the formation of micro-pyramids presenting (100) facets, a way to prevent the occurrence of the polar (111) surface.

Room-temperature NiO growth on the Al_2O_3 substrate was reported by Kakehi et al. [Kake02] using the PLD♣ ("*Pulsed Laser Deposition*") technique. They found similar results as in the case presented above (for MBE growth at high temperatures), i.e. formation of domains. In addition, the authors conclude that the crystalline quality of the NiO(111) films

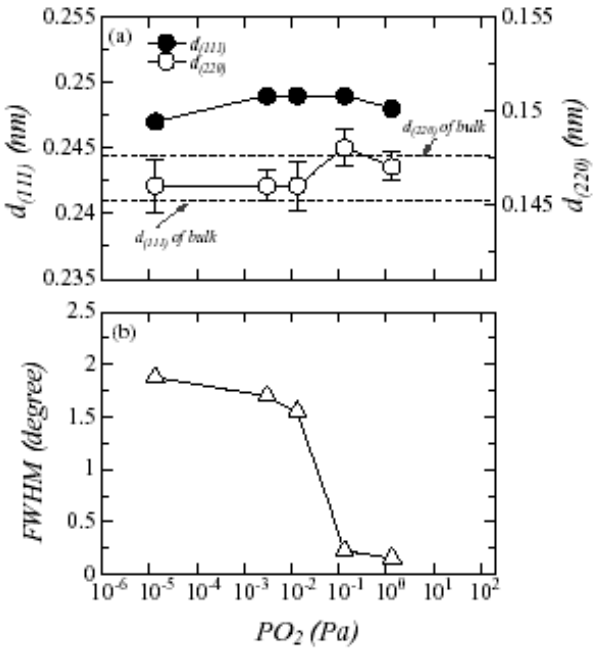

Figure 1.6:
a) Dependence on oxygen pressure of both, the out-of-plane ($d_{(111)}$) and the in-plane ($d_{(220)}$) lattice parameters of the epitaxial films;
b) The FWHM of the epitaxial films as a function of the oxygen pressure ([Kake02]).

can be improved by expanding the in-plane lattice parameter, $d_{(220)}$. However, taking into account the reported error bars, reproduced in figure 1.6, we consider their conclusion as speculative, since the improvement of the crystalline quality, proved by the decrease of the FWHM ("*Full-Width Half-Maximum*"), can also correspond to the reduction of the domains size when increasing the oxygen pressure.

♣ The PLD evaporation technique is very well suited for the elaboration of thin films presenting complex stoichiometries.

The *wustite* ($Fe_{1-x}O$) is not stable in the bulk at temperatures below 580°C and therefore less attention was granted to its properties. Like NiO and CoO, $Fe_{1-x}O$ is insulator in the *Fm3m* rock-salt structure. In the case of thin films deposited on sapphire (α-Al_2O_3(0001)) the wustite-like phase presenting a 4% - 6% expanded in-plane lattice is obtained only for thicknesses below 1 or 2 ML (1 ML = 1 monolayer), while for thicknesses above ~2 ML either α-Fe_2O_3(0001) and Fe_3O_4(111) phases are formed [Gota01, Gota00, Gota99, Yi99, Fuji96].

1.2.1.2 *The growth on metallic substrates*

In order to perform charged-particle measurements, several groups have used metallic substrates. Due to their small lattice mismatch with the NiO lattice, Au(111) and Ag(001) were typically used as substrates. Ventrice et al. [Vent94] grew NiO(111) on Au(111) evaporating Ni in an O_2 atmosphere of 2×10^{-6} torr maintaining the substrate at 300°C. These authors were able to image the resulting surface with STM ("*Scanning Tunneling Microscopy*"), the recorded images corresponding to a p(2×2) NiO reconstruction.

Figure 1.7 reproduces the STM images obtained for different tunneling conditions, the differences between the images being related to the presence (figure 1.7-a) or the absence (figure 1.7-b) of an oxygen atom on the wolfram (W) tip. The three-atom clusters appearing in figure 1.7-b are interpreted as being Ni ions observed with an oxygen contaminated STM tip. A fourth atom was imaged at the apex of each triangle when the tip was considered to be clean (tungsten tip) and was related with the O ions present in the top layer of the film. This

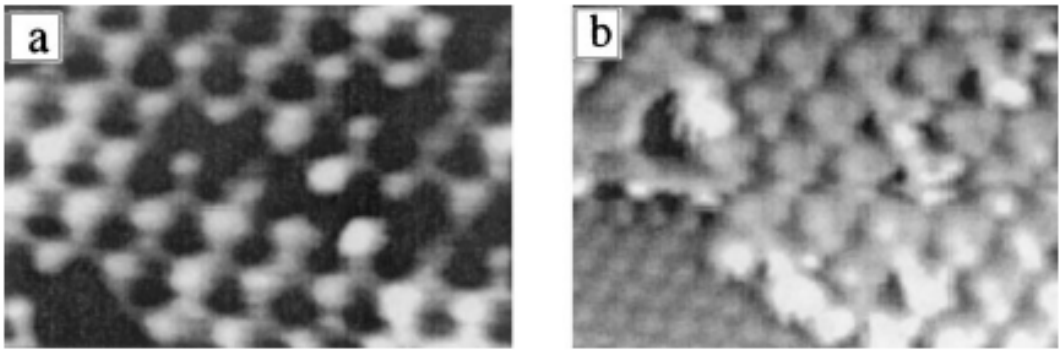

Figure 1.7: *STM images from thin NiO(111) p(2´2) films grown on Au(111):*
a) clean tip, U = -5 V;
b) oxygen adsorbed tip, U = -0.3 V. The tripod structures are related with Ni atoms position and the bright structures in a) are thought to be O atoms. (from [Vent94])

structure would satisfy the charge neutrality for the polar surfaces, as suggested by Wolf [Wolf92]. As it can be observed in the left side in figure 1.7-b, patches considered to be uncovered Au(111) appear. This behavior was suggested to be in relation with a possible diffusion of Ni in the gold substrate.

An experimental proof for the octopolar reconstruction proposed by Wolf [Wolf92] and observed by Ventrice [Vent94] was reported by Barbier et al. [Barb00a] using GIXD. Using the same experimental procedure as given by Ventrice et al. [Vent94], thin NiO films have been grown on Au(111). A perfect 2D growth was observed between 3 and 8 ML, before 3D crystallites of NiO are formed, as observed by RHEED. Interestingly, they found the same

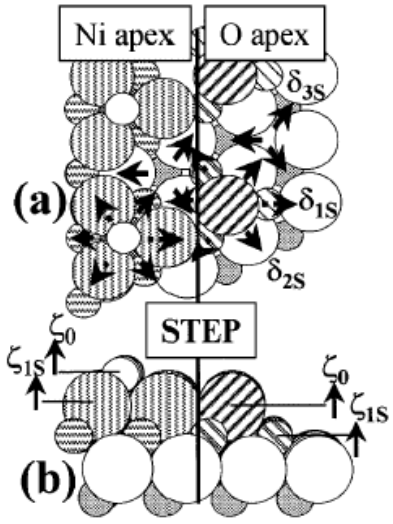

Figure 1.8: Top (a) and side (b) views of the two possible octopolar reconstructions with Ni- and O-terminated terraces, separated by a single step (solid line). Large circles are oxygen atoms, and small circles are Ni. For either termination, the top two layers are 75% and 25% vacant compared to the bulk lattice. The possible symmetry-compatible relaxations, δ and ζ, are shown as arrows, indicating a positive relaxation (taken from [Barb00a])

reconstruction as in the case of the NiO(111) single crystal surface [Barb00b, Barb99], but with the difference that the NiO(111) film can exhibit both Ni- and O-terminated octopoles. In figure 1.8 we reproduce the two possible octopolar terminations, as suggested by the authors (from [Barb00a]). Due to the existence of both types of terminated octopoles, single atomic steps should appear on the surfaces (formed by oxygen or nickel atoms). This model is in contradiction with the STM observations presented above, where double steps were observed to separate adjacent domains [Vent94]. The authors concluded that the STM results previously reported might be affected by the poor out-of-plane sensitivity of the STM, which hampers the possibility to observe single NiO(111)-p(2×2) steps (a perfect octopolar reconstruction is characterized by 25% vacant layer and 25% adatoms of the other species). To probe the chemical (hydroxylation) stability, the authors tested their NiO films dosing the surface with up to 10^6 L (1 L = 1 Langmuir = 10^6 torr×sec.) of H_2O at 3×10^{-5} mbar partial pressure at room temperature. Contrarily to other reported results [Rohr94, Kita98a, Kita98b]

where the NiO films are characterized by many defects, there were no surface modifications, suggesting that the reactivity of NiO(111) against water takes place mainly at surface defects.

Erdman et al. [Erdm00] suggested an alternative model where both octopolar reconstructions are stacked on each other.

Intensive work was carried out by different groups on the silver (100) surface. The Ag(100) has only a 2% lattice mismatch relative to the NiO lattice parameter, allowing therefore both good epitaxial conditions and charged-particle measurements. Sebastian et al. [Seba99 – see also [Bert96]] grew both NiO(100) and CoO(100) thin films studying them using LEED and STM techniques. They report the formation of NiO(100) and CoO(100) films both by subsequent annealing (450-550 K) of the room-temperature deposited films and by condensation of the films on the hot Ag(100) substrate (450-550 K). For room-temperature deposition an O/metal precursor state is identified that appears to have a height of one atomic layer both on top of the substrate and in the vacancy islands of the substrate. These vacancies are generated during the deposition process. In the initial stage, a 2D growth of the oxide is found which switches to a 3D growth for thicker films. The overall morphology and the chemical nature of the deposited films and of the substrate depend strongly on the deposition and annealing temperature.

Portalupi et al. [Port01] performed combined PE ("*Photoemission*") and IPE ("*Inverse Photoemission*") studies on NiO(100) thin films deposited on Ag(100) (unfortunately these authors do not specify the temperature of the substrate during the evaporation). The authors

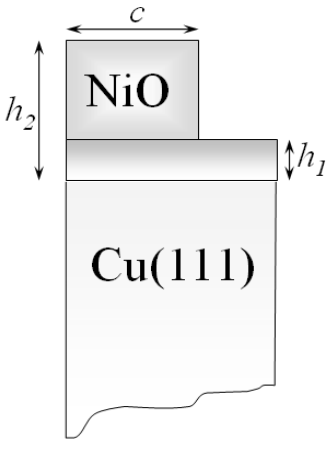

Sample	Height h_1 (Å)	Height h_2 (Å)	Coverage c (%)
0 min	0	0	—
19 min	2.7	0	0
49 min	3.8	>30	8
74 min	4.3	>30	20
104 min	5.0	>30	28
164 min	5.5	>30	44
284 min	10	>30	71

Figure 1.9: *NiO/Ni/Cu(111) layering:*
The table gives the evolution of the parameters describing the layering (h_1 – metallic Ni layer height, h_2 – adsorbate total height, and c – NiO top layer coverage) as a function of the deposition time. (from [Sanc00])

evidenced that by Ni evaporation under O_2 atmosphere the resulting NiO(100) surface phase

is closer to the ideal one (Fermi level localized near to the mid-gap) than those obtained by bulk single crystals (cleaved surfaces with a Fermi level strongly pinned at the valence band maximum).

Combined surface chemical analysis using XAS and XPS ("*X-ray Photoemission Spectroscopy*") was carried out on NiO films deposited by evaporating Ni under O_2 atmosphere on a Cu(111) substrate held at room temperature [Sanc00]. Quantitative analysis of the XAS and XPS spectra revealed the formation of a complete Ni metallic layer (~3 Å thick) at the interface entirely covering the Cu(111) substrate. On the top, defective NiO aggregates of ~30-40 Å high forms. The spectroscopic measurements also revealed formation of oxidized Cu. Annealing the NiO films up to 400°C lead to ordering of the NiO layer and the reduction of the Cu^{2+} to metallic Cu. In figure 1.9 we reproduce the evolution of the calculated parameters which characterize the NiO/Ni/Cu(111) layering. We remark that at the beginning of the growth only metallic Ni is present (deposition time of 19 min.) and that the oxide grows directly in a 3D mode with islands higher than 30 Å. The authors report that for higher thicknesses the 3D islands coalesce into a continuous stoichiometric NiO film.

Several groups have grown iron oxide films on Pt(111) by evaporating single or

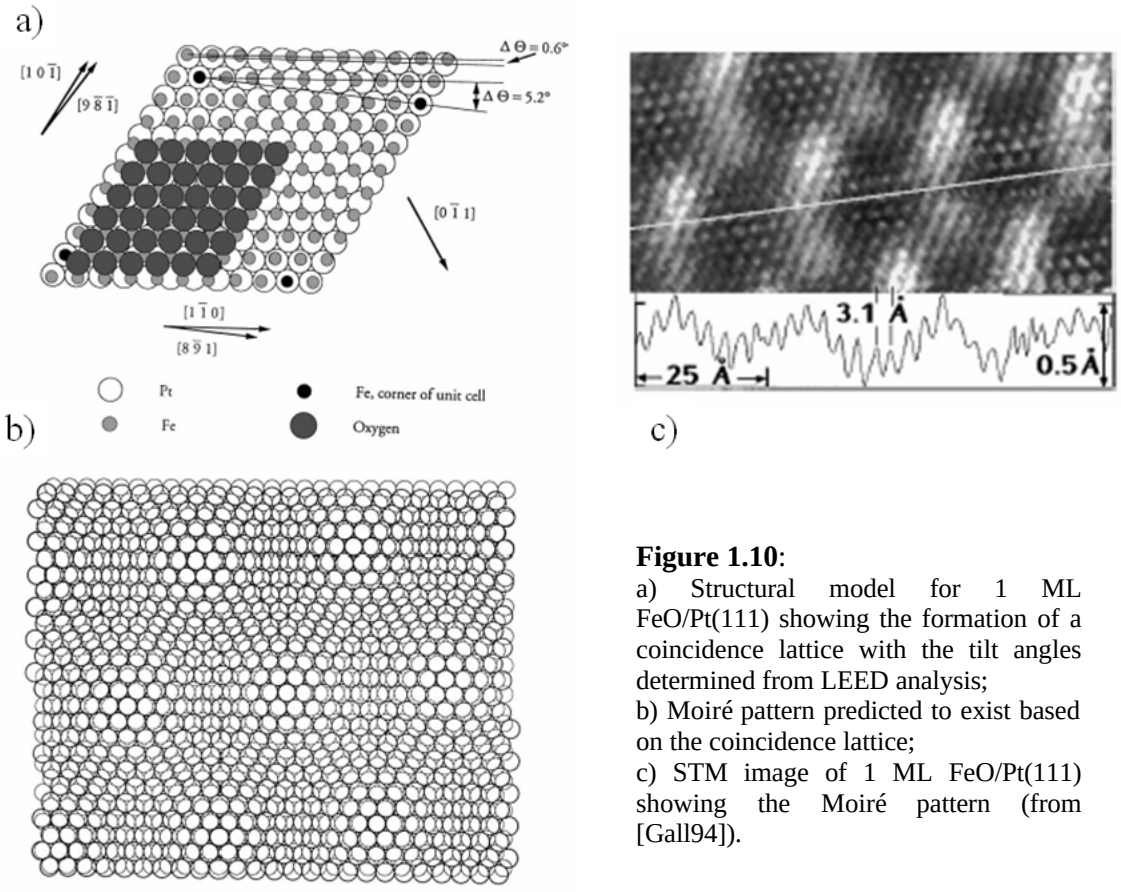

Figure 1.10:
a) Structural model for 1 ML FeO/Pt(111) showing the formation of a coincidence lattice with the tilt angles determined from LEED analysis;
b) Moiré pattern predicted to exist based on the coincidence lattice;
c) STM image of 1 ML FeO/Pt(111) showing the Moiré pattern (from [Gall94]).

multiple monolayers of Fe with the substrate held at room temperature followed by annealing in an O_2 atmosphere at pressures of ~10^{-6} torr and temperatures of 900-1000 K [Shar83, Vure88, Weis93, Gall93, Gall94, Gall96, Gao97a, Kim97a, Ritt97, Weis97, Cai98, Kim98, Sche98, Shai99a, Shai99b]. Like in the case of sapphire substrate, the stabilization of the wustite-like phase was found in the early growth stages (< 2ML) of Fe_3O_4 and α-Fe_2O_3. The first full monolayer nucleates in the FeO rock-salt structure. The large mismatch between FeO(111) and Pt(111) (~10 %) results in a coincidence lattice, as it can be observed in figure 1.10 [Gall94, Kim98]. The small misalignment of the rows of atoms along the $[1\bar{1}0]$ (0.6°) leads to a 5.2° rotation of the resulting 9×9 overlayer superlattice relative to the substrate, producing the Moiré pattern evidenced by LEED and RHEED and shown in figure 1.10-b. This Moiré pattern was also observed by STM, as seen in figure 1.10-c [Gall94]. The coincidence lattice acts as a template for the Fe_3O_4(111) overgrowth. Subsequent annealing in O_2 atmosphere at ~1100 K convert the film to α-Fe_2O_3(0001).

☑ *Although well characterized in epitaxial films grown on oxide or noble metals, the NiO thin films remain however poorly studied. In particular, the NiO/metal interfaces, of huge interest in innovative technological applications, yield questions concerning the phenomena governing the chemical and physical properties. Several of such points are the main subject of my work and will be discussed in the chapters dedicated to the experimental results of this manuscript: interdiffusion and dynamic at atomic level (the role of the oxygen), morphology, crystalline quality function of elaboration conditions, etc.*

In the following sections we present very briefly some major results concerning other oxide structures (corundum, spinel and rutile), not directly related with the subject of my work, but which allow a better comprehension of the general problematic of the thin oxide film growth.

1.2.2 Corundum oxides: a-Fe_2O_3, a-Cr_2O_3

1.2.2.1 *a-Fe_2O_3 growth and properties*

The iron oxides are one of the most thoroughly studied classes of thin film oxides. Like wustite, the α-Fe_2O_3 (*hematite*) is insulator and exhibits a nearest neighbor spacing of 2.90 Å. As already presented in the case of the rock-salt oxides, the mostly used substrates to grow iron oxides are Pt(111) and sapphire.

The primary advantage of the Pt(111) substrate [Shar83, Vure88, Weis93, Gall93, Gall94, Gall96, Gao97a, Kim97a, Ritt97, Weis97, Cai98, Kim98, Sche98, Shai99a, Shai99b] is that the resulting conductivity is sufficient to perform STM measurements. However, the major disadvantage is that on the Pt(111) surface only one epitaxial relationship is available,

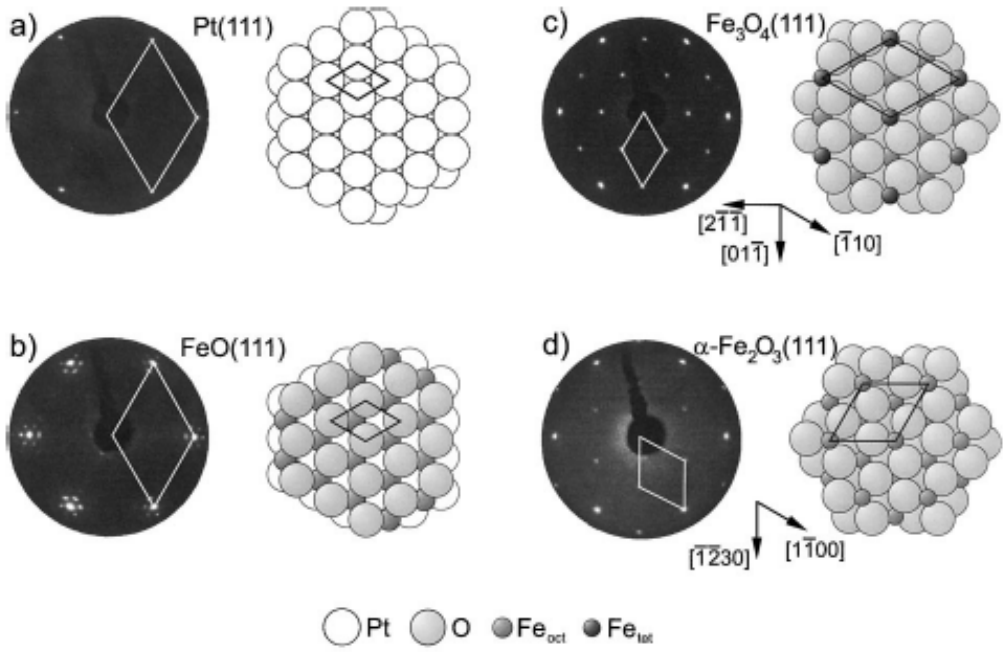

Figure 1.11: *LEED patterns at E = 60 eV for:*
a) Pt(111);
b) 1 ML FeO(111)/Pt(111);
c) > 150 Å Fe_3O_4(111)/Pt(111);
d) > 150 Å α-Fe_2O_3(0001)/Pt(111). (from [Weis99])

i.e. $(0001)_{Fe_2O_3} \parallel (111)_{Pt}$, and therefore only one surface is available for the thin film. The hematite phase, α-Fe_2O_3, is obtained by annealing the *spinel* phase Fe_3O_4 (*magnetite*) at ~1100 K under an O_2 atmosphere at pressures of 10^{-5} torr up to ~0.1 torr. These different iron

oxide phases obtained by epitaxy on the Pt(111) surface are reproduced in figure 1.11 [Weis99].

OPA-MBE and NO_2-assited MBE growth of hematite was also been carried out on sapphire [Thev99, Gao97a, Gao97b, Fuji96, Gota01, Gota00, Gota99, Yi99, Cham98, Guio98, Kim97b, Tiet89, Fuji94a]. The advantage of the sapphire substrate is that several surfaces may be achieved in contrast to the Pt(111). The primary disadvantage of sapphire substrates for α-Fe_2O_3 is that both the substrate and the film are insulators, limiting therefore the measurements to non-charging techniques, or imposing some clever film dopings. Due to the large compressive lattice mismatch between α-Fe_2O_3 and α-Al_2O_3, a heavily strained wetting layer of fully stoichiometric α-Fe_2O_3 is formed along the $[11\bar{2}0]$ direction [Yi99]. This strained layer transforms to 3D nanocrystals above a coverage of few monolayers. An initial elevated growth rate (~0.1 Å/sec) kinetically impedes the transition from the strained layer-by-layer to relaxed 3D islands that leads to the nucleation of well ordered α-Fe_2O_3. Instead, a γ-Fe_2O_3 layer is nucleated and exhibits domains with 180° rotational twinning and surface orientations that deviate substantially from (111). The formation of single phase α-Fe_2O_3 does not occur once this γ-Fe_2O_3 layer has nucleated. The 3D islands gradually coalesce with film thickness into a reasonably flat surface. Gota et al. [Gota99] showed that for a deposit equivalent to one hematite unit cell, the islands coalesce and α-Fe_2O_3(0001) grows in a two-dimensional mode, with the hematite bulk in-plane parameter. Chambers et al. [Cham99a] performed STM measurements on such films which were doped with Fe(II) to enhance the conductivity. In conformity with their STM results, i.e. the step heights (~2 Å) equal to the difference between structurally equivalent planes in the corundum (0001) structure, the authors conclude that the surface consists of a single termination (terminated plane = 1/3 ML Fe). This result is in contradiction with that of Wang et al. [Wang98, Shai99a], whose calculations and STM images suggest that both the 1/3 ML Fe and O terminations can be stabilized on this surface.

1.2.2.2 *a-Cr_2O_3 growth and properties*

Chromium oxide ultra-thin films are of great interest due to the wide variety of their technological application. The most stable phase of chromium oxide is the corundum structured α-Cr_2O_3. This corundum-like antiferromagnetic material has found use as an industrial catalyst [Yerm75, Conn69]. The corundum phase has a reasonable lattice matched

with sapphire (~3 %). Also, like in the case of iron oxides, the oxygen sublattice of the (0001) orientation aligns with Pt(111) with an in-plane mismatch of ~2.5%. We note also that oxidation of Cr(110) single crystals produces a α-Cr_2O_3(0001) overlayer of thickness equal to at least 10 Å.

Chromium oxide was grown on Pt(111) surfaces [Zhan97a, Robb98, Zhan97b] by evaporating Cr metal at a rate of ~0.2 ML/min in an O_2 background of 2×10^{-6} torr maintaining the substrate at 300°C. The LEED results indicate that the films initially grow forming a p(2×2) overlayer with respect to the Pt(111) substrate. Comparison of UPS spectra with band structure calculations give evidence that Cr_3O_4(111) is stabilized at the interface for at most a fraction of a monolayer, followed by transformation to a metastable phase γ-Cr_2O_3. At ~3 ML, a second phase appears with a $(\sqrt{2}\times\sqrt{2})$R30° orientation relative to Pt(111). This latter phase appears to be the corundum one, α-Cr_2O_3(0001), which predominates increasing the film thickness. STM images obtained at submonolayer coverages show that nucleation of both chromium metal and chromium oxide occurs at the steps of the Pt(111) surface.

The chromium oxide corundum phase was also elaborate on sapphire substrates by OPA-MBE at a growth rate of ~0.1 Å/sec, an oxygen pressure of 2×10^{-5} torr, a plasma power level of 250 W, and a substrate temperature of 500°C [Cham00b]. Periodic RHEED oscillations were observed after deposition of ~5 ML, persisting up to ~16 ML. The in-plane lattice parameter steadily increased from that of the substrate to that of bulk α-Cr_2O_3(0001). In addition, the film surface shows a much higher step density than the starting substrate surface. Therefore the authors describe the growth as a quasi-layer-by-layer growth accompanied by a structural transformation of the film. High-resolution Cr 2p and O 1s core-level spectra for films of ~120 Å thickness revealed well defined multiplet splitting characteristic of the Cr(III) state, as expected from well ordered material.

1.2.3 Spinel oxides: Fe_3O_4

As its corundum counterpart, the spinel Fe_3O_4 known as *magnetite* is the most common and stable iron oxide phase. In contrast with the α-Fe_2O_3 the spinel Fe_3O_4(111) contains fcc layers of oxygen with different arrangements of Fe cations in between. The oxygen nearest neighbor spacing is 2.97 Å. Charging is not an issue for the spinel phase because this oxide is conductive at room temperature. Probe charges can thus be conducted away through the film.

On Pt(111) substrates the spinel phase is stabilized by evaporating metallic Fe with the substrate at room temperature followed by annealing in an O_2 atmosphere at temperatures of 900-1000 K [Shar83, Vure88, Weis93, Gall93, Gall94, Gall96, Gao97a, Kim97a, Ritt97, Weis97, Cai98, Kim98, Sche98, Shai99a, Shai99b]. The first full monolayer nucleates in the rock-salt phase which acts as a template for the Fe_3O_4 overgrowth in the Stranski - Krastanov growth mode. Islands coalescence occurs for film thicknesses in excess of 150 Å, giving rise to relative flat surfaces of good crystallographic quality.

Another substrate used extensively to grow the iron oxide spinel phase was MgO presenting different surface orientations [Gao97b, Gao97c, Gao98, Lind91, Lind92, Fuji99, Voog95, Voog97a, Voog97b, Voog99, Cham99b, Bloe96, Cham98, Kim97b, Ande98, Voog98, Cher97, Ande97, Akta97, Gain97a, Band85, Hibm99, Heij98, Font97, Heij95, Fuji94b, Fuji90a, Fuji90b]. The lattice mismatch between Fe_3O_4 and MgO(001) is of 0.38%, taking into account the factor-of-two difference in lattice parameter between the spinel and the MgO. The Fe_3O_4/MgO(001) interface is thermodynamically unstable, leading to cation interdiffusion for substrate temperatures higher than 450°C [Voog99]. Despite the intensive use of the STM and the possibility of obtaining images with atomic resolution [Bloe96, Ande97, Gain97a, Gain97b, Gain97c, Stan00], there is a controversy and ambiguity concerning the interpretation of these images (existence of different possible stable terminations, tetrahedral Fe or octahedral Fe [Cham00a]). Without detailing this topic, it seems that the termination of the Fe_3O_4(001) surface depends exclusively on the sample history. Another important aspect concerning the iron spinel/MgO(001) heteroepitaxy is that antiphase boundaries forms in the films as a natural consequence of the different crystal symmetries and the factor-of-two difference in lattice parameters of the films and the substrate. The nucleation of 2D platelets of spinel can lead to the formation of antiphase boundaries upon coalescence due to the improper stacking within the cation sublattice [Marg97]. The presence of such defects can explain the anomalous saturation magnetization behavior of Fe_3O_4 films compared to bulk materials [Marg96]. It is possible to grow Fe_3O_4 on MgO(110), although faceting on the substrate surface results in poor film quality and very rough surfaces.

1.2.4 Rutile oxides: CrO_2

Another stable phase of the chromium oxide is the rutile-like structure, CrO_2. It is a conducting ferromagnet and is used in magnetic recording media because of its resistance to

corrosion and high coercivity. CrO_2 crystallizes in the tetragonal rutile-type structure (space group: $P4_2/mnm$) where the chromium atoms form a tetragonal unit cell. The Cr sites are octahedrally surrounded by oxygen atoms. The lattice parameters of the unit cell are a = 4.421 Å and c = 2.916 Å [Tham57]. The CrO_2 phase is a metastable oxide phase that degrades at temperatures above 400 K and atmospheric pressure into the thermodynamically more stable Cr_2O_3 phase (a = 4.951 Å; c = 13.566 Å; space group: $R3c$) [Fing80]. Therefore the preparation process is very sensitive to changes in temperature and oxygen pressure [Cham77]. The theoretically predicted 100% spin polarization at the Fermi energy EF of CrO_2 [Schw86] makes it a promising material for magnetoelectronic devices. According to Jullière's model [Jull75] the magnetoresistance (MR) of ferromagnet/insulator/ferromagnet tunnel junctions depends on the spin polarization of the ferromagnetic electrodes used. The MR increases with increasing spin polarization of the electrode materials involved. This resulted in revived research interest for CrO_2 [Li99a, Yang00, Li99b, DeSi00, Yang01, Spin00].

1.3 MAGNETICALLY EXCHANGE COUPLED SYSTEM

Metal-oxide interfaces are used in many innovating technologies. In particular, the interfaces made of a ferromagnetic medium with an antiferromagnetic one, are of a great interest. They are used in the fabrication of spin-valves sensors (magnetic read heads [IBMa, Read, Seag]), position sensors [Chai97] and *Magnetic Random Access Memory* (MRAM) elements [IBMb, Motorola]. The phenomenon underlying their functioning is the *magnetic*

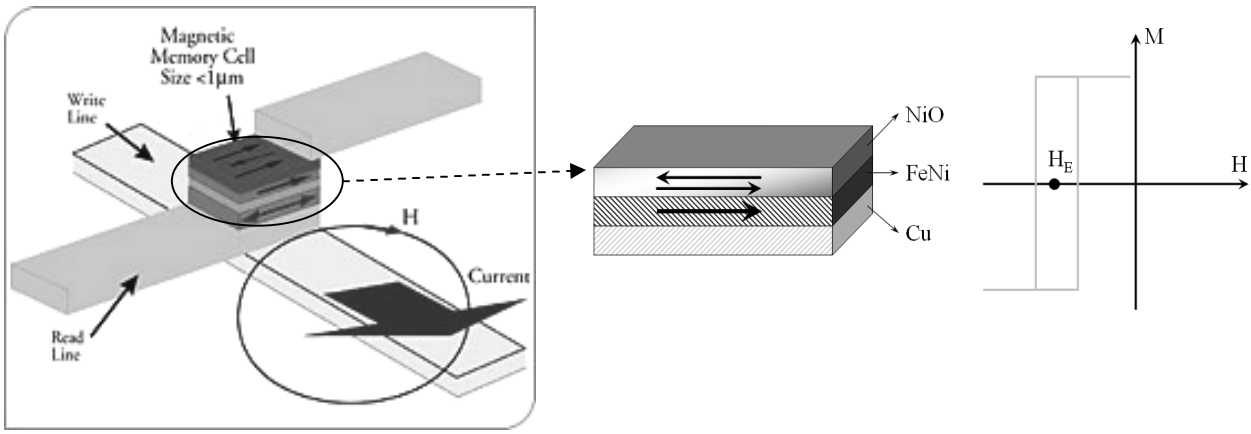

Figure 1.12: *exchange coupled system with FeNi and NiO:*
The ferromagnetic layer (FeNi) is pinned by the antiferromagnetic one (NiO). The resulting hysteresis loop will be characterized by a shift equal with the exchange field (H_E). The MRAM picture (left) is reproduced from [beyond2000].

exchange coupling which appears at these interfaces: the ferromagnetic layer is magnetically pinned by the antiferromagnetic one (figure 4.1). Therefore, the magnetic response of the ferromagnetic layer will depend on its coupling with the antiferromagnetic one by a quantity called “exchange field” or “exchange bias” (H_E). The magnetic exchange coupling is characterized by the hysteresis loop (M = f(H)) shift with a value equal to H_E and by the increasing of the coercive field (H_C).

A wide variety of coupled interfaces (review articles: [Kool96, Nogu99]) was studied until now but the results concerning their characteristics and behavior are mainly based on speculations relative to interface properties as roughness, diffusion, etc. In addition, the preparation techniques generally used in these studies (rf or dc magnetron sputtering, ion beam sputtering, electron beam deposition, or even molecular beam epitaxy) yield polycrystalline interfaces, which are not suitable for detailed characterization, especially concerning the liaison between the structure and the magnetic behavior.

In the present work we focused on the structural characterization of magnetically coupled interfaces with a special attention devoted to the different interfaces that may appear for a typical top spin-valve made of NiO/NiFe/Cu/NiFe/Substrate. Indeed, NiO is an antiferromagnetic oxide of choice because the high stability of rock-salt NiO and the lack of other stoichiometries allow an easy evaporation allowing implementation in industrial devices. The strong chemical stability of NiO makes it a good capping layer too. While the Cu/NiFe interface is well known, the overall properties of NiO/NiFe/Cu bilayers is not yet well understood, as well as many metal/oxide interfaces. Many morphological and structural questions about effects like pin-holes (direct contact between NiO and Cu) or oxidation quality remain open. In the present work we have not performed extensive magnetic measurements, many groups and/or laboratories (academic or industrial) are already involved in the optimization of complete spin-valve structures. Here we have chosen a more fundamental approach, in which we tried to provide a better knowledge of the interfaces as far as the structural, chemical and morphological properties are concerned.

The set of studies we provide about Ni, NiO nuggets evaporation and Ni under oxygen aims at understanding the way oxidation occurs and in which respect this affects the overall interface when pin-holes are formed. Some first studies of NiFe/NiO/Cu(111) interfaces were also undertaken in order to understand the growth of the ferromagnetic overlayer when bottom type spin-valves are considered.

Chapter 2:

EXPERIMENTAL TECHNIQUES

The results presented in this work were obtained using a wide range of *in-situ* laboratory and synchrotron radiation techniques. I will present here an overview of the characterization techniques, emphasizing the specificity of each of them related with the surface chemistry, structure, morphology, and magnetic properties.

2.1 SURFACE CHEMISTRY

One of the important characteristics of metal/metal and ultra-thin oxide/metal interfaces is the chemical composition. The spectroscopic techniques are intensively used in this cases due to the strong surface sensitivity (electron inelastic mean free path – IMFP – between 5 and 20Å) and to the element dependent sensitivity. Furthermore, using the classical attenuation law, $I(d) \propto I(0) \times e^{-d/l}$ these techniques can be successfully used in the determination of the growth modes. This approach is widely used for the thickness calibration of adsorbates in the ultra-thin thickness range (0-50Å).

2.1.1 Auger Electron Spectroscopy (AES)

Harris [Harr68] developed for the first time the Auger Electron Spectroscopy (AES) as a surface technique (proving the Auger electron signal enhancement using the derivative mode detection) in 1968. The technique derives its name from the effect first observed by the French physicist Pierre Auger, in the mid-1920 [Auge25, Auge26]. It can be used as a surface sensitive technique using the emission of low energy electrons (energies in the range 30-1500 eV).

Auger electron emission involves three basic steps (figure 2.1):

- atomic ionization (by removal of a core electron);
- relaxation and Auger emission;
- Auger electrons counting.

The last stage is simply a technical problem of detecting low counting rates of charged particles selected in energy.

Ionization (figure 2.1-a and 2.1-b): The Auger process is initiated by the creation of a core hole - this is typically carried out by exposing the sample to X-rays (energy 1-2 keV) or to a beam of high-energy electrons (primary energy in the 2 - 5 keV range). In figure 2.1,

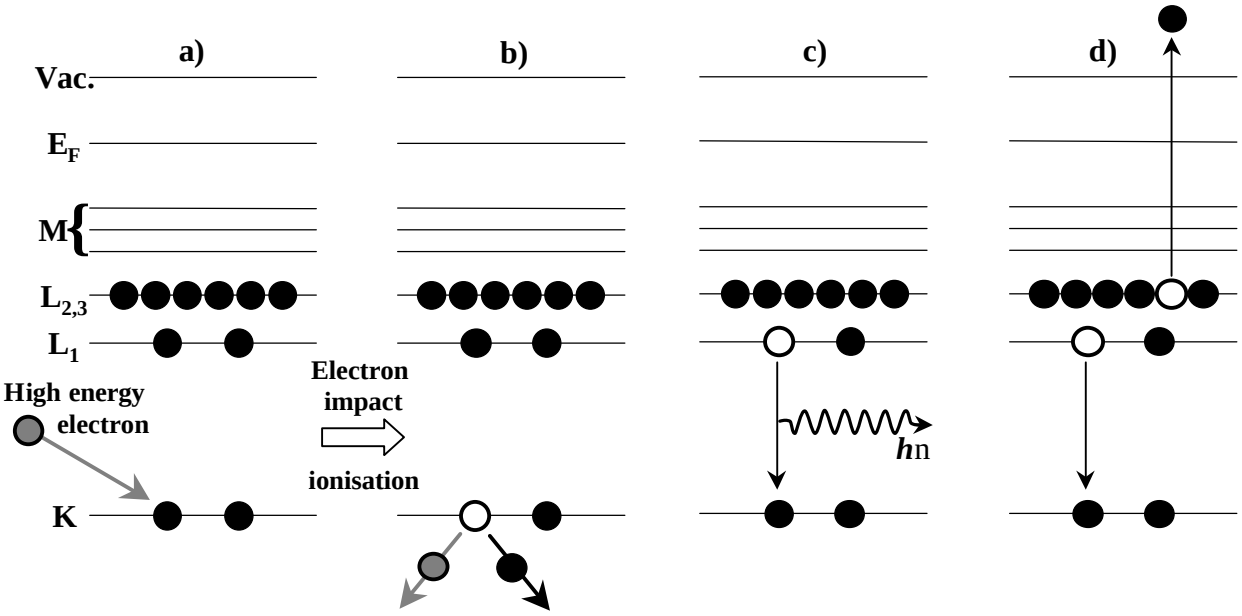

Figure 2.1: *Schematic representation of the Auger process*:
After the ionization of the atom (a, b), a hole is left on the K shell. The hole can be occupied by an L-shell electron; the transition towards the final state can be radiative: emission of a photon (c) or non-radiative: an Auger electron is emitted (d).

ionization is shown to occur by removal of a K-shell electron, but in practice, ions with holes in a variety of inner shell levels are common.

Relaxation & Auger Emission (figure 2.1 c) and d)): The ionized atom that remains after the removal of the core hole electron is in a highly excited state and will rapidly decay to a lower energy state either by :

- X-ray fluorescence (figure 2.1-c), or
- Auger emission (figure 2.1-d).

In the example of figure 2.1-d, an electron transition occurs between the core level L_1 to an empty initial core hole in the K-shell and the energy difference is simultaneously transferred to a second electron. A fraction of this energy is required to overcome the binding energy of this second electron, and the remaining one will be the kinetic energy of the outgoing Auger electron. In the Auger process, the final state is a doubly-ionized atom with core holes in the L_1 and $L_{2,3}$ shells in figure 2.1-d. We can roughly estimate the kinetic energy (E_c) of the Auger electron from the binding energies of the various levels (E_K, E_{L_1} and $E_{L_{2,3}}$). In our example, we will find:

$$E_c = (E_K - E_{L_1}) - E_{L_{2,3}} = E_K - (E_{L_1} + E_{L_{2,3}})$$

The two energy terms (E_{L_1} and $E_{L_{2,3}}$) in the previous equation are symmetric. It is impossible to determine which electron fills the initial core hole and which is ejected. An

Auger transition is therefore characterized by an initial state depending on the initial hole and the incident electron and a final state depending on the final two holes. There will be a discrete number of possible Auger transitions for a given element. Each element present in a sample gives rise to a characteristic spectrum with peaks at various kinetic energies, allowing a chemical analysis of the surface composition.

Analysis of the emitted Auger electrons: Auger electrons are not the only electrons emitted from a solid when probed by high-energy electrons. Most of the emitted electrons are inelastically scattered electrons. A plot of the number of electrons emitted from the solid as a function of the kinetic energy, N(E), would display only small peaks at particular Auger-electron transition energies. In order to enhance the detection of Auger-electron peaks a synchronous detection (*lock-in*) is used. The energy of the emitted electrons is analyzed using, for example, a *Cylindrical Mirror Analyzer* (CMA). The CMA, characterized by a coaxial geometry between the electron gun and the analyzer, present an enhanced sensitivity for the low energy Auger electrons. The disadvantage of the CMA is related to the low analyzer-sample distance of 7 mm. Due to this limitation, all the kinetic measurements presented in this work were realized on a second chamber equipped with a MAC2 analyzer. The advantage of the MAC2 (*double cylinder*) analyzer is the use of electrostatic lenses modifying the focus point to several centimeters. In addition, the resolution is constant over the entire electron energy domain. Moreover, such a setup allows signal recording during evaporation.

In summary, Auger Electron Spectroscopy (AES) is a surface-sensitive spectroscopic technique used for elemental analysis of surfaces; it offers:

- high sensitivity (typically 1% monolayer for all elements, except H and He);
- a mean for monitoring surface cleanliness of samples;
- quantitative compositional analysis of the surface and the interface region.

2.1.2 X-ray Photoemission Spectroscopy (XPS)

Similar to the case of Auger electron emission, the photoemission effect was discovered theoretically well before its use in spectroscopy. In fact, the photoemission is based on the photoelectric effect, evidenced at the beginning of the 20th century by Einstein [Eins05]. From a theoretical point of view, the photoemission effect was widely studied by Spicer in 1958 [Spic58] which introduced its semi-empirical model, completed and discussed by many other authors. Hagström et al [Hags64] initiated the detailed core-level photoemission spectra analysis, evidencing the potentialities of this technique. The

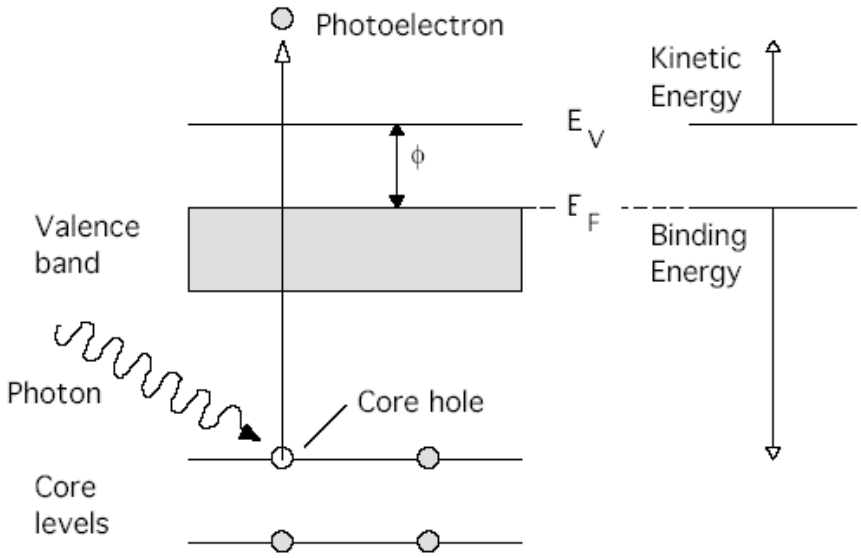

Figure 2.2: *Schematic representation of the photoemission process*:
The incoming X-ray radiation will create a photoelectron characterized by a kinetic energy directly related with the binding energy ($E_K \cong h\nu - E_B$). (E_F – Fermi level, E_V – vacuum level, ϕ - the work function)

quantitative analysis and the interpretation of photoemission spectra became possible due to the well-known formula introduced by Doniach and Sunjic [Doni70]. Finally, Citrin et al. [Citr78] introduced in 1978 the surface contribution in the interpretation of photoemission spectra.

I will limit the presentation of the photoemission effect to a brief description, pointing out only some aspects of the electronic effects that influence the XPS spectra. More details on this topic can be found in several review articles [Kota, Carr90, S-EF90, Span85, Egel86, Will80].

In a first approach, the photoemission process can be considered as the direct interaction between an incoming photon and a core level electron (figure 2.2). The photon energy is entirely transferred to the core level electron and the interactions of the emitted photoelectron with the other levels or the valence band electrons can be neglected in a first approximation. Then the kinetic energy of the emitted photoelectron can be written in conformity with Koopman's theorem (energy conservation):

$$E_K + E_B + f = hn \qquad (2.1)$$

where E_K is the kinetic energy of the photoelectron, E_B is the electron binding energy in the atom, f is the photoelectron work function, and (hn) is the photon energy.

Despite its simplicity, equation 2.1 is sufficient for a XPS analysis, since the variation of the binding energy of the electronic shells between the atomic and the solid state is not significant. This description allows the identification of the chemical species, but it cannot explain the complex origin of all electronic transitions present in the XPS spectra. Koopman's theorem fails when considering many-body effects: the photoelectron interaction with the

other electrons, with the valence band or with the hole created in the core level. The many-body effects introduce peak asymmetry and/or the apparition of satellites in the XPS spectra for several materials.

In the following paragraph, we present briefly several limit situations that characterize the XPS spectrum. In figure 2.3 we present the basic approximations related with the photoemission effect. The first case (figure 2.3-a), already presented above (Koopman's approximation), describes the final state characterized by a core hole and the emitted photoelectron. The energy calculated within this approximation cannot be observed due to the many-body effects (intra- and inter-atomic excitations and screening). In the second case (figure 2.3-b), when the emission of the photoelectron occurs slowly (slow or adiabatic photoemission), the final state is characterized by the relaxation of the system in a ground ionic state. The difference in energy will therefore be found in the energy of the emitted photoelectron, resulting in a shift of the XPS spectrum to higher kinetic energy (lower binding energy). It is important to note that this final state effect is different from the *chemical shift* which is a specific initial state effect (initial state already in a ground ionic state). The chemical shift is a specific feature of the XPS shape in the case of oxides. As in the first case, the energy associated with this process cannot be observed in the XPS spectrum because the atom does not have the time to fully relax in the ground ionic state before the photoelectron is

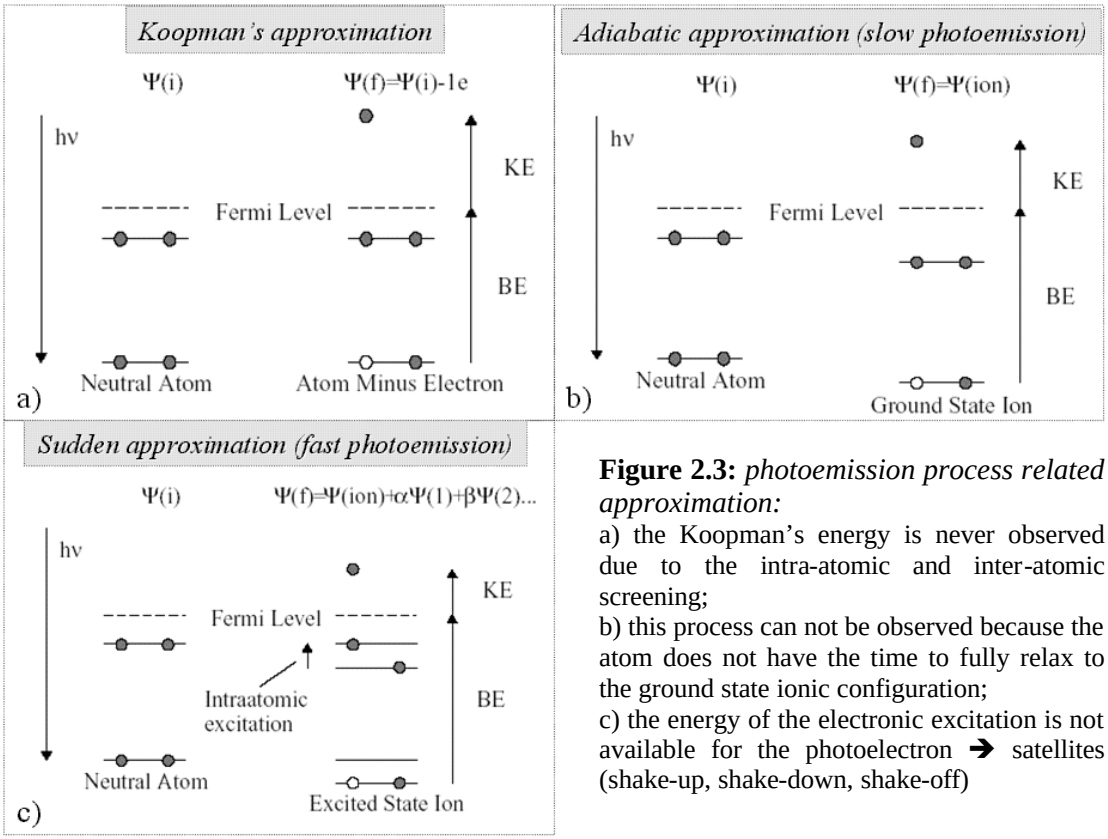

Figure 2.3: *photoemission process related approximation:*
a) the Koopman's energy is never observed due to the intra-atomic and inter-atomic screening;
b) this process can not be observed because the atom does not have the time to fully relax to the ground state ionic configuration;
c) the energy of the electronic excitation is not available for the photoelectron ➔ satellites (shake-up, shake-down, shake-off)

created. In fact, while the photoelectron is created the ion can be in different excited states. The emitted photoelectron can therefore show several satellites:

- *shake-up satellite* if the energy results from an electronic excitation to a bounded state (appears at higher binding energies);

- *shake-off satellite* that characterizes the excitation to an unbounded state (vacuum);

- *shake-down satellite* related with the hole excitations (very seldom events).

Generally when using techniques measuring charged particle emission from insulators (XPS and AES), we have to take into account the *surface charging effect* of the sample. Since the electrical insulators cannot dissipate charges generated by the photoemission process (as in the case of metallic films), an external source is used, exposing the surface to neutralizing flux of low energy electrons (*flood gun*). However, in our case, taking into account the ultra-thin thickness domain of the deposited NiO films, such surface charging effects are limited because of reduced symmetry and structural defects in the thin films.

For the XPS results presented in this work we used the basic approximation given by the energy conservation relationship in the Koopman's approximations (2.1). The recorded XPS lines were compared to reference data reported in the literature. In addition, the apparition of the shake-up satellites and the chemical shift of the Ni $2p_{1/2}$ and $2p_{3/2}$ transitions were used as a qualitative indication for the oxide formation. Quantitative analysis was performed using the Doniach-Sunjic deconvolution method. The parameters obtained from the fitting procedure are given in chapter 4.

2.2 MORPHOLOGICAL AND STRUCTURAL INVESTIGATIONS

2.2.1 Scanning Tunneling Microscopy (STM)

The base of what is known nowadays as a common laboratory tool, the *Scanning Tunneling Microscopy*, was predicted by the quantum mechanics in the second decade of the last century: an electron has a non-zero probability to tunnel through a potential barrier.

Even if the first evidence of the tunneling current was reported by Young et al. [Youn71, Youn72] in the years 1971-72, the technical concept of the first STM was proposed by Gert Binnig and Heinrich Rohrer [Binn82a, Binn82b] in 1981. They were recompensed for their work in 1986 with the Nobel Prize for Physics [www-nobel]. In this section, I will present very briefly, and from a phenomenological point of view, the STM principle, reviews [Binn86, Grif90, Saku90, Leem92] and books [Chen93, Guen93, Stro93, Wies98, Bonn01] on the subject being abundant in the literature.

In figure 2.4 we schematically draw the phenomenon of the electronic tunneling.

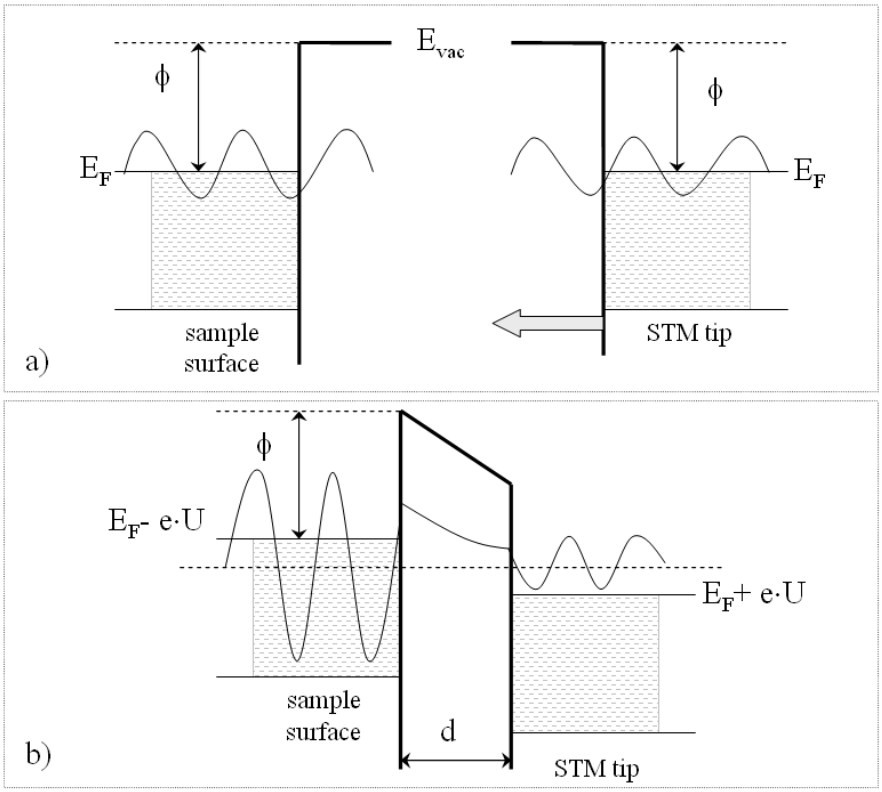

Figure 2.4 : *Schematic representation of the tunneling process*:
a) the two metals are too far for the electronic wave functions to overlap so no tunneling appears;
b) overlap of the electronic wave functions ➔ tunneling; applying a small voltage (*U*) a current *I* will flow through the vacuum gap.

Tunneling current is originated from the wavelike properties of particles (electrons, in this case) in quantum mechanics. When an electron is incident upon a vacuum barrier with potential energy larger than the kinetic energy of the electron, there is a non-zero probability that it crosses the forbidden region and reappears on the other side of the barrier. This behavior is related with the extent of the electron wave function leaking out from the barrier, as suggested in figure 2.4-a. If two conductors are very close, their leak out electron wave functions will overlap and therefore electron tunneling occurs. In addition, applying a small voltage (*U*) between the two conductors a net tunneling current, $I \neq 0$ is generated. The electron wave functions at the Fermi level have a characteristic exponential inverse decay length *K* given by:

$$K \cong \frac{\sqrt{2 \cdot m \cdot f}}{\hbar} \tag{2.2}$$

where *m* is the mass of electron, f is the local tunneling barrier height or the average work function of the tip and the sample. At low voltage and temperature, the tunneling current can be expressed as:

$$I \propto \exp(-2 \cdot K \cdot d) \tag{2.3}$$

with *d* – distance between the tip and the surface. It is evident from the equation 2.3 that small modifications in the distance *d*, e.g. 1 Å, results in a tunneling flow variation of one order of magnitude, obtaining therefore strong vertical distance sensitivity. However, since the current exponentially depends on both, gap distance and local barrier height, changes of current might be due to corrugation of the surface or to the variation of the barrier height. In theory, both contributions may be separated via the expression:

$$f \propto \frac{\partial \ln I}{\partial d} \tag{2.4}$$

but this is often impossible to realize experimentally, even if maps of the local barrier heights can be obtained, the images will contain also topographic features.

It is very important to remark that the STM is a topographical technique employing cartography of the surface electronic states. Therefore, atomic resolved STM images will not

necessarily describe crystallographic positions, but are also related to the extension of the electronic orbitals at the surface. In fact, the STM images are sensitive to the *Local Density of States* (LDOS) which characterizes the number of electrons at a specific energy value. The tunneling conductance s (or I/V) is directly proportional to the LDOS:

$$s \propto r(r_0, E) \tag{2.5}$$

For specific experiments, the STM will probe the LDOS of the surface keeping constant the gap distance and varying the applied voltage (figure 2.5). This feature is used when performing *Scanning Tunneling Spectroscopy* (STS) measurements since each element is characterized by a specific surface LDOS. In addition, as shown in figure 2.5, by changing the bias polarity of the STM tip we can probe alternatively the filled and the empty electronic

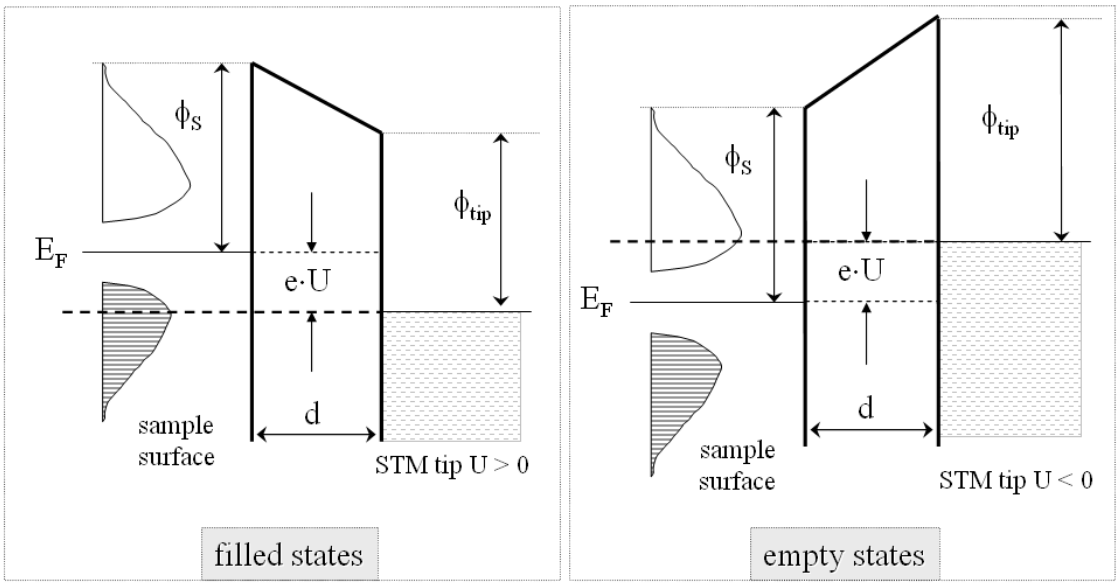

Figure 2.5: *Filled and empty states:*
- the electrons near the Fermi level of the sample tunnel toward the empty levels of the STM tip ➔ surface filled states STM image;
- the electrons from the STM tip tunnel toward the surface empty states ➔ surface empty states STM image.

states of the surface. If negative bias is applied on the tip, the electrons tunnel from the occupied states of the tip to the unoccupied states of the sample. If positive bias is used, the electrons tunnel from the occupied states of sample to the unoccupied states of the tip. This change of the tunneling current flow direction is recorded in the STM images as a contrast reversal.

In this work, we used exclusively the topographic mode of the STM scanner (constant current mode). However, the STM contrast reversal was largely observed during this work and was used in the localization of the oxygen and nickel atoms for ultra-thin films of NiO/Cu(111). A complete description of this specific STM feature is given in chapter 4.

2.2.2 Low Energy Electron Diffraction (LEED)

LEED is a well-established surface science technique [Hove86, Pend74, Hove79, Marc82, Jona78, Jona82] and is used to study the structure of crystalline surfaces [Zang88, Wood86, Prut75, Hove85, Veen88, Tong91]. Normal incidence low-energy electrons (20-250 eV, λ~Å) give access to the surface structure. The wavelengths are comparable to the spacing between atoms both parallel and perpendicular to the crystal surface, hence, for an ordered surface, the electrons might diffract through elastic back-scattering. Since the cross section for scattering of low-energy electrons is very large, the incident electron beam is damped within a few surface layers. The back-scattering is strongly dependent on the type of atoms and it may be used for different purposes:

1. *Qualitatively* (geometrical approach): when the diffraction pattern is recorded and only the spot positions are used to extract the size, symmetry and rotational alignment of the adsorbate unit cell with respect to the substrate unit cell. A surface layer on a crystal can be described as a two-dimensional net of atoms. From this net, the reciprocal lattice can be constructed using the LEED patterns.

2. *Quantitatively* (dynamical approach): when the *intensities* of the various diffracted beams are recorded as a function of the incident electron beam energy to generate so-called $I(V)$ curves which, by comparison with theoretical curves, may provide accurate information on atomic positions. This approach needs the use of the complex theory of multiple scattering. Theoretical models for LEED spectra can be found in [Hove86, Pend74, Hove79, Tong88, Huan88, Huan90a, Huan90b, Fan89, Zana77, Pend80, Hove77].

Experimentally (figure 2.6), a well-collimated mono-energetic beam of electrons, created by an electron gun (EG), impinges on a clean sample surface, usually at normal incidence. The diffracted electrons radiate out from the sample toward a display detector, passing through a Retarding Field Analyzer (RFA).

When the energy of the electron increases its wavelength and the diffraction angle decreases and vice versa; therefore, with increasing energy, the beams move toward the

specularly reflected electron beam. In practice, the patterns not only compress with increasing energy, but the intensities of discrete beams are modulated. If single scattering and infinite penetration were exactly applicable, then the beams would only have intensity for discrete energies. If the theory of the single scattering of one layer would be applicable, then the diffracted beam would have constant intensity for all energies. However, none of this is the case, and the intensity modulation results from multiple scattering within the top few atomic

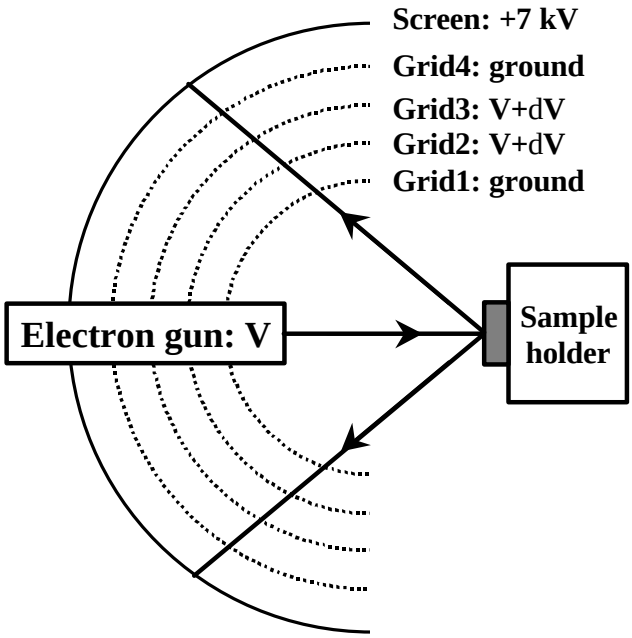

Figure 2.6: *Schematic representation of a LEED retarding field analyzer (RFA):* The electron beam is emitted from the gun. Back-scattered electrons from the grounded sample travel first in a free-field region, and are high-pass filtered by the second and third grid (potential several volts less than the electron-beam voltage). The screen is held at several thousand positive volts in order that the electrons can excite the phosphorous screen.

layers, and the beam position can be derived from the kinematic approximation.

In our study we used the first approach, the geometrical one, reproducing the positions of the diffracted spots on the LEED cliché (§5.2.3). In the following paragraph, we give therefore some details related with this approximation.

In the case of the surface diffraction, we can use von Laue's relations:

$$\begin{cases} \left(\vec{k}_i - \vec{k}_f\right) \cdot \vec{a}_S = 2 \cdot p \cdot m \\ \left(\vec{k}_i - \vec{k}_f\right) \cdot \vec{b}_S = 2 \cdot p \cdot n \end{cases} \tag{2.6}$$

where m and n are integers, $\vec{a}_S$ and $\vec{b}_S$ are the surface lattice vectors. These relations can be better understood using Ewald's construction, as presented in figure 2.7. The loss of periodicity following a given direction is characterized in reciprocal space by the formation of

rods instead of points, as it is the case for bulk X-ray diffraction. Therefore, the diffraction conditions will be "relaxed": diffraction spots appear when the diffracted beam passes through any intersection of these rods with the Ewald sphere (in the case of bulk diffraction,

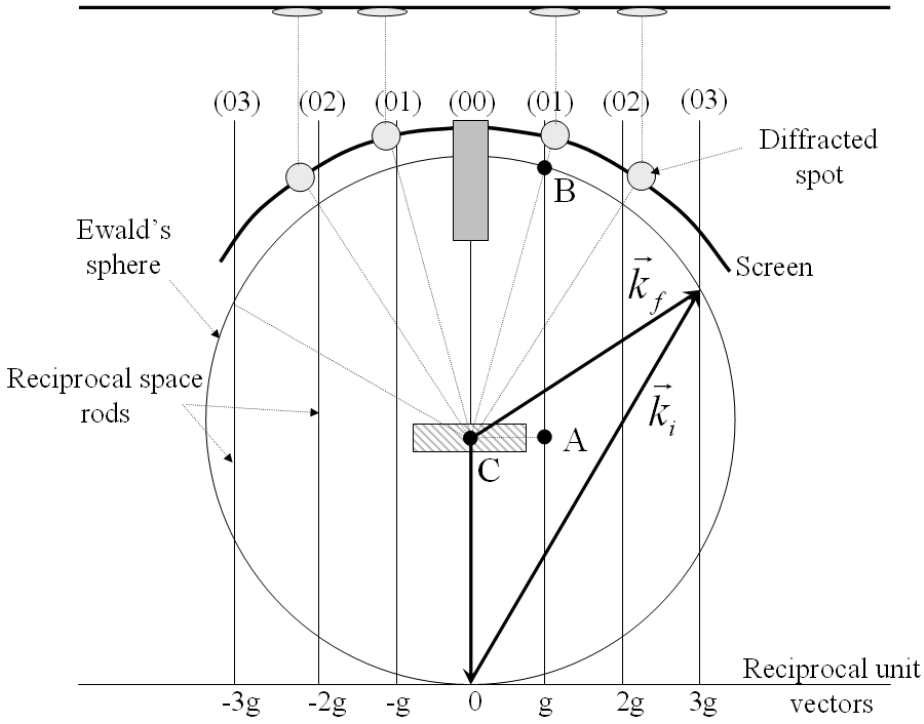

Figure 2.7: *LEED – geometrical approach - Ewald's construction*

the point in the reciprocal space has to be on the Ewald sphere, given by the Bragg condition: $\vec{k}_f - \vec{k}_i = \vec{Q}$ with $\vec{Q}$ a vector of the reciprocal space). Since the diffraction conditions are relaxed, it is obvious that for a surface presenting structural disorder the diffraction will occur in any direction, resulting in a continuous background without spots. In addition, the diffraction spots size and sharpness are related with the structural order quality.

The LEED spots position on the cliché allow the extraction of the diffraction angle, if the geometry is known. Since the wave length, l, is related to the energy of the electronic beam, we can calculate the distances (d_{10}) in the reciprocal space:

$$1/d_{10} = CB \cdot \sin j = R \cdot \sin j = \sin j / l \qquad (2.7)$$

Using this formula, we can calculate (via an inverse Fourier transform) the actual inter-atomic distances.

Since the electronic beam has a coherence length of ~300 Å, the diffraction will occur only if the size of the ordered regions on the surface has at least an extent of ~300 Å.

High-energy electrons can also be used to investigate the surface structures. In order to extract surface structural information from the diffraction of high-energy electrons, therefore, the technique has to be adapted and the easiest way of doing this is to use a reflection geometry in which the incidence of the electron beam is at grazing angle - it is then known as Reflection High Energy Electron Diffraction (RHEED). This technique was few used in this study due to the reduced azimuthal information for a given sample position in our chamber during the growth of the NiO films.

2.2.3 Grazing incidence X-ray techniques

Laboratory techniques as STM and LEED (presented above) give multitude of information with regard to the surface and interface properties. However, they remain limited to a reduced scale, STM, or are difficult to treat using simple kinematic approximations, LEED. Surface and interface structural and morphological studies of strongly reduced-dimensional systems (as the ultra-thin films) can be performed nowadays using the synchrotron radiation based techniques. *Grazing Incidence X-ray Diffraction* (GIXD) and *Grazing Incidence Small Angle X-ray Scattering* (GISAXS) were successfully used during my work to obtain a complete description of interfacial properties. The diffraction (GIXD) and scattering (GISAXS) of X-rays by a surface allow acceding the crystallography, morphology and growth process.

The following section is dedicated to a brief introduction of the GIXD and GISAXS techniques. In the first part I will review several considerations related with the use of *grazing incidence* X-rays. The GIXD and GISAXS principles are depicted briefly thereafter. Practical considerations, limitations and order of magnitudes will be also discussed. A more comprehensive description of the standard diffraction and crystallography can be found in several textbooks and reviews [Jame65, Ware69, Wool70, Feid89, Robi91, Russ91, Robi92, Guin94, Borc95].

2.2.3.1 Refraction from surfaces

For a sharp interface between the vacuum and the surface of a material (with

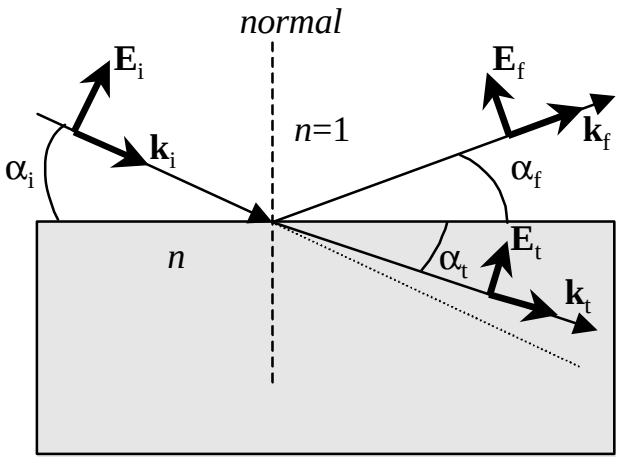

Figure 2.8:
Refraction and reflection of a plane wave with amplitude E_i incident upon the interface between vacuum and a material of index *n*.

wavelength dependent index of refraction *n*), the refraction geometry is given in figure 2.8. An incident beam made (linearly polarized plane wave) impinges a surface under an incidence angle a_i, and amplitude $\mathbf{E}_i$ and a wave vector $\mathbf{k}_i$; the reflected beam leaves with an angle a_f, an amplitude $\mathbf{E}_f$ and a wave vector $\mathbf{k}_f$ and the transmitted beam makes an angle a_t with the surface and has an amplitude $\mathbf{E}_t$ and a wave vector $\mathbf{k}_t$. The Snell-Descartes' law gives:

$$\cos a_i \cdot n = \cos a_f \text{ and } a_f = a_i \tag{2.8}$$

As long as $n>1$, total reflection cannot occur when light travels from the vacuum to the material, even if $a_i = 0$. Fortunately, unlike visible light, when hard X-rays (i.e. energy above several keV) are considered, the index of refraction is generally less than unity:

$$n = 1 - d - i \cdot b \text{ with } \begin{cases} d = \dfrac{l^2 \cdot e^2 \cdot N_A \cdot r}{2pmc^2} \cdot \dfrac{\sum_{j \in Cell} \left(Z_j - f_j'\right)}{\sum_{j \in Cell} A_j} \\ b = \dfrac{l^2 \cdot e^2 \cdot N_A \cdot r}{2pmc^2} \cdot \dfrac{\sum_{j \in Cell} f_j''}{\sum_{j \in Cell} A_j} = \dfrac{lm}{4p} \end{cases} \tag{2.9}$$

where the summation is over all atomic species *j* present in the unit cell; N_A, $(Z_j\text{-}f_j')$, f_j'', A_j, r, m and l are, respectively, Avogadro's number, the scattering factor, the anomalous dispersion

factor, the atomic weight of species *j*, the density, the photoelectric absorption coefficient and the wavelength.

When $n<1$, total external reflection occurs on the vacuum side, although for very grazing angles, since d and b are respectively in the 10^{-5} and 10^{-6} range, leaving a critical angle for total external reflection $a_c \approx \sqrt{2 \cdot d}$ in the 0.1°- 0.6° range. The value of $n<1$ is the key allowing surface investigations with hard X-rays; it also fully defines the geometry of the experiments. When $a_i<a_c$ the component of the transmitted wave-vector normal to the surface becomes imaginary and the refracted wave is exponentially damped as a function of the distance below the surface, being an evanescent wave traveling parallel to the surface. The penetration depth of the X-rays becomes [Feid89]:

$$\Lambda = \frac{l}{4p \cdot \mathrm{Im}(\sqrt{a_i^2 - a_c^2 - 2ib})} \tag{2.10}$$

The reflection and the transmission coefficients of the surface are critically dependent on a_i and their variations are given by Fresnel's formula:

$$R(a_i) = \frac{I_f}{I_i} = \left| \frac{\sin a_i - \sqrt{n^2 - \cos^2 a_i}}{\sin a_i + \sqrt{n^2 - \cos^2 a_i}} \right|^2 \; ; \; T(a_i) = \frac{I_t}{I_i} = \left| \frac{2 \sin a_i}{\sin a_i + \sqrt{n^2 - \cos^2 a_i}} \right|^2 \tag{2.11}$$

I will now discuss some of the important features of these formulas. Figure 2.9 reproduces the calculated Λ and T for some typical situations. For $a<a_c$, R=1 and total external reflection occurs and, as expected, the penetration depth is minimum and in the nanometer range, highlighting the great surface sensitivity that can be achieved. When $a_i>>a_c$ the reflectivity falls off rapidly as a_i^{-4}, enabling tunable depth analysis and the investigation of buried interfaces (up to micrometer depth); it allows also growth monitoring up to fairly thick deposits. For a crystalline surface, the diffracted intensity will be proportional to the transmission coefficient because it is related to the electrical field strength at the dielectric boundary, *i.e.* at the surface. Although the wave does not propagate below a_c, the signal will be enhanced by a factor 4 for a non-absorbing material when $a_i=a_c$. Due to time micro-reversibility, the diffracted beam experiences exactly the same refraction effects and a second enhancing factor can be obtained when the exit angle from the surface is equal to a_c. A

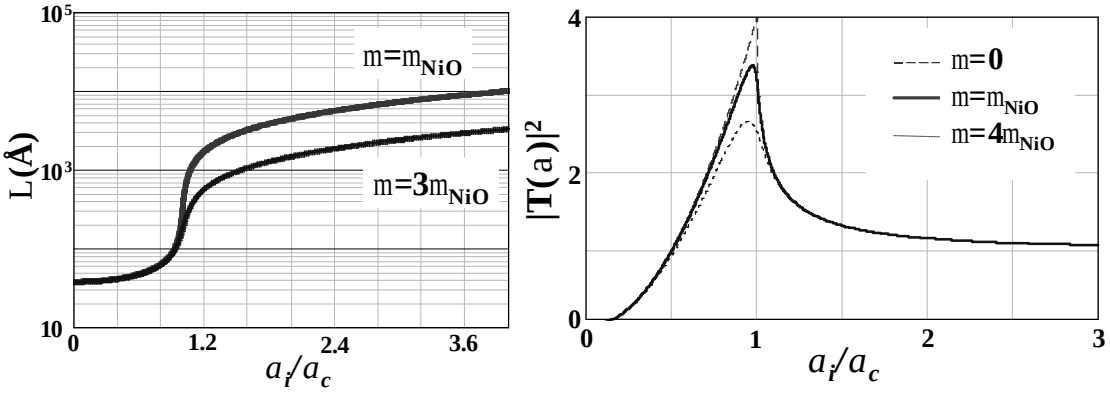

Figure 2.9: Calculated penetration depths (left) as a function of the reduced grazing incidence angle, a_i/a_c, for a NiO surface (upper curve), and a more absorbing surface (lower curve). Calculated transmission coefficients (right) versus the reduced incidence angle a_i/a_c for an ideal non-absorbing material (----), for NiO (———) and a more absorbing surface (·····). The beam energy used was 18 keV (l=0.688 Å).

comprehensive discussion of the refraction effects of the outgoing beam can be found in [Feid89]. Working at grazing incidence allows reducing drastically the background: except the fluorescence contribution, most of the background originates from the bulk (thermal diffuse scattering, point defect scattering…) and can be removed or strongly reduced by limiting the incidence and/or the emergence angle to a_c.

When $a_i=a_c$, great care must be taken to keep a_i strictly constant during the whole data collection. Large intensity variations are obtained for very small variations of the incidence, since $a_i=a_c$ corresponds to the maximum of the $T(a_i)$ function (figure 2.9). Working at $2a_c$ or $3a_c$ allows for more comfortable measurement conditions, if the background remains acceptable. Anyway, grazing incidence remains often the mandatory condition to investigate surfaces with hard X-rays. This principle is used for *Grazing Incidence X-ray Diffraction* (GIXD) (structure) as well as for *Grazing Incidence Small Angle X-ray Scattering* (GISAXS) (morphology).

2.2.3.2 Grazing Incidence X-ray Diffraction (GIXD)

- ✔ **Surface Diffraction**

Considering the remarks of the previous section, the general geometry of a GIXD experiment is given in figure 2.10. An incident beam with wave vector $\mathbf{k}_i$ falls on a surface under an incidence angle a_i that is kept close to a_c. If the material is a single crystal the reflected beams will organize, for given incidence conditions with respect to the atomic

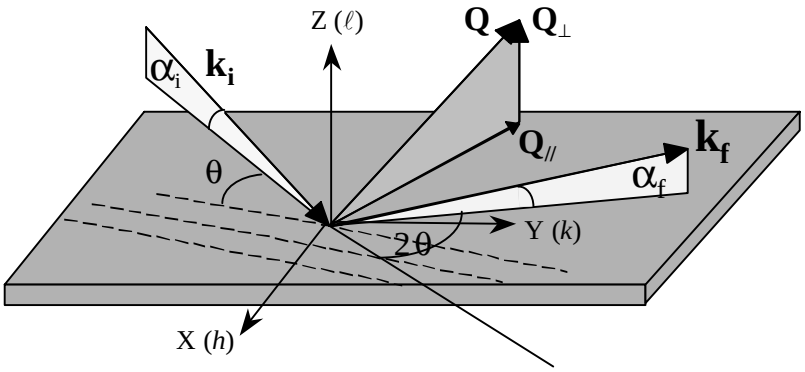

Figure 2.10: Grazing incidence X-ray diffraction geometry. See text for the definition of the notations.

planes, along well-defined directions with a wave vector $\mathbf{k}_f$ and an exit angle a_f: they are diffracted by the well-organized array of atoms. It is convenient to define the momentum transfer $\mathbf{Q} = \mathbf{k}_f - \mathbf{k}_i$ and to decompose it in a parallel, $\mathbf{Q}_{//}$, and in a perpendicular to the surface, $\mathbf{Q}_\perp$, component.

For hard X-rays and small objects, the kinematical approximation of single scattering is valid [Ware69]. The intensity, $I(\mathbf{Q})$, elastically scattered in a direction defined by the momentum transfer $\mathbf{Q}$ is proportional to the square modulus of the coherent addition of the amplitudes scattered by all electrons in the diffracting object. The field seen at large distance R from a scattering electron of charge e and mass m at $\mathbf{r}$' is given by the well-known Thomson formula. Within the *Born approximation*, a single atom at $\mathbf{r}$ diffracts an amplitude obtained by integrating over its electronic distribution function $r(\mathbf{r}')$ about $\mathbf{r}$. Defining the atomic form factor, $f(\mathbf{Q})$, as the Fourier transform of $r(\mathbf{r}')$, a unit cell of a crystal with N atoms diffracts an amplitude:

$$A_{Cell} = \sqrt{P} A_0 \frac{e^2}{mc^2 R} \sum_{j=1}^{N} \left(f_j(\mathbf{Q}) \cdot e^{i\mathbf{Q}\cdot\mathbf{r_j}} \cdot e^{-M_j} \right) = \sqrt{P} A_0 \frac{e^2}{mc^2 R} \cdot F(\mathbf{Q}) \qquad (2.12)$$

which defines the structure factor, $F(\mathbf{Q})$, of the unit cell, where P, $A_0{}^2$ and e^{-M_j} are, respectively, the polarization factor, the incident intensity in photons per unit area per second and the Debye-Waller factor [Ware69, Deby14] for species j; M may be written as $B\sin^2\theta/\lambda^2$ where $B = 8p^2\left\langle u_x^2 \right\rangle$ is called the temperature factor and $\left\langle u_x^2 \right\rangle$ is the mean square component of vibration of the atom along the direction of momentum transfer. The polarization factor, P, describes the dependence of $\mathbf{E}_i$ on the polarization of the incoming wave. Since the direction of the electrical field determines the direction of the electron motion that will radiate the

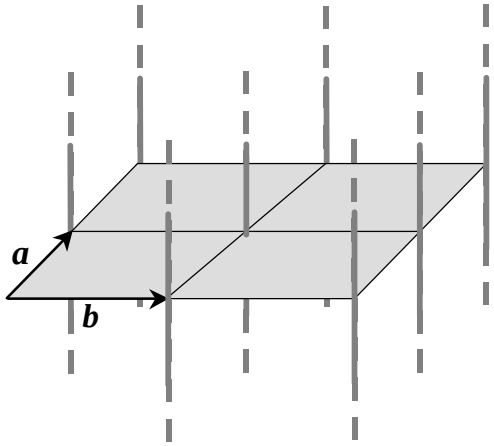

Figure 2.11: Reciprocal space of one atomic layer.

wave, the angle $2q$ between the incident and the exit beams will modulate the observed intensity. When $\mathbf{E}_i$ is normal to the scattering plane (plane spanned by $\mathbf{k}_i$ and $\mathbf{k}_f$) P is unity, and when $\mathbf{E}_i$ is in the scattering plane, $P=\cos^2 2q$.

If we now consider a two-dimensional surface build with N_1 and N_2 atoms along the $\mathbf{a}_1$ and $\mathbf{a}_2$ directions, the scattered intensity is obtained by summing the amplitudes over the $N_1 \times N_2$ unit cells. It is convenient to express $\mathbf{Q} = \mathbf{q}_1+\mathbf{q}_2+\mathbf{q}_3$ in the reciprocal space basis as $\mathbf{Q} = h\mathbf{b}_1+k\mathbf{b}_2+\ell\mathbf{b}_3$ with the reciprocal $\boldsymbol{b}_i$ vectors related to the direct vectors by $\mathbf{b}_i=2\pi(\mathbf{a}_j\times\mathbf{a}_k)/(\mathbf{a}_i,\mathbf{a}_j,\mathbf{a}_k)$; $\mathbf{a}_3$ can be any vector perpendicular to the $(\mathbf{a}_1,\mathbf{a}_2)$ plane. Convention in surface diffraction: ℓ (respectively Z) is always chosen perpendicular to the surface and h and k (respectively X and Y) span the surface plane (figure 2.10). Defining the function $S_N(x)=\sin^2(Nx/2)/\sin^2(x/2)$, the intensity of the total scattered signal from the surface is:

$$I_S^{2D}(\mathbf{Q}) = PA_0^2 \frac{e^4}{m^2c^4R^2}\left|F(\mathbf{Q})\right|^2 S_{N_1}(\mathbf{Q}\cdot\mathbf{a_1})\cdot S_{N_2}(\mathbf{Q}\cdot\mathbf{a}_2) \qquad (2.13)$$

For large N_1 and N_2 values, $I_S^{2D}(\mathrm{Q})$ yields significant intensities only when both Laue conditions are fulfilled simultaneously: $\mathbf{Q}\cdot\mathbf{a_1}=2\pi h$ and $\mathbf{Q}\cdot\mathbf{a_2}=2\pi k$ with h and k integer, defining a two dimensional reciprocal lattice. Since the intensity is independent of $\mathbf{q}_3$, the scattering is diffuse in the direction perpendicular to the surface and the reciprocal space is made of continuous rods (figure 2.11). The intensity in the diffraction rods reduces to:

$$I_{hk}^{2D} = PA_0^2 \frac{e^4}{m^2c^4R^2}\left|F_{hk}\right|^2 \cdot N_1^2 \cdot N_2^2 \qquad (2.14)$$

valid as long as only exactly one layer diffracts. This is the case when the surface layer has a different periodicity than the bulk *i.e.* in the case of surface reconstruction or if a 2D film with a mismatched lattice parameter is deposited on a substrate.

As soon as several layers exist in the perpendicular direction, the diffraction rods become modulated because the periodicity in the third direction must be taken into account and the intensity will take the usual form:

$$I_{hkl}^{3D} = PA_0^2 \frac{e^4}{m^2 c^4 R^2} \left|F_{hkl}\right|^2 S_{N_1}(\mathbf{Q}\cdot\mathbf{a_1}) \cdot S_{N_2}(\mathbf{Q}\cdot\mathbf{a}_2) \cdot S_{N_3}(\mathbf{Q}\cdot\mathbf{a}_3) \tag{2.15}$$

For small N_3 values, the rods will modulate along $\mathbf{Q}_\perp$. Contrarily, for large N_3 values, the intensity will concentrate along a discrete array in the third direction too, leading to a third Laue condition: $\mathbf{Q}\cdot\mathbf{a_3}=2\pi\ell$ with ℓ integer. This situation corresponds to the classical 3D diffraction where Bragg peaks correspond to the possible *h*, *k* and ℓ's.

An intermediate situation is obtained when a physical surface is considered, *i.e.* the truncation of a bulk material, that is only semi-infinite, and equation (2.15) will no longer apply because it assumes infinite extension of the diffracting object in all three directions. Taking into account the summation from -∞ to 0 along $\mathbf{a}_3$ of $N_1 \times N_2$ surface unit cells, the scattered intensity for a perfectly sharp surface becomes:

$$I_{hkl}^{CTR} = PA_0^2 \frac{e^4}{m^2 c^4 R^2} \left|F_{hkl}\right|^2 S_{N_1}(\mathbf{Q}\cdot\mathbf{a_1}) \cdot S_{N_2}(\mathbf{Q}\cdot\mathbf{a}_2) \cdot I_\ell^{CTR} \tag{2.16}$$

$$\text{with } I_\ell^{CTR} = \frac{1}{2\sin^2(\mathbf{Q}\cdot\mathbf{a_3}/2)} \tag{2.17}$$

The intensity variation along a crystal truncation rod (CTR) contains now Bragg peaks for integer values of *h*, *k* and ℓ, not excluded by the 3D extinction rules that are still valid, and diffuse scattering in between. Importantly, this means that, as far as the two first Laue conditions are fulfilled, ℓ must be considered as a continuous variable for surface diffraction. Even half ways from Bragg peaks some intensity remains, since the last term in equation (2.16) is then ½ unity; this remaining intensity is comparable to the intensity of a single layer, $I_S^{2D}(\mathbf{Q})$. Real surfaces have roughness, *i.e.* the probability distribution of the atoms is less sharp than a simple step. In that case, the intensity will concentrate nearer to the Bragg peaks

and decrease in the zone centre. This effect can be taken into account within the b^n model for simple unit cells [Robi86]:

$$I_\ell^{CTR} = \frac{(1-b)^2}{1+b^2-2b\cos(\mathbf{Q}\cdot\mathbf{a}_3)} \cdot \frac{1}{\sin^2(\mathbf{Q}\cdot\mathbf{a}_3/2)} \tag{2.18}$$

where $0<b<1$ stands for the roughness and $b=0$ (respectively 1) corresponds to a perfectly flat (respectively infinitely rough) surface. Alternative models, in which the roughness is treated like an additional Debye-Waller factor where also proposed [Hara92].

A last important feature of the CTR's is their great sensitivity to surface relaxation. Relatively small variations of the last layer spacing are able to produce measurable asymmetries in the shape of the intensity variation along CTR's. If, for example, the last inter-planar distance is b instead of a_3, the intensity along the CTR will obey to:

$$I_\ell^{CTR} = \left| \frac{e^{ip\ell}}{2i\sin(p\ell)} + e^{2ip\ell b/a_3} \right|^2 \tag{2.19}$$

This effect increases by increasing the perpendicular momentum transfer. In practice, the geometry of the diffractometer and the wavelength will limit the maximal reachable ℓ value.

Alternatively, the surface (bulk truncation) can be understood as the multiplication of an infinite lattice by a step function. This leads to the convolution of the reciprocal space of the infinite 3D crystal with the Fourier transform of a step. The result is a smearing of the intensity of each Bragg point in the direction perpendicular to the surface. Note that, in the case the crystalline surface and the optical surfaces are not identical (miscut or vicinal surfaces), the smearing is still perpendicular to the optical surface and not to the lattice, leading to partial CTR's emerging from each Bragg peak without continuity along ℓ.

✔ **Practical considerations**

How these intensities can be efficiently measured and which are the practical limitations? The reciprocal space is a space of directions (scattering geometry in figure 2.10). One will need at least 4 settable angles: the incidence angle, a rotation of the sample around

its normal to be able to bring the atomic planes into diffraction conditions, and two degrees of freedom to position the detector arm in order to reach all $\mathbf{Q}_{//}$ and $\mathbf{Q}_{\perp}$ positions in space. Since an extra angular degree of freedom is available (3 angles are enough to define any direction of **Q**), one condition can be imposed. For standard 4-circle diffractometers, the most popular working conditions in surface diffraction are incidence fixed, emergence fixed or incidence equals emergence. Including one of these conditions, all (h, k, ℓ) positions in reciprocal space are connected in a unique manner to an angular setting. It is convenient to add two additional cradles below the sample to align the optical surface.

Light elements and large reconstructions require high flux synchrotron radiation sources like the ESRF (European Synchrotron Radiation Facility, Grenoble, France) [ESRF]. When considering deposited layers of only a few monolayers, the flux condition becomes even more stringent. Importantly, the synchrotron beam is strongly polarized in the horizontal (electrons orbit) plane. For crystallography, vertical sample geometry is then preferred because the polarization factor will remain unity for all in plane reflections whereas in the horizontal sample orientation the scattering at 90° would vanish.

Another thing to keep in mind is the contamination during the measurements, which can drastically change the structure of the surface. Moreover, surface signals are small, so the measurements and sample preparation are time consuming. Preventing contamination when studying surfaces or interfaces imposes to work in UHV conditions. The GIXD experiments reported in this work were performed with the setup located at the ESRF [ESRF] on the beamline BM32-SUV [Baud99].

✔ **Data collection, integrated intensities and corrections**

Surface diffraction is diffuse, at least in the direction perpendicular to the surface. Peak broadening may occur in various well-defined directions depending on its physical origin. When the diffracting object has a finite size D (for example an island) it means that the number of planes N_1 and/or N_2 in $I_S^{2D}(\mathrm{Q})$ will be small and the Laue condition will be partially relaxed: the intensity is no longer strictly peaked at integer (h and k). The finite domain size leads to a constant broadening with respect to $\mathbf{Q}_{//}$. Relative disorientation between individual grains will lead to a constant angular broadening (in $\mathbf{Q}_{//}$) because each grain has its own reciprocal space with some angular deviation from the average reciprocal space. Finally, when a parameter distribution is present, reciprocal spaces with different basis

vectors will superimpose about the average lattice and the diffraction features will accordingly broaden. Measuring the angular and radial in-plane widths of several orders of diffraction (*i.e.* as a function of $Q_{//}$) allows de-correlating at least the two first effects.

Because all these line shapes may coexist at any point of the reciprocal lattice, the pertinent intensity is the integrated one, which is obtained by scanning one or several angles through the investigated position. In simple words, it allows collecting all the intensity that should ideally be present at a given point of the reciprocal space. In practice, this corresponds to scanning one reciprocal space direction while integrating along the perpendicular one using sufficiently opened slits, *i.e.* an adapted resolution function. This strategy applies well for in-plane measurements and works in principle for measuring CTR's through a scan along ℓ, but actually, the other broadening perpendicularly to the CTR are often so large that not all intensity reaches the detector. Moreover, scanning along a CTR implies a perfect stability of all angles of the diffractometer. Successive rocking scans with a constant angular speed, Ω, around the surface normal for discrete ℓ values is thus the usual and preferred measurement strategy, although the slice of integrated intensity depends now on the aperture of the slits before the detector. The measured intensity depends thus on geometrical settings; the integrated momentum width $\Delta Q_{\perp}$ is nearly constant for small ℓ's and is simply related to the exit slit size L by:

$$\Delta Q_{\perp} = \frac{2pL}{lR}\cos b \tag{2.20}$$

Since the integration is performed over an angular unit volume and not a momentum unit volume, the measured intensity will depend on the relationship between the reciprocal space coordinate and the angular coordinate. The corresponding factor that divides the intensity is called Lorentz factor, L. In particular, it means that the intensity will depend on the type of scan that is performed and that each type of scan will produce a different Lorentz factor. Finally, the measured integrated intensity will also sit on a background B and will be proportional to the active area of the sample defined by the slits before and after the sample because they define the number of atoms ($N_1 \times N_2$) that contribute to the signal. Finally, if ω is the rocking angle, the integrated intensity that is really measured during a rocking scan is:

$$I_{hk\ell}^{Mes} = \int_w \left\{ \mathbf{B} + \frac{PA_0^2}{\mathbf{L}\Omega} \frac{e^4}{m^2 c^4 R^2} \left|F_{hk\ell}\right|^2 \cdot N_1 \cdot N_2 \cdot \int_{\ell-\Delta O_\perp / 4p}^{\ell+\Delta O_\perp / 4p} I_u^{CTR} du \right\} dw \qquad (2.21)$$

The measured intensity in itself is not of direct use. The important quantity is $|F_{hk\ell}|$, although the phase is definitively lost. Deducing a quantity proportional to the structure factor from a measurement needs to correct the integrated intensity for the factors that are introduced by the experiment and the geometry. The background subtraction (generally a linear regression) needs large enough scans to reach points where no scattering contributes.

Generally, a beam monitor is mounted before the sample in order to normalize the intensity with respect to the incident photon flux and allows in turn re-scaling scans that were not performed at the same speed. Another correction comes from the integration in equation (II.14); since $\Delta Q_\perp$ varies slowly and since the slope of the rod along ℓ may vary much faster, the actual ℓ corresponding to a measurement is shifted when the slope is large. Finally, the Lorentz, Area and Polarization factors depends on the diffractometer geometry and on the beamline characteristics that include the degree of linear / elliptical / circular polarization and must be calculated for each setup (adapted reference for such corrections, for different experimental setups, can be found in [Scha93a, Tone93, Vlie97, Roba00, Vlie98]).

Once the structure factors have been extracted from the measured signal, they have to be averaged with their symmetry related equivalents either in order to find the right symmetry of the signal, either, and complementarily, to deduce the systematic error that generally is close to 10% for GIXD experiments.

In the absence of a model and since the phase information is missing the Patterson map analysis is a convenient tool to test at least in-plane projected structures for reconstructions. The Fourier transform of the structure factor modulo does not give the electron density map in the unit cell, $r(\mathbf{r})$, but the density-density correlation function (auto-correlation function). Its planar section in the direct space is referred as the Patterson map:

$$P(\mathbf{r}) = \sum_{hk\ell} \left|F_{hk\ell}\right|^2 \cdot e^{-i\mathbf{Q}\cdot\mathbf{r}} = \int r(\mathbf{r}) \cdot r(\mathbf{r}+\mathbf{r}') \cdot d^3\mathbf{r}' = \left\rangle r(\mathbf{r})\, r(0) \right\langle \qquad (2.22)$$

For in plane measurements (*i.e.* ℓ=0), because of Friedel's law ($|F_{h,k,0}|=|F_{-h,-k,0}|$), the Patterson function is real and reduces to:

$$P(\mathbf{r}) = 2\sum_{hk} \left|F_{hk}\right|^2 \cos(2p\,(hx + ky)) \tag{2.23}$$

where x and y are the coordinates within the unit cell (real space).

To test the agreement between a model structure and the experimental data, two criterions can be used. The first is the chi-square, c^2, approach. For N measured diffraction peaks, p parameters in the model and an experimental uncertainty s_{hkl}^2 for an (h, k, ℓ) peak, one can write:

$$c^2 = \frac{1}{N-p}\sum_{hk\ell}\left(\frac{\left|F_{hk\ell}^{\exp}\right| - \left|F_{hk\ell}^{calc}\right|}{s_{hk\ell}}\right)^2 \tag{2.24}$$

A good agreement is obtained when c^2 is close to 1 and no new parameter should then be introduced in the model. The second criterion is the reliability factor R that is given by:

$$R = \frac{\sum_{hk\ell}\left|\left|F_{hk\ell}^{\exp}\right| - \left|F_{hk\ell}^{calc}\right|\right|}{\sum_{hkl} F_{hk\ell}^{\exp}} \tag{2.25}$$

When R approaches $(1/N)\sum_{hk\ell}\left(s_{hk\ell} \middle/ \left|F_{hk\ell}^{\exp}\right|\right)$ the agreement is good. Both criterions are helpful to discriminate between different possible models.

✔ **Application to structure determination and growth mode studies**

A complete structural determination needs for the recording of in-plane diffraction peaks, reconstruction rods and CTR's. When an epitaxial thin film is deposited on a crystalline substrate surface, all the features (in reciprocal space) that have been listed above may exist for the epilayer, plus interferences between the film and the substrate. The deposited film will exhibit its own reciprocal lattice that will superimpose to the reciprocal space of the substrate. Since the penetration depth of X-rays is large, attenuation of the substrate features will only occur for thick overlayers (several nanometers). If the film is fully incoherent, with a parameter different from the substrate, both reciprocal spaces will be fully

resolved and can be studied separately due to Fourier filtering. The peak positions during growth give a direct access to the strain relaxation of the layer and the widths of the peaks to the quality of the growing film. Such investigations were performed for the Ni/Cu(111) - (vicinal 1.2°) (chapter 3), for the growth of NiO at room temperature on the Cu(111) single crystal substrate (chapter 4), for the Ni deposited under oxygen atmosphere at 250°C (chapter 5) and for the bilayer system NiO/FeNi/Cu(111) (chapters 4 and 5). Since GIXD allows investigating the reciprocal space in 3D, it is also easily able to discriminate and to quantify different out-of-plane stacking with the same in-plane structure like twins and stacking faults in the face centered cubic (fcc).

2.2.3.3 Grazing Incidence Small Angle X-ray Scattering (GISAXS)

Determining the morphology of islands during their growth on a substrate is a very important step in the control of nanometer-sized objects (nano-objects) during their fabrication. For that sake, a new method, called *Grazing Incidence Small Angle X-ray Scattering* (GISAXS), has been developed in the last decade [Levi89, Naud97, Babo99, Rena99], and very recently applied *in situ*, in UHV, *in real time* during growth [Rena99, Rena00]. I will briefly describe below some useful characteristics of this new method.

The periodicity at the atomic level, *i.e.* with typical periods of a few 0.1 nm, can be characterized by measurements of the scattered intensity in reciprocal space far away from the origin. If objects of much larger dimensions (typically between a few nanometers and several tens of nanometers), are present in the sample, additional scattering will be found close to the origin of the reciprocal space. Its measurement and analysis for bulk samples is the object of a very well known and old method: *Small Angle X-ray Scattering* (SAXS) [Poro82], for which measurements are usually performed in transmission.

This method has recently been extended to analyze the morphology of nanometer-scale particles deposited on, or embedded below the surface of a sample, by combining the SAXS technique with grazing-incidence conditions, thus making it surface sensitive [Levi89]. GISAXS is performed under conditions close to total external reflection conditions. One of the most exciting possibilities of GISAXS is the *in situ* UHV investigation of the evolution of the morphology of deposits growing 3D on a substrate, in particular when the use of imaging techniques is difficult. *In-situ* investigation of the NiO/Cu(111) interface will be presented in this work (§4.5).

The experimental geometry of GISAXS is schematically represented in figure 2.12. The incident beam impinges on the sample under grazing incidence close to a_c, and a 2D detector is placed behind, recording the intensity in the ($\mathbf{Q}_{//}$, $\mathbf{Q}_{\perp}$) plane of the reciprocal space. This scattering contains information on the islands shape, height and lateral size, as well as on the organization of the islands with respect to each other. Since this scattering is very small,

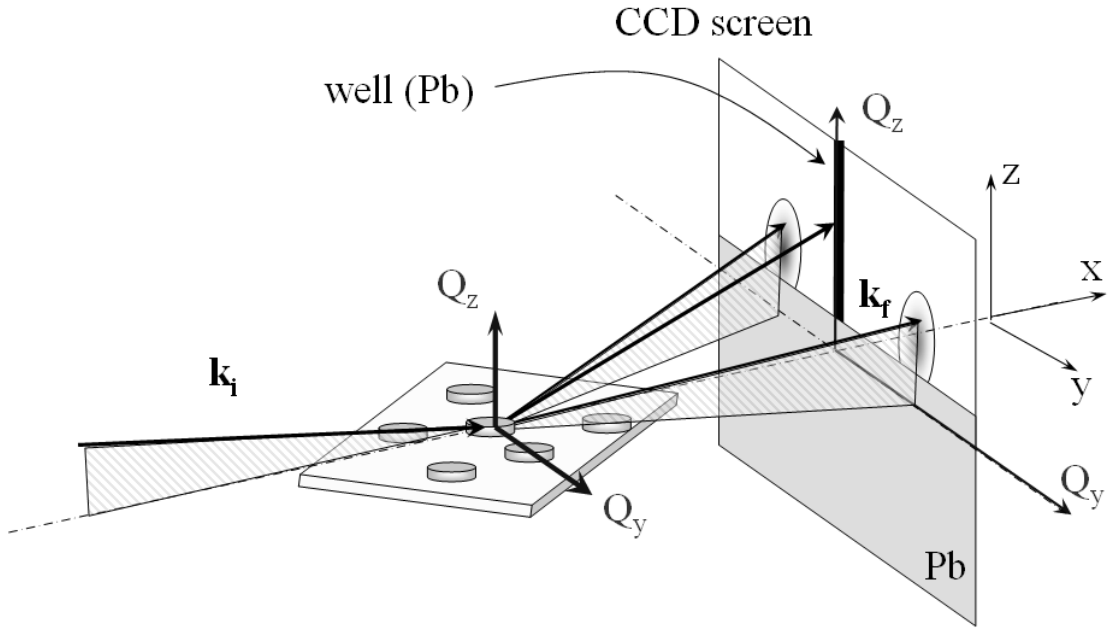

Figure 2.12: Typical geometry for a GISAXS experiment

the direct, transmitted and reflected beams are completely stopped by a beam-stop before the detector, to avoid saturation.

Because the investigated distances are large compared to inter-atomic distances, the particles are generally treated as a continuum. For a dense system of N_p identical and isotropic particles, the scattered intensity $I(\mathbf{Q})$ can be expressed as :

$$I(\mathbf{Q}) = A \cdot N_p \cdot P(\mathbf{Q}) \cdot S(\mathbf{Q}) \cdot T(a_f) \tag{2.26}$$

where A is a constant, $P(\mathbf{Q})$ is the form factor of one particle, $S(\mathbf{Q})$ the interference function and $T(a_f)$ the transmission factor which reflects the effect of refraction of the scattered wave.

The form factor $P(\mathbf{Q})$ is the square of the amplitude $F(\mathbf{Q})$ scattered by a single island of volume V:

$$F(\mathbf{Q}) = \int_V r(\mathbf{r}) \cdot e^{-i\mathbf{Q}\cdot\mathbf{r}} dV \tag{2.27}$$

where r is the electronic density within the island.

The interference function $S(\mathbf{Q})$ enters the expression only if the particles are correlated. It is related to the particle-particle pair correlation function $g(\mathbf{r})$ by:

$$S(\mathbf{Q}) = 1 + r_S \int \left(g(\mathbf{r}) - 1\right) \cdot e^{-i\mathbf{Q}\cdot\mathbf{r}} d\mathbf{r} \tag{2.28}$$

where r_S is the surface density of islands. This statistical $g(\mathbf{r})$ function tells us how the particles are distributed with respect to each other. Further details about all of the functions describing the scattering process are given in the chapter 4.

In practice, the form factor $P(\mathbf{Q}, R, H)$ can be analytically calculated for most simple shapes usually taken by islands growing on a surface (truncated cylinders, ellipsoids or pyramids). The resulting intensities have characteristic profiles with a series of well-defined zeros (minima when dealing with experimental data). The position of the minima as well as the profile of the intensity unambiguously allows determining the shape, as well as to estimate the average height and lateral size. If the particles are correlated, the main resulting feature is an interference peak as a function of $Q_{//}$, whose position Q_p directly yields a rough estimation of the average centre to centre inter-particle distances D, according to $D = 2\pi/Q_p$ [Levi91, Naud98, Schm99, Babo00]. However, this crude approximation yields a systematic error. Finally, the distributions of dimensional parameters yield large variations of the intensity in the minima, from which the distribution parameters σ can be estimated. Using a more detailed analysis, it is even possible to fully reproduce the 2D GISAXS pictures.

In the particular case of NiO deposited at room temperature, a complete analysis was performed reproducing entirely the GISAXS patterns. Details concerning the used methodology to calculate the GISAXS patterns are given in chapter 4.

2.3 MAGNETIC MEASUREMENTS

2.3.1 X-ray Magnetic Circular Dichroism (XMCD)

In 1975, Erskine and Stern [Ersk75] considered excitations between a *core* state and a *valence* state and performed a simple calculation on the expected effect for the $M_{3,2}$ edges in metallic Ni. This paper constitutes the birth of what is known as X-ray magnetic circular dichroism (XMCD).

For a medium in an external magnetic field, the absorption coefficient μ is related to the imaginary part of the refraction index Im(*n*), *n* being connected to the dielectric tensor, which is polarisation dependent. *The dependence of m on the state of (circular) polarisation of the light is called x-ray magnetic (circular) dichroism.*

$\mathrm{XMCD} = \frac{\mu^+ - \mu^-}{\mu^+ + \mu^-}$, + (respectively -) indicating the parallel (respectively antiparallel) orientation of the helicity to the majority (respectively minority) spins.

The edge energy levels of transition metal compounds in the samples implied to use soft X-rays. Since it is an X-ray absorption technique, it is mainly surface sensitive in this energy range. Informations from ultra-thin layers can be obtained because the dichroic signal is strongly enhanced (factor ~100) in resonant conditions (the energy of the X-ray beam corresponds to the absorption edge).

Depending on the magnetic material, *linear* or *circular* polarised X-rays must be used (we deal thus with XMLD (signal proportional to $<M^2>$ value for AF) or XMCD (signal proportional with <M> value for F)).

Two important *sum rules* have been derived for XMCD, allowing to deduce element specific orbital and spin magnetic moments from X-ray absorption spectroscopy (XAS) and its associated magnetic circular dichroism data [Thol92, Carr93].

When the axis of the magnetic field (quantization axis) is parallel or antiparallel to the propagation direction of the circularly polarized photon, a simple selection rule is obtained for this particular experimental geometry: $\Delta m = m_{final} - m_{initial} = \pm 1$. Figure 2.13 shows an energy level scheme of an hypothetical system exhibiting XMCD. It is clear that the transition corresponding to $\Delta m_\ell = -1$ (right side) is forbidden (low probability for absorption of this channel). As the transition happens only near the resonance, one of the important features of XMCD is its element-specificity. In an alloy or multilayer, the magnetic characteristics of a

specific element/layer can be investigated by recording the signal at the correspondent absorption edge. Figure 2.14 (from [Stoh98]) shows the way 3*d* electrons are probed in conventional X-ray absorption experiments (a) and in XMCD (b,c).

Unfortunately, the most important edges at which the sum rules can be applied for transition metals lie in the soft X-ray range, where measurements of the absorption by transmission measurements can often not be applied. One needs to resort to yield methods, in which the flux of secondary emission produced by the primary absorption process is used, to measure the absorption coefficient. Different working modes can thus be used to detect the

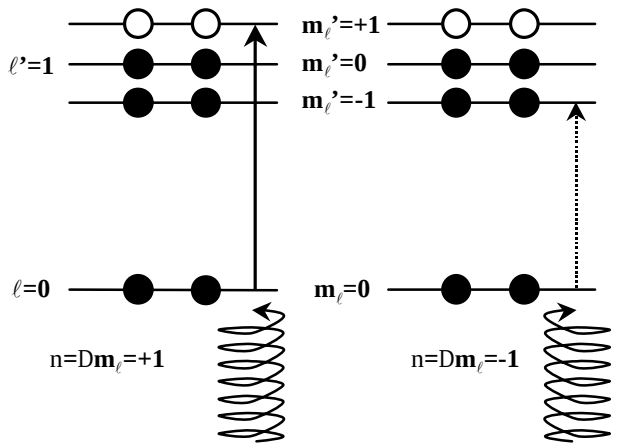

Figure 2.13: An energy level scheme of an hypothetical system exhibiting XMCD. Although the selection rule is satisfied, the transition corresponding to Δm_l=-1 (right side) is forbidden (since the m_l=-1 level is occupied, the probability of absorption of this channel is small).

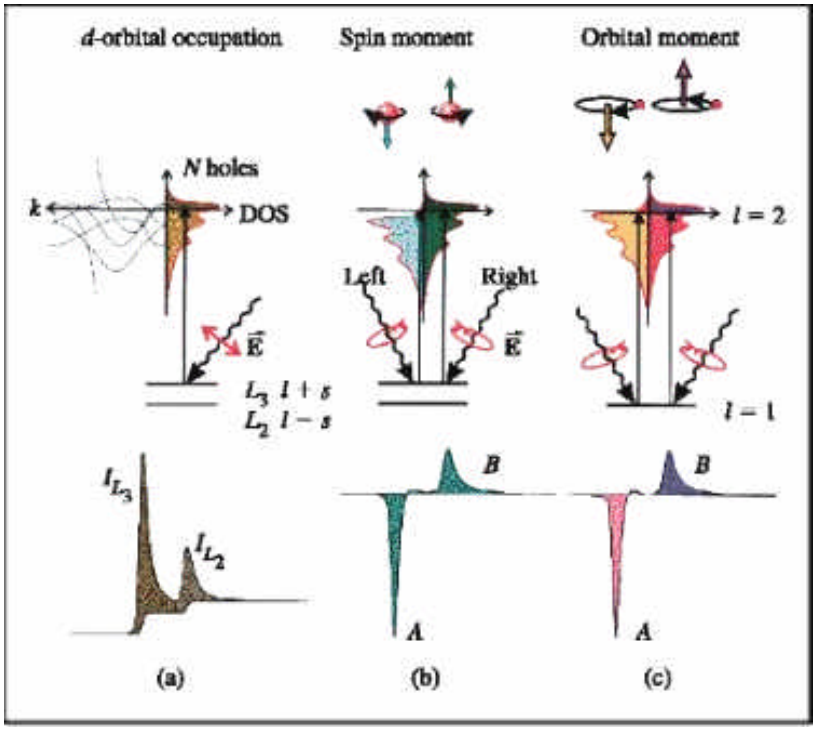

Figure 2.14: Electronic transitions in the conventional L-edge X-ray absorption (a) and in XMCD (b,c) illustrated in the one-electron model. The transitions occur from the spin-orbit split 2*p* core shell to empty conduction bands states above the Fermi level, E_F. In conventional X-ray absorption (see note), the transition intensity measured as the white-line intensity is proportional to the number of *d* holes, N. By use of circular polarised X-rays, the spin moment (b) and orbital moment (c) can be determined from the dichroic difference intensities A and B using the sum rules.

dichroic signal when varying the incident photon energy across the edge:

✔ ***Fluorescence yield detection***: In this case, the detector is a photodiode detecting the X-ray fluorescence signal from the sample in the X-ray beam. This technique works for insulating samples (which is the case of the NiO single crystalline substrates), but the results are qualitative. Indeed, for thick samples (and it is the case of NiO substrates, which have thickness 0.5-1 mm), the necessary absorption corrections for the fluorescence spectra (in order to extract quantitative results with the sum rules) are very difficult to apply (known to suffer from saturation and self absorption effects [Voge94a, Ydze94, Eise93, Veen96]) and can lead to errors that are much larger than the signal. Moreover, the fluorescence yield method is insensitive to the applied magnetic field, but the yield is intrinsically not proportional to the absorption cross section. It is well adapted for qualitative measurements. This is why the other detection mode was used for our samples.

✔ ***Electron yield detection***: In this case, the measured signal is the drain current appearing in the sample during X-rays irradiation. This drain current is recorded for each X-ray energy point. The above mentioned sum-rules show how, from dichroism spectra recorded in electron yield, it is possible to quantitatively determine the orbital and spin moment. However, to get reliable data, a conducting sample (metallic) is needed. In our case, we overcome the insulating character of the sample by using thick films (70 Å Co and 20 Å Au capping) and focusing the X-ray beam near the edge of the NiO substrate, thus helping the collection of emitted electrons by the metallic fixations on the edge. The practical experimental conditions were however tricky. The total electron yield method is sensitive to the varying applied magnetic field, with possible effects in changing the electron detecting efficiency, or, equivalently, the sample photo-current. Saturation effects may also appear for thicker films [Naka99]. However, due to the possibility of extracting quantitative data, it is the preferred method in most experiments.

XMCD experiments can be performed, with the same result, in two ways: either the magnetisation of the sample is reversed (applying an external magnetic field) while the helicity of the X-ray beam is maintained constant, or the helicity of the beam is reversed at constant magnetisation. Then, the difference spectra should present dichroic signals only near the absorption edges like in figure 2.15 (from [Chen95]).

A typical treatment of the absorption spectra is given in figure 2.15. The dichroic signal (XMCD) is calculated as the difference between the two absorption spectra obtained for two different configurations between the helicity and the external magnetic field, shown in

figure 2.15-b. Pairs of absorption spectra can be obtained either by changing the helicity or the direction of the applied field. Integrating the XMCD curve we can extract two valuable quantities used in the XMCD sum rules: *p* and *q*. In a very simple description, since the $L_{2,3}$ splitting appears due to the spin-orbit coupling, the *p* and *q* values describe in fact the spin and orbital contribution in the magnetic momentum, respectively.

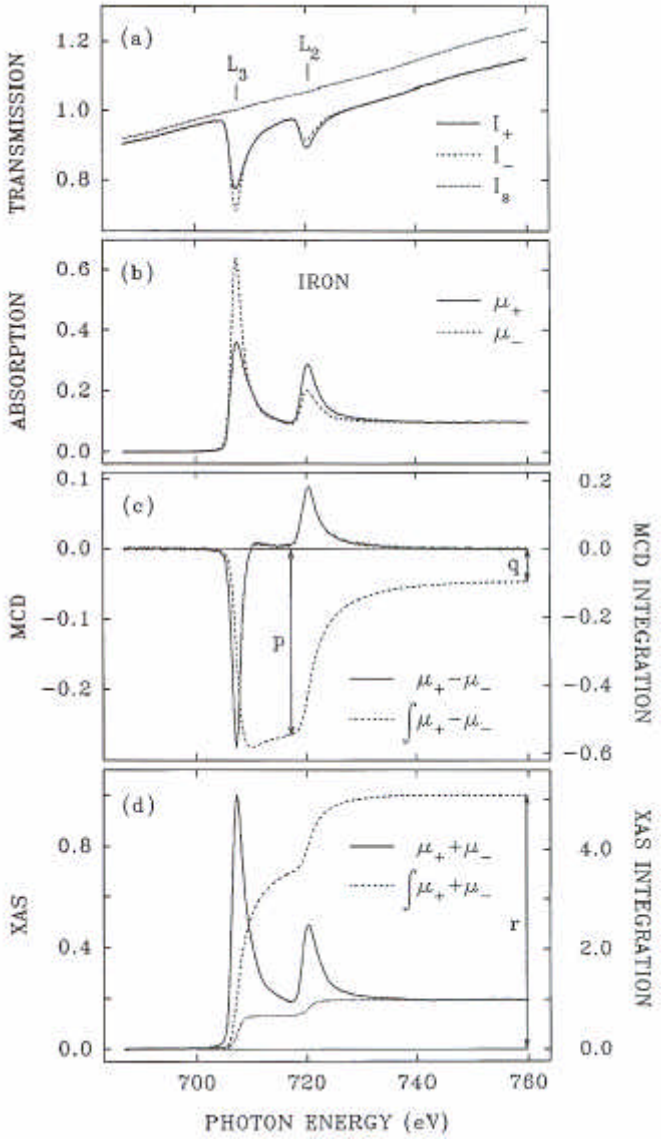

Figure 2.15: (from [Chen95]) $L_{2,3}$-edge XAS and XMCD spectra of iron:
a) transmission spectra of Fe/parylene thin films, and of the parylene substrates alone, taken at two opposite saturation magnetizations;
b) the XAS absorption spectra calculated from the transmission data shown in (a);
c) and d) are the XMCD and summed XAS spectra and their integrations calculated from the spectra shown in (b) The dotted line shown in (d) is the two-step-like function for edge-jump removal before the integration. The p and q shown in (c) and the r shown in d) are the three integrals needed in the sum-rule analysis (2.29).

The sum rules defined by B.T. Thole [Thol92] and P. Carra [Carr93] and demonstrated by Altarelli [Alta93], give the possibility to separately estimate the spin and the orbital magnetic moments values. They are related with the *p*, *q* and *r* (integrated XAS sum) values by:

$$\begin{cases} M_L = \dfrac{2}{3} \cdot \dfrac{q}{r} \cdot n_h \\ M_S^{eff} = \dfrac{3 \cdot p - 2 \cdot q}{r} \cdot n_h \\ M_S^{eff} = M_S - 7 \cdot M_T \end{cases} \tag{2.29}$$

We remark that in the sum rules the measured spin term is the *effective spin moment* depending on the *spin moment* and *dipolar moment* values. The last term is related to the spin moment anisotropy and, in the case of transition metals, is generally neglected. It is important to note that the sum rules written in the form 2.29 give the *magnetic moments per atom* (in μ_B/atom), through the number of holes per atom n_h. Measuring the magnetic orbital moment along several directions with respect to the sample surface allows the determination of the *orbital anisotropy* which is therefore related to the *magnetocrystalline anisotropy energy* (MAE). Their specific calculation is detailed in chapter 3.

Chapter 3:

METALLIC Ni/Cu(111) INTERFACE

3.1 INTRODUCTION

For magnetic materials, studying the correlation between the structure, the morphology, and the induced magnetic properties, is of fundamental interest: it allows a better understanding of the magnetic behavior of low-dimensional systems and offers new insights of the magnetic properties at a microscopic scale. Compared with bulk materials, these systems exhibit a wide range of magnetic phenomena due to the reduced symmetry, finite cluster size and hybridization of the electronic states at the interface. The magnetic anisotropies are directly related with the microscopic structure of the artificially grown nanostructures. Therefore, a detailed study of their structure together with the resulting magnetic properties is of crucial importance. In this context, ultra-thin Ni films deposited at room temperature on non-magnetic single crystal Cu(111) substrates have been investigated for structure and magnetic properties.

Let me summarize here some important results of the literature. First studies concerning the structure of the Ni/Cu(111) ultra-thin films have been realized by means of helium atom scattering and LEED [Wulf98]. The authors conclude that six-fold in-plane symmetry (twinned fcc structures) island growth dominates at room temperature, whereas higher temperatures promote the step-flow growth.

Due to the interplay between atomic mobilities and step distances, the step-flow growth can be favored either via temperatures effects, increasing the atomic mobility, or by decreasing the distances between steps. Therefore, by choosing a vicinal Cu(111) surface with miscut angle of 1.2°, we have produced at room temperature self-organized and small size clusters aligned and oriented along the steps which are naturally formed on the vicinal surface. By STM we established that the step-flow dominates the growth and that below 0.5 ML Ni bilayer stripes are aligned along the steps. Large triangular shaped islands, one monolayer high, are located on the (111) surface only on terraces wider than 500Å. The monolayer islands growth contrasts with the results obtained for Co [Figu93, Pede97] and Fe [Brod93, Jenn96] on Cu(111). The Cu(111) 1.2°-miscut vicinal surface shows typical step distances of 80-100Å [Cher01a] leading thus to the formation of only a few number of large triangular islands.

The magnetic anisotropies in thin films and multilayered systems are mostly considered relative to the in-plane vs. out-of-plane directions. The azimuthal dependence of the in-plane anisotropy is generally neglected. Studies using the magneto-optic Kerr effect performed on stepped surfaces show that for ultra-thin Fe/W(001) [Chen92] and Co/Cu(100)

[Berg92, Webe96] uniaxial in-plane anisotropies are present. Recently, we showed that ultra-thin $Fe_{65}Ni_{35}$/Cu(111) 1.2°-miscut [Cher01a, Cher01b, CherPhD] present large in-plane orbital magnetic moment anisotropy, related to strained and oriented stripes promoted by the step-decoration growth. The magnetic moments and the anisotropy of ultra-thin Ni/Cu(001) films have been studied both experimentally an theoretically. In agreement with theoretical studies [Ters82, Hjor96], the spin magnetic moment of the Ni films was found to be reduced compared to bulk Ni [Sriv98]. This behavior is due to the 3d hybridization at the Ni-Cu interface, leading to a quenched exchange splitting. Moreover, the measured orbital magnetic moments were found strongly lowered for ultra-thin films, whereas theory predicts increased orbital moments, on the basis of a surface reduced coordination number. Tensile stress present in the nickel film up to 30-50Å [Hope97, Lee97] are shown to be responsible for the reduced orbital and spin magnetic moments.

In this chapter I will focus on the effect of the growth of Ni/Cu(111) on the magnetic moments and magnetic anisotropies. The magnetic moments and the anisotropies will be discussed as a function of the specific Ni/Cu(111) morphology and structure. Thus, I will evidence the direct relationship between the structural (morphological) and electronic anisotropies and the magnetocrystalline anisotropy energy (MAE).

3.2 EXPERIMENTAL SETUP

The experiments were carried out in an UHV system (base pressure 10^{-10} mbar), equipped with AES, LEED and STM facilities. The particular UHV chamber geometry allowed us to perform real-time AES measurements during the nickel growth, to establish the *As-t* kinetic. For the reason described in the introductory part, we chosen an Cu(111) single crystal, cut at 1.2° with respect to the [111] direction. In this way, we obtain a vicinal surface with monatomic steps parallel to the $[1\bar{1}0]$ direction and perpendicular to the $[11\bar{2}]$ one, which leads to (111) microfacets (figure 3.1). The substrate was cleaned by repeated cycles of Ar^+ sputtering and annealing at a temperature close to the surface fusion temperature (about 800K). The high quality crystallization of the Cu(111) surface was checked *in situ* by LEED. The cleanliness of the substrate was probed before Ni evaporation by wide range AES spectra, assuring thus that the average contaminants (especially carbon) presence is below 3%. The chemical cleanliness being achieved, STM was used to verify if straight and parallel steps are obtained. Ultra-thin Ni films were elaborated from a nickel rod of 99.998% purity,

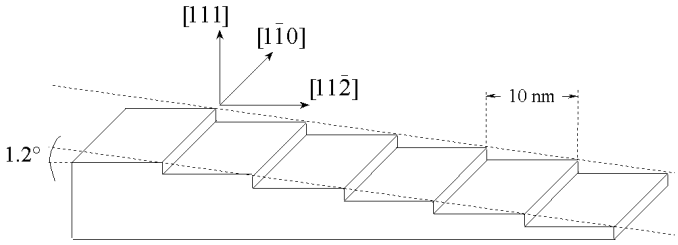

Figure 3.1: 1.2° vicinal Cu(111) single crystal substrate; the average terrace width is of 10 nm

by electron bombardment, into an EFM3-Omicron UHV evaporator. During evaporation, the substrate was held at room temperature. Thickness calibration was made using Auger electron spectroscopy, and confirmed later with a quartz micro-balance during synchrotron experiments. A complementary thickness calibration was made through the measurements of the heights of X-ray absorption at the Ni L_3 edge. The error in the calibrations, mainly due to uncertainties in the cross-section values obtained from [Yeh85], are estimated to be less than 10%.

Structural investigations were performed using the GIXD technique, on the BM32 (SUV – "*Surface Under Vacuum*") beam-line at ESRF ("*European Synchrotron Radiation Facility*"), Grenoble (France). The substrates were mounted vertically in an UHV chamber equipped with Be windows and supported by a four-circle goniometer [Baud99]. The surface diffraction work condition was established fixing the incidence angle to the value corresponding to total external reflection of copper at 18 keV, 0.187°. All measurements were carried out with a beam energy of 18 keV, in order to avoid the fluorescence background of Ni and Cu. For the quantitative out-of-plane measurements, along the crystal truncation rods (CTRs) [Andr85, Robi86, Roba00], the acceptance of the detection slits was fixed to an angular acceptance of 4x4 mrad. They were set at 4x12 mrad for the in-plane measurements. Typical focused beam size is 4-600 μm (horizontal) x 3-400 μm (vertical) [Baud99]. The measured intensities were corrected in all cases for background, active area, Lorentz, monitor and polarization factors [Vlie97, Vlie98, Roba00, Scha93a, Tone93]. A triangular unit cell is used to describe the 3-fold symmetry of the (111) surface. The h and k indexes describe the in-plane momentum transfer ($q_{\|}$) and the ℓ index the perpendicular one ($q_{\perp}$), expressed in reciprocal lattice units (r.l.u.). The [h00] and [0k0] in-plane directions are defined in such a way that a Bragg peak is found at the (101) position in the reciprocal space. For the in-plane measurements, the exit angle of the detector was set equal to the incidence one ($b = a$). Therefore, the real surface plane, characterized by $\ell = 0$, is not accessible. All reported in-plane measurements were in fact performed at a ℓ value of ≈ 0.1.

The magnetic properties of the ultra-thin Ni films were investigated by XMCD, using a 90±5% circularly polarized X-ray beam. The measurements were performed on the ID08 (former ID12b) beam line at ESRF. The data were recorded at 10K at the Ni $L_{2,3}$ absorption edges, in the total electron yield detection mode and under a permanent magnetic field applied parallel to the incoming photons. For each situation two sets of dichroic spectra were obtained by scanning the Ni $L_{2,3}$ edge energy area at a given helicity of the circularly polarized light for two opposite applied magnetic fields and by applying the same procedure after having reversed the helicity. For all measurements, the applied magnetic field was set at 4T to ensure the magnetic saturation of the sample, checked by a hysteresis curve performed at the Ni L_3 edge. The XMCD geometry will be detailed later in §3.5.

3.3 GROWTH AND MORPHOLOGY – COPPER DIFFUSION AND CAPPING

Auger electron spectroscopy was used, in a first approach, for the description of the Ni ultra-thin films growth on Cu(111). Using the As-t representation of the substrate and adsorbate intensities we can compare whether the growth follows a layer-by-layer growth, or a 3D one (islands formation). It is important to note that the extraction of the Ni LMM transition intensity from the Auger spectra is not trivial. In figure 3.2, we show the evolution of the AES spectrum with the thickness. The strongest nickel Auger transition, at 848 eV LMM, is confounded with the copper LMM transition at 849 eV, due to our CMA analyzer resolution (>1eV). Therefore, we have to extract the Ni contribution in peak B, considering

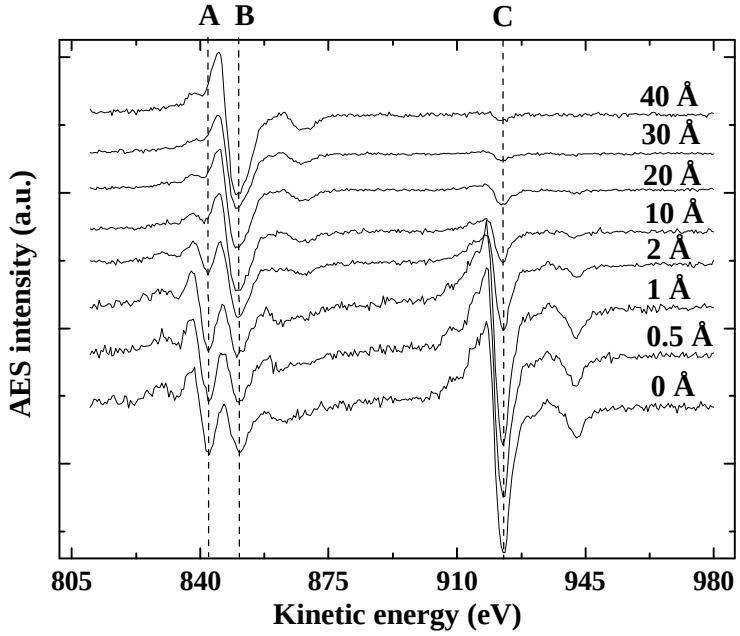

Figure 3.2: *Evolution of the AES spectrum as a function of the deposited Ni quantity*:
A, B and C stand for Cu 841eV, Cu 849eV and Cu 920eV Auger LMM transitions respectively. Due to the energy position of the Ni 848eV LMM transition, there is an overlap with the Cu 849eV LMM one.

the ratio $I_C(0)/I_B(0) \cong 3$, which characterizes the clean copper Auger spectrum. Thus, considering that the above ratio is constant, at a moment *t*, the Ni intensity can be written as:

$$I_B^{Ni}(t) = I_B(t) - \frac{I_C(t)}{3} \tag{3.1}$$

Besides the qualitative growth description, the As-t representation was used in order to calibrate the Ni deposition/evaporation rate. Using an IMFP λ = 10Å [xps-nist], the resulting calibration was determined from:

$$d(t) = f \cdot t = l \cdot \cos q \cdot \ln \frac{I_0^{Cu}}{I_t^{Cu}} \tag{3.2}$$

In practice, the flux f was adjusted in equation (3.2) in such a way that the substrate calculated curve best fit the corresponding experimental data in the very low coverage regime (below 1ML), so that the experimental data remain always "upper" compared with the theoretical layer-by-layer one (the layer-by-layer curve describe the fastest decay). In this manner, we obtain what is called "the equivalent thickness". In the following discussions, the *equivalent thickness* will be simply addressed as the "*thickness*".

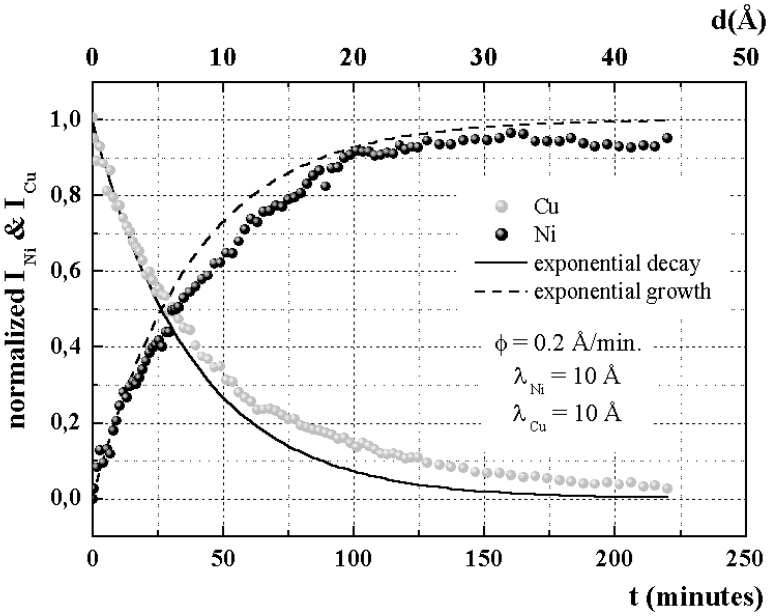

Figure 3.3: *As-t representation of the LMM Cu(920eV) and Ni(848eV) transitions*:
The axis transformation from minutes to film thickness (Å), is made according to an exponential layer-by-layer growth of Ni/Cu(111), and taking into account an inelastic mean free path (IMFP) λ=10Å. The resulting evaporation rate is of 0.2Å/min. The intensities are normalized relative to the I_0 value for the copper.

In figure 3.3, we show the As-t representation for both, Ni and Cu. Together with the measured data, we represented also calculated curves, describing an ideal layer-by-layer growth. These calculated curves are obtained using the well known formulae for the exponential decay and exponential growth, respectively:

$$\begin{cases} I_t^{Cu} = I_0^{Cu} \cdot e^{-\frac{d}{l \cdot \cos q}} \\ I_t^{Ni} = I_\infty^{Ni}(1 - e^{-\frac{d}{l \cdot \cos q}}) \end{cases} \quad (3.3)$$

where: I_0^{Cu} - stands for the pure copper surface signal, I_∞^{Ni} - AES intensity of pure nickel, d - is the Ni thickness, l - the IMFP ("*Inelastic Mean Free Path*"), and $\cos q$ - is the geometric factor given for the AES analyzer (the angular acceptance of the CMA system).

In this way, it can be observed that the experimental data correspond to a 3D growth, characterized by island formation. Another characteristic aspect of 3D growth, is that even for relatively high coverage the copper substrate signal is still non-negligible, corresponding to a fraction of non-covered Cu(111) surface or with very low coverage. Anyhow, this is strictly a qualitative description and only STM measurements will give a detailed description of the growth and morphology.

The STM measurements (figure 3.4) show that, in the 0.1ML – 0.6ML coverage range, the Cu(111) surface is covered by stripes along the $[1\bar{1}0]$ direction. In figure 3.4-b and 3.4-c it can be clearly observed that the stripes appear on the upper part of the terraces. As presented in §3.1, at room temperature, due to the terraces width of about 10 nm (figure 3.4-

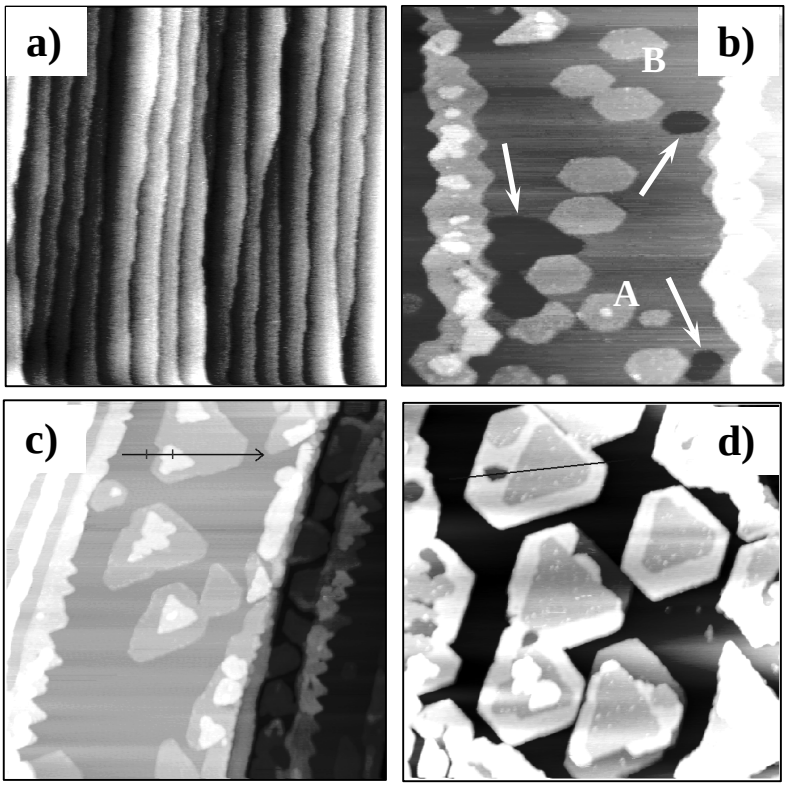

Figure 3.4: *evolution of the Ni/Cu(111) morphology with respect to the Ni thickness*:
a) (150x150 nm^2) *clean Cu stepped surface*: straight and equidistant terraces with a mean width of about 80Å;
b) (110x110 nm^2) *0.3ML Ni*: hexagonal shaped islands are present on terraces larger than 500Å;
c) (200x200 nm^2) *0.6ML Ni*: large triangular islands (about 400Å) are present on the terraces and are characterized by a height of two atomic layers;
d) (145x145 nm^2) *1.8ML Ni film*: the islands are similar with those observed for the 0.6ML Ni film, but their height is of 3 atomic layers.

a), the Ni will grow mainly via the step-flow growth mode. On large terraces (width > 500Å), we notice the presence of wide islands. We conclude therefore that Ni adatoms have reduced mobility, less than 500 Å until the atoms are trapped on one site. Although step-flow growth predominates at the sample scale the characteristic Ni/Cu(111) morphology on large terraces deserves further discussions. Thus, even if in figure 3.4 we present only large terraces, they are not typical STM images of the Ni morphology. However, in the further discussions the conclusions apply also for the step edges Ni stripes, since, as it can be observed in figure 3.4-b and 3.4-c, they are characterized by the same height as the islands.

For the 0.3ML Ni film (figure 3.4-b), the islands show an hexagonal shape and are mainly of one atomic Ni layer height. Some islands (A) present also small fractions of the second Ni layer (figure 3.4-b). Arrows in figure 3.4-b indicate the formation of holes in the copper substrate. Observed also in other systems where Cu(111) was the substrate [Cher01a, Figu94], the hole formation was related to the high surface copper atoms mobility at room temperature. Diffusing on the surface, a copper atom could experience 3 different mechanisms: a) once an Ni island (or Ni stripes at the step edge) is reached, the copper atom will borrow/adsorb into/on the island by alloying; b) the copper will cover the Ni island, or c) the copper will diffuse till the lower step edges part, where it will be trapped. As was suggested by theoretical studies [Raek92, Pour99], from an energetic point of view the Cu/Ni/Cu sandwich is the most stable configuration. Moreover, the formation of a Ni-Cu alloy does not occur even for elevated temperatures as 900K (Ni preferring a dissolution process in the copper substrate [Auff01, Erde02]). It would thus be possible that the diffusing copper atoms cover the Ni islands. However, for the 0.3ML Ni film there is no evidence supporting clearly this mechanism. The height analysis correspond very well to pure Ni layers on Cu(111) (1.6Å for the 1st Ni layer and 2.2Å for the 2nd one), without capping.

The transition from 0.3 ML to 0.6 ML (figure 3.4-c) thickness is characterized by the change in shape and size of the islands: while at 0.3ML they show equally distributed (110) and (111) facets (related to the presence in equal quantities of faulted and unfaulted fcc stacking), at 0.6 ML they show mainly (110) facets. The same (110) preferential orientation was observed in the case of the homoepitaxial growth of Pt(111) and Cu(111) [Mich93]. In the case of Ni/Cu(111), previous helium diffraction and SPALEED studies [Wulf98] show preferential (110) island edges formation. The authors explain this behavior by a faster growth speed of the (111) compared with the (110) edges. As it can be observed in figure 3.4-c, the stripes also changed, following the same mechanism as described above. On top of triangular

islands, we can distinguish the apparition of the second Ni layer, characterized by a height of 2.2Å. At this stage, no copper diffusion was observed.

Increasing the Ni thickness above 1 ML, for the 1.8 ML film, the islands shape and size are similar to those observed at 0.6 ML, but the number of Ni layers has risen to 3. Due to the different electronic sensitivities between adjacent Ni and Cu layers, a relative STM contrast appears on the top of the islands (figure 3.4-d). This contrast is related to copper capping of the Ni islands, the Cu on top layer surrounding the partially formed 3rd Ni layer (figure 3.5-b). The line profile in figure 3.5-b, shows an apparent z contrast on the top of the island of 1.1Å, due to the constant current mode acquisition. Height analysis shows three

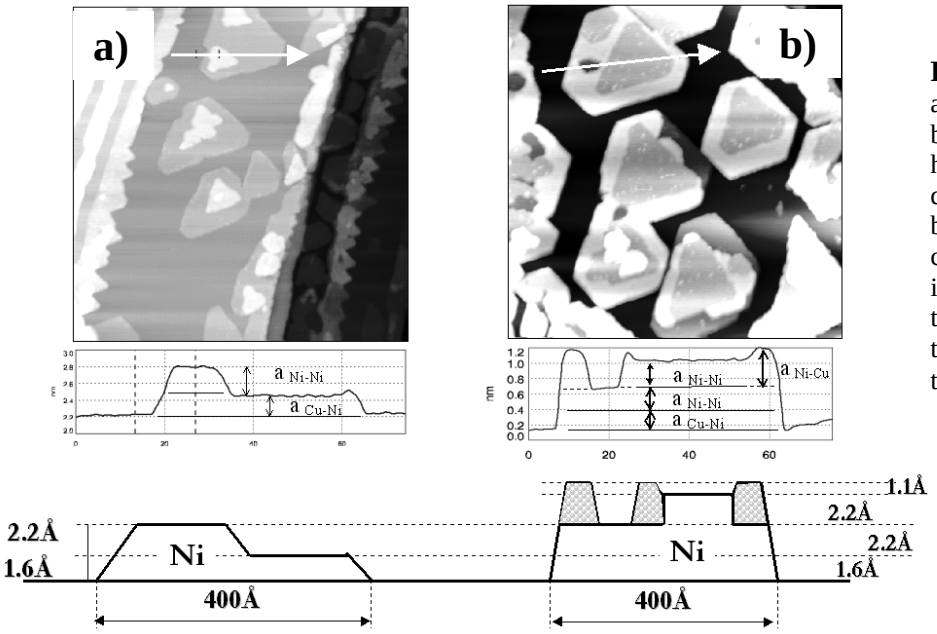

Figure 3.5: *copper capping*:
a) *0.6ML Ni film*: characterized by islands of 2 atomic layers high; no sign of copper diffusion can be observed
b) *1.8ML Ni film*: a relative contrast appears on top of islands. As described in the text, this contrast corresponds to the copper diffusion on the top of Ni islands.

different z levels: a) at the Ni/Cu bottom interface, $a_{Cu\text{-}Ni}$ = 1.6Å, b) Ni-Ni interlayer distance, $a_{Ni\text{-}Ni}$ = 2.2Å, and c) the Cu/Ni top interface, $a_{Ni\text{-}Cu}$ = 3.3Å. In the absence of any chemical contrast, the bottom and the top Ni/Cu interlayer distance should be identical. Taking into account the real topographic interlayer distance of 2.2Å (for both Cu and Ni layers), we can explain the difference between the bottom and the top distance values, adding the corresponding electronic contrast: -0.6Å (1.6Å-2.2Å = -0.6Å) when probing Ni overlayer on Cu, and respectively +1.1Å (3.3Å-2.2Å = 1.1Å) when probing Cu overlayer on Ni. But, even considering this additional electronic effect, the chemical contrast should be equal in both cases (top and bottom), with reversed sign, which is not the case. The difference 1.1Å-0.6Å = 0.5 Å can then be attributed either to structural effects (compression of the first Ni layer), or to sunken Ni islands into the Cu(111) surface. These values are in good agreement with those reported by Pons et al. [Pons01] given for the same system. However, their argumentation is

based on the differences between three different islands families (mono- and bilayer with and without Cu capping). They do not have a direct proof of the chemical contrast in the top of islands, as in our case. As presented above, theoretical calculations have already shown that the minimization of the surface free energy for this system can be achieved by copper capping the Ni islands [Raek92, Pour99].

☑ *In summary, we established two major stages in the Ni/Cu(111) growth: a) the films with thickness below 1ML present large Ni islands, of 1 or 2ML height and an average width of about 400Å, and b) above 1ML, the Ni islands are partially covered by a Cu layer, giving rise to a second Ni/Cu interface.*

3.4 STRUCTURE – TETRAGONALIZATION

Taking into account the three-fold symmetry of the (111) surface, we chose in our description a hexagonal surface unit cell, instead of the cubic fcc one. In this way, we can simplify both, measurements set-up and the data analysis. The transformation from the bulk cubic fcc cell to the surface hexagonal one, is shown in figure 3.6. The a_s, b_s and c_s hexagonal modulus of the basis vectors are related to the bulk basis by:

$$\begin{cases} a_s = \frac{1}{2}[\bar{1}10] \\ b_s = \frac{1}{2}[0\bar{1}1] \text{ and } a_s = b_s = 90°, g_s = 120° \\ c_s = [111] \end{cases} \quad (3.4)$$

Thus, instead of $a_c = b_c = c_c = 3.61$Å for Cu and 3.52Å for Ni, we use $a_s = b_s = 2.556$Å, $c_s = 6.261$Å for Cu, and $a_s = b_s = 2.492$Å, $c_s = 6.104$Å for Ni, respectively. All the h, k and ℓ indexes are expressed in the reciprocal lattice units of the Cu surface unit cell (Cu r.l.u.).

In figure 3.7 we show the reciprocal space of Cu(111) and the expected positions for epitaxial Ni/Cu(111). Due to the surface hexagonal symmetry, in the reciprocal space, Bragg peaks will appear at $h = k = 3\times m$, with m integer, along the in-plane [h00] and [0k0] directions, respectively. In the [hh0] direction Bragg peaks are located at each integer h value.

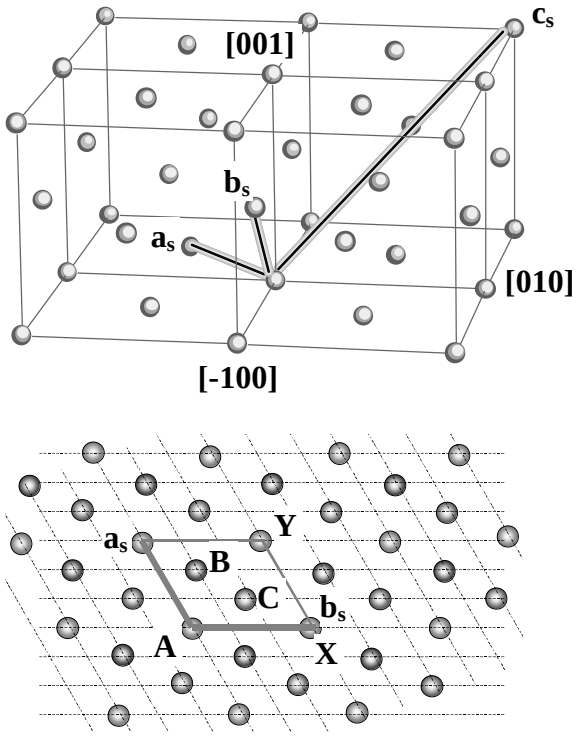

Figure 3.6: *transformation from cubic to hexagonal surface lattice*:
On the top side of the image the relation between the fcc cubic structure and the surface cell basis vectors; on the bottom side, the projection in the (111) plane of the fcc stacking (ABCABCA…), and the in-plane surface basis vectors.

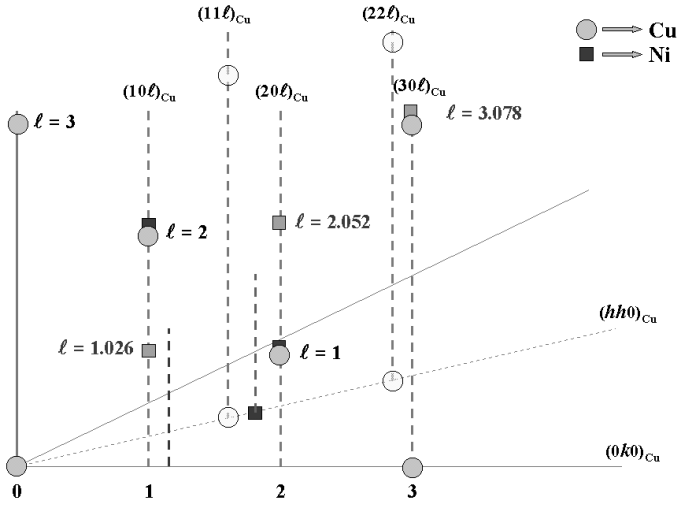

Figure 3.7: *Cu(111) - reciprocal space*:
The circles and the squares stand for Cu(111) and Ni(111) Bragg peaks, respectively; ℓ values shown in the diagram, characterize the bulk Ni(111) lattice parameter (the fully relaxed one); twinned fcc Ni is also displayed (i.e.: at ℓ = 1.026 on the (10ℓ) rod)

Out of the surface plane, with our orientation convention, the particular fcc stacking along the cubic [111] direction (ABCABCA…) leads to three types of CTRs in the reciprocal space:

a) [00ℓ] like, with Bragg peaks at $\ell = 3\times m$, m integer;

b) [10ℓ] like, with Bragg peaks at $\ell = 3\times m+1$, m integer;

c) [01ℓ] like, with Bragg peaks at $\ell = 3\times m+2$, m integer;

In figure 3.7 we show also Bragg peaks, along CTRs, corresponding to twinned-fcc Ni (Ni 60°) obtained through a 60° rotation of the lattice. A twin corresponds to the modification of the normal fcc substrate ABCABCA… stacking, into the ACBACBA… one. In this case, besides the bulk Cu Bragg peaks listed above, along the CTRs, we will find Bragg peaks corresponding to twinned Ni at:

a) $\ell = 3\times m+2$, m integer, on the $[10\ell]_{\text{Ni r.l.u.}}$ CTR;

b) $\ell = 3\times m+1$, m integer, on the $[01\ell]_{\text{Ni r.l.u.}}$ CTR;

The $[00\ell]$ CTR is not sensitive to a 60° rotation, since it reflects the perpendicular periodicity of the atomic planes. Therefore, a 60° in-plane rotation will bring the atom labeled X (figure 3.6) on the position of the atom Y, which also belongs to plane A.

Due to the small lattice parameter mismatch between Cu and Ni lattices, of 2.5%, we may expect a pseudomorphic growth. Previous studies of the Ni structure on Cu(111) [Grad64, Gidl89] show that Ni grows pseudomorphically up to film thicknesses of 7 ML and then relaxes *via* dislocations formation. No stacking faults at the interface were observed by means of X-ray photoelectron diffraction and LEED [Zhan93, Tear82]. In all cases, a strong roughening was observed increasing the thickness.

In figure 3.8 we show the evolution of the main reciprocal space in-plane directions and CTRs as a function of the Ni thickness. Up to 2.3 ML, the Ni film adopts the in-plane Cu(111) lattice parameter (2.556Å), showing thus pseudomorphic growth, in agreement with previous studies. However, relaxation can be observed for the 4.7 ML Ni film (figure 3.8-a), in contrast with the 7 ML value reported in the literature [Grad64, Gidl89]. The decrease of the $[10\ell]_{\text{Cu}}$ rod with increasing Ni thickness (figure 3.8-a), up to 4.7 ML, can be explained by the perfect epitaxy of the Ni film, leading to destructive interferences. The minimum in the $[10\ell]_{\text{Cu}}$ intensity coincides with the beginning of the in-plane lattice relaxation, at 2.3 ML. In fact, the $[10\ell]_{\text{Cu}}$ rod disappears and is progressively replaced by the $[10\ell]_{\text{Ni}} \equiv [1.026,0,\ell]_{\text{Cu}}$ one. Increasing the thickness, the in-plane lattice relaxation continues, following an asymptotic shape (figure 3.9). Even for high coverage (19 ML), the Ni layer is not completely relaxed, with a ~10% unrelaxed fraction.

The out-of-plane lattice parameter shows a different behavior. Firstly, it is important to note that due to the little misfit between Ni and Cu lattices, we cannot directly distinguish the unfaulted Ni fraction. However, a broadening of the Cu Bragg peaks can be observed (marked with a dashed arrow in figure 3.8-c). Thus, all the values given here were extracted from the twinned fraction, which can easily be observed along the CTRs. In figures 3.8-c and 3.8-d, it appears clearly that for the whole investigated thickness range (0.15 ML – 19 ML), the intensity of the twinned Ni Bragg peaks increases with the Ni thickness, but their position remains constant at a value corresponding to a Ni interlayer distance of 5.975Å. Thus, compared to the corresponding bulk value (6.104Å), the Ni is compressed in the direction perpendicular to the sample surface. The decrease of the surface signal along the CTRs,

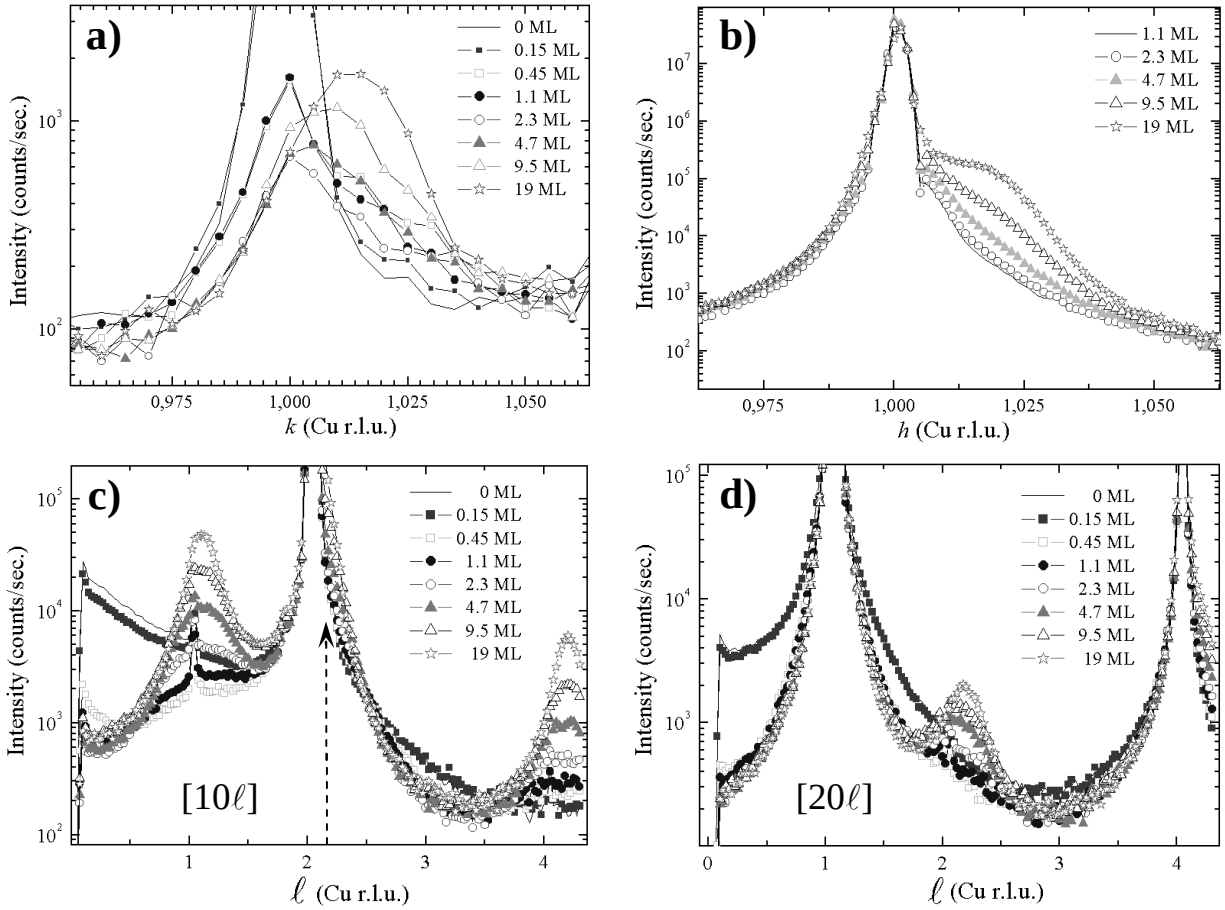

Figure 3.8: *Evolution of the reciprocal space as a function of the Ni thickness on Cu(111):*
a) [0*k*0] in-plane scan passing through the $(010)_{Cu}$ position;
b) [*hh*0] in-plane scan passing through the $(110)_{Cu}$ position;
c) the (10ℓ) rod: characteristic twinned Ni structure give rise to reflections at ℓ = 1.026 and ℓ = 4.104 Cu r.l.u. (the Cu(111) fcc stacking give Bragg peaks at ℓ = 2 and 5).
d) the (20ℓ) rod: the twinned Ni structure is characterized by a peak at ℓ = 2.052 Cu r.l.u. (Cu(111) Bragg peaks appear at ℓ = 1 and 4). Several selected thicknesses of Ni, until 19 ML, are shown.

indicates a strong roughening of the Ni film with the Ni thickness, as evidenced also by the STM measurements.

Summarizing, we evidenced an anisotropic evolution of the in-plane (a_S), respectively out-of-plane lattice parameters (c_S). In figure 3.9 we report the a_s and c_s values evolution as a function of the thickness. The corresponding bulk values are also presented. Up to ~2 ML, the Ni film exhibit a pseudomorphic growth, with a_s (Ni) ≡ a_s (Cu) = 2.556Å. The out-of-plane lattice parameter presents a lower value (5.975Å) compared to the bulk one (6.104Å). In this thickness domain, the resulting atomic volume is thus: $V_{Ni}(2ML) = \frac{a_s^2 \cdot c_s}{4} = 9.76\text{Å}^3$, higher than the one of bulk Ni ($V_{Ni\text{-}bulk}$ = 9.48Å^3). Above 2 ML Ni, while the out-of-plane parameter remains constant, the in-plane parameter decreases asymptotically toward the bulk value.

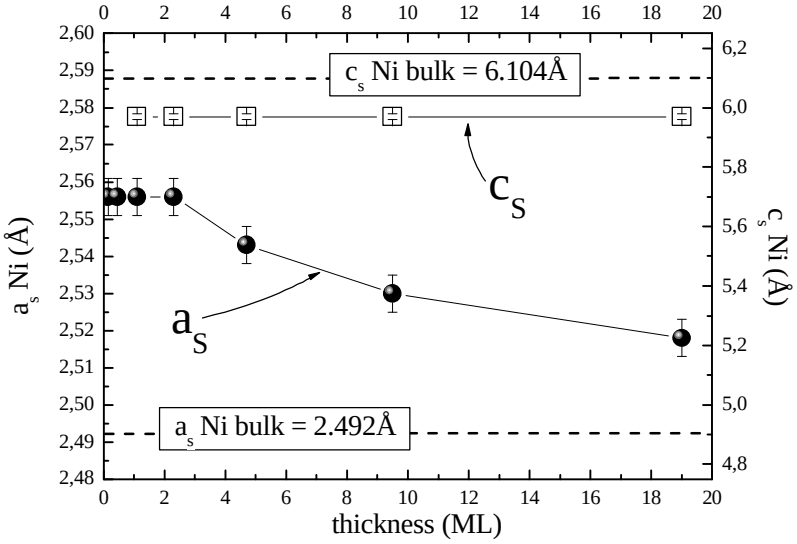

Figure 3.9: GIXD *tetragonalization*:
The relative evolution of the a_s and c_s parameters of Ni during the growth of Ni on Cu(111). The system relaxes in such a way that the atomic volume of Ni evolves towards the bulk Ni volume value = 9.48Å^3 (a_{Cu} = 2.56 Å and c_{Cu} = 6.26 Å).

Even for the thickest Ni film, 20 ML, the lattice parameter is not completely relaxed. However, at 20 ML, the atomic volume coincides with the bulk one.

☑ *Thus, we evidenced a tetragonalized (fct) structure for the whole thickness domain studied here (0.15 – 20 ML) where the in-plane Ni lattice parameter decreases asymptotically toward the bulk Ni value.*

3.5 MAGNETIC PROPERTIES: RESULTS AND DISCUSSION – HYBRIDIZATION AT THE INTERFACE

The magnetic properties (magnetic moments and anisotropies) were investigated using XMCD, on the ID08 beamline at ESRF. Figure 3.10 shows the XMCD geometry used to determine the magnetic data. After the preparation, the sample was transferred and mounted vertically into a superconductor coil system, with an available magnetic field of 9 T and a lower limit temperature of 4 K. As shown in figure 3.10, the incoming circular polarized X-ray beam describes an incidence angle *q*, with respect to the normal direction at the surface. Varying the incidence angle allows us to measure out-of-plane vs. in-plane magnetic moments components. A second freedom axis characterizes the angle between the incidence plane and the substrate steps direction, φ. A magnetic field is applied along the direction of the incoming light, assuring the full magnetic saturation of the sample along the measurement direction. Hysteresis loops were recorded at the Ni L_3 edge in order to verify the magnetic

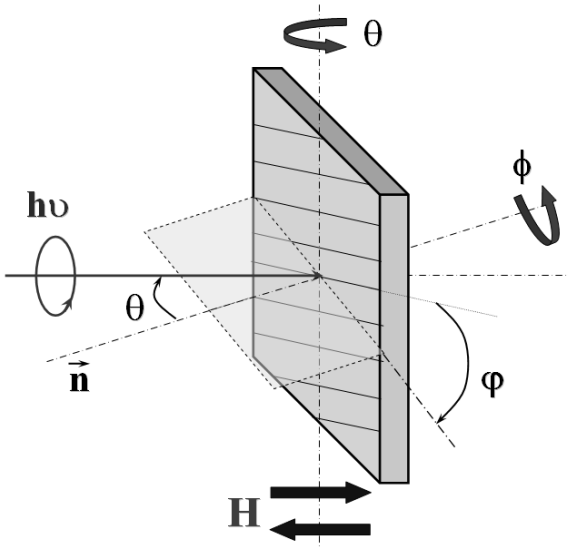

Figure 3.10: *XMCD geometry*:
θ stands for the incidence angle with respect to the direction of the normal at the surface, and φ for the azimuth angle relative to the in-plane step edges direction ([1$\bar{1}$0] crystallographic direction). The applied external field is collinear to the light incidence, assuring the complete alignment of the magnetic moments on the measurement direction.

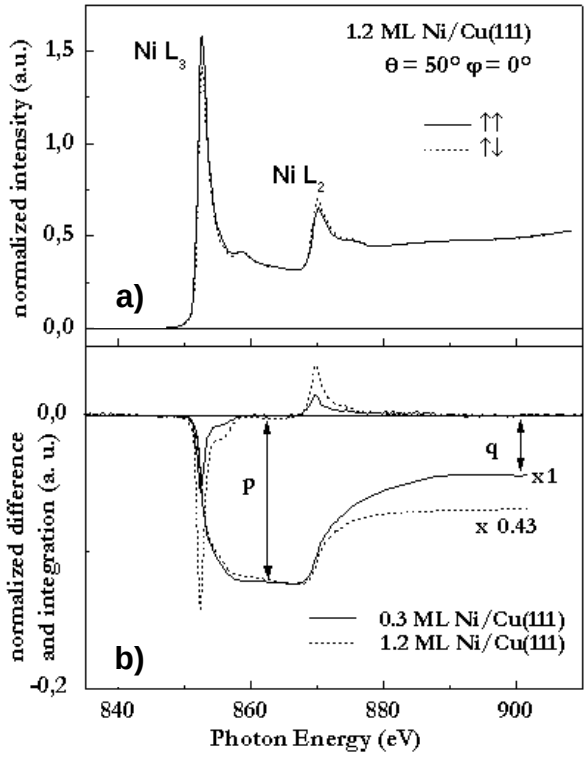

Figure 3.11: *absorption spectra at Ni $L_{2,3}$ edges*:
a) The normalized absorption spectrum at Ni $L_{2,3}$ for 1.2ML Ni/Cu(111). The applied external field is parallel (continuous line) or antiparallel (dashed line) to the spin momentum, oriented at θ = 50° and φ = 0°.
b) The dichroic spectrum and the integrated XMCD difference for 0.3ML and 1.2ML Ni, respectively. A scale factor was used for the 1.2ML spectrum, in order to compare the value of m_l ($\propto q$) with the film of 0.3ML.

saturation condition. In practice an applied magnetic field of 4 T and at a temperature of 10 K provides the magnetic saturation for the thickness range studied here.

A typical treatment of the Ni $L_{2,3}$ dichroic signal measured at θ = 50°, is shown in figure 3.11. Taking into account the possible relative orientation between the circular polarization of the incoming light and the applied magnetic field, each dichroic data point is obtained from two sets of two absorption spectra: $d_1 = (\varphi\uparrow, M\uparrow)-(\varphi\uparrow,M\downarrow)$ and $d_2 = (\varphi\downarrow,M\uparrow)-(\varphi\downarrow,M\downarrow)$. The final data point is obtained as the arithmetic average of d_1 and d_2. Several absorption spectra are recorded for each situation, assuring thus good statistics, within the

lowest error bars. The integrated XMCD difference clearly shows at θ = 50° a three times smaller magnetic moment for the 0.3ML Ni film than for the 1.2ML one. The total integrated intensity, directly proportional to the orbital moment M_L, is 3 times larger for the 1.2ML than for the thinnest Ni film. It appears thus clearly that in the ultra-thin thickness range M_L and M_S^{eff} are extremely sensitive to the structural and electronic characteristics.

thickness (ML)	$\mathbf{M_L^{(Z)}}$ μ_B/at ± 0.01 θ = 0°	$\mathbf{M_S^{eff\ (Z)}}$ μ_B/at ± 0.01 θ = 0°	$\mathbf{M_L^{(j=0°)}}$ μ_B/at ± 0.01 θ = 50°	$\mathbf{M_S^{eff\ (j=0°)}}$ μ_B/at ± 0.02 θ = 50°	$\mathbf{M_L^{(j=90°)}}$ μ_B/at ± 0.01 θ = 50°	$\mathbf{M_S^{eff\ (j=90°)}}$ μ_B/at ± 0.02 θ = 50°
0.3 ML (*locally 1ML*)	0.007	0.04	0.015	0.07	0.011	0.05
1.2 ML (*locally 3ML*)	0.020	0.13	0.037	0.20	0.041	0.23
1ML Ni/Cu(111)[1]	-	-	-	0.1	-	-
3ML Ni/Cu(111)[1]	-	-	-	0.55	-	-
1ML Ni/Cu(001)[2]	-	-	0.09	0.70	-	-
Bulk[3]	-	-	0.06	0.58	-	-

Table 3.1: XMCD results obtained for the 0.3 ML and 1.2 ML Ni/Cu(111). The experimental magnetic moments are compared with theoretical and experimental values.
[1] Calculated values for 1 ML and 3 ML Ni/Cu(111) [Ters82]
[2] Calculated values of Ni surface magnetic moments for the Ni/Cu(001) [Hjor96]
[3] Theoretical and experimental Ni bulk magnetic moments [Erik92, Voge94b]

Angle dependent (θ,φ) XMCD measurements allowed to extract the in-plane and out-of-plane components of the spin and orbital magnetic moments. The effective spin magnetic moment $M_S^{eff}(\theta,\varphi)$ and orbital magnetic moment $M_L(\theta,\varphi)$ measured at an incidence angle θ and azimuth angle φ, can be determined quantitatively from the XMCD integrated difference intensities at the L_3 and L_2 edge using the XMCD sum-rules (§2.3.1). These quantities are given in table 3.1 in Bohr magneton per atom. The 10% hole number variation in the ultra-thin film limit between 0.3 and 1.2 ML is not included. A constant d hole number of 1 ML Ni $n_h(Ni) = 1.20$ [Dhes99], was used to transform these values from Bohr magneton per hole, in

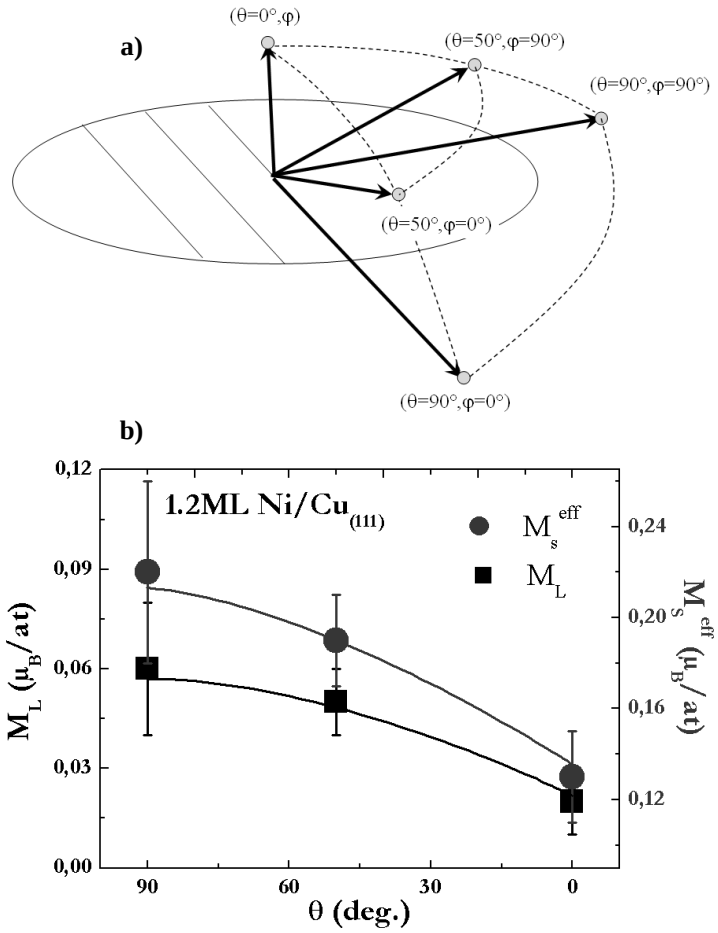

Figure 3.12:
a) Evolution of the non-isotropic magnetic moments between different possible orientations: out-of-plane vs. in-plane, and in-plane parallel, respectively perpendicular to the steps. The measured points at θ = 50° are also indicated.
b) Anisotropic evolution of the M_L and M_S^{eff} from the out-of-plane direction (θ = 0°) to the in-plane direction (θ = 90°). The points corresponding to θ = 0° and θ = 50° are directly measured, and the θ = 90° is calculated as described in text.

Bohr magneton per atom. The values at saturation given in table 3.1 measured at incidence angle θ = 50°, show for the 1.2 ML Ni film the in-plane isotropic orbital moment M_L = 0.037±0.01 μ_B/at, 3 times smaller than the calculated value (0.09 μ_B/at) for 1ML Ni/Cu(001) [Hjor96] and two times lower than for bulk fcc Ni (0.06 μ_B/at) [Erik92, Voge94b]. The 0.3 ML Ni film exhibits a strongly reduced orbital moment value, M_L = 0.015±0.01 μ_B/at. Considering the Ni morphologies observed by STM for 0.3 ML and 1.2 ML respectively (1 atomic layer and 3 atomic layers, respectively), the experimental XMCD orbital magnetic moment values show opposite variations to that expected for a 2D – 3D transition. The structural tetragonalization observed by GIXD (§3.4) and the specific chemical environment of Ni in these films must be considered in order to explain this behavior.

In a first approach, for the discussion of spin magnetic moment values, we neglect the 5% correction due to the dipolar moment M_T, and we compare the experimental spin magnetic moment M_S^{eff} with the theory. The observed M_S^{eff} evolution toward lower values when going from 3D-like islands to 2D-like ones, corresponds to the calculated evolution between 3 ML toward 1 ML Ni/Cu(111) [Ters82]. We notice that for the monolayer Ni islands (0.3 ML Ni film), we do not measure the calculated 0.70 μ_B/at found for surface Ni

atoms [Hjor96], in the case of Ni/Cu(001). For the 0.3 ML film, we can explain the small magnetic spin moment by the strong Ni-Cu 3d hybridization at the interface, as it was proposed by theoretical predictions in the case of Ni/Cu(111) [Ters82]. As described in §3.3, we notice that in fact, the 0.3 ML *equivalent thickness* Ni film is locally characterized by nanostructures of 1 atomic layer height, while the 1.2 ML *equivalent thickness* Ni film have locally 3 atomic layers height. In this way, we can compare our results to those calculated for 1 ML and 3 ML Ni/Cu(111), respectively. The M_S^{eff} = 0.07±0.02 μ_B/at value for the 0.3 ML Ni film fits very well with the calculated one, of 0.10 μ_B/at. This is not the case for the 1.2 ML Ni film, where the measured value M_S^{eff} = 0.20±0.02 μ_B/at is more than 2 times smaller than the calculated one, of 0.55 μ_B/at [Ters82]. Taking into account the copper capping of the Ni islands observed by STM in this thickness range, we explain the reduced M_S^{eff} value by the formation of the second Ni-Cu interface, thus increasing the electron hybridization effects.

Figure 3.12 shows the measured and calculated magnetic moments components (a), and the evolution of the orbital and effective spin moment, respectively, for the 1.2 ML Ni film (b). Due to the geometric condition of the colinearity between the applied magnetic field and the direction of the X-ray beam, we cannot directly perform in-plane measurements, at $\theta = 90°$. Therefore, a supplementary measurement point is necessary (i.e., $\theta = 50°$) in order to extract the in-plane value, using the angular dependence determined by Bruno [Brun89] (equation 3.5). The angular evolution of $M_S^{eff}(\theta)$ shows that large in-plane anisotropy, dipolar in origin, is present in the 1.2 ML Ni film. In order to determine the spin magnetic moment, M_S, and the magnetic dipole contribution M_T to the effective spin moment, we can follow the description given by Stöhr et al. [Stöh95, Well95]. In the absence of in-plane anisotropy, as will be shown later for 0.3 ML and 1.2 ML respectively, the magnetic dipole term $M_T(\theta)$ is expected to vary as:

$$M_T(q) = M_T(0°) + \left[M_T(90°) - M_T(0°)\right] \cdot \sin^2 q \tag{3.5}$$

and since:

$$\begin{cases} M_S^{eff}(q) = M_S - 7 \cdot M_T(q) \\ M_T(0°) + 2 \cdot M_T(90°) = 0 \end{cases} \tag{3.6}$$

we can write:

$$M_S^{eff}(q) = \left[M_S - 7 \cdot M_T(0°)\right] + \frac{21}{2} \cdot M_T(0°) \cdot \sin^2 q \tag{3.7}$$

In this way, we obtain an expression depending only on the out-of-plane component that can be directly measured *via* the effective spin moment. The derived dipole magnetic moment for

the 1.2 ML Ni film is $M_T(0°) = 0.012\pm0.01\ \mu_B$/at, and the dipolar moment anisotropy: $\Delta(7M_T) = 0.04\pm0.02\ \mu_B$/at. We can now extract the spin magnetic moment, obtaining thus a value $M_S = 0.21\pm0.02\ \mu_B$/at. This shows that for the 1.2 ML Ni film an unusual[♣] high dipolar moment (of ~5%), is present. It is not the case for the 0.3 ML Ni film, where the extracted dipolar moment is $M_T(0°) = 0.003\pm0.01\mu_B$/at, and the resulting spin magnetic moment $M_S = 0.07\pm0.05\ \mu_B$/at. These data could be explained by the formation of the second Ni-Cu interface, favoring stronger dipolar moments. However, the presence of such a high dipolar moment is moreover a signature of the structural changes observed by diffraction experiments, namely the structure tetragonalization.

Assuming that the largest component of the orbital moment defines the easy magnetization axis [Brun89, Laan98], it is clear from the table 3.1 that for both presented Ni films the out-of-plane direction is the hard axis and the easy axis is in the plane. Considering the error bars for M_L, the in-plane easy axis could be either along the steps direction ($[1\bar{1}0]$ crystallographic direction), or perpendicular ($[11\bar{2}]$ direction) to the steps. Thus, no in-plane orbital anisotropy could be evidenced, contrary to the FeNi nanostructures deposited on the same 1.2° vicinal substrate [Cher01a].

Bruno [Brun89] has calculated the angular dependence of M_L taking into account the variation with the polar angle, q. For a given orientation in the surface plane, we can write the following dependence:

$$M_L(q) = M_L(0°) + \left[M_L(90°) - M_L(0°)\right]\cdot \sin^2 q \qquad (3.8)$$

where the $M_L(0°)$ is directly measured as the out-of-plane component, the $M_L(\theta)$ is the measured component at an angle θ (i.e. 50°), and the $M_L(90°)$ is the extracted in-plane component. We obtain thus an $M_L(90°) = 0.05\pm0.01\ \mu_B$/at value for the 1.2 ML film, while for the 0.3 ML one a strongly reduced value $M_L(90°) = 0.02\pm0.01\ \mu_B$/at is found. This demonstrates a strong in-plane orbital moment anisotropy for the 1.2 ML film, which is unexpected for ultra-thin films, but is similar to the Ni/Cu(001) system [Lee97, Plat99]. Structural tetragonalization and magnetocrystalline effects are probably at the origin of the in-plane strong orbital anisotropy, as shown also in the case of Ni/Cu(001) [Lee97, Plat99].

One can now turn to the calculation of the *magnetocrystalline anisotropy energy* (MAE) for the 1.2 ML Ni film. The angular dependence of the orbital and effective spin

[♣] In conformity with [Carr93], in the case of transition metals (Fe, Ni, Co) the dipolar contribution should be neglected, due to symmetry considerations.

magnetic moments extracted from the XMCD data, leads to orbital and spin moment anisotropies, which can be linked to the MAE [Stöh95]. This energy is due to the direct influence of the crystal field on the orbital magnetic moment and to the spin magnetic dipolar moment (M_T), originating from the indirect interaction through the spin-orbit coupling ($x \cdot L \cdot S$), as described by Bruno [Brun89] and by van der Laan [Laan98]. The MAE can be written as:

$$MAE = \frac{x}{4\mu_B} \cdot \left(M_L^{q=90°} - M_L^{q=0°}\right) - \frac{3x^2}{2\mu_B \cdot E_{ex}} \cdot \left(7M_T^{q=90°} - 7M_T^{q=0°}\right) \qquad (3.9)$$

For the 3d transition metals, the quadratic term $\frac{3x^2}{2\mu_B \cdot E_{ex}}$ related to the spin moment anisotropic part (M_T) can be neglected. As a matter of fact, the exchange splitting E_{ex} (~1eV) is much larger than ξ, which is equal to 100meV for nickel [Brun89]. Moreover, the difference related with the dipolar moment anisotropy, $\Delta(7M_T)$ = 0.04±0.02 μ_B/at, is of the same order of magnitude as the orbital anisotropy ΔM_L. In this case, the MAE is directly linked to the anisotropy of the orbital moment and proportional to ΔM_L. Thus, for the 1.2 ML film, which presents an orbital anisotropy $\Delta M_L = M_L(90°) - M_L(0°)$ = 0.03±0.015 μ_B/at, we obtain a large MAE of 750±200 μeV/at. If one introduces the correction factor α which depends on the structure of the Ni and can vary from 0.05 to 1 (we will consider α = 0.1), the orbital moment anisotropy provides a MAE of 75 μeV/at very close to 60 μeV/at found for 12 ML Ni film by Kuch et al. [Kuch00], or for homogenously strained 30 ML Ni films, where the authors report an overall orbital anisotropy of ΔM_L = 0.028±0.014 μ_B/at. [Dürr96]. We can explain the in-plane anisotropy and the large value of the MAE for 1.2 ML Ni film by the formation of the second Ni-Cu interface and by the tetragonalized fct Ni structure observed in this thickness domain. The lower MAE value of 350 μeV/at obtained for the 0.3 ML Ni film (1 atomic layer high nanostructures) is proportional to the lower total magnetic moment. By a simple mathematical approach, it can be observed that the ratio between the total magnetic moment and the MAE for the 0.3 ML and 1.2 ML, respectively, is 2 and corresponds well to the ratio between the number of interfaces in both cases.

3.6 CONCLUSIONS

STM experiments shows that the Ni ultra-thin films are characterized by islands growth, partially capped by one atomic Cu layer, after the first Ni monolayer. Structural

analysis performed by GIXD describes the ultra-thin Ni films as tetragonalized in the 0-20 ML thickness range. Angle dependent XMCD measurements were performed at the Ni $L_{2,3}$ edges of fct Ni ultra-thin films grown on a stepped Cu(111) substrate. The orbital moment for 1.2 ML coverage induces a strong MAE, favoring an in-plane magnetization easy axis. No in-plane anisotropy with respect to the steps directions could be determined within the error bars. In fact, taking into account the specific growth and the 3-fold twinned symmetry (global 6-fold symmetry) of the Ni films, there is no privileged crystallographic direction and therefore, no in-plane structural anisotropy. The 0.3 ML Ni film, which presents locally nanostructures of 1 atomic layer height, shows strongly reduced magnetic moments. In agreement with theory, this reduction is based on the hybridization effect at the Ni-Cu interface. Contrary to theoretical calculations, the 1.2 ML Ni film shows reduced magnetic moments. This behavior is related with the copper capping of the Ni film in this coverage range, originating thus a second Ni-Cu interface, enhancing the hybridization effect. The unusual in-plane anisotropy can be explained by the Ni fct tetragonalized structure, compressed along the out-of-plane [111] direction, and expanded along the in-plane directions, for the whole investigated thickness range.

Chapter 4:

ROOM TEMPERATURE GROWTH OF NiO / Cu(111)

4.1 INTRODUCTION

In the last decade, an enormous work has been dedicated to the study of the NiO, due to his implementation in diverse application domains: electronics (e.g. sensors, microchips), high-density data storage technologies (GMR – "*Giant Magnetoresistance*"), catalysis. Directly used in complex structures, the NiO thin films properties are still not well understood and the NiO/metal interface remain poorly understood. As a matter of fact, the electrical, mechanical, chemical or thermal properties of many technologically important devices are intimately related to the atomic structure and changes in the chemical environment of the interface.

As a matter of fact, in multilayered complex systems (e.g. spin-valves), the interfaces are rarely formed by NiO with other oxides or noble metals. In order to better describe and control effects as, for example, the "orange-peel" or the oscillatory exchange coupling [Chop97, Chop00] present at the NiO/metal interfaces, it is mandatory to study in detail the NiO growth on metals like Cu (intensively used in GMR-like systems) and the evolution (as a function of the thickness, temperature, etc.) of the NiO/metal interface. Furthermore, as a first step, we chose the deposition at room temperature in order to avoid the thermally activated diffusion, which is demonstrated to be one of the most undesired effects at these interfaces, leading to the formation of compounds which can modify the expected magnetic behavior [Mocu00b].

We observe experimentally that during NiO growth at room temperature on a Cu(111) substrate, in the first growth stages, NiO has a metallic character, the electronic structure following an evolution from metallic toward oxide's specific electronic structure. Photoemission and absorption studies [Sanc00] have already shown that ultra-thin nickel oxide film can not be obtained below a critical thickness of a few monolayers, the authors speculating on the formation of a pure Ni film at the interface. However, they do not take into account the possibility of interfacial intermixing, which could also explain the metallic character observed in the very low thickness range.

The aim of the two following chapters is to present a detailed study of the NiO growth in the ultra-thin film range (0.1 – 10Å), on a Cu(111) single crystal substrate. In chapter 4, I will present the elaboration of oxide films at room temperature including growth, morphology, electronic and crystallographic structure. In chapter 5, I will present the temperature effects on the crystalline quality of NiO films.

4.2 EXPERIMENTAL SETUP

Since in the exchange coupled layers (spin-valves) the NiO layer is deposited onto an easily oxidizable ferromagnetic metallic layer, it is important to take into account the possibility of the metallic layer oxidation. Thus, a direct MBE deposition method was set-up to elaborate the NiO ultra-thin films (0 – 10 Å), by electron bombardment from a NiO source (figure 4.1), in UHV (ultra-high vacuum - 10^{-10} mbar) environment. The molybdenum crucible adapted into an EFM3 – Omicron evaporator, is filled-up with NiO f = 3-5 mm nuggets of 99.995 % purity. Due to the indirect NiO heating, the resulting evaporation rate is very low, of about 0.03 Å/min. (~2Å/h), as determined by AES calibration and verified with a quartz microbalance. During the evaporation the substrate was held at room temperature (R.T.). It is important to note here that a Cu(111) substrate with no miscut (Cu(111) – miscut 0°) was used (different from the substrate used for Ni/Cu(111) – chapter 3). In order to

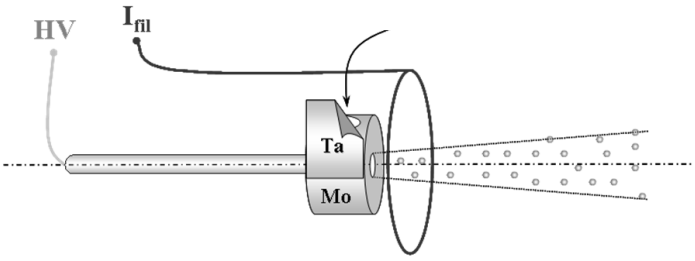

Figure 4.1: *NiO evaporation cell:*
The Mo crucible is filled up with 3-5 mm NiO nuggets and then closed with a Ta foil. A high voltage (HV) is applied to the crucible, while the filament is kept at the ground, resulting thus in an electron bombardment heating indirectly the NiO nuggets.

improve the crystalline quality, we also performed NiO growth at elevated temperatures and annealed the NiO films after the R.T. growth. The preparation chamber is equipped with AES and LEED and is connected to a second one, with a STM facility. A second UHV chamber is equipped with a XPS (X-ray Photoemission Spectroscopy) hemispherical analyzer. Core level 2p XPS spectra were obtained using the monochromatized Al K_a radiation, with a primary energy of 1486.6 eV and a resolution of 0.7 eV.

Quantitative structural investigations were realized by GIXD on the BM32 (SUV) beam-line at the ESRF, Grenoble. We used the same setup as described in §3.2, with the only difference that the energy of the X-ray beam was fixed at 13 keV (instead of 18 keV), in order to allow the simultaneous GIXD and GISAXS acquisition. At 13 keV, we avoid on one hand the fluorescence background in the diffracted intensity and satisfy on the other hand the GISAXS geometric conditions: the sample – CCD camera distance of 670 mm and the 16 bits 2D CCD screen size (f = 93 mm). The small angle scattering measurements (GISAXS) are used in order to investigate in real time, during growth, the evolution of the morphology, and

more precisely the spatial correlations between the deposited nano-objects on the surface. Since with STM we established a mean value of ~4 nm for these objects (as will be shown latter in §4.4), and taking into account the geometrical values given previously, the best choice for the X-ray beam energy was 13 keV. It is important to note that the CCD camera resolution is given by the size (56 μm) of one pixel. In order to extract a reliable GISAXS signal, a typical exposure time of 100 sec was necessary. Several images were recorded for each situation, and the treated image is the sum over all images for a given situation (thickness), after subtraction of the clean copper image taken as reference. A lead beam-stop is mounted in front of the transmitted beam in order to avoid the CCD camera saturation and to make visible the diffused beams. All diffraction measurements were realized at an incidence angle equal to the total external reflection angle for Cu at 13 keV, $a_c = 0.257°$, while the scattering ones were performed at $a = 0.15°$. A triangular unit mesh was used to describe the 3-fold (111) surface symmetry, as shown in §3.4.

4.3 STOICHIOMETRY AND ELECTRONIC STRUCTURE

Auger electron spectroscopy (AES) was used in order to calibrate the NiO deposition rate and to study the evolution of the stoichiometry. The AES spectra were recorded for the Ni LMM, O KLL and Cu LMM transitions at 848 eV, 505 eV and 920 eV respectively (figure 4.2-b). Figure 4.2-b shows a typical AES spectrum obtained for a 5 Å NiO film thickness. To better visualize the O KLL transition (505 eV) in this figure its intensity is not corrected for the chemical sensitivity (a factor ~2 compared with Ni and Cu), neither for the lock-in sensitivity (two "windows" were defined to record separately Ni and Cu – 3 mV, and O – 1 mV AES signal respectively). The extraction of the Ni LMM intensities is detailed in §3.3.

In figure 4.2-a we present the As-t representation, as a function of the NiO equivalent thickness. The transformation from the temporal (in minutes) into the thickness axis was made using an evaporation rate of 0.03 Å/min, taking into account an ideal exponential decay for the copper substrate AES signal, with an IMFP of $\lambda = 10$Å. All intensities were determined in the peak-to-peak manner and were corrected with the relative sensitivities for Ni, Cu and O. The error lies within 10% in the very low coverage regime (0-2Å), where the overlap between the Cu LMM (849eV) and the extracted Ni LMM (848eV) transitions is important.

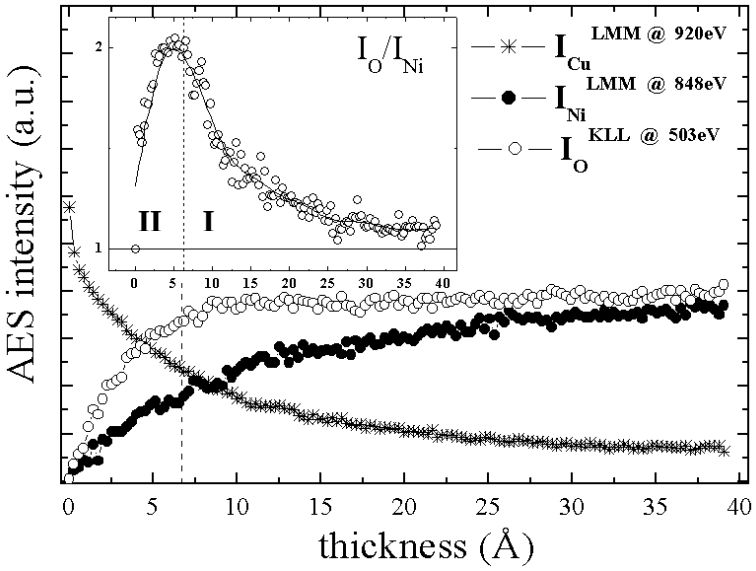

Figure 4.2 a): *As-t representation of the Ni(848eV), O(505eV) and Cu(920eV) transitions:*
The nickel and oxygen AES evolution presents different features: the oxygen signal reach his saturation at ~10Å, while the nickel increase continuously up to ~40Å. Both Ni and O intensities were corrected with their AES sensitivities (Ni:O sensitivities ≅ 1:2). The axis transformation from minutes to thickness was made taking into account an IMFP λ = 10Å, for a deposition rate of ~0.03Å/min. The inset presents the evolution of the Ni and O ratio as a function of thickness.

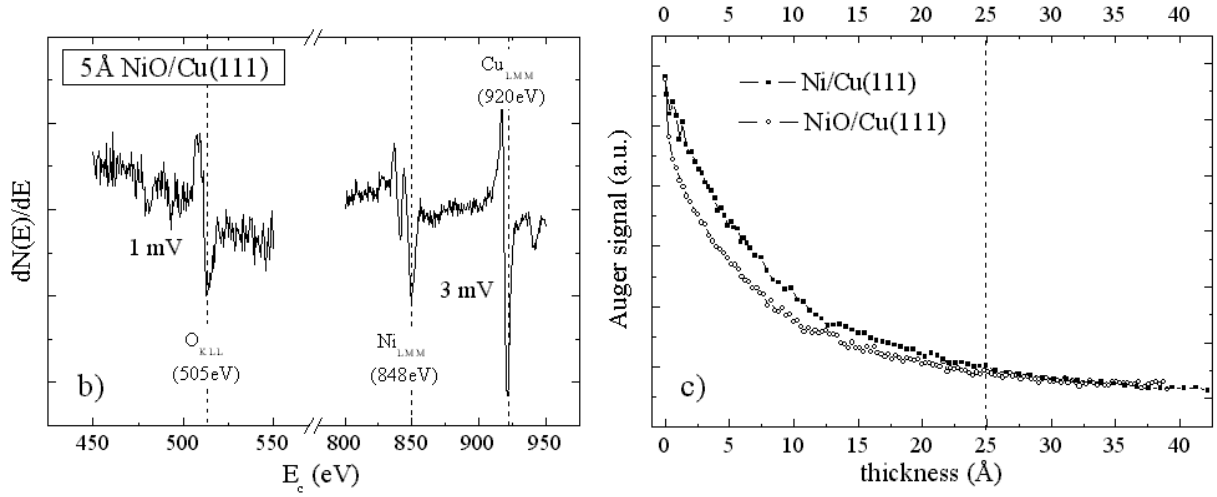

Figure 4.2 b) and c):
b) Typical AES spectrum obtained for 5 Å thickness showing the O (505eV), Ni (848 eV) and Cu (920 eV) electronic transitions. The O KLL was recorded with a higher sensitivity (1 mV) which is not corrected in this figure.
c) Comparison between the evolution of the Cu substrate AES signal for Ni/Cu(111) and NiO/Cu(111), respectively.

As it can be observed in figure 4.2-a, the Ni and O Auger intensities present disparate features: the O intensity increases rapidly and reaches its saturation regime at 10 Å, while the Ni intensity increases slowly with the NiO thickness, reaching the O value only above 25 Å.

The rapid increase of the O KLL intensity follows a typical layer-by-layer growth, characterized by an exponential increase with the NiO thickness. Its saturation at 10 Å thickness for a mean free path of ~5 Å describes an evolution very close to a perfect layer-by-layer growth. Contrary to the O KLL evolution, the Ni LMM Auger intensity evolution is typical for a 3D growth and/or diffusion. Two regimes can be extracted, as specified in the figure 4.2-a inset, where we present the ratio between the O and Ni Auger lines as a function of the NiO thickness: the regime II, for thickness < 7Å is characterized by a strong divergence

between the two of the Auger intensities, and the regime I describes the convergence toward the 1:1 NiO stoichiometry. The maximum in the I_O / I_{Ni} ratio is obtained for a thickness of ~7Å NiO, and corresponds to the maximum divergence of the Ni:O stoichiometry and with the beginning of the convergence regime. Thus, we conclude that stoichiometric NiO is obtained only for thicknesses larger than ~30Å. Similar behaviors of oxide layer growth was already reported [Sanc00, Kita98b, Jesu96, Galt99b, Öfne97]. The authors assume that the non-stoichiometry for the very low coverage regime is related to the formation of a metallic Ni layer [Sanc00] and a substrate oxidation (CuO), or with the formation of defective NiO aggregates [Kita98b, Jesu96, Galt99b, Öfne97].

At this stage it is difficult to conclude whether the observed non-stoichiometry is or not based on the formation of defective NiO and/or presence of adsorbed hydroxyls. Since for relatively thick films we obtain the stoichiometric oxide, we can assume that the evaporated Ni:O is in a 1:1 proportion. Thus, the difference between the Ni and O relative AES intensities could be explained by a *differential diffusion* in the copper substrate. In this way, from the first growth stages, the Ni atoms would diffuse into the Cu substrate, while the O atoms remain on top of the surface. This is indeed what we observe with STM and GIXD, as it will be shown later in this chapter. The difference between the Ni and O Auger intensities could be related with the AES sensitivity for the topmost layers in the presence of diffusion. In fact, compared to an ideal layer-by-layer growth, the Ni As-t evolution (figure 4.2-a) clearly shows a very slow signal increase with the NiO thickness which, in agreement with our STM topographic images, can not be attributed to a 3D growth. Furthermore, compared with the case of Ni/Cu(111) (chapter 3), the copper substrate AES intensity decreases more rapidly with the NiO thickness for the NiO/Cu(111) (figure 4.2-c). Taking into account the typical 3D growth of the Ni/Cu(111) interface, it is obvious that the NiO/Cu(111) is closer to a layer-by-layer growth. In addition, considering both the evolution of the O and Ni intensities, the most attractive hypothesis is the *differential diffusion* of the Ni atoms in the copper substrate: it can explain the slow evolution of the Ni intensity and the layer-by-layer feature of the O Auger intensity. Within this assumption, it is interesting to remark that in figure 4.2-c, both curves cross each other at ~25 Å, evolving thereafter in the same manner. The 25 Å could thus stand for the upper limit thickness for the proposed diffusion process. This shows also that we deposit effectively Ni and O in equal proportions with our evaporation cell.

Figure 4.3 shows several Ni 2p XPS spectra for different NiO thicknesses. Globally, the XPS spectra show a transition from a metallic Ni electronic structure, toward the specific oxide electronic structure (obtained for thicknesses above 30Å).

The thickest recorded NiO film, 30Å, present a six-peak XPS Ni 2p spectrum, characterizing a mixture of metallic and oxidized Ni, as it was observed also in the case of the Ni foil oxidation [Jesu96]. In agreement with the literature [xps_nist], we find the characteristic Ni metallic XPS lines at 852.16 eV and 869.65 eV. Besides metallic Ni transitions, we can identify the oxide XPS lines at 855.26 eV and 873.04 eV, and their shake-up satellites at 861.65 eV and 880.69 eV, respectively. These XPS transitions values are in good agreement with those reported for bulk NiO [Geun91, Veen93, Laan86, and Hüfn94]. Furthermore, the O 1s line position at 529 eV corresponds very well to the O^{2-} state in NiO [Hüfn94, Alde96]. However, the splitting Δ_{NiO} = 17.8 eV between the $2p_{3/2}$ and $2p_{1/2}$ NiO

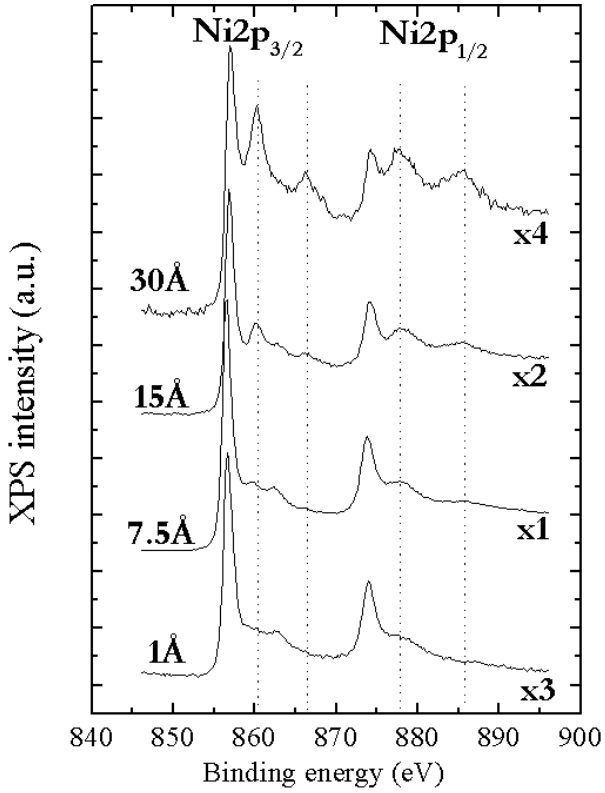

Figure 4.3: *XPS evolution as a function of the thickness:*
Four thicknesses are presented, from 1Å to 30Å. For comparison, a scale factor is used as specified in the figure. With vertical lines we show the characteristic nickel oxide electronic transitions (their spectral position is detailed in the text)

transitions is not in agreement with the bulk characteristic value of 18.4 eV [xps_nist]. Accordingly to the literature [Galt99a], this Δ_{NiO} value could be a signature of a Ni_2O_3 stoichiometry. This is not the case since the Ni_2O_3 stoichiometry should be characterized also by a splitting of the O 1s XPS line. The apparent contradiction can be explained if we take into account the Ni diffusion into the Cu substrate. This will lead to a mixed Ni chemical

environment. Since the spectroscopic measurements integrate over several layers, the result is an average over all different possible Ni-O bonds, leading to an intermediate splitting Δ_{NiO}.

Following the NiO thickness (figure 4.3), we observe that at very low coverage (1-7 Å), the XPS spectra show only metallic features. However, we record also the O 1s transition, which confirms that we deposit Ni and O. The binding energy of 529 eV, which should characterize the O^{2-} state in NiO, was measured for the whole thickness range presented here (0-30 Å). Since there is a strong Ni metallic signal, and since we depose NiO in the correct proportion, we can deduce that there is an oxygen fraction which is adsorbed or diffused. Moreover, as it was shown by XPS and XAS ("X-ray Absorption Spectroscopy") measurements by Sanchez et al. [Sanc00], there could be an oxygen fraction which oxidizes the Cu substrate. However, the Cu 2p XPS transitions do not show any sign of oxidation. Therefore, at this time, we can only conclude that a fraction of oxygen is not bonded with nickel. It is important to note that there are 2 options for the adsorbed O: a) adsorbed on a clean copper surface, and b) adsorbed on regions with diffused nickel. The distinction between the two cases is impossible by XPS spectroscopy, since the O adsorbed on Cu is almost at the same binding energy as the one adsorbed on Ni [xps_nist].

At 7.5 Å, the Ni 2p XPS intensities exhibit a maximum intensity observed in the XPS spectra (all other spectra presented in figure 4.3 are multiplied with a scale factor) and correspond in thickness with the critical point observed in AES. Moreover, for this thickness oxide features start to form. Above 7.5Å, increasing the thickness, the XPS signal decreases due to the formation of stoichiometric but disordered NiO, as it will be discussed in §4.5. At 15 Å, we remark already the presence of NiO characteristic transitions, however in small quantity (~30%) compared with the metallic ones.

For a given thickness, the XPS line shape can be described as a linear combination of metallic Ni and NiO. In figure 4.4-a we show the fitted XPS curve obtained for the 30Å NiO thick film. The non-linear background was subtracted according to the iterative Shirley method [Shir72] and the peaks were obtained as Gaussian-Lorentzian curves with asymmetrical corrections, following the deconvolution method proposed by Doniach and Sunjic [Doni70]. The used fitting parameters are: gaussian width of 0.68 eV, lorentzian width for Ni lines of 0.30 eV and lorentzian width for NiO lines of 1.60 eV.

From left to the right, in figure 4.4-a, the peaks are indexed as following: **peak1** – Ni $2p_{3/2}$ (852.16 eV), **peak2** – NiO $2p_{3/2}$ (855.26 eV), **peak3** – NiO $2p_{3/2}$ shake-up satellite (861.65 eV), **peak4** – Ni $2p_{1/2}$ (869.65 eV), **peak5** – NiO $2p_{1/2}$ (873.04 eV), and **peak6** – NiO

$2p_{1/2}$ shake-up satellite (880.69 eV). The oxidized fraction can be calculated from the NiO/(NiO+Ni) intensity ratio:

$$\begin{cases} \dfrac{NiO}{NiO+Ni} = \dfrac{S^{corr}_{peak2} + S^{corr}_{peak3} + S^{corr}_{peak5} + S^{corr}_{peak6}}{S^{corr}_{peak1} + S^{corr}_{peak2} + S^{corr}_{peak3} + S^{corr}_{peak4} + S^{corr}_{peak5} + S^{corr}_{peak6}} \\ S^{corr}_{peak_i} = \dfrac{S_{peak_i}}{s_i \cdot l_i} \end{cases} \quad (4.1)$$

where: s_i – XPS cross section at the i spectral line, and l_i – photoelectron IMFP at the kinetic energy of line i (all σ and λ values are extracted from [xps_nist]).

Figure 4.4-b shows the evolution of the metallic and oxidized Ni proportion as a function of the thickness. Three regimes describe the evolution of the NiO proportion: II-A, from 0 to 2 Å, the NiO quantity increases rapidly with the thickness reaching about 20% for the 2 Å; II-B, from 2 to 7.5 Å, the NiO proportion follows a saturation regime. Since the

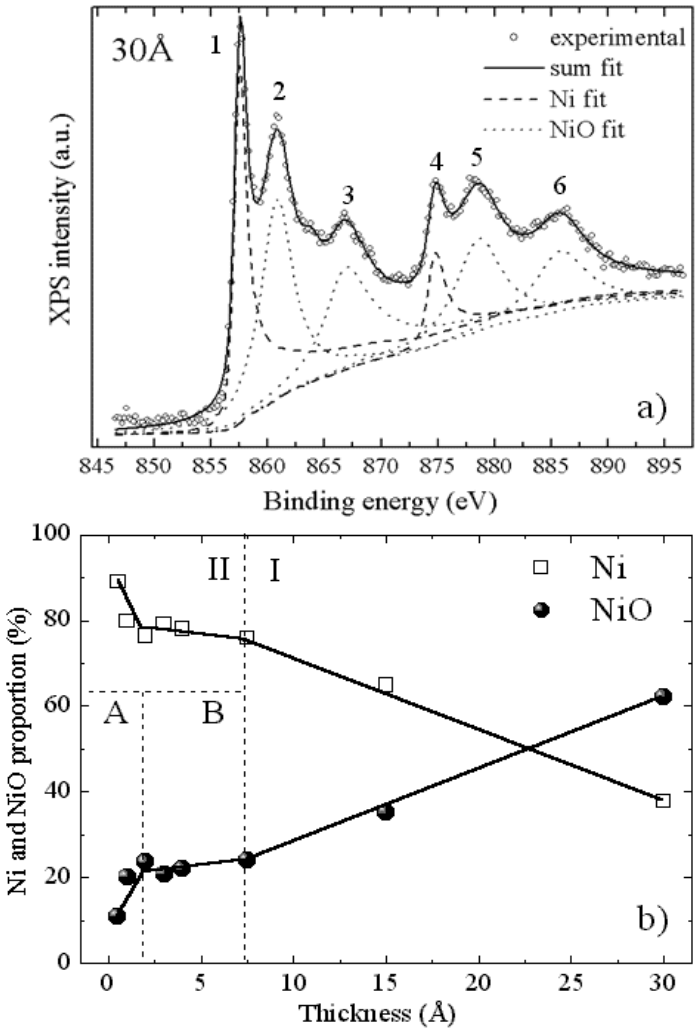

Figure 4.4: *typical XPS fitting treatment (a) and evolution of the NiO composition as a function of the thickness (b):*
a) The six-peak spectra correspond to a linear combination of Ni and NiO XPS characteristic transitions. The dashed lines represent the Ni peaks, while the dotted ones represent the four NiO transitions, as described in the text.
b) The regions I and II correspond to the on-top and diffused interface regions, respectively. The first region (0-7.5Å) is characterized by a linear growth (0-2Å), followed by a saturation plateau (2-7.5Å). Then a linear evolution with the deposited quantity is observed (7.5-30Å). Even for the thickest NiO film, there are still ~40% metallic Ni.

deposited NiO quantity increases linearly, this saturation regime could characterize the equilibrium in the differential diffusion process proposed previously and represented in figure 4.5. The Ni and O atoms arriving on the Cu surface will give rise to equal proportions of Ni-Ni bonds and Ni-O bonds, respectively. Thus, the apparent NiO proportion will remain constant.

Above 7.5 Å, increasing the deposited thickness leads to an increase of the NiO proportion, marked in figure 4.4-b as region I. The linear NiO proportion increases with a small slope, leading even for a 30 Å thick NiO film at ~40% metallic Ni. This high concentration of metallic Ni suggests that metallic Ni is formed in the top layer also (as confirmed by quantitative diffraction measurements). Assuming that above 7.5 Å the deposited quantity leads only to the formation of NiO, we should obtain an exponential increase of the NiO quantity. This is not the case and therefore we can conclude that even for thicknesses larger than 7.5 Å, the formation of metallic Ni continues. The measured metallic Ni quantities are reported in the figure 4.4-b and vary from ~100 % down to ~40% for the thickest film.

Compared with AES, XPS presents an opposite behavior: while in AES we obtain an oxygen over-stoichiometry, the XPS measurements show a nickel over-stoichiometry. In order to understand the origin of this difference between the two of the spectroscopic techniques, we have to consider on one hand the Ni atoms diffusion and, on the other hand,

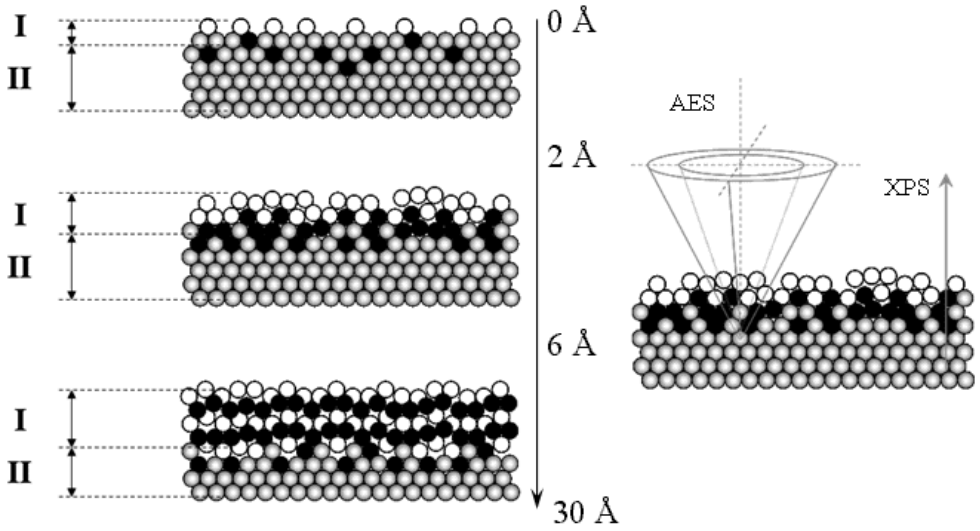

Figure 4.5: *interface evolution during the NiO growth:*
The regions I and II correspond to the on-top and diffused interface regions, respectively. The arrow at right indicates the thickness increase. The gray circles stand for Cu atoms, the black ones for the Ni, and the white ones for O. At the right, the geometric acquisition difference between AES and XPS is shown.

the difference between the acquisition geometry in AES and XPS. In figure 4.5 we show the schematic representation of the interface evolution function of thickness, evidencing two zones – I and II – corresponding to the "on-top" and "diffused" regions, respectively. Since the AES and XPS electronic transitions are nearly at the same energy values (800-900 eV), characterized by an IMFP l = 10-12 Å [xps-nist], we can consider that both, the AES and the XPS, probe the same depth (= zone I + zone II). Thus, even in the presence of the diffusion the composition evolution should be similar in both cases. Nevertheless, the Auger cylindrical mirror analyzer (CMA) integrates over a cone angle of ~35°, while in our experiments the hemispherical XPS analyzer is set along the direction normal to the sample surface (figure 4.5).

Assuming that the diffused Ni atoms occupy the Cu sites into the Cu lattice (zone II) – as it will be shown later by GIXD -, their XPS peak intensity could be enhanced on the direction normal to the surface, which corresponds to the [111] crystallographic direction. In fact, photoelectron diffraction (XPD) experiments performed on NiO(111) [Saik89, Scha93b] have shown that the photoemission signal can vary up to 65% as a function of the emission angle. Therefore, the photoemission signal could be influenced by a factor 1.65, if the measurements are performed along a preferential direction. Due to its sensitivity to the crystallographic order, the XPS signal will be affected whether the deposited NiO is ordered or not. Indeed, following the evolution of the overall XPS signal (figure 4.3), we can notice the decrease of the intensity which can be thus related to a disordered NiO film. Moreover, the structural disorder leads to deviance from the expected 1:1 nickel oxide stoichiometry, as was observed both by AES and XPS. Since the XPS signal is affected by the crystalline quality of the NiO films, the AES results are more appropriate when investigating the NiO stoichiometry.

☑ *Summarizing, the spectroscopic investigations have shown that no stoichiometric NiO can be obtained in the ultra-thin films domain (0-10 Å). The origin of this behavior is related with the differential diffusion of Ni atoms into the Cu substrate, leading to non-stoichiometric NiO films. For large thicknesses (> 25 Å), both AES and XPS measurements show stoichiometric NiO. However, even for the thickest film studied in the present work, there is still ~40% metallic Ni fraction in the film, probably buried near the NiO / Cu interface.*

The XPS measurements reveal the presence of molybdenum contamination, from the evaporation cell. In figure 4.6 we show a wide scan performed on the 7.5 Å NiO film, the different XPS lines for the major electronic transitions of the concerned species are indexed: Cu 2p, Ni 2p, O 1s and Mo 3p and 3d. The contaminant present in the deposited film has been estimated to 10±5%. The thickest NiO film of 30 Å elaborated during the XPS experiments shows a large concentration of ~25% Mo in the film. In order to evaporate this large amount of NiO we strongly increased the deposition rate (from 0.06 to 0.2 Å/min.). The higher contamination for this film is due to the higher temperature of the crucible during the evaporation. In the case depicted in figure 4.6, the estimated fraction of molybdenum contamination is of about 15%, obtained for a deposition rate of about 0.06 Å/minute. The origin of the Mo contamination is related with our experimental setup. In order to evaporate NiO (fusion temperature of 1960°C) the molybdenum crucible is heated by electron bombardment. We estimate that we evaporate molybdenum by direct electron sputtering. To

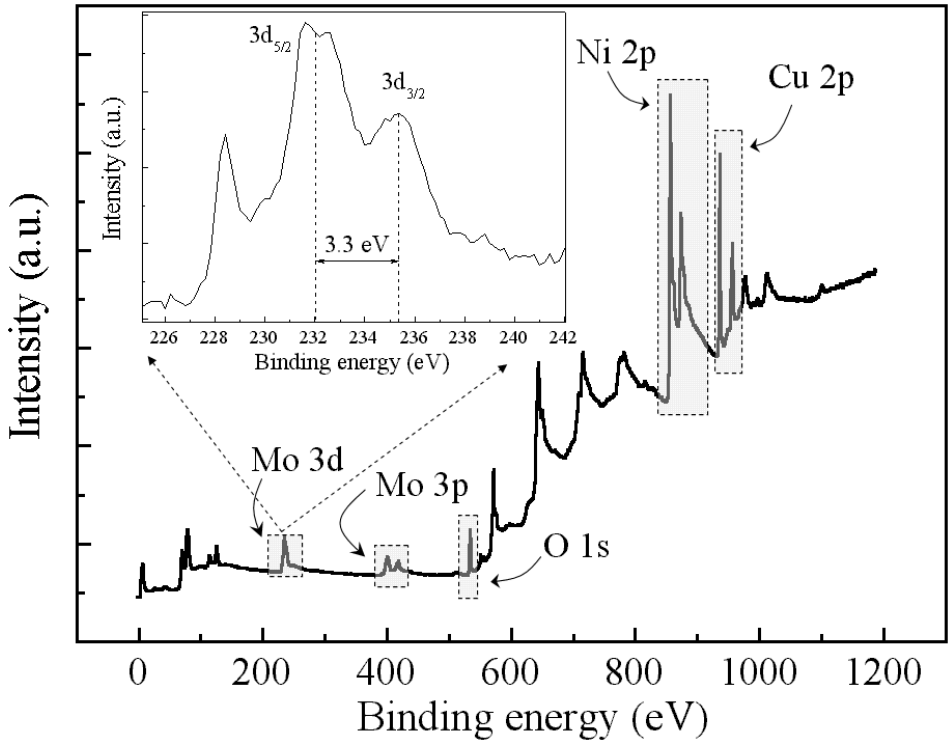

Figure 4.6: *XPS wide scan – 7.5 Å NiO equivalent thickness:*
Only the main electronic transitions are marked in the figure (Cu 2p, Ni 2p and O 1s). The Mo contaminant is characterized by the apparition of 3d and 3p XPS lines. The inset show the Mo 3d line fine structure characterizing the formation of molybdenum oxide (MoO_3 or MoO_2), $\Delta 3d = 3.3eV$.

increase the deposition rate we have to increase the number of the emitted electrons and their energy, which results in a larger sputtering rate of the molybdenum crucible. Visual control of

the crucible revealed its roughening on the front part related to the sputtering process when large fluxes were used.

The inset in the figure 4.6 shows the XPS fine structure of the Mo 3d 5/2 and 3/2, characterizing the formation of oxidized molybdenum, MoO_3 or MoO_2. The binding energies of the $3d_{5/2}$ and $3d_{3/2}$ XPS lines (232 eV and 235 eV respectively) reveal that the Mo is in an oxidized state.

During the XPS measurements the deposition rate was strongly increased in order to reduce the deposition time. During the AES kinetic acquisition, for example, the estimated deposition rate of 0.03 Å/minute is 2 times smaller than the one used to obtain the XPS spectrum presented in figure 4.4-a. The STM measurements were performed on ultra-thin NiO films (0.1 – 7.5 Å) obtained by evaporation with small deposition rates (< 0.06 Å/minute), ensuring less than 10% molybdenum contamination. The quantitative determination of the interface composition by surface diffraction measurements (§4.6), performed using the same low flux conditions as for the STM, shows that only nickel atoms diffuses on the copper lattice sites. No molybdenum atoms have been observed at the interface[♣].

☑ *The NiO films obtained by direct evaporation shows ~10% molybdenum contamination. This contamination does not affect the models proposed in this work. The differential diffusion proposed here explains well the morphology observed by STM, i.e. disruptive growth with formation of holes in the Cu substrate and is quantitatively confirmed by GIXD. Nevertheless, we can not exclude a possible role of the molybdenum at the origin of the poor epitaxy of the deposited films on the Cu(111) substrate.*

[♣] If we assume that Mo atoms are diffused in the Cu substrate, the scans along the direction perpendicular to the surface (rod scans) are capable to discern between Ni, Cu and Mo atoms (Mo has 14 electrons more than Ni and the structure factor is proportional with the square of the Z atomic number).

4.4 REAL SPACE (STM) MORPHOLOGICAL STUDY

4.4.1 Growth and morphology

The morphology of the NiO films grown on Cu(111) in the 0-6 Å thickness range was studied using STM. Figure 4.7 shows one of the main characteristics of the NiO morphology: the holes formation in the Cu(111) substrate. From the first growth stage, at 0.1 Å (figure 4.7), holes characterized by an average diameter of about 4 nm and a depth equal to the step height appear, i.e. one Cu atomic layer (~2 Å). The same behavior of the substrate was also observed in the case of FeNi/Cu(111) [Cher01a], Fe and Co/Cu(111) [Kief93, Figu94], or in the case of Ni/Cu(111) [Boeg01] (section §3.3). In the cited references, the authors explain the formation of large monatomic high holes taking into account the relative surface free energy (SFE). Since the copper has a small SFE (1.934 J/m^2 [Meze82]) it will have the tendency to occupy on-top sites, leading thus to holes formation. The calculation of the NiO(111) surface energy is a controversial topic, and the results vary from one author to another. While Wolf [Wolf92] gives a value of 4.284 J/m^2 proposing an octopolar NiO(111)

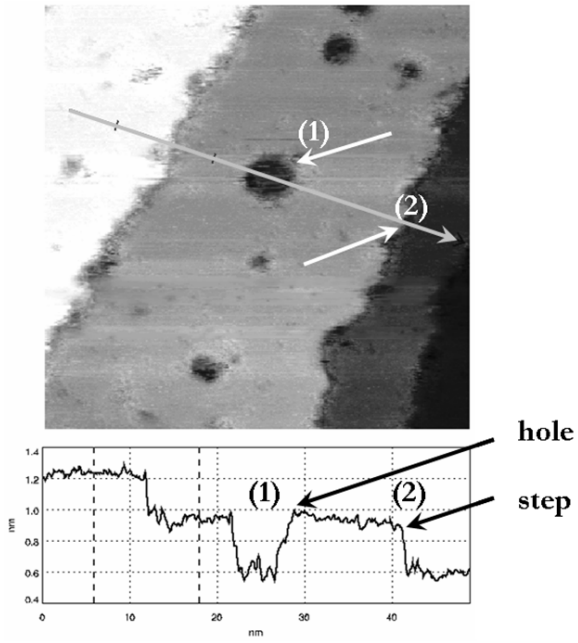

Figure 4.7: *Holes formation in the Cu substrate:*
0.1Å thick NiO; from the very first growth stage we remark the formation of holes (1) on the Cu surface, with a depth equal to the steps height (2).

surface reconstruction to overcome the diverging electrostatic potential problem of polar surfaces, recent results [BengPhD] report a SFE of 1.67 J/m^2 and 2.60 J/m^2 for a relaxed and a non-relaxed (111) octopolar reconstructed surface, respectively. However, in our case we can not explain the holes formation by a simple energetic argumentation. The NiO SFE values are calculated in the case of a perfect NiO(111) surface, that is a NiO(111) single crystal surface.

Since we observe the holes apparition from the very beginning of the growth (0.1 Å), when a NiO(111) surface does not really exist, we can not simply compare the Cu SFE with the NiO's one. Nevertheless, it is obvious, from an energetic point of view, that the formation of holes is related with a dramatic change in the energetic equilibrium of the Cu(111) surface. In the case of Ni/Cu(111) films we evidenced (§3.3) the tendency of copper atoms to cover the nickel islands. Therefore, considering that the evaporated NiO is dissociated at the Cu(111) surface, we can explain the holes formation by the SFE difference between Cu and Ni. In this very crude approach we neglect the role of the oxygen. However, as it will be discussed latter in this section, oxygen acts as a surfactant, enhancing the hole formation process.

Increasing the deposited NiO quantity, we observe an evolution of the morphology characterized by a *multiplication process*: the number of holes increases, while their shape and size remain constant, as suggested by the STM images. In figure 4.8 we show the evolution of the morphology in the thickness range 0.1 to 1.5 Å, together with the distribution of the holes diameters. The STM images presented in figure 4.8 have the same scale, 50×50 nm^2, so we can directly observe the multiplication process of the holes that are monodispersed with a hole diameter of ~4 nm.

In order to understand this unusual behavior, we have to take into account the *oxygen*

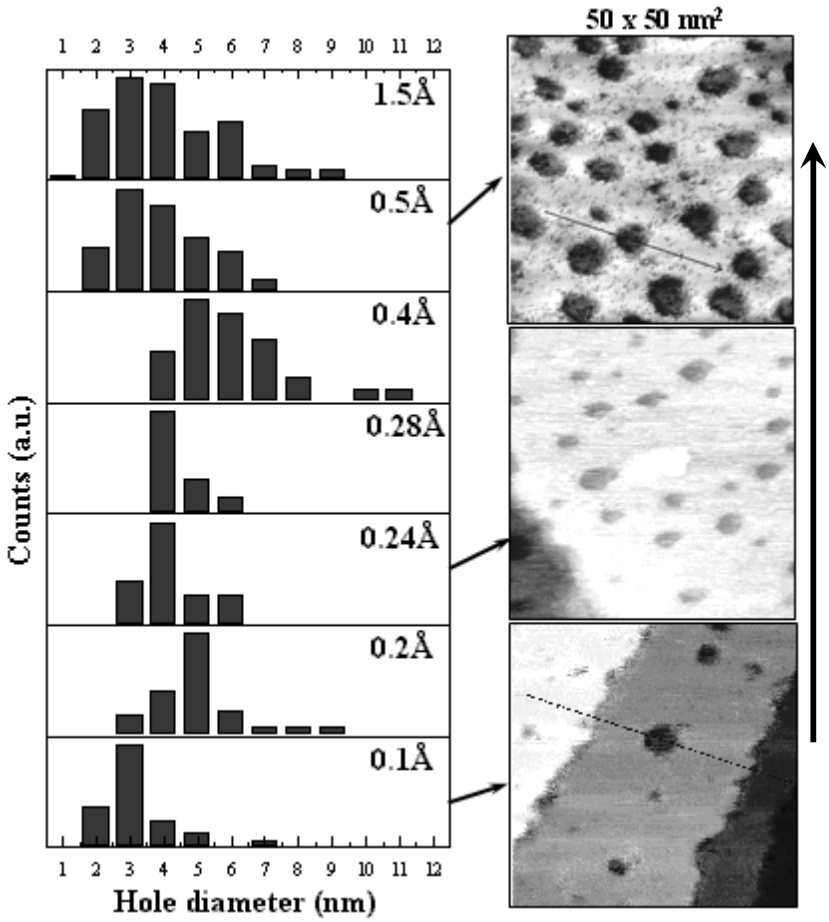

Figure 4.8: *Topographic STM images for NiO/Cu(111) in the very low coverage regime (0-1.5 Å) and statistics extracted from the STM images:*
STM images for 0.1, 0.24 and 0.5Å NiO films are shown. The histograms are deduced by counting the holes on a single terrace as a function of their diameter (the hole diameter dispersion). The average hole diameter is ~4 nm (40Å) and is constant as a function of the thickness. The arrow at right indicates the thickness increase. For a better visualization of the multiplication process, all images are shown at the same scale, i.e.50x50 nm^2.

surfactant effect. The role of the surfactant is to raise the barrier height ("Ehrlich – Schwoebel barrier") for the surface diffusion of the adatom [Ferr00]. On the Cu(111) surface, impressive work was made using mainly Pb [Mull01, Cama01a, Cama01b, Gome01, Pass00, Cama98, Kuch98] and Sb [Noak01] as surfactant. In the last two years, several studies addressing the issue of a Cu surface with O as surfactant were also reported. For example, in the case of the Co grown on the Cu(110) surface [Ling01], combined AES, LEED and STM measurements revealed the surfactant role of oxygen, with a resulting flat and ordered Co film growth, opposed to the 3D islands growth found for the Co grown on clean Cu(110) [Kief93]. By STM observations, in the case of Fe deposited on the oxygen absorbed Cu(111) surface [Li01], it was shown that a high density of small islands is nucleated on the surface instead of a step edge decoration growth.

As was observed in the case of Ni deposited on the Cu(111) surface [Boeg01] (presented also in the §3.3), the growth is characterized by islands formation. Theoretical calculations have demonstrated that for the Ni/Cu interface, the stable configuration is a sandwich like Cu/Ni/Cu, without intermixing. This is obtained by Cu atoms diffusing on top of the Ni islands [Raek92, Pour99]. Assuming that the Ni and O atoms are dissociated when deposited on the Cu surface, the presence of the O surfactant could inhibit the Ni islands formation, promoting the intermixing (*via* a direct exchange process) between the Ni and the Cu atoms. In this way, Cu adatoms are formed and diffuse on the surface. Since the hopping rate of a Cu adatom on the Cu(111) surface is of about 10^{10} hops/second [Evan96], we can assume that the Cu adatom can diffuse until it will be trapped on the surface steps. The strongly perturbated morphology of the step edge in figure 4.8 validates this assumption.

However, a simple interlayer atomic exchange cannot explain the shape and the size of the holes. Unfortunately there are no calculation to predict the energy of a such system, with Ni and O dissociated species on the Cu(111) substrate. However, we can conclude that oxygen acts as a surfactant hindering the Ni diffusion on the surface on one hand, and promoting the interlayer exchange with the Cu, on the other hand. Likewise the Fe/Cu(111) interface [Li01], the O atoms are likely to segregate on the surface.

After the first stage of the growth (0-2 Å), characterized by the holes formation *via* the multiplication process, we observe by STM morphology modifications. Between 2 Å and 4 Å (figure 4.9-a and 4.9-b), the holes evolve in depth and width. At 2 Å (figure 4.9-b), we observe the formation of the second level as patches. The hole density reaches a maximum and therefore a second level appears. Taking into account the Cu adatoms diffusion, we can explain the apparition of this second level in terms of *trapping probability*.

The Cu atoms emerging from the Cu(111) surface diffuse on the surface until they are trapped on a step edge. The large amount of holes characterizing the surface at 2 Å, presents a large number of trapping sites for the Cu adatoms. Since the hole number (density)

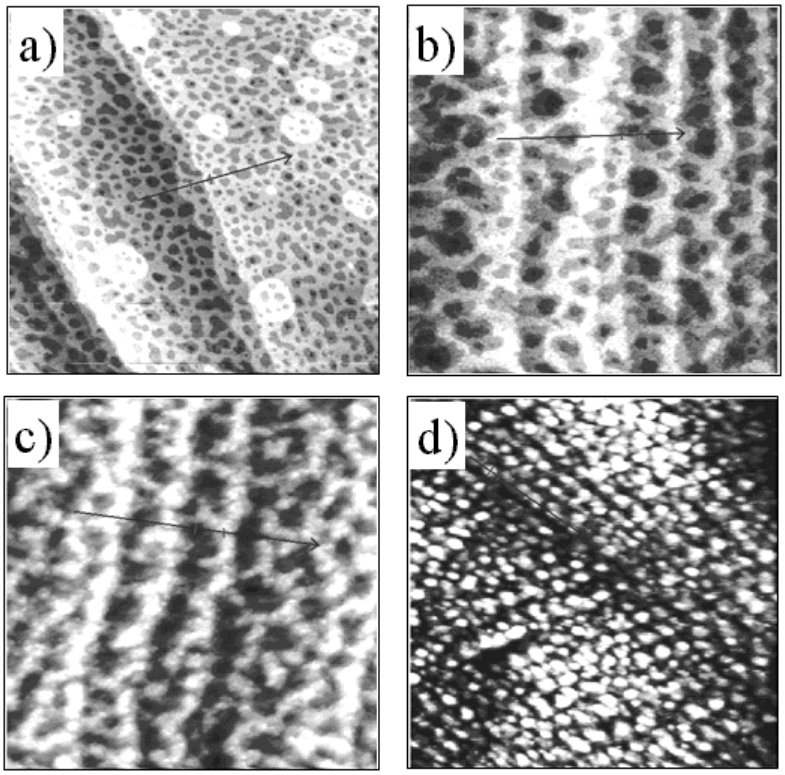

Figure 4.9: *evolution of the NiO morphology above 2 Å:*
a) 2 Å NiO, 200×200 nm^2 – the hole density reaches a saturation point. A second level can be observed on the surface as patches;
b) 4 Å NiO, 100×100 nm^2 – the growth follows an evolution along the z-axis (normal to the surface) and is characterized by holes with several depth levels (pyramidal islands with the small axis at the bottom);
c) 5 Å NiO, 100×100 nm^2 – the hole-like aspect disappear and 3D islands are formed;
d) 6 Å NiO, 200×200 nm^2 – the morphology is characteristic to a typical 3D growth

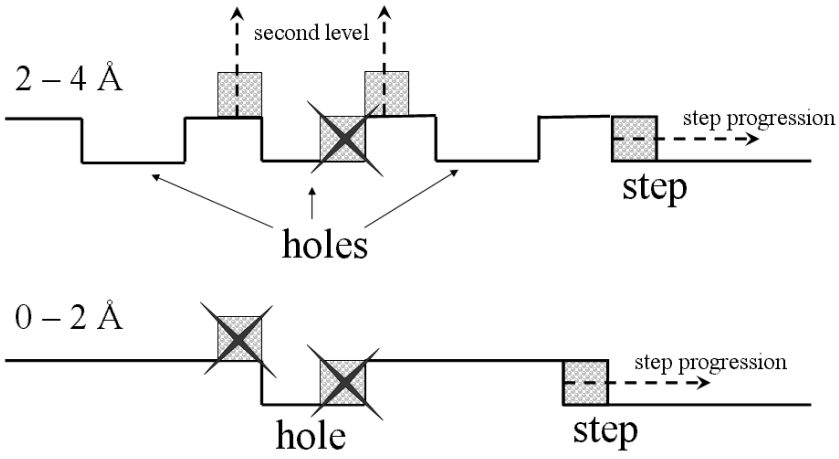

Figure 4.10: *schematic drawing of the Cu/Cu(111) diffusion and trapping process:*
- between 0 and 2 Å STM measurement revealed no agglomeration on the holes and on the step edges;
- between 2 and 4 Å the morphology can be described by an evolution on the direction perpendicular to the surface ➔ strong roughening

increases with the NiO thickness (between 0 and 2 Å), the number of trapping sites on the holes edges will also increase with the NiO thickness. If the Cu atoms would be trapped equivalently on the steps of holes and on steps edges, the morphology would be characterized by a "step-flow" growth of Cu/Cu(111) with steps progression and by a reduction of the hole

diameter in the thickness range from 0 to 2 Å (figure 4.10). The last process was never observed by STM on the 40 Å diameter holes. We also did not observe step decoration between 0 and 1.5 Å. Therefore, we conclude that all the Cu adatoms are trapped on the step edges, as shown in figure 4.10. The origin of this behavior may be related to a difference between the surface potentials near the holes and steps edges respectively, the step edges being more favorable for the Cu adsorption in this thickness range. At 2 Å, as observed in the STM image (figure 4.9-a), a second level can be observed surrounding the holes. This abrupt change toward a second level growth can thus be understood by a simple model involving the hole density, as presented in the following.

Taking into account the different trapping probabilities of Cu atoms on a hole edge and on a step edge, the ratio between the probability for a Cu adatom to be trapped on a step edge (p_s) and on a hole edge (p_h) will follow 2 thickness regimes:

a) 0Å < d < 2Å, $\frac{p_s}{p_h} >> 1$ ➔ the holes density is low and the trapping occurs mainly on the step edges; no trapping occurs on the holes edges.

b) d ≥ 2Å, $\frac{p_s}{p_h} \leq 1$ ➔ the holes density reaches its maximum and the trapping on holes edges probability becomes significant with respect to the trapping on the steps edges. For the 2 Å NiO film, the holes coverage is of about 80% and the probability that the Cu adatoms are trapped on the holes edges is non-negligible. This situation corresponds to the appearance of the first patches in figure 4.9-a. Since the mean hole diameter is of 40 Å, we can estimate the number of Cu atoms (N_h) along the hole perimeter (L_h):

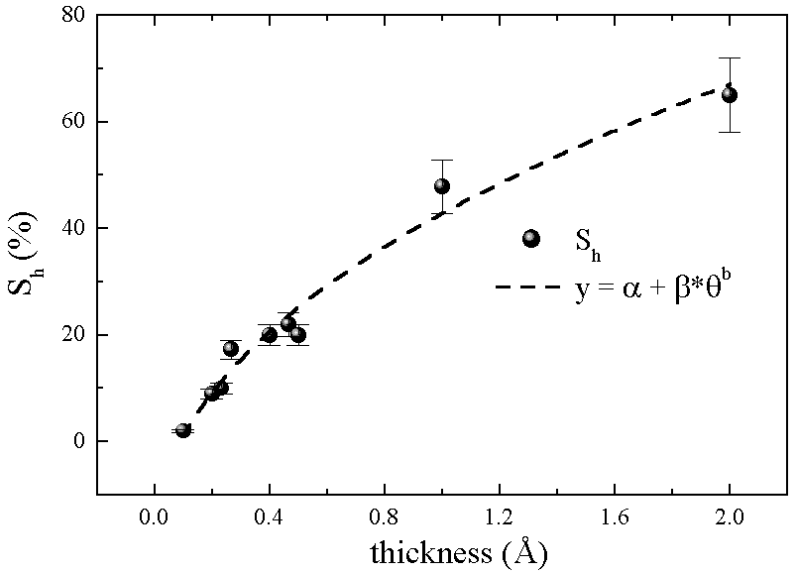

Figure 4.11: *evolution of the holes coverage (S_h) with respect to the NiO thickness:*
The dashed line stands for a power law, where *q* is the thickness. Best agreement with the experimental data is obtained for b ≅ 0.47.

$$\begin{cases} L_h = 2 \cdot p \cdot \dfrac{f}{2} = p \cdot f \cong 125 \mathring{A} \\ l_{Cu-Cu} = 2.56 \mathring{A} \end{cases}$$

$$. \Rightarrow N_h = \frac{L_h}{l_{Cu-Cu}} \cong 50 \quad atoms$$

where $l_{Cu\text{-}Cu}$ is the nearest neighbor Cu-Cu distance on the Cu(111) surface. In figure 4.11, we show the evolution of the holes surface coverage (S_h) as a function of the NiO thickness. Increasing the NiO thickness, S_h increases following a power law $y = a + b \times q^b$, with b ≅

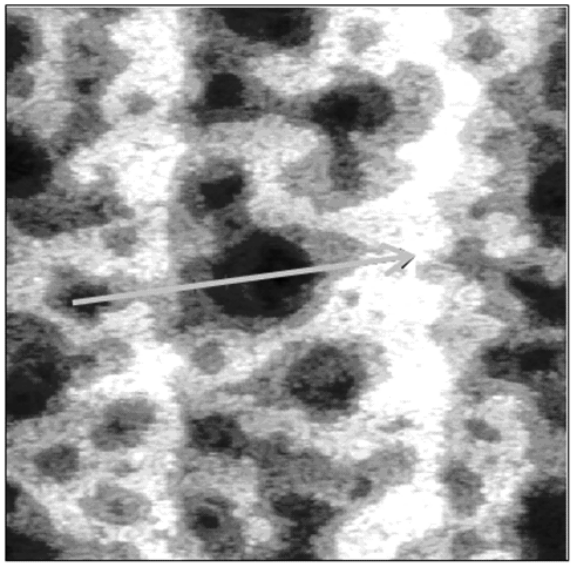

	Δz1 (Å)	Δz2 (Å)	Δz3 (Å)
1.	2.1	2.2	2.5
2.	2.3	1.9	2.2
3.	2.5	2.1	2.2
4.	2.0	2.5	1.9
	2.2	2.2	2.2

Figure 4.12: *pyramidal holes:*
50×50 nm^2 STM image corresponding to 4Å NiO on Cu(111). Following the schematic representation at right we can measure the Δz_1, Δz_2 and Δz_3, respectively. Their values are given in the table, where the bottom line stands for the average over several holes.

0.47 (θ - thickness). Therefore, since the number of trapping sites on the holes edges, N_h, vary as S_h: $N_h \propto S_h$, and since the in-plane hopping mean free path is inversely proportional with N_h, the diffusion process of the Cu adatoms has to evolve from the first to the second atomic level (perpendicular direction). This occurs at 2 Å. In fact, for NiO thicknesses ≥ 2Å, the differential diffusion proceeds, but the Cu adatoms will no longer diffuse along the in-plane directions, but on a vertical direction. In this way the second level preserves a hole pattern morphology, as it can be observed in figure 4.9-b.

Increasing the NiO thickness above this saturation value, leads to the formation of pyramidal holes, with the small basis at the bottom ("negative pyramids"). Each pyramidal hole is characterized by well defined levels, as it can be observed in figure 4.12. The holes depth measured on the STM images, varies from 7 to 10 Å, corresponding to 3-4 atomic

levels. At this point, using the chemical STM contrast (the difference between Cu and NiO electronic sensitivities, as it was the case for Ni/Cu(111) - §3.3), we may check the chemical nature of these levels: Cu or NiO. Figure 4.12, right, presents the schematic line profile, evidencing 4 different levels. In the table we give the average heights for each level calculated for several holes (1, 2, 3 and 4). The overall value, equals to 2.2±0.3 Å, shows large dispersion of the Δz values contrarily to Ni/Cu(111) (§3.3)[♣]. Therefore, it is impossible to conclude on the composition of these levels by STM. The situation of 4 Å thickness corresponds to the plateau observed in photoemission spectroscopy (figure 4.4) and characterizes the evolution in equal quantities of metallic and oxidized Ni. Thus, since the differential diffusion process continues even for this thickness, we conclude that these planes contain mixed Ni, O and Cu atoms.

Above 4 Å, the growth is characterized by the transition from the specific hole morphology to a 3D islands morphology (figure 4.9-c and 4.9-d). A second critical point in the diffusion process is thus reached (~6Å): the diffusion stops and the NiO is deposited on a surface which has reached his energetic equilibrium. This 3D growth regime corresponds to zone II in the XPS evolution (figure 4.4-b) and characterizes the formation of NiO. Structural measurements (§4.6) will demonstrate that at the interface the Cu-Ni exchange process continues even for relatively high thicknesses (12 Å). Only after 12 Å the differential diffusion, which dominated the growth up to ~6 Å, is strongly reduced and the NiO evaporation leads to the formation of stoichiometric NiO.

☑ *Summarizing the STM results, we have shown that the NiO morphology evolution as a function of the NiO thickness can be described by 3 characteristic stages, fully in agreement with the chemical evolution studied by AES and XPS:*

(0 – 2) Å ➔ *the growth is characterized by hole nucleation and discrete multiplication. The balance between the surface free energies of Ni and Cu with O as surfactant is responsible for this unusual behavior: O inhibits the surface diffusion of Ni atoms and favors the direct Ni-Cu atomic exchange. Moreover, the holes size and shape reflect an unequal Ni-Cu atomic exchange.*

(2 – 6) Å ➔ *at 2 Å, the surface reaches the maximum hole density and therefore the maximum number of trapping sites. The surface diffusion of Cu adatoms stops*

[♣] We compare these value with the pure Ni layers because along the [111] direction, the NiO is characterized by the alternation of Ni and O pure atomic planes.

and further increase of the deposited thickness leads to a modification in size (width and depth) of the holes. In this way pyramidal holes are formed characterized by well defined levels, composed by a mixture of Cu, Ni and O. The overall roughening becomes very large.

(6 → 12) Å ➔ *the growth presents a transition to a typical 3D morphology, characterized by islands formation. The differential diffusion presents a second critical point at ~6Å, defined by the strong decrease of the Ni-Cu atomic exchange, leading to the formation of stoichiometric NiO.*

4.4.2 STM chemical contrast

STM can exhibit chemical sensitivity by varying the tip bias. In the following paragraph we describe in detail the chemical nature, in particular the oxygen localization at the surface for the early stage of the growth (< 1 Å). In fact, for very low thicknesses (< 1 Å), we observe the STM contrast reversal when changing the tip bias.

Due to the high probability that adsorbed O_2 are present on the surface, several aspects related with the possible STM tip contaminations have to be discussed in addition before presenting the experimental results. Ideally, as it was shown in the literature [Cast97, Duda97, Cast99], the NiO STM measurements can be made in both, positive and negative biases, due to the STM contrast reversal which appears in such strongly correlated ionic systems. This STM contrast reversal can give direct indications concerning the oxide character, especially in the thickness range presented in our work. Nevertheless, we have to keep in mind that the authors cited above used the STM on single crystal samples and as a consequence, the possibility of the tip contamination was excluded. Ruan et al. [Ruan93] showed that in the case of oxygen adsorbed on Ni(110) and oxygen adsorbed on Cu(110) one can apply the following convention with respect to the tip apex:

- for a metallic tungsten tip apex, only oxygen atoms can be resolved as protrusions (or bright structures defined by the STM color scale);

- for an oxygen apex, only the metallic atoms appear as protrusions.

However, the authors neglected the influence of the tip bias on the STM contrast, all reported STM images being recorded for very small positive biases. Therefore, if we consider both the tip apex and the tip bias, in the case of the ultra-thin NiO films we can imagine the schema presented in figure 4.13. Thus, for example, for a negative bias and a clean tip (tungsten apex) the O atoms will appear as protrusions (“positive contrast”) and for a contaminated tip (oxygen apex) Ni atoms will appear, for the same bias. However, this approach is too simple

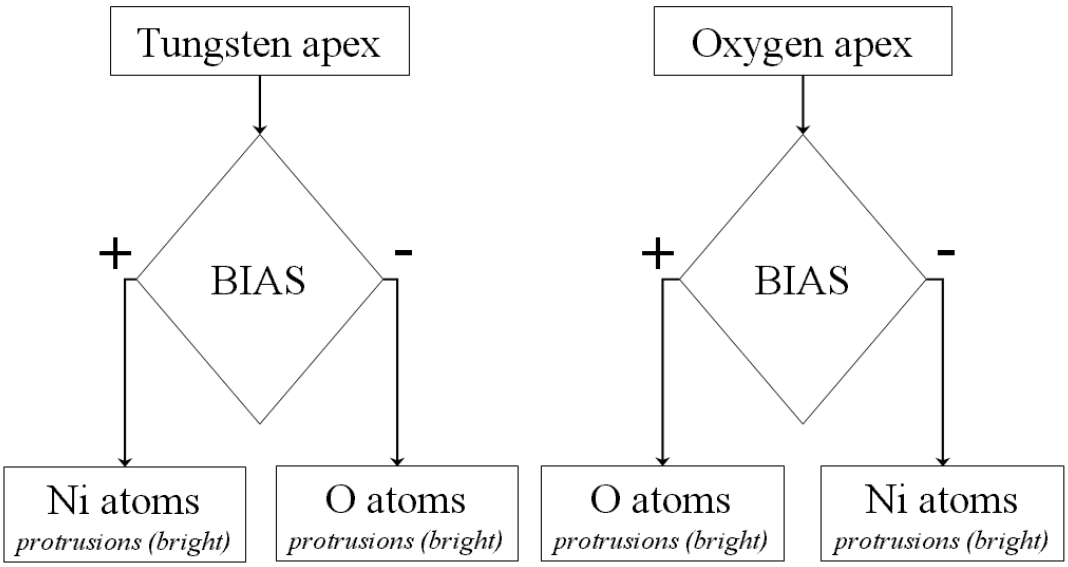

Figure 4.13: *schematic drawing of the STM sensitivity as a function of the tip apex and tip bias*

to describe different situations which may appear for different combinations of tip apex and biases. In addition, the STM tip contamination leads not only to changes of the STM contrast, but can give rise to a completely modified topographic image, due to complex changes in the STM tip electronic states which strongly influences the tunneling current.

In figure 4.14 we show the STM contrast reversal for a 0.3 Å NiO film. Changing the bias, we should obtain for U < 0 V the *filled electronic states*, while using a positive bias (U > 0 V) we should image the *empty electronic states* [Cast97, Duda97, Cast99]. The *Dz* contrast (the corrugation height) is different for negative bias (1.05 Å – bright contrast) compared to the positive one (1.40 Å – dark contrast), in agreement with theoretical predictions and previous experimental results [Cast97, Duda97]. The quoted authors have calculated the corrugation heights as 0.49 Å for a negative and 0.88 Å for a positive applied bias and for a tip-sample distance z = 4 Å. The deviance of our values compared to the calculated ones certainly originates from the difference of the tip-sample distance.

It is important to remark that in the case of STM imaging on NiO single crystals, using the negative bias, for example, results in bright contrast for the O^{2-} in the same time with dark contrast characterizing the Ni^{2+}. In fact, it was shown that integrating the *density of states* (DOS) of the surface states over the energy interval from -0.4 eV to 0.1 eV (negative bias), approximatively 83% corresponds to the filled states above oxygen sites and 17% is associated with the empty states above nickel sites. Therefore, using a metallic apex and a negative bias, the STM contrast is mainly sensitive to the filled states localized over the O sites. In our case, changing the bias (positive bias) results only in the change of the contrast (dark contrast) assimilated with the same filled O states observed with negative bias. The Ni

characteristic empty states which should appear as protrusions in the STM image are not observed. *We conclude therefore that the STM contrast is related with on-top localized O atoms and that no Ni atoms are present at the surface*.

Moreover, these oxygen atoms are not simply absorbed on the surface. The STM contrast (specific for the O^{2-} state) is an evidence that they are bounded in a similar way as in NiO (Ni^{2+}-O^{2-}). However, it is difficult to say if the O atoms are bounded with the Ni or with

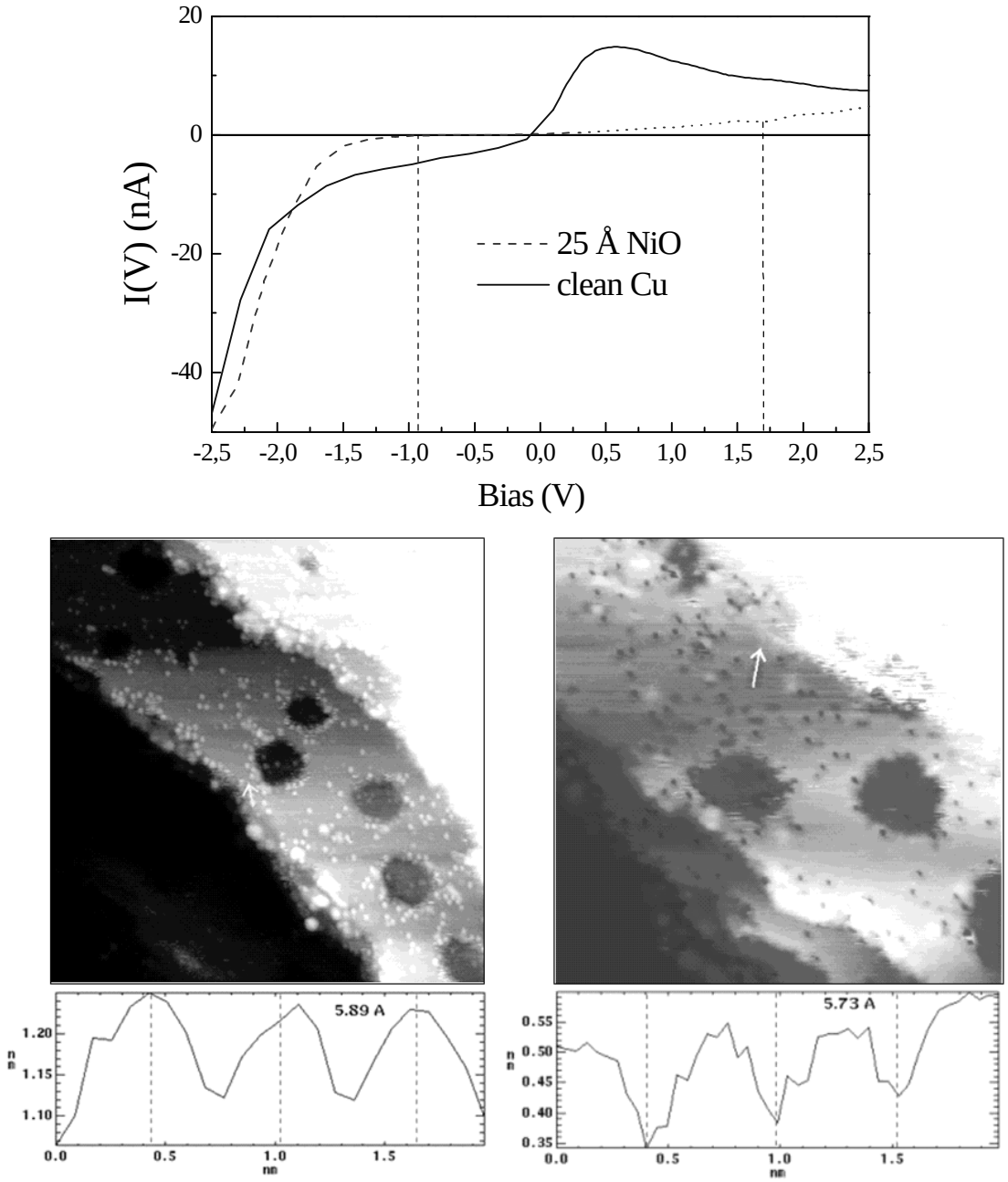

Figure 4.14: *Filled and empty electronic states – STM contrast reversal:*
Spectroscopic STM data and images taken at -0.8 V bias (0.6 nA tunneling current – left STM image, 20×20 nm^2) compared with the STM image for +1.7 V bias (1.5 nA tunneling current – right STM image, 15×15 nm^2). The dashed lines in the *I*(*V*) representation indicate the biases used to image the empty and the filled states of the surface.

the Cu atoms. Nevertheless, the photoemission results show only Ni-O bounds, without any sign of Cu oxidizing. It is important to specify that the term “bound” in the case of the STM contrast reversal has not only a chemical connotation, but it defines also the “bound orientation”. We can distinguish therefore between an “in-plane Ni-O bound” (parallel to the surface plane) and an “out-of-plane Ni-O bound” (perpendicular to the surface plane). The absence of the Ni^{2+} empty states excludes the presence of the Ni atoms on the surface (in the same atomic layer as the oxygen atoms), but does not exclude the possibility of a Ni-O “out-of-plane bound”. In addition, if we assume that the Ni atoms diffuse in the topmost layers of the Cu substrate, the on-top oxygen atoms could be bounded with Ni atoms located in the first Cu sub-surface layer.

Figure 4.15 shows a high resolution STM image for a 0.6 Å deposited NiO film. This image was obtained for a tip bias of -0.8 V and a tunneling current of 0.7 nA. As discussed above, the STM contrast is obtained over the filled states of the oxygen atoms. The oxygen atoms are homogenously spread and occupy sites even into the holes created in the Cu

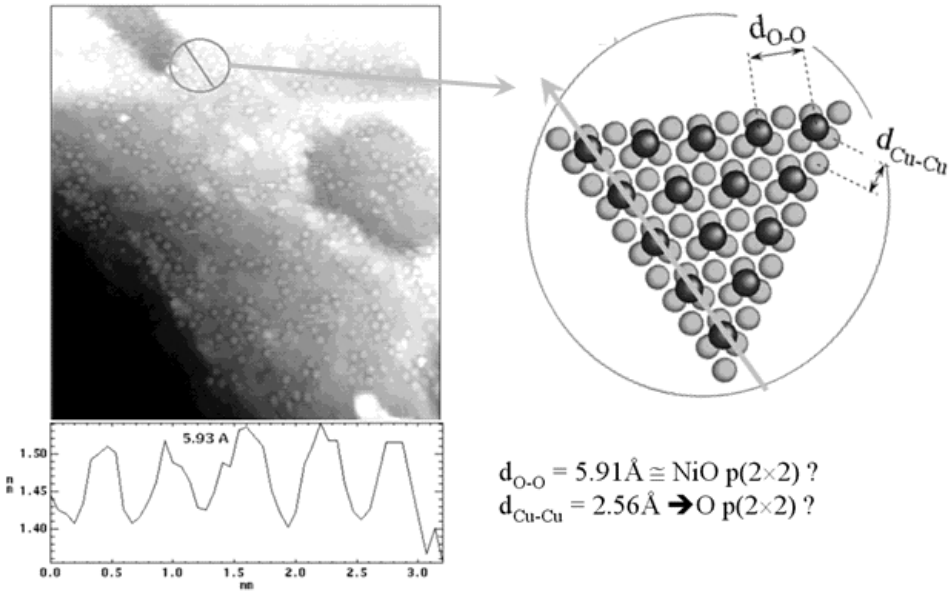

Figure 4.15: *short-range surface order:*
12×12 nm^2 STM image for 0.3Å NiO film (U = -0.8 V and I = 0.7 nA). At the left, a schematic representation is drawn. The periodicity observed on the STM image (5.93Å) is in perfect agreement with an p(2×2) NiO or p(2×2) O reconstruction. Dark circles stand for the on-top O atoms and the gray ones for the Cu atoms.

substrate. This homogeneity is a direct proof for the surfactant effect of the O atoms, which inhibits the surface diffusion of the incoming atoms [Ling01, Li01]. The selected area in figure 4.15 presents locally surface ordered structures.

Line-profiles reveal a periodic arrangement of O atoms of 5.93 Å, which agree well with the NiO p(2×2) surface reconstruction (5.92 Å) or to O-Cu p(2×2) reconstruction (5.12 Å), as presented in the schematic view in figure 4.15. Assuming the Ni atoms diffusion in the first Cu surface layer, we may conclude that this periodicity corresponds to the NiO p(2×2) reconstruction. However, this is strictly a local feature of the surface structure or, in other words, of the arrangement of O atoms on the surface. As it will be described in §4.6, the surface diffraction measurements do not show long-range surface ordering. Therefore, even if the p(2×2) reconstruction is locally present, it characterizes only short-range (< 100 Å) surface ordering.

☑ *Taking benefit from the STM contrast reversal, we evidenced a chemical contrast corresponding to oxygen atoms localized on the top of the Cu surface. This confirms the differential diffusion model suggested by AES and XPS.*

4.5 RECIPROCAL SPACE (GISAXS) MORPHOLOGICAL STUDY

Due to several limitations of the STM and GIXD techniques (short observation scale and sensitivity only to ordered structures, respectively) and to fully describe the growth we used a complementary technique, *Grazing Incidence Small Angle X-ray Scattering* (GISAXS). We will show in the following section that additional information can be extracted from GISAXS measurements, especially for thicknesses larger than 2 Å, where STM and GIXD are strongly influenced by the specificities of the NiO films grown at room temperature (3D growth and structural disorder). In addition, GISAXS allows the characterization of larger objects (islands of several tens of angstroms) on the surface than GIXD (sensitive at the atomic arrangement).

In figure 4.16-a we show the evolution of the GISAXS pattern as a function of the thickness, from 0.6 Å to 10.8 Å. Let me first describe qualitatively the GISAXS patterns. The low coverage regime (0-3 Å) is characterized by very elongated diffusion perpendicularly to the surface. As observed by STM, in this thickness regime monatomic high holes are formed. Indeed, in reciprocal space monatomic deep objects (holes or islands) provide an almost constant signal along the momentum transfer along the *z*-axis (Q_z). Since GISAXS patterns give a direct picture of the reciprocal space, this observation is coherent with our STM results.

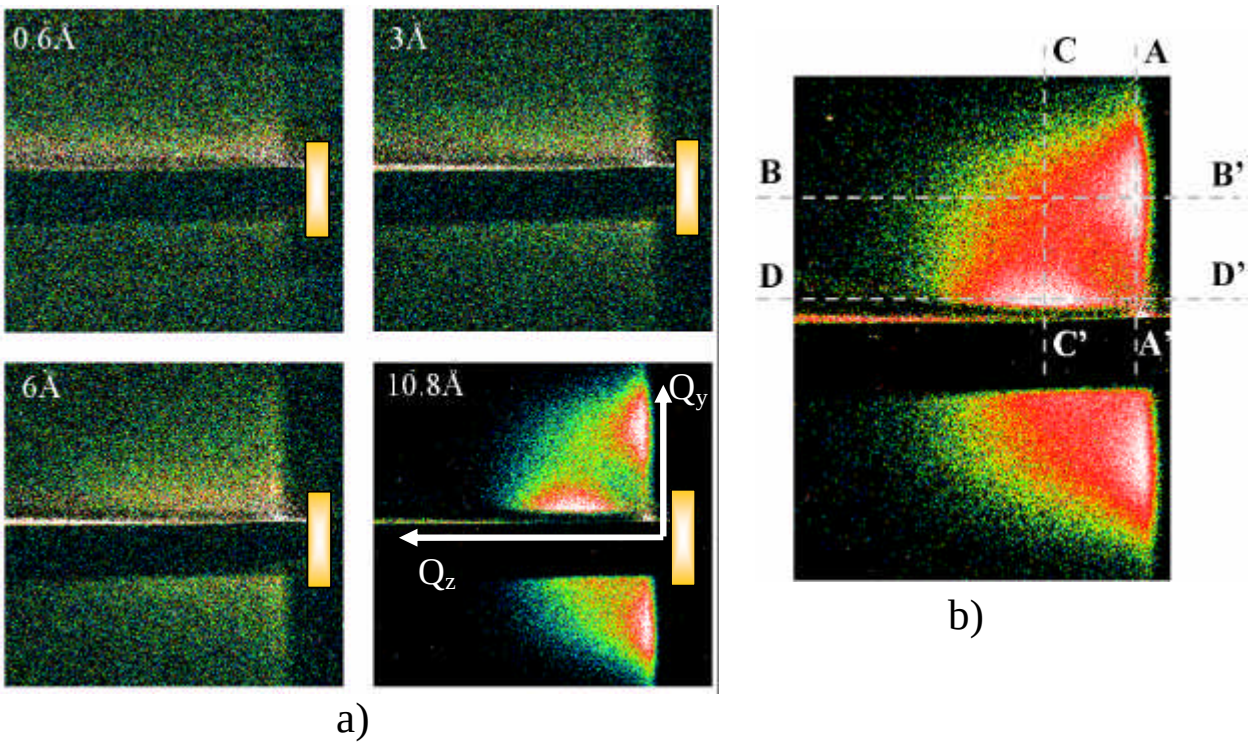

Figure 4.16:
a) Evolution of the GISAXS patterns as a function of the thickness; the evolution is characterized by a continuous transition from the hole pattern to a GISAXS pattern characterizing islands distribution (3D growth) on the surface.
b) Cross section positions in the GISAXS pattern (at 10.8 Å): A-A' characterizes the holes distribution (holes radius and correlation length), B-B' is related to the islands height, C-C' and D-D' were chosen to describe the spot along Q_z, corresponding to the reflectivity, as detailed in the text.

To the best of our knowledge, this is one of the seldom experiments which show the reciprocal space image of a single atomic layer. In a first crude approach (using the transformation relationship between the direct and the reciprocal space, $r = \frac{2 \cdot p}{\Delta Q_y}$, ΔQ_y being the width of the diffused signal), we conclude that the GISAXS pattern characterizes monatomic holes of ~40 Å diameter, without any characteristic correlation length. The evaluation of this value takes into account the distance between the sample and the CCD camera (L = 670 mm), the energy of the incoming x-ray beam (13 keV = 0.995 Å^{-1}) and the size of a pixel on the CCD camera (56 µm).

For larger thicknesses (3-6 Å), the scattered spots present a limited spread with respect to Q_z which decreases with thickness. Taking into account the inverse evolution of the Q_z compared with the objects (holes) height, this behavior corresponds well with the second growth regime described by STM: the holes become deeper, resulting in a morphology characterized by pyramidal holes. The GISAXS patterns for this thickness regime are difficult to treat in a simple manner due to the large incertitude in estimating the holes depth (very

weak scattered signal). In addition, the apparition of a supplementary spot along the direction perpendicular to Q_z makes this estimation almost impossible for this particular thickness range.

Above 6 Å, the GISAXS patterns are typical for a 3D growth with formation of islands characterized by *the existence of a well-defined correlation length*. The existence of this correlation length is directly suggested by the splitting of the scattered spot along the in-plane momentum transfer (Q_y). The estimation of the correlation length from the GISAXS patterns for this thickness range results in a value of 45±5 Å. Due to the scattered spot which appears along the perpendicular momentum transfer (Q_z) it is impossible to easily estimate the height of the islands. The global envelope of the scattered pattern is given by the form factor and is related with the islands width of about 12 Å.

However, these values, obtained using the simple transformation between direct and reciprocal space, are affected by large error bars due to the convolution between the form factor P_{island} (island shape) and the interference function S_{island} (§2.2.3.3). The spot which appear along Q_z can be related with the reflectivity signal characterizing a film with ~35 Å thickness.

☑ *In a first qualitative approach, the GISAXS patterns describe the main stages of the growth, previously observed by STM: hole formation and island growth.*

More quantitative data can be obtained through a complete simulation of the GISAXS patterns. A detailed statistical description of the morphology at the sample can be obtained. In order to calculate the entire GISAXS pattern we firstly calculate several important cross sections which are significant for the scattering process and allow some de-correlation of the parameters. Therefore, as shown in the figure 4.16-b (10.8 Å thickness), we have chosen 4 cross sections:

- **A-A' -** the position of the lobes along the Q_y gives the in-plane correlation length between the islands,
- **B-B'** – this cross section characterizes the islands height (Q_z),
- **C-C'** – characterizes the extent along the Q_y of the additional spot related to the reflectivity signal,
- **D-D'** – characterizes the extent along Q_z of the reflectivity spot.

Before presenting the step-by-step procedure used to reproduce the GISAXS patterns, note that only basic formulas related with the scattering process are used here.

To calculate the cross sections we used a classical angular formalism, as shown in figure 4.17. The basic relationship is the Bragg relation, which relates the emergent wave vector k_f with the incident one, k_i: $\vec{k}_f - \vec{k}_i = \vec{Q}$, with the condition that the momentum transfer Q is a vector in the reciprocal space. Therefore, using the angles description of k_f and k_i wave

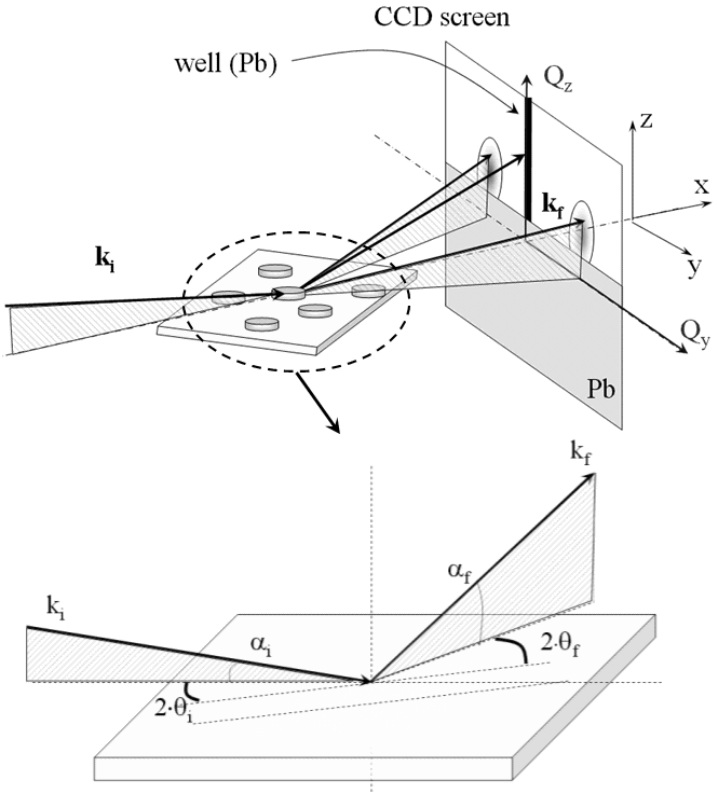

Figure 4.17: *scattering geometry:* The schematic drawings present the liaison between the *Q*-space and the angular description used to calculate the GISAXS patterns (via the Bragg relation).

vectors (figure 4.18), we can deduce the formula for the momentum transfer vector:

$$Q(a_i, a_f, q_i, q_f) = \frac{2 \cdot p}{l} \times \begin{pmatrix} \cos(a_f) \cdot \cos(2 \cdot q_f) - \cos(a_i) \cdot \cos(2 \cdot q_i) \\ \cos(a_f) \cdot \sin(2 \cdot q_f) - \cos(a_i) \cdot \sin(2 \cdot q_i) \\ \sin(a_f) + \sin(a_i) \end{pmatrix} = \begin{pmatrix} Q_x \\ Q_y \\ Q_z \end{pmatrix} \qquad (4.2)$$

During the following discussions we will always use the notion of *momentum transfer Q*, but all quantities are related with only geometric scattering parameters (angles) *via* relation 4.2. This relation allows the transition from the angular space to the reciprocal space which is characterized by the wave vector *Q*.

As shown in §2.2.3.3, the scattered intensity is described by the multiplication of several functions related with the scattering phenomenon:

$$I_{scattering} \propto P(Q,R,H)\cdot S(Q)\cdot T(a_f) \tag{4.3}$$

a) The *form factor P(Q,R,H)* is the Fourier transform of the island volume (thus island shape sensitive) characterized by its geometrical parameters (height, width, etc.). Many islands shapes were tested, in the present case, best simulations were obtained considering cylindrical islands, characterized by a radius R_0 and a height H (figure 4.18). Its form factor can be written as (after calculation of the Fourier transformation) [ThiaPhD]:

$$P_{cyl}(Q,R_0,H) = \left[\sin_c\left(Q_z\cdot\frac{H}{2}\right)\right]^2 \times \left[\frac{J_1(Q_y\cdot R_0)}{Q_y\cdot R_0}\right]^2 \tag{4.4}$$

where $J_1(x)$ is the first order Bessel function and $\sin_c(x) = \dfrac{\sin(x)}{x}$.

b) The *interference function S(Q)* is related with the correlation length, which characterize a distribution of islands on a surface, as shown in figure 4.18. It is related to the real space correlation function *g(r) via* the formula:

$$S(Q_y) = 1 + 2\cdot p\cdot r_S\cdot\int_0^\infty [g(y)-1]\times J_0(Q_y\cdot y)\cdot y\cdot dy \tag{4.5}$$

where r_S is the particle density per surface unit, and J_0 is the Bessel function of zero order. In order to describe the island distribution on the surface (figure 4.18), several correlation functions were tested (Dirac, Debye hard core, Lennard-Jonnes pair correlation, Venables pair correlation, etc.), the best in our case is the so-called "*Gaussian pair correlation function*" given by:

$$g(r)=\begin{cases}0, & for \quad 0\le r\le R_0\\ \dfrac{e^{-\frac{(r-D)^2}{w^2}}-e^{-\frac{(R_0-D)^2}{w^2}}}{e^{-\frac{(D_1-D)^2}{w^2}}-e^{-\frac{(R_0-D)^2}{w^2}}}, & for \quad R_0\le r\le D_1\\ 1, & for \quad D_1\le r\le\infty\end{cases} \tag{4.6}$$

with: w – the width of the Gaussian function, D_1 – superior limit for the Gaussian distribution extent (figure 4.18-a).

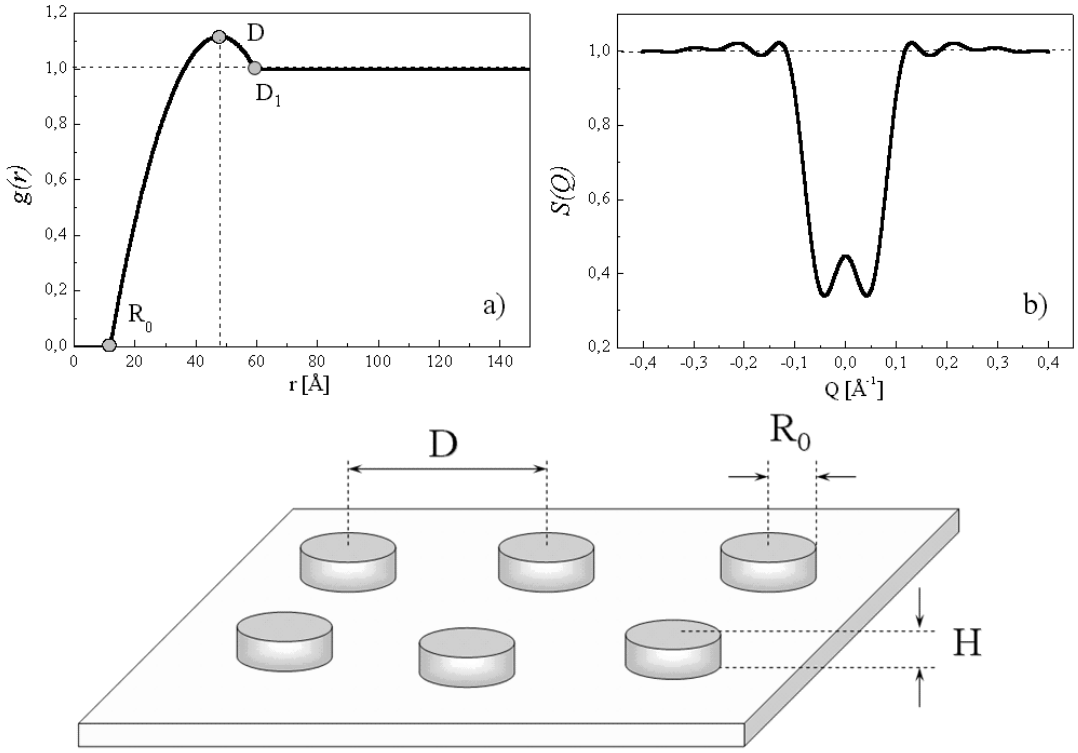

Figure 4.18: *the correlation (g(r)) and the interference function (S(Q)):*
a) the Gaussian pair correlation function *g(r)* describes the island distribution characterized by the parameters shown in the figure;
b) the interference function *S(Q)* obtained via a Fourier transformation of the *g(r)* as described in the text.

From a physical point of view, the *g(r)* function formalizes the islands distribution in probabilistic terms (with values from 0 to 1); knowing that an island exists at $r = 0$:

- $0 \le r \le R_0 \rightarrow$ in this domain the notion of *correlation length* has no meaning since the islands can not overlap and therefore in this domain there will be no (zero) islands;

- $R_0 \le r \le D_1 \rightarrow$ stands for the domain where we can find a characteristic length which describe the correlation between the islands. The Gaussian shape introduces the

correlation length (*D*) between islands and the *dispersion of the correlation length via* its width, *w*. In other words, taking a reference island, the nearest neighbors (which are similar in shape and size) will be placed preferentially at a distance equal to the correlation length. Due to numerical considerations for equation 4.5, the D_1 value was chosen to be equal to $D+R_0$ (figure 4.18-a).

- $D_1 \leq r \leq \infty \rightarrow$ the correlation function $g(r) = 1$, which means that the position of the next nearest island is not influenced any more by the island at $r = 0$. For a distribution without correlation, the probability to find an island anywhere on the surface is equal to 1, i.e. the position of a given island is not linked to the position of any other island.

The correlation and interference functions express one of the most basic laws of the physics: the matter conservation. Therefore, while the $g(r)$ function "re-distribute" the deposed matter in the direct space, the $S(Q)$ function acts in the same manner on the scattered intensity in the reciprocal space. For an equivalent deposited quantity, if no correlation exists, the scattered intensity is recorded near the lead well (figure 4.17), while in the case of a correlation, the same scattered intensity will be found splitted around the well (re-distributed by the interference function). In figure 4.18 we show the shape of the correlation function (a) and the interference function (b) for the parameters used to simulate the GISAXS pattern at a NiO thickness of 10.8 Å (R_0 = 11.65±0.05 Å and D = 47.7±0.1 Å).

Equation 4.5 describe only the interference function along the *y* in-plane direction and is related therefore only to the in-plane correlation length between the islands. In the case of a distribution of buried islands (for example) we can describe the out-of-plane correlation using a similar interference function (4.5), changing the *y*-axis related parameters with the ones characterizing the *z*-axis.

c) The last factor in equation 4.3, $T(\alpha_f)$, is the *transmission factor* which reflects the effect of the refraction of the scattered wave. It depends on the critical angle (α_c) and absorption coefficient (μ) of the deposit (or surface) *via* the complex index of refraction, *n*:

$$\begin{cases} T(a_f) = \dfrac{2 \cdot k_f^z}{k_f^z + \tilde{k}_f^z} \\ \tilde{k}_f^z = \sqrt{k_0{}^2 \cdot n(a_c,\mu)^2 - \left|k_\parallel\right|^2} \end{cases} \text{ with } \begin{cases} k_0 = \dfrac{2 \cdot p}{l} \\ \left|k_\parallel\right| = \sqrt{(k_f^x)^2 + (k_f^y)^2} \\ n(a_c,\mu) = 1 - d(a_c) - i \cdot b(\mu) \\ d(a_c) \cong \dfrac{a_c{}^2}{2} \\ b(\mu) = \dfrac{\mu \cdot l}{4 \cdot p} \end{cases} \tag{4.7}$$

Generally, for a distribution of islands as the one depicted in figure 4.18, equation 4.3 is sufficient to reproduce the scattered intensity. However, in figure 4.17 we remark the apparition of a spot along the direction of the perpendicular momentum transfer Q_z which can not be reproduced simply using formula 4.3. The position of this spot is linked to the *reflectivity* signal given by a layer♣ of ~35 Å thickness (for the 10.8 Å film). The analytic form of the reflectivity is:

$$R(a_f) = \frac{k_f^z - \tilde{k}_f^z}{k_f^z + \tilde{k}_f^z} \cdot e^{-2 \cdot s^2 \cdot k_f^z \cdot \tilde{k}_f^z} \tag{4.8}$$

where s stands for the roughness of the film. Therefore, considering the adsorbate (NiO) layer characterized by a thickness *De* "sitting" on the substrate (Cu), we can write the expression of the Kiessig fringes (interference between the adsorbate and the substrate):

$$R_{Kiessig}(a_f) = \frac{R_{NiO}(a_f) + R_{Cu}(a_f) \cdot e^{i \cdot Q_z \cdot \Delta e}}{1 + R_{NiO}(a_f) \cdot R_{Cu}(a_f) \cdot e^{i \cdot Q_z \cdot \Delta e}} \tag{4.9}$$

In addition, by STM we observed that for the very low coverage regime (0 – 2 Å), the morphology is characterized by the holes formation. In order to complete the formula 4.3 we have to take into account also the scattered intensity coming from the holes, which can be expressed in a similar manner as the scattering related with the islands (equation 4.3). Therefore, similar to the case of islands, we introduce the *hole form factor* (P_h), the *hole*

♣ In this context the "layer" concept refers to the entire thickness (adsorbate layer + diffuse interface) characterized by a different index of refraction compared with the Cu substrate.

correlation length (g_h) with the resulting *hole interference function* (S_h) and the *hole transmission factor* (T_h). The *total scattered intensity* will be defined therefore as:

$$I_{scattering} \propto A_1 \cdot P_i \cdot S_i \cdot T_i + A_2 \cdot P_h \cdot S_h \cdot T_h + A_3 \cdot R_{Kiessig} \tag{4.10}$$

where the *i* index stands for the islands. Each of the three terms is ponderated using relative intensity factors (A_1, A_2, A_3).

Taking into account all these elements, we have calculated the cross sections through the GISAXS pattern using formula 4.10. It is important to remark that no additional artificial coefficients were used, e.g. an additional broadening. The actual broadening is in fact a direct result of the correlation function *g(r)* shape, which already describes a Gaussian dispersion of the correlation length. In addition, in order to avoid the utilization of a scale factor, the calculated curves have been normalized with respect to a point of the experimental curves, the whole curve being then reproduced with the formula 4.10.

Figure 4.19 shows the experimental (symbols) and calculated (solid lines) cross sections for the thickest NiO film, of 10.8 Å. We note that for this situation, the scattered intensity corresponding to the holes was neglected, considering that the morphology is no more affected by the holes, as suggested by the STM measurements (anyhow, during the calculations the hole existence hypothesis was taken into account, but the experimental cross sections was reproduced only considering the islands scattering). We present in the following the morphological parameters used in the calculations:

A–A': along this cross section the scattered intensity depends only on the in-plane correlation length between the islands (D_i) and on the islands shape and radius (R_0). The best agreement between the experiment and calculation was found for cylindrical shaped islands with R_0 = 11.65±0.05 Å and a correlation length D_i = 47.7±0.1 Å, with a dispersion of about 47.7×2 Å. This value of the dispersion has to be understood as a minimal dispersion, all *w* values larger than 47.7×2 Å giving good results. This prohibits the existence of any other correlation length in the length domain from 0 to 47.7×2 Å than the 47.7 Å one. Since the rule applies for all the islands, within a "nearest neighbor" algorithm we obtain strictly the 47.7 Å value for the correlation length and therefore leads to a unique and well defined solution.

Interestingly, after fitting the calculated surface density r_S in relation 4.5 exactly corresponds to the form:

$$r_S = \left(D^2 \cdot \frac{\sqrt{3}}{2} \right)^{-1} \tag{4.11}$$

which defines a hexagonal lattice of parameter D = 47.7 Å. Therefore, the correlated islands are disposed in average on a hexagonal lattice characterized by a lattice parameter equal to the correlation length (47.7 Å).

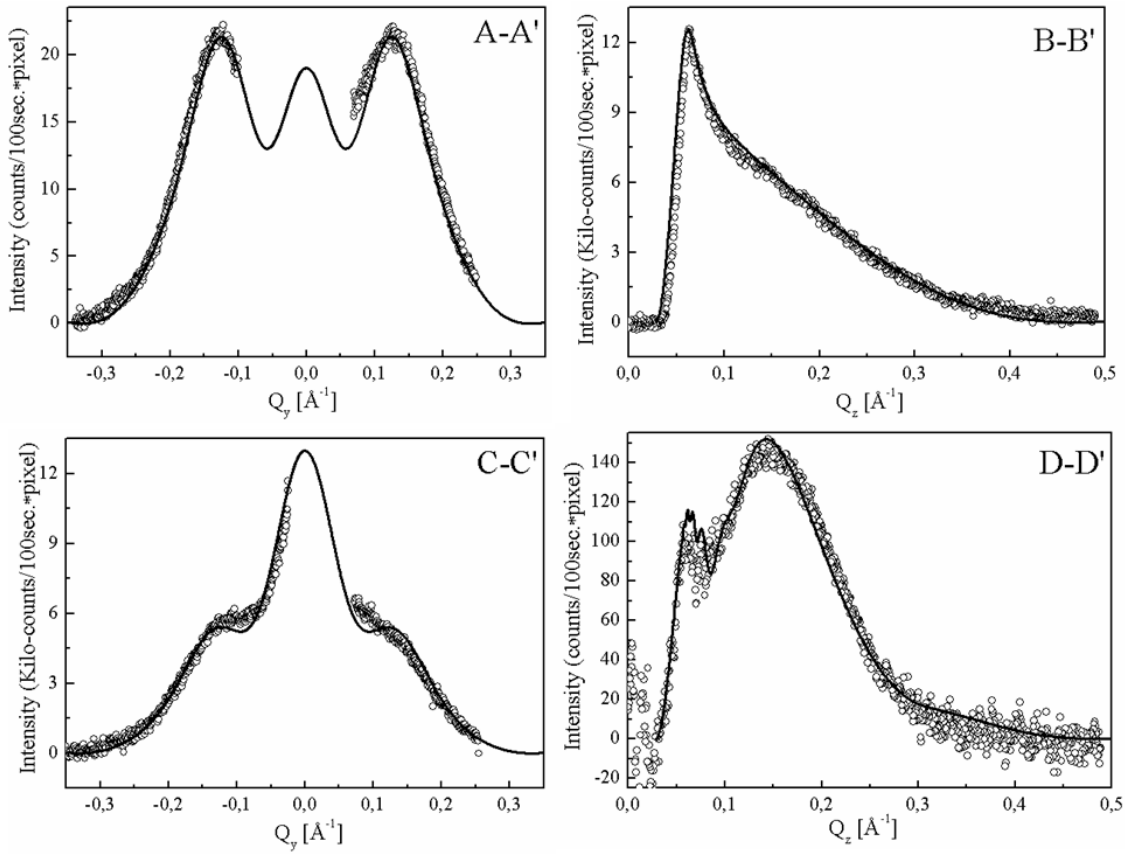

Figure 4.19: *calculated and experimental GISAXS cross sections for 10.8 Å thickness:*
A-A' – best calculated curve is obtained for R_0 = 11.65±0.05 Å and D = 47.7±0.1 Å.
B-B' – the cut-off is best reproduced with: H = 13.4±0.1 Å and taking into account the reflectivity of a layer characterized by a thickness of 32.5±0.5 Å and a roughness of 2.7±0.2 Å. The parameters describing the reflectivity fit very well the other cut-offs, C-C' and D-D'.

B–B', C–C', D–D': These cross sections were treated together because all of them are influenced by the reflectivity signal. From these cross sections we extracted the parameters related with the transmission factor (refraction) for the adsorbed layer: critical angle α_c and absorption coefficient. Due to the disruptive morphology and to the intermixing, the chemical character of the top layer is not well defined and we have to extract these parameters from the calculated cross sections. We found a value for the critical angle α_c of $5.35\pm0.05\times10^{-3}$ rad (0.306°), larger than the one corresponding to the copper substrate of 4.48×10^{-3} rad (0.257°). The calculated absorption coefficient μ is $10.3\pm0.1\times10^{-5}$ Å^{-1}.

Compared with the μ value for copper, μ_{Cu} = 9.39×10^{-6} Å^{-1}, we can conclude that the X-ray scattered intensity is given by the deposited matter (presenting an absorption 10 times higher than copper) and not by the copper substrate. Unfortunately, we can not use these values to determine the chemical nature of the scattering layer because of the strong 3D morphology (leaving therefore vacuum parts in the layer, which have to be taken into account when estimating the density) and of the intermixing between Ni, Cu and O.

The B-B' cross section characterizes also the height of the islands. The best value for the islands height is obtained when in the region between 0.3 and 0.4 Å^{-1} (figure 4.19 B-B') the experimental and the calculated curves are in the best agreement. The value extracted for the 10.8 Å deposit is H = 13.4±0.1 Å.

The scattered spot near the Pb beam-stop (along Q_z) was reproduced considering the reflectivity of a layer with an overall thickness of 32.5±0.5 Å and with a roughness σ = 2.7±0.2 Å. This value (32.5 Å) is large for only 10.8 Å deposited thickness, but confirms well the STM observations, which have evidenced that above ~4 Å the interface is characterized by pyramidal holes composed by different atomic levels with a total height of ~11-12 Å. The calculated value, of 32.5±0.5 Å, reproduces only the position of the scattered spot. In order to reproduce the entire GISAXS pattern (figure 4.20-a), we had to find a suitable shape for the reflectivity in the 3-dimensional reciprocal space (figure 4.20-c). The best agreement between the experimental and the calculated patterns was obtained describing the reflectivity by two dependent Bessel functions: the first one (B_1) is modulated by a width given by a second one (B_2). The amplitude of the B_2 Bessel function is the width of the B_1. A 3-dimensional representation of the as defined reflectivity shape is given in figure 4.20-c. The choice of Bessel functions to describe the reflectivity shape is related with the cylindrical shape of the islands formed on the surface. Many other analytical descriptions were tested but failed.

Summarizing, the morphological parameters for the 10.8 Å film used to reproduce the GISAXS cross sections are:

- *Island shape*: cylindrical, R_0 = 11.65±0.05 Å and H = 13.4±0.1 Å;

- *Correlation length*: D = 47.7±0.1 Å;

- *Surface density* (particle density per surface unit): $r_S = \left(D^2 \cdot \frac{\sqrt{3}}{2} \right)^{-1} = 5.075 \cdot 10^{-4} \text{Å}^{-2}$

- *Reflectivity and transmission*: De = 32.5±0.5 Å, s = 2.7±0.2 Å, a_c = 5.35±0.05×10^{-3} rad, μ = 10.3±0.1×10^{-5} Å^{-1}, B_1, B_2

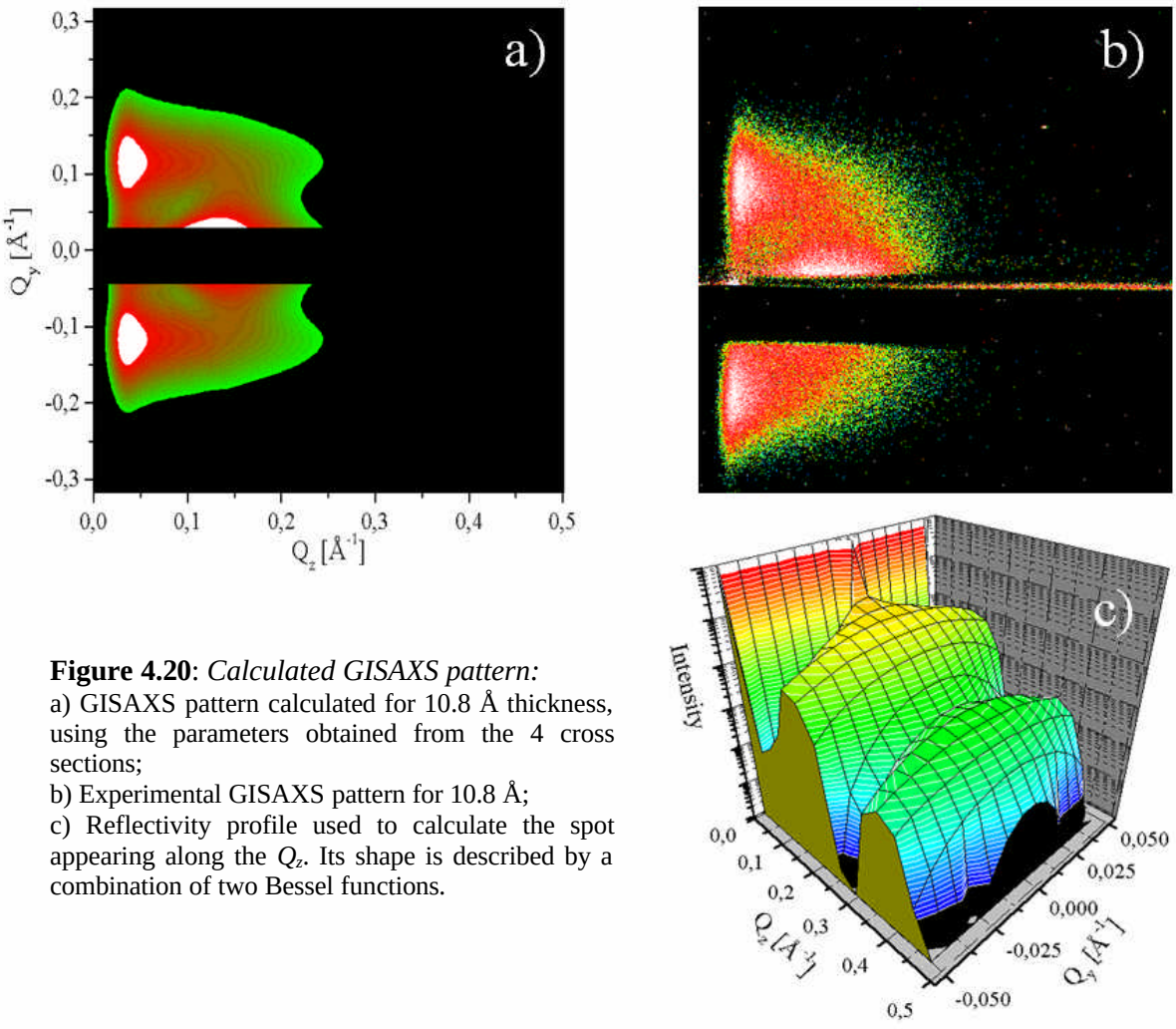

Figure 4.20: *Calculated GISAXS pattern:*
a) GISAXS pattern calculated for 10.8 Å thickness, using the parameters obtained from the 4 cross sections;
b) Experimental GISAXS pattern for 10.8 Å;
c) Reflectivity profile used to calculate the spot appearing along the Q_z. Its shape is described by a combination of two Bessel functions.

Figure 4.20 compares the calculated (a) and experimentally recorded (b) GISAXS patterns for the 10.8 Å NiO film. A slight misalignment between the experimental and the calculated GISAXS patterns can be observed, due to the difference between the origin of the CCD camera and the origin of the reciprocal space which is marked on the calculated image. All the representations are reported in a logarithmic scale.

Using the same procedure, the GISAXS patterns were also calculated for 0.54 and 6.12 Å thicknesses (figure 4.21). In the first case (0.54 Å), relation 4.9 was reduced only to the hole terms (as observed by STM the morphology is characterized only by holes), while in the second case (6.12 Å), we used all the terms, describing therefore a morphology characterized by a mixture of holes and islands. For the thinner film, of 0.54 Å, the GISAXS pattern was reproduced considering a morphology characterized by holes with a radius R_h = 20±2 Å and a depth of H_h = 2.07 Å (the height of one Cu atomic layer) in perfect agreement with the STM values. No correlation length was found between the holes. Therefore, the scattered pattern describes only the holes form factor (P_h). We have to note that the

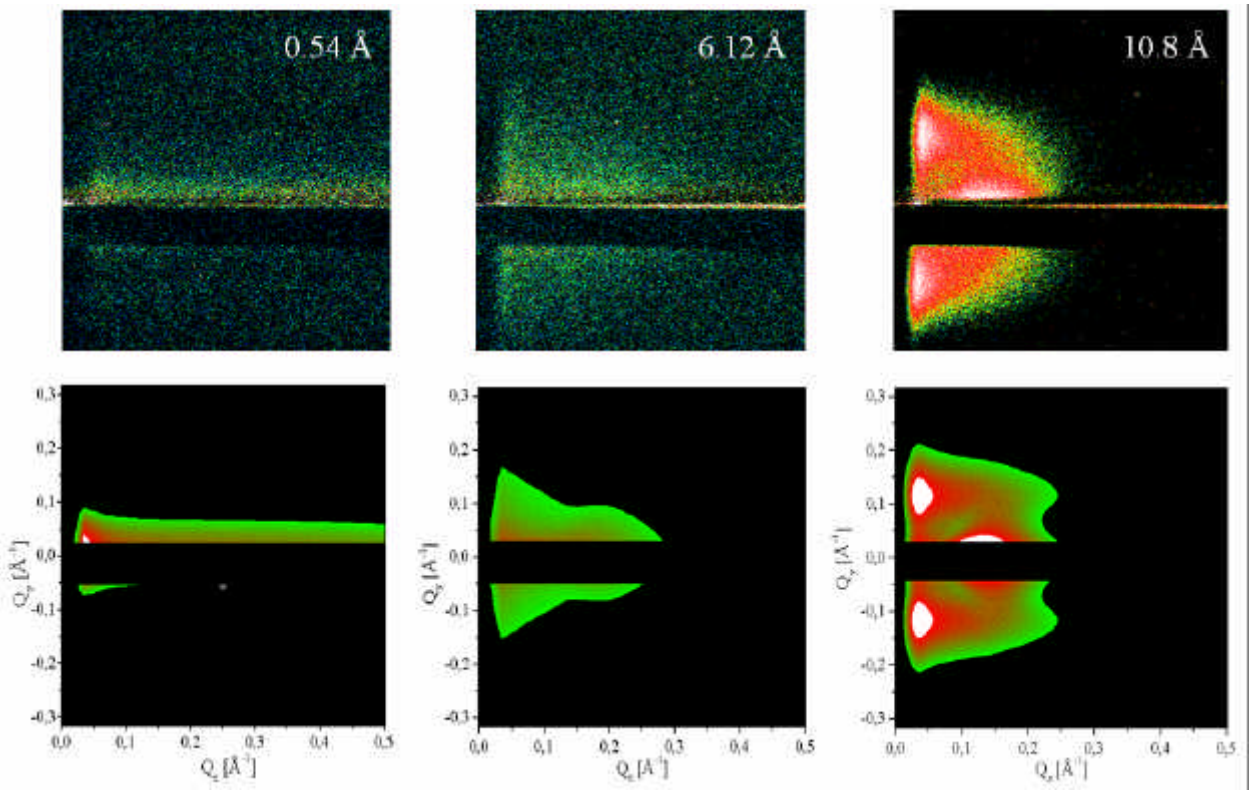

Figure 4.21: *experimental (top) and calculated (bottom) GISAXS patterns for 0.54, 6.12 and 10.8 Å*
The best calculated GISAXS images were obtained for:
♦ 0.54 Å – holes depth of 2.07 Å and holes radius of 20±0.5 Å (no island contribution)
♦ 6.12 Å – combination of holes (radius 23.85±0.05 Å / depth 11.75±0.05 Å) and islands (R_0 = 11.65 ±0.05 Å / D = 47.7±0.1 Å / H = 13.4±0.1 Å / Δe = 24±0.5 Å and σ = 3.2±0.1 Å)
♦ 10.8 Å – islands parameters used to simulate the GISAXS image are given in figure 4.20.

comparatively large error which characterizes this very low thickness is a direct result of the very weak scattered intensity recorded by the CCD camera. The calculated transmission factor revealed that already for this very low coverage regime, the critical angle (a_c) and the absorption coefficient (μ) have the same values as for the 10.8 Å film. This means that the holes observed by STM are not defined only by copper atoms but by the Ni-Cu-O mixture which characterize the thickest films (in fact it is characteristic for the entire thickness range).

Taking into account the differential diffusion process (by direct exchange between Ni and Cu) we may imagine that the Ni atoms are diffused/adsorbed on the hole edges. This process could explain the difference between the trapping probabilities on the step edges and on the hole edges of the Cu adatoms (§4.4). Considering that the Ni atoms diffuses into the hole edges where they would decorate the inside part of the holes, the resulting local surface potential will be modified compared with the surface potential near the step edges. In addition, the substitutional inclusion of the Ni atoms into the hole edges could explain also the

shape and the size of these holes (energetic stabilization of the hole shape), and especially their evolution with the thickness (multiplication process without coalescence).

Contrarily to the very low coverage regime (0-2 Å), at 6.12 Å the GISAXS pattern was reproduced taking into account all the terms in formula 4.10: holes, islands and reflectivity. The best agreement between calculation and experiments was obtained for the following morphological parameters:

- *Holes shape*: cylindrical, R_h = 23.85±0.05 Å and H_h = 11.7±0.1 Å;
- *Correlation length between holes*: none;
- *Island shape*: cylindrical, R_0 = 11.65±0.05 Å and H = 13.4±0.1 Å;

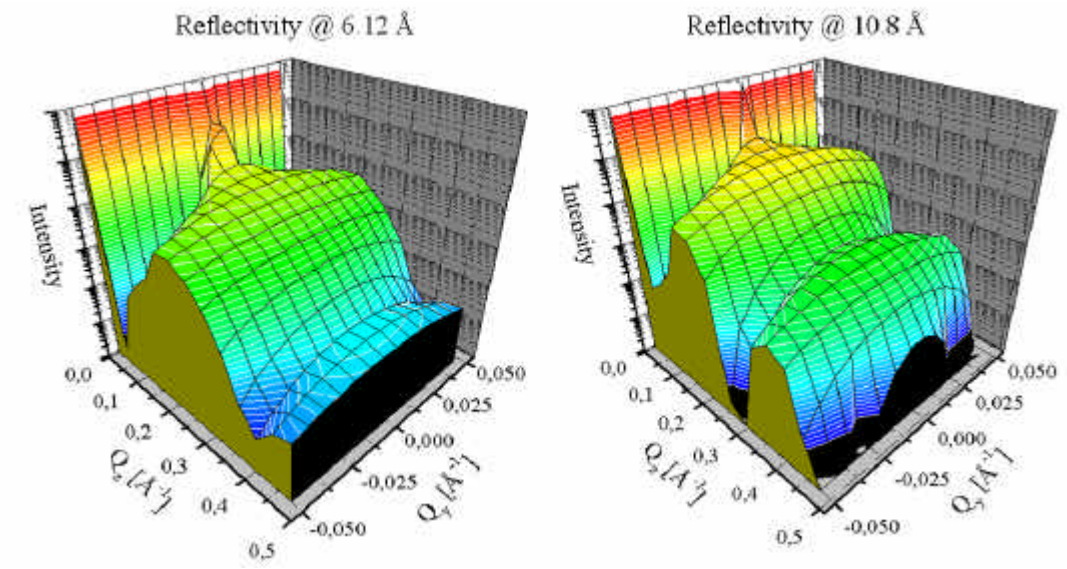

Figure 4.22: *The reflectivity profile for the 6.12 Å (left) and for the 10.8 Å (at right) films*

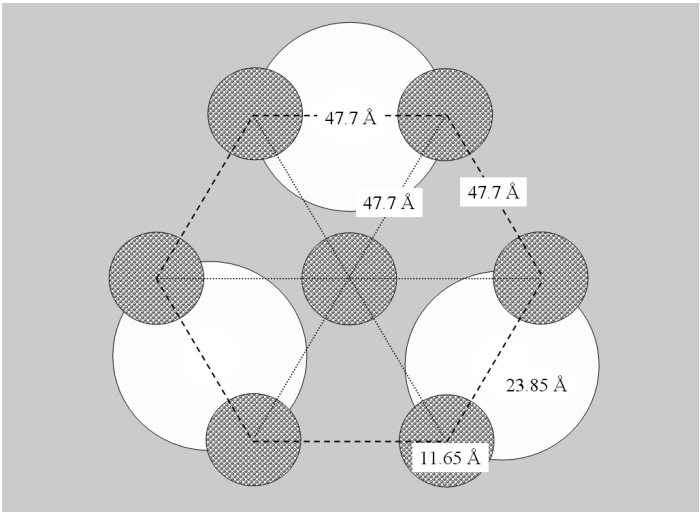

Figure 4.23: *morphological model deduced from the GISAXS simulation: islands self-organization*
The large white circles stand for the holes with 23.85 Å radius formed in the Cu substrate and the dark ones for the islands with 11.65 Å radius. The proposed geometry leads to a correlation between the islands (dark), but no correlation between the holes (white) is supposed to exist. Experimentally no evidence was found for such correlation between holes.

- *Correlation length between islands*: D = 47.7±0.1 Å;

- *Surface density* (particle density per surface unit): $r_S = \left(D^2 \cdot \frac{\sqrt{3}}{2} \right)^{-1} = 5.075 \cdot 10^{-4} \text{Å}^{-2}$

- *Reflectivity and transmission*: De = 24±0.5 Å, s = 3.2±0.2 Å, a_c = 5.35±0.05×10^{-3} rad, μ = 10.3±0.1×10^{-5} Å^{-1}, B'_1, B'_2

Note that for the 6.12 Å thickness, only a combination of the three different contributions could reproduce the cross sections and the entire GISAXS pattern. Even if in the calculations we used a relatively large number of parameters, they are in perfect agreement with the STM observations. In addition all the deduced morphological parameters are coherent one with each other. For example, the depth of the holes is H_h = 11.7±0.1 Å and the height of the islands is H = 13.4±0.1 Å. Therefore, the total thickness of the layer is around the 24-25 Å value which was found to fit the best the reflectivity signal.

Interestingly, the morphology of the islands is identical to the one found at 10.8 Å. The islands are characterized by the same shape, size and correlation length. In addition, they are disposed following the same hexagonal lattice as deduced for the thicker film (same density per surface unit). The differences between the GISAXS patterns comes only from the supplementary holes contribution (at 6.12 Å) and from the different reflectivity profiles, as shown in figure 4.22.

It is important to note that in this thickness range (~4-6 Å) GISAXS is sensitive to the *mean radius* and to the *mean height* of the pyramidal holes. The STM measurements revealed that for the films with ~4 Å thickness the surface is characterized by pyramidal holes with 4-5 atomic levels and a height of ~11-12 Å. Therefore, in this thickness range the pyramidal shape can be reduced to a cylinder characterized by a mean radius of 23.85 Å and a height of 11.7 Å (values calculated from the GISAXS cross sections).

The NiO/Cu(111) is clearly a self-organized system, characterized by islands grown in a regular manner on the surface. Moreover, the GISAXS measurements show an unusual behavior of the film growth: the islands do not modify their shape and size when increasing the thickness above 6 Å (in general the 3D growth is characterized by an evolution of the islands morphology). Furthermore, they have the same density as the one deduced for the thicker films. Therefore, increasing the thickness results only in the increase of the overall thickness of the layer, as suggested by the calculated reflectivity (figure 4.22), without any modification of the islands. In addition, we remark that the radius characterizing the holes (R_h = 28.35 Å) is equal to the half of the correlation distance between the islands (D = 47.7 Å).

Therefore we could imagine that the islands are disposed in average on a hexagonal lattice which is imposed by the holes diameter (47.7 Å), as is schematically drawn in figure 4.23. In this figure, the position of the holes is only hypothetic, but it could explain the absence of any correlation distance between the holes, since they are disposed on non-equivalent crystallographic positions with respect to the islands hexagonal lattice[♣]. In other words, the islands growth on the holes edges which imposes the characteristic correlation length of 47.7 Å between the islands.

☑ *The GISAXS measurements and in particular the calculated GISAXS patterns allow to extract valuable informations which are not accessible with other techniques (STM or GIXD). Taking into account the evolution of the calculated morphological parameters, we can conclude that the NiO/Cu(111) is a* ***self-organized system without substrate patterning****. In the absence of any preferential nucleation sites on the flat Cu(111) surface (steps, dislocations, or particular surface reconstruction as in the case of Au(111)), the holes created in the first stages of the growth reorganize the surface generating thus the necessary nucleation sites for the self-organization.*

[♣] Rotating this unit mesh with ±60° we can reproduce the islands distribution on the hexagonal lattice, but the holes will occupy different positions from one mesh to another.

4.6 RECIPROCAL SPACE – STRUCTURE OF NiO/Cu(111)

The ultra-thin NiO film structure was investigated using *Grazing Incidence X-ray Diffraction* (GIXD) with synchrotron X-ray radiation at ESRF, Grenoble, on the BM32(SUV) beamline. For simplicity, we used the Cu(111) surface unit mesh (hexagonal cell) [Grüb93], derived from the fcc one, as was previously described in §3.4.

Figure 4.24 shows the reciprocal space for an ideal epitaxy between NiO(111) and Cu(111). For a better visualization, we chose to split the 3D reciprocal space in two cut-offs: along the ($h0\ell$) and ($hh\ell$) planes, respectively. The reciprocal space positions of the Bragg reflections are given by the generalized reflections rules which apply for the fcc *Fm3m* space group. Since the NiO lattice parameters are 15% larger than the Cu(111) one, their position in the reciprocal space will be characterized by smaller distances compared to the Cu(111) ones.

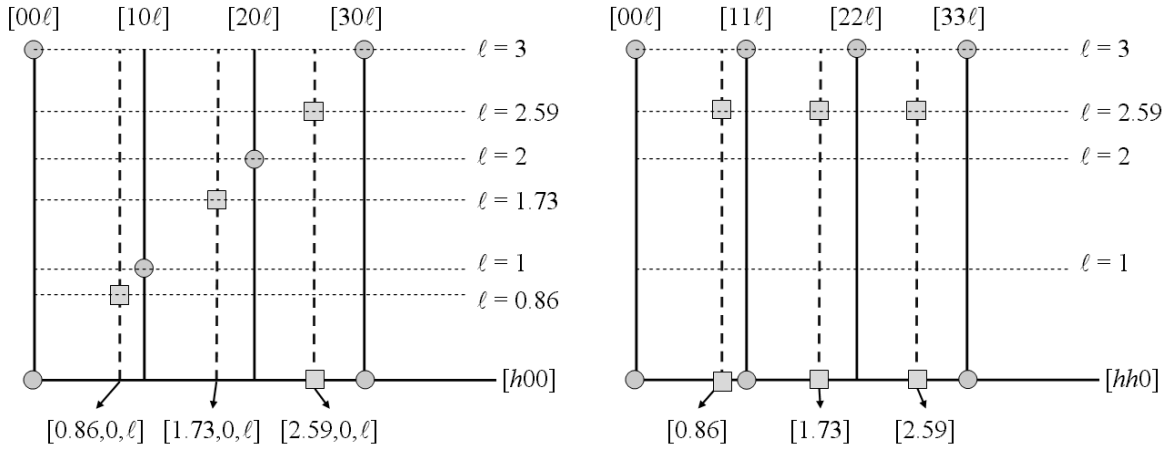

Figure 4.24: *NiO(111)/Cu(111) reciprocal space:*
Upper side, the ($h0\ell$) cut-off and the bottom side, the ($hh\ell$) cut-off are shown. The representation is made in the Cu(111) reciprocal lattice units taking into account the bulk NiO characteristic lattice parameters.

Therefore, for a fully relaxed NiO(111) lattice, the expected positions along the [$h0\ell$] and the [$hh\ell$] directions are at $h = 0.86 \times i$ with i integer, in the Cu(111) reciprocal lattice units.

Large in-plane scans (from h = 0 to h = 3.5) along the [$h0\ell$] and the [$hh\ell$] directions were recorded for the whole thickness range, from 0 to 12 Å. Apart the Cu(111) specific Bragg peaks and rods, no supplementary reflections were observed. Thus no ordered NiO is formed on the surface. Therefore, the NiO(111) p(2×2) reconstruction-like structure observed by STM measurements, is a very local feature of the surface ordering, with an extent well below the coherence length necessary for diffraction to occur. The evolution of the Cu(111) rods (figure 4.26-c, (01ℓ) rod) as a function of the thickness is characterized by a strong and

asymmetric diffracted intensity decrease, related with surface roughening, as already suggested by STM (hole formation and substrate roughening). The out-of-plane scans (perpendicular to the surface) are characterized by the same absence of the expected reflections corresponding to NiO ordered structure. Therefore, we conclude that the NiO grown on the Cu(111) surface at room temperature shows no long range order.

The integration of the crystal truncation rods (CTRs) [Robi91, Robi86] of Cu(111) was performed through rocking scans around the direction perpendicular to the surface. The result for each ℓ point was then corrected for monitor, background, sample area, Lorentz and polarization factors [Vlie98]. Figure 4.26-c presents the Cu(111) (01ℓ) rod obtained for several NiO deposits in the 0 – 12 Å thickness range. Both experimental data and best fits are presented.

Either a substrate roughening or an interference due to foreign atoms included in the Cu lattice may be responsible for the strong decrease of the signal along the CTRs. Assuming a surface structure model including 3 atomic layers (figure 4.25), a description of the experimental data only in terms of substrate surface topographic roughening [Robi91] was unable to reproduce (figure 4.26-a) the clear interference point at ℓ = 0 in reciprocal lattice units (r.l.u.) although the overall signal reduction could be simulated.

A second attempt to reproduce the measured data was done taking into account substitutional Ni diffusion in Cu crystallographic sites. From a practical point of view, the substitutional Ni quantity is described by the *occupancy* parameter, which gives the quantity of foreign atoms lying in the considered structure.

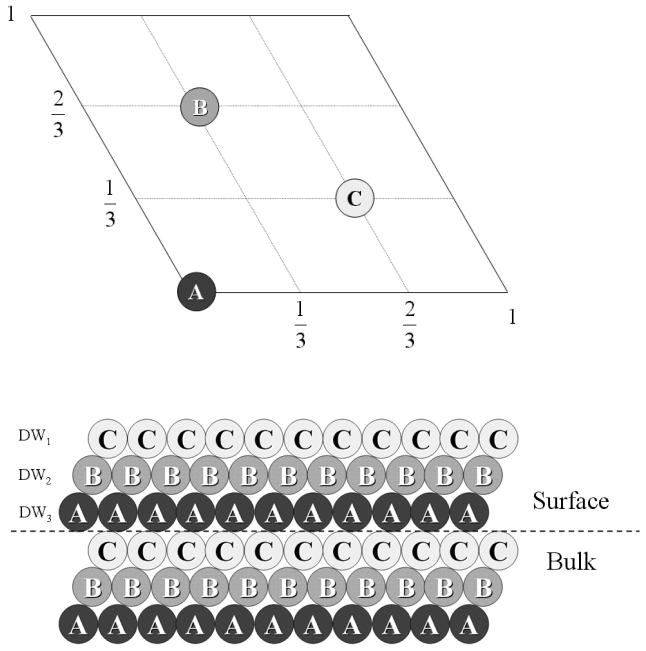

Figure 4.25: *ABCAB … fcc stacking and fitting parameters:*
Only copper atoms are represented in the fcc stacking. In the upper part of the figure the Cu(111) unit cell is described with the position of B and C atoms projected in the A plane.

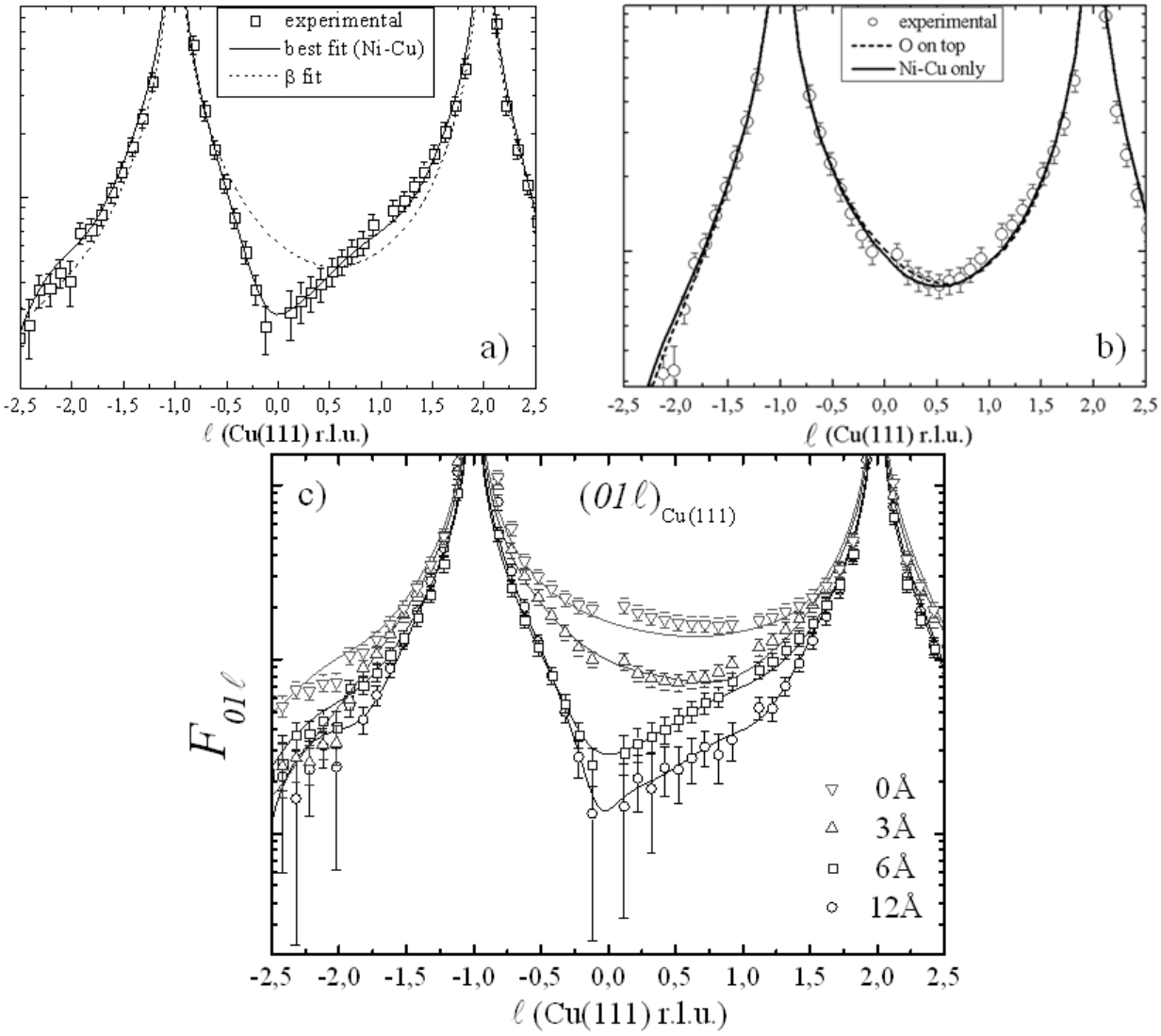

Figure 4.26: *(01ℓ) – Cu(111) crystal truncation rod (CTR) evolution function of thickness:*
a) topographic roughness (*b*) model fit (6 Å NiO thickness);
b) influence of the on-top O atoms in the structural model fit (3 Å NiO thickness);
c) Four thicknesses are presented from 0 to 12Å. Symbols stand for the measured intensity (after integration of the rocking scans and corrections) and the continuous lines are the best fits using the model described in the text.

This description can be understood as a chemical roughening and provides good CTRs shapes, but an interference point at ℓ = 0.5 r.l.u.. Since the interference point in the experimental data is at ℓ = 0 r.l.u., the assumption that the Ni atoms occupy the Cu sites is not fully satisfactory. In order to overcome this discrepancy, we had to introduce a fraction of Ni atoms sitting in twinned sites (Ni R60°) that corresponds to fcc stacking faults. Thus our final model assumes that each layer contains a fraction of Ni atoms occupying exact and twinned Cu(111) sites. Note that in conformity with STM results, for low thicknesses (< 3 Å), oxygen

atoms are present on the surface. Our final structural model does not take into account the oxygen atoms, due to their very weak influence[†] on the diffracted intensity (figure 4.26-b).

Table 4.1 gives the values of the proportion of Ni and Ni R60° in the different layers corresponding to the best fits (figure 4.26-c). Taking into account the structural disorder of the

thickness (Å)	1st atomic layer (C)			2nd atomic layer (B)			3rd atomic layer (A)		
	Ni	Ni R60°	DW	Ni	Ni R60°	DW	Ni	Ni R60°	DW
0	0 %	0 %	12.75	0 %	0 %	5.43	0 %	0 %	2.53
3	25 %	4 %	14.65	2 %	0 %	4.58	0 %	0 %	1.62
6	56 %	20 %	7.05	15 %	0 %	2.95	0 %	0 %	1.45
12	70 %	9 %	3.22	30 %	0 %	1.25	0 %	0 %	2.05

Table 4.1: *atomic composition of the NiO/Cu(111) interface layers (from GIXD measurements)*: Besides Ni and NiR60° composition for each layer, we present also the Debye-Waller factors as extracted from the ROD program [ana-rod].

NiO film, our description applies to the interface layers belonging to the Cu(111) lattice only.

Therefore, even for large thicknesses (6 Å – 12 Å) the diffraction measurements and the proposed model are always sensitive to the same interface layers, that is the outermost Cu(111) layers. Interestingly, the Debye-Waller[♣] (DW) values decrease when increasing the NiO thickness. This can nicely be understood considering that the probed layers are deeper when increasing the thickness. The agreement between the experimental CTRs and the best fits is very good for all investigated thicknesses.

The global Ni and faulted Ni quantities increase (Table 4.1) with thickness showing that Ni diffusion into the Cu substrate is active even for relatively large thicknesses, *viz.* above 6Å. In the top-most plane, while the Ni proportion increases steadily with thickness from 0% to 70% (for the 12 Å NiO film), the faulted Ni proportion presents a maximum of 20% at 6 Å NiO thickness and decreases strongly to 9% at 12 Å NiO. This is not surprising since the increase of the unfaulted Ni fraction will proportionally reduce the faulted Ni quantity. The second layer is characterized only by the presence of unfaulted Ni, its amount

[†] The diffracted intensity is directly proportional with the square of the atomic number, *Z*. For O, *Z* = 8 while for Cu, *Z* = 29.

[♣] The Debye-Waller coefficients characterize the oscillatory atoms motion around the equilibrium position, whereas the atom position in the unit cell.

increasing with thickness. For all NiO films studied in the present work, the Ni diffusion remains however always limited to the sub-surface Cu(111) layer. Moreover the Ni diffusion process found through GIXD is able to quantitatively explain the measured AES intensities for Cu, Ni and O, strongly supporting our differential diffusion model.

Within a simple estimation for the 3 Å and 6 Å situations in table 4.1, we observe that not all the Ni atoms are incorporated in the Cu(111) lattice. The XPS measurements revealed that in this thickness range approximatively 80% of the deposit is metallic Ni (~2.4 Å metallic Ni for the 3 Å thickness), which can not be found entirely diffused in the Cu(111) substrate (for the 3 Å thickness, only 0.6 Å metallic Ni was found to be diffused on the Cu(111) lattice sites). Therefore, there is a fraction of metallic Ni formed in the disordered top layer, i.e. NiO + Ni (figure 4.27-b), and/or diffused in the substrate (but not on Cu(111) sites).

☑ *Quantitative GIXD analysis allowed calculating the differential diffusion magnitude. Unfaulted and faulted Ni occupies Cu sites at the interface, their quantity varying as a function of the NiO thickness. For the thickest film (12 Å) an entire Ni atomic layer is incorporated in the Cu substrate, giving rise to the NiO/Ni/Cu(111) layering.*

In the following we present the quantitative estimation of the AES Cu intensity for three different thicknesses: 3, 6 and 12 Å. Figure 4.28-a shows the evolution of the Ni atomic fraction present by substitution in the Cu layers, as described above by GIXD in the proposed interface model. To simplify the representation, the overall Ni and NiR60° atomic composition is drawn. Taking into account the schematic drawing presented in figure 4.27-b, we can write the Cu Auger intensity as a sum of several contributions:

$$I_{Cu} = I_{bulk} + I_A + I_B + I_C \qquad (4.12)$$

where: I_{bulk} is the Auger signal coming from the Cu substrate, and I_A, I_B, I_C stand for the contribution in the AES signal of the Cu atoms laying in the A, B and C layer, respectively (figure 4.28-b). For simplicity, we consider that the height of one atomic Ni or Cu plane is identical and equal to 2 Å:

$$\begin{cases} I_{bulk} = I_0 \times e^{-\frac{d'+3\cdot 2}{l\cdot\cos(q)}} \\ I_A = I_1 \times c_A \times e^{-\frac{d'+2\cdot 2}{l\cdot\cos(q)}} \\ I_B = I_1 \times c_B \times e^{-\frac{d'+2}{l\cdot\cos(q)}} \\ I_C = I_1 \times c_C \times e^{-\frac{d'}{l\cdot\cos(q)}} \end{cases} \quad (4.13)$$

where: I_0 – the Auger intensity corresponding to clean Cu substrate (without adsorbate), I_1 – the Auger intensity given by one Cu atomic layer, d' – the thickness of the mixed Ni + NiO

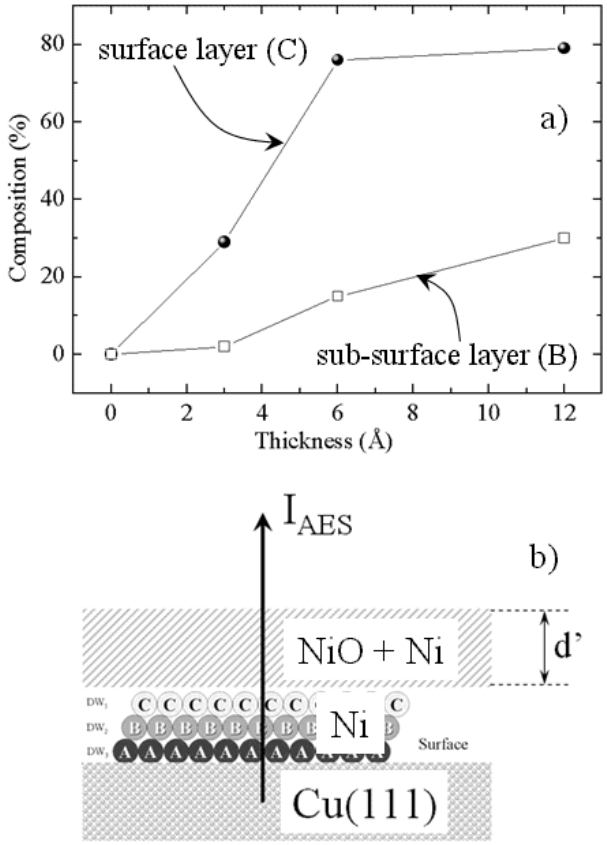

Figure 4.27:
a) Evolution of the interface layers composition as a function of the thickness. The curves describe the sum of Ni and NiR60° fractions.
b) Model describing the Cu substrate AES intensity attenuation through the metallic Ni interface and the disordered (NiO + Ni) layer of thickness d'.

top layer, l - the inelastic mean free path of the Auger electrons (10 Å), $cos(q)$ – the CMA angular acceptance ($cosq$ = 0.82), and c_A, c_B, c_C are the Cu concentration in each of the three interface layers A, B and C respectively. I_0, c_A, c_B, c_C are determined experimentally and I_1 can be calculated writing the I_0 intensity as the contribution of all Cu atomic layers in the crystal (thickness of one Cu atomic plane = 2Å):

$$I_0 = I_1 + I_1 \times e^{-\frac{1\cdot 2}{l\cdot\cos(q)}} + I_1 \times e^{-\frac{2\cdot 2}{l\cdot\cos(q)}} + I_1 \times e^{-\frac{3\cdot 2}{l\cdot\cos(q)}} + \ldots = I_1 \times \sum_{n=0}^{\infty} e^{-\frac{n\cdot 2}{l\cdot\cos(q)}}$$

$$\Rightarrow I_1 = I_0 \times \left(1 - e^{-\frac{2}{l\cdot\cos(q)}}\right) \qquad (4.14)$$

thickness (layer-by-layer) (Å)	**d' (Å)**	**$d_{Ni} = (c_B + c_C)\,´\,2$Å (Å)**	**thickness d' + d_{Ni} (Å)**	**error (%)**
3	3.87	0.6	**4.47**	33 %
6	5.32	1.8	**7.12**	15 %
12	9.53	2.2	**11.73**	2 %

Table 4.2: *Quantitative estimation of the AES intensity for the Cu substrate*:
The *d'* values were deduced using the 4.12 formula and the d_{Ni} values are calculated as shown in the table.

In this way we can estimate the thickness of the deposited NiO films and compare it with the layer-by-layer approximation used till this point, pointing out the errors affecting our thickness calibration. In table 4.2 we present the calculated equivalent thickness for 3, 6 and 12 Å, with the corresponding error. The thinnest films are the most influenced by the layer-by-layer reduction. The large difference between the intensities for the layer-by-layer growth estimation and the calculated ones in the very low coverage regime is normal in the case of Ni diffusion. The layer-by-layer approximation underestimates the adsorbate quantity, neglecting the diffused matter, and as it can be observed in table 4.2 the 3 Å equivalent thickness NiO film (layer-by-layer estimation) has actually $d' + d_{Ni} = 4.47$ Å. For larger thicknesses, the error diminishes since the topmost disordered layer thickness (*d'*) increases and the diffused interface contribution fall off.

☑ *In conclusion, using the quantitative determination of the differential diffusion process, we can refine the thickness calibration on the one hand, and quantify the oxidized fraction, on the other hand. As a general remark, we observe that both AES and XPS measure stoichiometric NiO for large thicknesses (> 25 Å), where the photoelectron-diffraction effects can be neglected.*

4.7 NiO/FeNi/Cu(111) BILAYER GROWTH

In order to artificially introduce uniaxial anisotropy for the ferromagnetic FeNi film, a *vicinal* Cu(111) substrate was used, cut along the $[11\bar{2}]$ crystallographic direction with a miscut angle of 1.2° (as shown in §3.2). The evolution of the FeNi morphology follows a typical step-flow growth, with specific step decoration from the first stages of the growth [CherPhD]. As shown by Cherifi et al. [Cher01b], the 3.5 ML film induces the largest magnetocrystalline anisotropy and the easy magnetization axis is in the plane oriented at ~45° with respect to the $[1\bar{1}0]$ step direction.

The magnetism of the FeNi nanostructures was found to be very sensitive to strains, related with structure relaxation function of the thickness. The magnetic coupling and the anisotropy of the NiO/FeNi bilayer is therefore expected to depend strongly on morphology and on the structure of the FeNi and NiO films, especially for small thicknesses [Cher01b] of the ferromagnetic (FeNi) layer. Therefore we chose to study the growth of the antiferromagnetic NiO on ultra-thin FeNi ferromagnetic films (3 – 20 Å) deposited on the vicinal Cu(111) substrate.

The STM images are presented in figure 4.28-a and 4.28-b. Stripes are formed along the step edges (~10 nm wide terraces) by depositing the ferromagnetic alloy (figure 4.29-a).

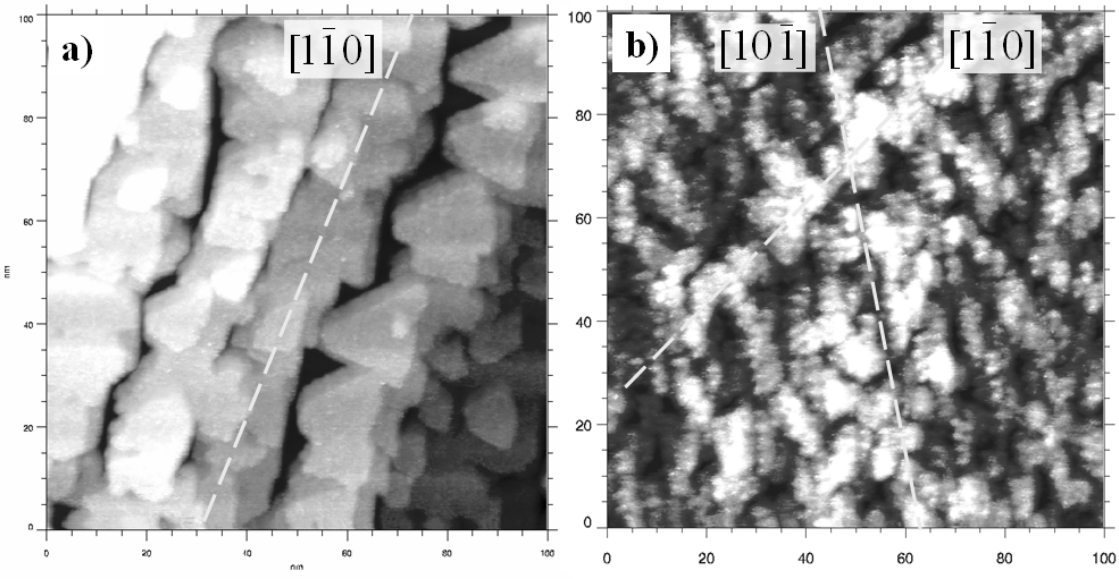

Figure 4.28: *NiO/FeNi/Cu(111)-1.2° miscut exchange coupled bilayer morphology (1):*
a) 7.5 Å thickness FeNi/Cu(111); U = 0.18 V and I = 0.12 nA; we remark the step-flow growth with the FeNi alloy ribbons aligned along the Cu(111) step directions, i.e. [1-10].
b) 3 Å NiO deposited on the FeNi alloy shown in a); U = -0.3 V and I = 0.14 nA; the NiO film is textured following the [10-1] direction, at 60° relative to the Cu(111) steps directions. The scale of both STM images is 100×100 nm^2.

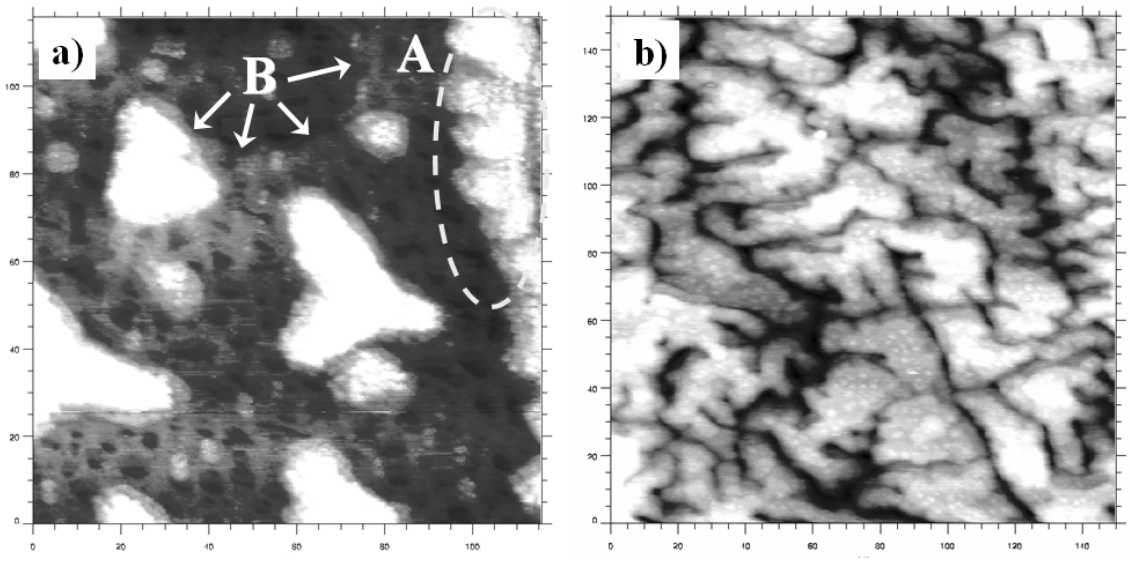

Figure 4.29: *NiO/FeNi/Cu(111)-1.2° miscut exchange coupled bilayer morphology (2):*
a) **NiO(1.5Å)/FeNi(3Å)/Cu(111)**; 115×115 nm^2, U = -0.36 V, I = 0.13 nA. The A region stress the NiO texturing on the FeNi islands. We remark also the disrupted NiO/Cu(111) interface.
b) **NiO(0.5Å)/FeNi(20Å)/Cu(111)**; 150×150 nm^2, U = -0.36 V, I = 0.12 nA. NiO appears as a granularity without special ordering.

Remark that actually these stripes are formed by the percolation of the FeNi islands grown at the step edges. Their mean width is of about 20 nm and the measured minimum to maximum height is of about 15 Å. It is important to mention that this value of 15 Å characterizes not only the height of the FeNi islands, but it includes also the depth of the copper vacancy from the topmost atomic plane which diffuses with the tendency to cover the FeNi islands.

The directly deposited NiO film (3 Å) presents a texture along the $[10\bar{1}]$ direction, at 60° with respect to the Cu(111) step direction (figure 4.28-b) – marked by the line along the $[1\bar{1}0]$ direction). In figure 4.29-a we observe the same texturing on the stripes formed along the step edges (zone marked with A), for terraces wider than ~1000 Å (FeNi thickness of ~3 Å). In this case, there is a large non-covered Cu(111) surface, which presents the disrupted morphology characterized by hole formation (~40 Å diameter), as observed in the case of direct NiO evaporation on Cu(111). We have to note also the presence of very large, monatomic deep holes (B) formed during the ferromagnetic alloy deposition. The formation of such holes is a common behavior and characterize generally the metal/Cu(111) systems [Cher01a, Cher01b, Kief93, Figu94, Boeg01].

Interestingly, the NiO/FeNi interface, seems to be sharper compared to the NiO/Cu(111) one. No holes can be observed, e.g. in figure 4.29-b where the FeNi thickness (> 20 Å) ensure the complete copper substrate covering. In addition, there are is no sign of interdiffusion: for 0.5 Å equivalent thickness the apparent covered surface with NiO

measured on the STM images correspond exactly to 0.5 Å (small, one atomic layer high islands, ~20 Å width). There is no particular ordering of the NiO islands for this thickness, but the islands have the same width, i.e. ~20 Å, as for the other NiO thicknesses studied here (1.5 and 3 Å). Note that the NiO island size (~12 Å radius) grown on FeNi corresponds with the values calculated by GISAXS (§4.5).

These few preliminary morphologic results are very encouraging: the NiO/FeNi interface is sharp, without the characteristic disruptive growth observed in the case of NiO/Cu(111). Furthermore, the NiO texturing along well defined crystallographic direction can be an indication of structural ordering at room temperature. However, at this point there are not any structural investigations (LEED or GIXD) to confirm the structural ordering.

The STM image in figure 4.29-a clearly shows the importance of studying the NiO/Cu(111) interface in the case of the spin-valves systems. Since the FeNi alloy has a 3D growth, there will be always uncovered copper parts where a NiO/Cu(111) interface is formed by MBE deposition.

☑ *Preliminarily studies on the bilayered NiO/FeNi/Cu(111) system evidenced a strong texturing along the* $[10\bar{1}]$ *crystallographic direction. The NiO/FeNi interface is sharp, contrary to the specific disrupted growth which characterize the NiO/Cu(111) interface. Interestingly, the NiO island size (~12 Å) formed on the FeNi alloys, is similar to the one calculated by GISAXS for the NiO/Cu(111) growth.*

4.8 CONCLUSIONS

Full description of the growth is given for the NiO films evaporated at room temperature on the Cu(111) single crystal substrate. The surface and interface chemistry is governed by the *differential diffusion* of the Ni atoms in the Cu substrate, while O atoms remain on top in the early stages of growth. Qualitatively suggested by spectroscopic measurements (AES and XPS), the differential diffusion process was successfully quantified using the surface diffraction technique. The diffused Ni quantity increases with the NiO thickness, giving rise to the formation of a Ni metallic layer at the interface. For large thicknesses (> 25 Å), stoichiometric NiO was evidenced. Therefore, our system can be characterized by NiO/Ni/Cu(111) layering, where one equivalent Ni atomic layer is buried at the interface. A spectacular morphology was observed by STM in the first stages of the

growth. Hole *nucleation* and *multiplication* characterize the very low coverage regime (0-2 Å). This behavior was explained taking into account the same differential diffusion process *via* a *direct exchange mechanism* between Ni and Cu atoms, promoted by the surfactant oxygen. Islands of typically 12 Å radius characterizes the high NiO film coverage. Small angle X-rays scattering (GISAXS) patterns calculations allowed to confirm the local STM observations (e.g. hole diameter of ~40 Å) and to evidence the *self-organized* nature of the NiO/Cu(111) system. Although organized at nanometric scale (~5 nm), the NiO ultra-thin films deposited at room temperature present no long-range crystallographic order, as evidenced by LEED and GIXD measurements. First STM studies on the NiO/FeNi/Cu(111) bilayered system revealed the formation of a sharp NiO/FeNi interface, contrary to the disrupted NiO/Cu(111) interface. Moreover, the NiO film texturing suggests the possible crystalline ordering of the NiO films deposited at room temperature, identifying the NiO MBE nuggets evaporation as a feasible method for the coupled-exchange bilayer elaboration, avoiding the oxidation of the ferromagnetic layer.

Chapter 5:

TEMPERATURE EFFECTS

5.1 TEMPERATURE EFFECTS ON NiO/Cu(111)

In order to improve the structural quality of the NiO films elaborated from NiO nuggets, several samples were made varying the substrate temperature or by post-deposition annealing.

5.1.1 Annealing of the NiO films

A first attempt was performed by annealing a room temperature elaborated NiO film in order to enhance the crystalline quality. A major issue during such treatments is the chemical stability of the layer, in particular when several species are present. Figure 5.1 shows the evolution of the AES spectrum recorded for a 5 Å NiO film, before and after annealing. Two successive treatments were applied: a first annealing at 200°C for 10 minutes, followed by a second one at 300°C for 10 minutes. No change of the Auger peaks intensity after annealing could be observed (figure 5.1). Since neither the I_O/I_{Ni} nor I_{Cu}/I_{Ni} ratio changes after

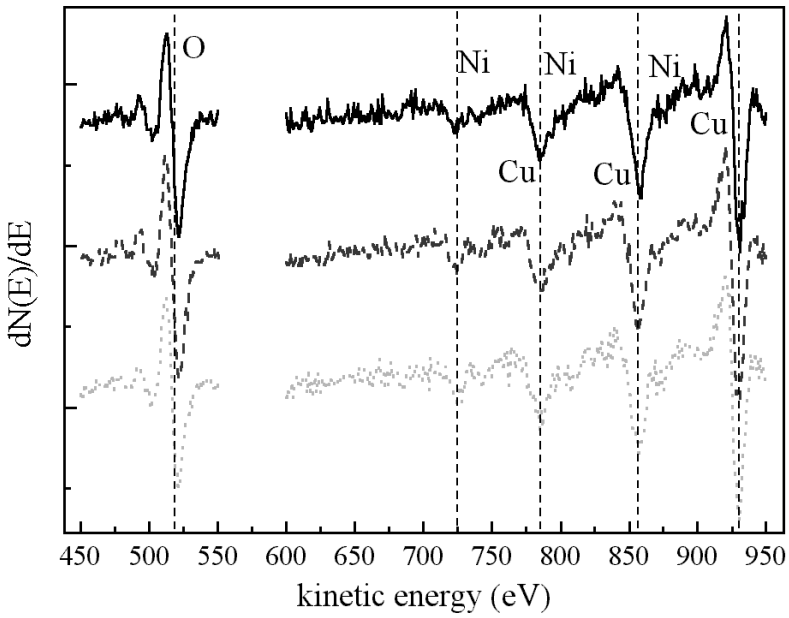

Figure 5.1:
AES spectra recorded for 5 Å equivalent NiO film elaborated at R.T. for different annealing temperatures: (—) NiO deposited at R.T., (---) annealing at 200°C, (????) annealing at 300°C. A factor ½ was applied to the oxygen AES intensity to correct the relative AES sensitivity between O and Ni.

annealing, we can safely conclude that the average stoichiometry is preserved and that the room temperature differential diffusion is not affected by a post-deposition annealing, i.e. the system has already reached its thermodynamic stable configuration. As a matter of fact Ni and Cu are immiscible, the temperature increase can only lead to a dissolution process, without alloying, and higher temperatures are required for the dissolution process (typical dissolution temperature for the Ni/Cu system is of about 450-550°C [Aufr01, Erde02]). As a

consequence, by heating the sample we expect only surface morphology modifications and recrystallization, due to the enhanced surface diffusion.

Therefore, we can conclude that the NiO/Ni/Cu(111) layering is not modified up to 300°C.

The structural investigations were performed by LEED (Low Energy Electron Diffraction) to control the crystallographic changes upon annealing.

Before annealing, the LEED cliché (not shown) presents only a fuzzy (diffuse) background related to the absence of the long-range crystallographic order. Figure 5.2-b presents the LEED pattern of the room temperature deposited NiO film (5 Å) after annealing at 300°C. For comparison we present also the diffraction pattern of clean Cu(111) (figure 5.2-a). As a guide for eyes, the LEED diagrams are schematically drawn below the experimental patterns. The Cu(111) surface (figure 5.2-a) shows the specific 6-fold symmetry of the (111) fcc surface, with brighter spots alternating with less intense ones at 120° apart. After annealing at 300°C during 10 minutes, we observe weak and fuzzy spots (figure 5.2-b). As shown in the corresponding schematic drawing, we can identify a 6-fold symmetry related to

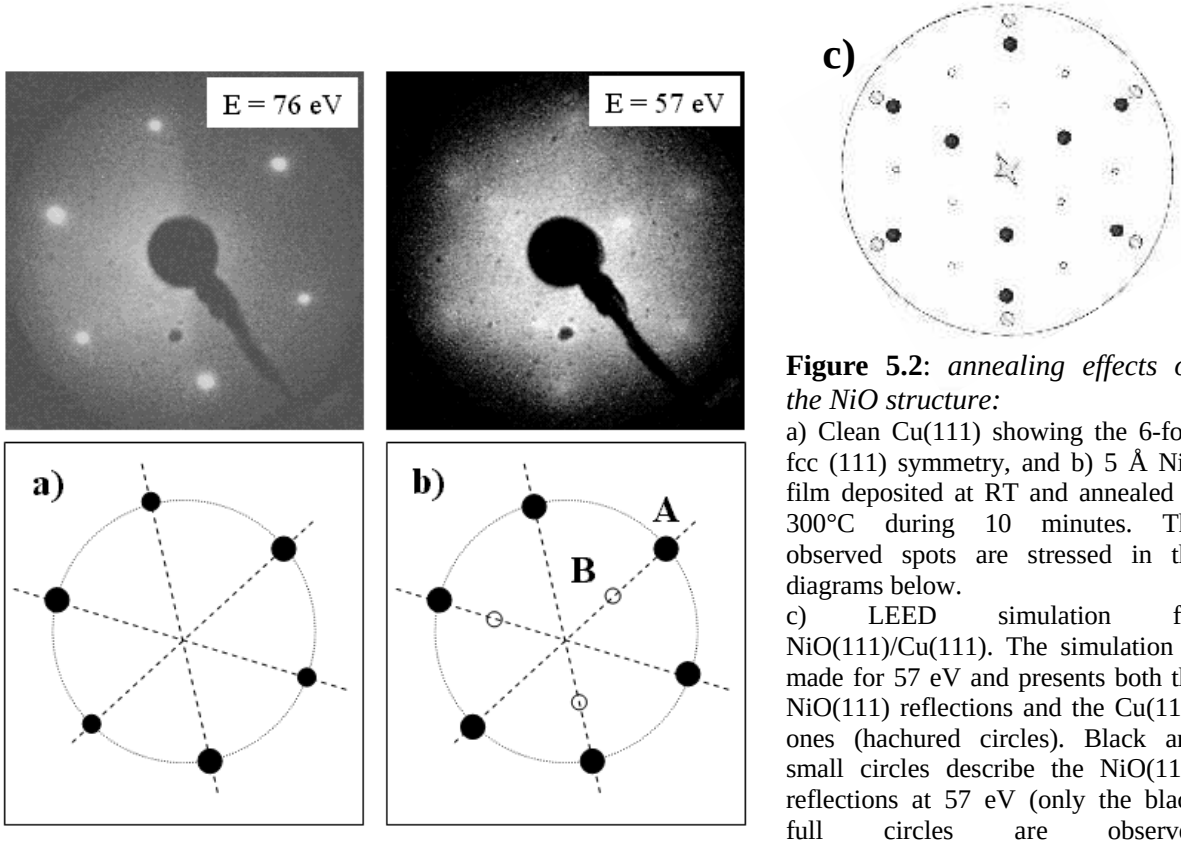

Figure 5.2: *annealing effects on the NiO structure:*
a) Clean Cu(111) showing the 6-fold fcc (111) symmetry, and b) 5 Å NiO film deposited at RT and annealed at 300°C during 10 minutes. The observed spots are stressed in the diagrams below.
c) LEED simulation for NiO(111)/Cu(111). The simulation is made for 57 eV and presents both the NiO(111) reflections and the Cu(111) ones (hachured circles). Black and small circles describe the NiO(111) reflections at 57 eV (only the black full circles are observed experimentally).

fcc (111) structures (black filled circles). In addition, three spots appear at half of their distance taken from the origin of the LEED diagram, given in the schematic drawing by small open circles. Simulating the LEED spots for the NiO(111)/Cu(111) epitaxy, we can reproduce the observed reflections (figure 5.2-c). In the simulated LEED cliché we reproduced also spots that are not visible in the experimental diagram: those corresponding to the Cu(111) substrate (hachured ones) and spots which belong to the NiO(111) structure (small circles) that are not observed experimentally probably due to the strong diffused background. The absence of the reflections corresponding to the Cu(111) substrate is obvious if we take into account the small value of the electron energy (57eV) and the thickness of the film (5 Å)

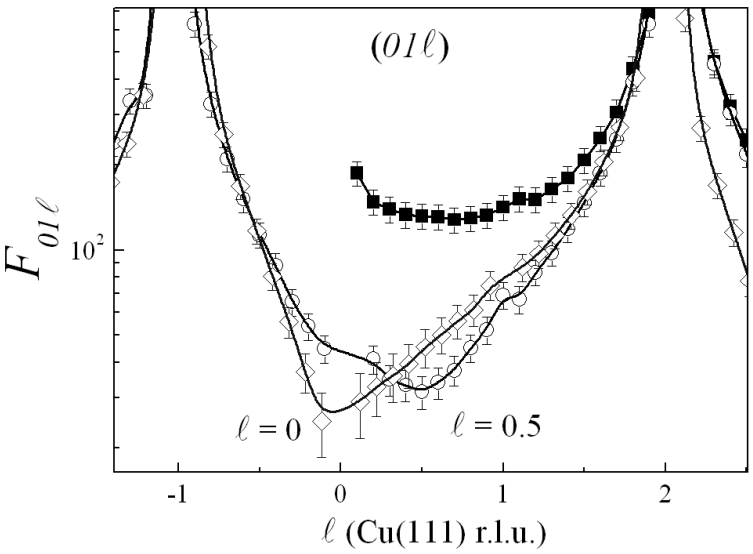

Figure 5.3: *structural changes after annealing by GIXD:*
(—■—) clean Cu(111) (01ℓ) crystal truncation rod (CTR);
(—◇—) 5 Å NiO deposited at R.T.;
(—○—) 5 Å NiO annealed at 300°C for 10 minutes.

completely covering the substrate. Since the AES spectrum indicates that the relative proportion between NiO and Cu is the same before and after annealing it implies that the NiO film fractioning[♣] after annealing can be excluded. Importantly, we obtain only a poorly visible LEED pattern for 57 eV energy with a strong diffused background, the obtained crystalline quality remains thus very poor. Small crystalline grains form in the NiO layer that are sufficiently large to uphold the coherence width condition for the LEED reflections to appear (coherence width of ~300Å).

The surface diffraction (GIXD) measurements confirm that the crystalline quality of the NiO film is not dramatically improved after annealing. In figure 5.3 we compare the (*01*ℓ) CTR before and after annealing at 300°C during 10 minutes for a 5 Å thick NiO film. We observe that the overall shape is the same in both cases. Since this shape is related to the Ni quantity diffused on Cu(111) sites (§4.6), we can conclude that by post-deposition annealing

[♣] In the hypothesis of the NiO film fractioning, there will be uncovered parts of the Cu(111) substrate, which could give reflections on the LEED cliché.

the diffused metallic Ni quantity is preserved, confirming the AES observations. However, the interference point along the (*01*ℓ) CTR changes from ℓ = 0 to ℓ = 0.5. This characterizes the formation of *only* unfaulted metallic Ni (following the Cu(111) stacking). Therefore, the NiO film annealing at 300°C results in a rearrangement of the Ni atoms diffused in the Cu(111) substrate, the faulted Ni quantity obtained by deposition at R.T. occupying after annealing unfaulted Cu(111) crystallographic sites. The presence of faulted Ni after R.T. growth (§4.6) is thus linked to a kinetic limitation.

☑ *We can conclude that the annealing of the NiO film yields in the formation of small crystalline grains inside the NiO layer and produces a rearrangement of the Ni atoms diffused in Cu sites, without a change in the composition of the NiO/Ni/Cu(111) layering.*

5.1.2 Growth of NiO films at 250°C

The second attempt to enhance the crystalline quality consist in depositing the NiO films on the Cu(111) substrate hold at 250°C, temperature which was reported in the literature adequate for obtaining well defined nickel oxide [Mocu00a, Vent94, Barb00a, Mull00, Span98]. Several ultra-thin NiO films were elaborated at 250°C: 0.25 Å, 0.5 Å, 1 Å and 2 Å, and were characterized using AES and STM.

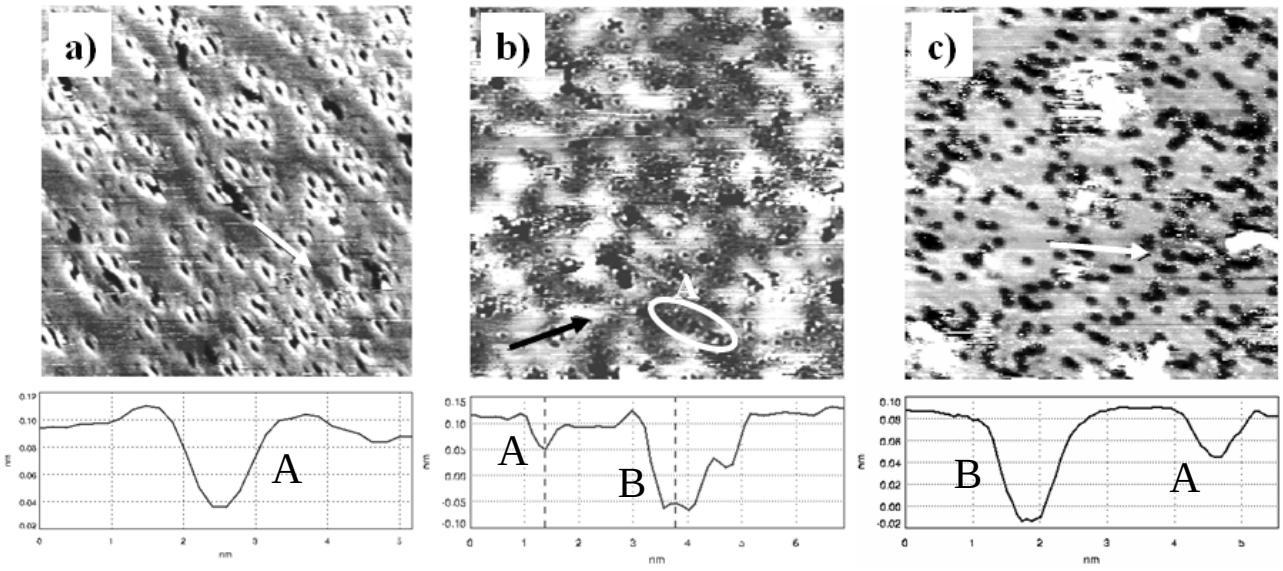

Figure 5.4: *Morphology evolution of the high-temperature (250°C) deposited NiO with respect to the NiO thickness:*
a) 0.25 Å NiO, U = 2.32V and I = 0.13 nA (25×25 nm^2)
b) 0.5 Å NiO, U = -1.58 V and I = 0.15 nA (30×30 nm^2)
c) 1 Å NiO, U = -1.58 V and I = 0.20 nA (25×25 nm^2)
Dark contrast correspond either to chemical or topographical contrast (see details in the text).

For all our films deposited at 250°C the Auger spectra show the same relative intensities for Cu LMM, Ni LMM and O KLL transitions as for the films deposited at room temperature. Therefore, we expect only surface modifications due to the higher surface mobility of the atoms, in particular changes of the surface morphology, without affecting the chemical composition.

The first stage (0-1 Å) of the NiO (deposited at 250°C) growth was studied by STM at room temperature in the topographic mode (constant tunneling current mode). The surface is characterized by a different morphology (figure 5.4) compared to the room temperature deposited NiO films. For the whole thickness range (0-1 Å) STM revealed the formation of two families of holes: a first one (**A**) which can be associated with a chemical contrast, and a second one (**B**) related with topographic contrast (monatomic holes in the Cu(111) substrate). The first family of holes (**A)** is characterized by a depth of ~0.5 Å and a width of ~10 Å, while the second family (**B**) is constituted by holes with ~1.5 Å depth and ~10 Å diameter (line-profiles in figure 5.4). Since no contrast reversal[♣] is observed when changing the STM tip bias (U > 0 and U < 0, in figure 5.4-a and 5.4-b, respectively), we associate the first family of holes (**A**) with the electronic states of Ni atoms incorporated in the Cu(111) surface (figure 5.5). The second family of holes (**B**) could correspond to 3-4 copper atoms vacancies.

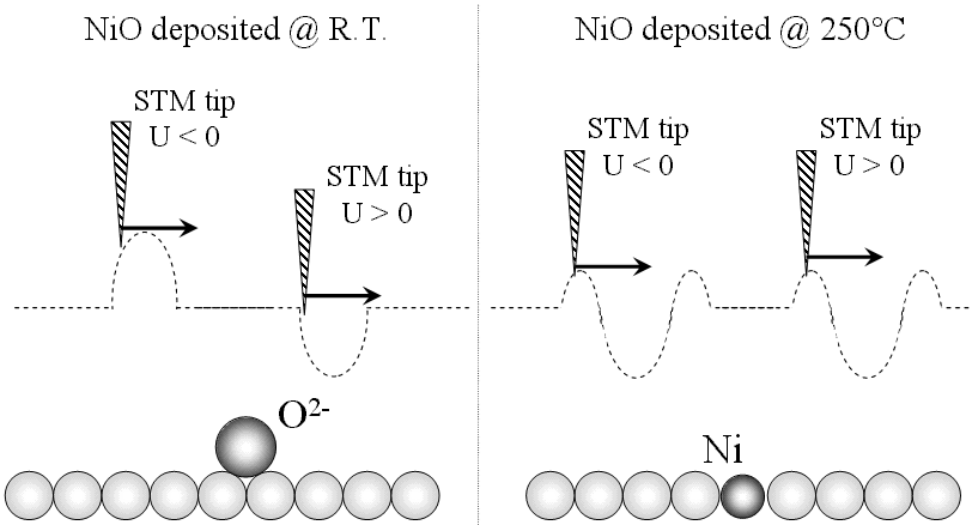

Figure 5.5: *STM typical chemical profiles of the NiO films deposited at room temperature and 250°C respectively:*
With dashed lines we represent the STM tip trajectory. In the lower part of the figure we show the presumed atomic disposition.

[♣] As explained in the case of the direct NiO deposition at R.T. (§4.4.2), for a positive bias the oxygen atoms appear as "dark" structures on the surface. Reversing the STM tip bias, the STM image should present protrusions corresponding to the oxygen atoms. In the case presented here, this is not the case and therefore the apparent STM contrast is attributed to the *metallic* Ni atoms lying in the topmost Cu(111) atomic layer.

For all the NiO films deposited at 250°C we observe a different behavior of the STM contrast compared to the NiO films deposited at room temperature (figure 5.5). A complex "up-down-up" feature is obtained on the STM line profiles. As explained above and shown in the figure 5.5, this behavior could correspond to metallic Ni atoms diffused in the topmost Cu(111) atomic layer, presenting different chemical environments at the surface compared with NiO films deposited at R.T.. This specific behavior could be attributed also to the influence of the STM tip contamination with oxygen, obtaining a different STM contrast than the expected one (see §4.4). However, the tip contamination is always accompanied by a strong perturbation of the entire STM image (strong STM tip instability which introduces parasite frequencies in the recorded image). Taking into account the quality of our STM images (figure 5.4-a, 5.4-b and 5.4-c) we can exclude this possibility.

In figure 5.6, we show a comparison between the morphology of a 0.5 Å NiO film

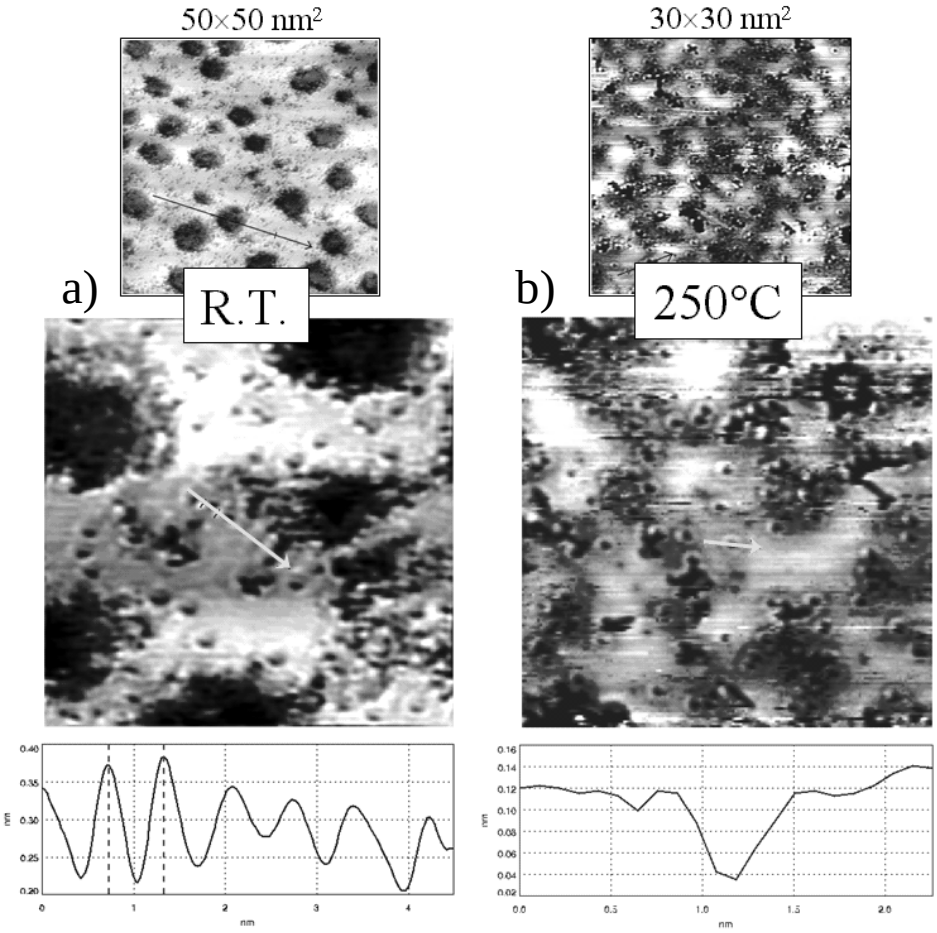

Figure 5.6: *Comparison between the morphology of the 0.5 Å NiO films R.T. (a) and at 250°C (b) at different scales:*
a) U = -0.7 V and I = 0.15 nA, 15×15 nm^2.
b) U = -1.58 V and I = 0.15 nA, 15×15 nm^2.
In the upper part of the figure we show larger STM images corresponding to the same thicknesses (and scanned with same STM parameters) to better evidence the 40 Å diameter holes absence at 250°C.

deposited at room temperature and a similar film deposited at 250°C. Firstly, we remark the absence of the 40 Å width holes for the film deposited at high temperature. Both images present a mixture of empty and filled electronic states, related with the oxygen and nickel sites respectively. Furthermore, the corrugation height is of the same order of magnitude in both images: ~0.5 Å for the filled electronic states (Ni sites) and ~1.5 Å for the empty oxygen electronic states.

Therefore, we can conclude that evaporating the NiO at higher temperatures leads to changes in the morphology, i.e. the absence of the 40 Å diameter holes. However, holes with smaller widths are observed at higher temperatures, suggesting a stronger mobility of the Ni and Cu atoms compared with the similar samples elaborated at room temperature. In other words, at room temperature the energetic equilibrium of the surface is achieved by the formation of large holes of 40 Å diameter, while at higher temperatures the steps are more perturbated and the residual holes show sizes of about 10 Å diameter. The density of vacancy holes (**B**) is very small, and increasing the thickness, their shape and size vary (they even disappear). In addition, as it can be observed in figure 5.7-b, for a 2 Å thickness the surface will be completely covered by a mixture of Ni, Cu and O atoms (suggested by the STM contrast for a negative tip bias), without the apparition of topographic holes (**B**). The large mobility of the Cu atoms is also suggested by the step edges morphology in figure 5.7-b. The chemical composition (measured by AES) is identical to the one measured in the NiO films elaborated at room temperature (figure 5.7-a), characterized by the differential diffusion

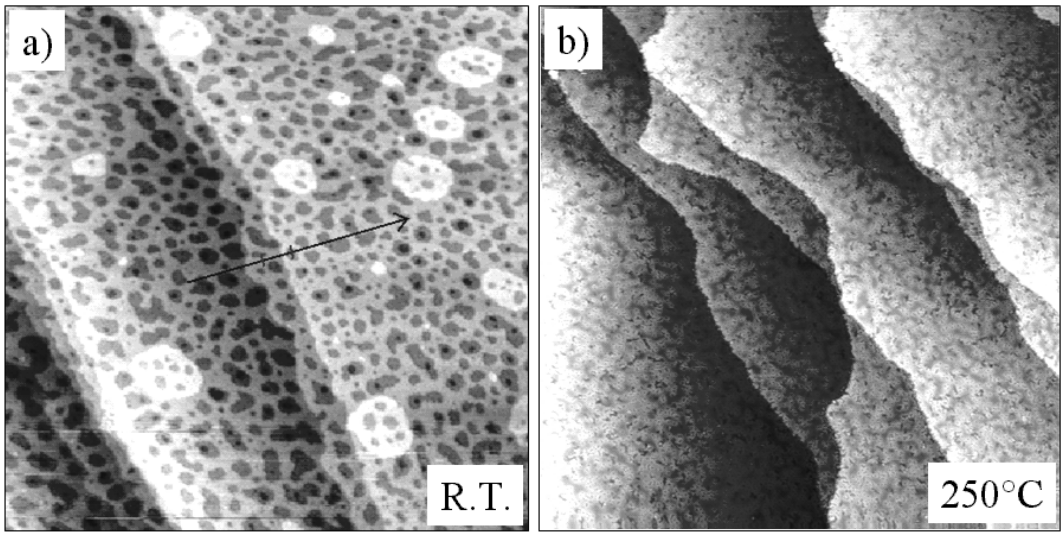

Figure 5.7: *Comparison between the morphology of the 2 Å NiO film deposited at R.T. (a) and 2 Å NiO film evaporated at 250°C (b):*
150×150 nm^2 STM images recorded for a U = -1.58 V bias and I = 0.11 nA tunneling current (a), and U = -0.9 V and I = 0.13 nA (b), respectively. We observe in both cases the strong influence of the deposition temperature on the step edges morphology.

between O and Ni atoms.

☑ *Increasing the substrate temperature during NiO evaporation leads to surface morphology modifications. As for the room temperature elaborated samples, the morphology is governed by the direct exchange process between Cu and Ni atoms, with an increased surface diffusion energy, leading to smaller topographic holes and larger step edge modifications.*

5.2 NiO FILMS ELABORATED BY Ni EVAPORATION IN OXYGEN PARTIAL PRESSURE AT 250°C

Until this point of my work all the results concerned the direct deposition of NiO from a NiO nuggets source, without oxygen adjunction in order to prevent the substrate oxidation. For a comparison purpose, several samples were elaborated by evaporating metallic Ni under a partial pressure of molecular oxygen. Following the literature [Vent94, Barb00a, Mull00, Span98, Imad96, Peac94, Guo98, Alde98, Mocu00a], an oxygen pressure of 10^{-6} mbar and a substrate temperature of 250-300°C characterize the best experimental conditions. AES, STM, LEED and GIXD techniques were used to characterize these samples for the stoichiometry, morphology and surface structure, respectively. In this chapter the results will be presented following this succession of used techniques. Special attention will be devoted to the comparison of these films with those elaborated by direct NiO evaporation at room temperature.

5.2.1 Stoichiometry and surface chemistry

Figure 5.8-a presents the AES spectra recorded for 4 different thicknesses between 0.5 and 7.5 Å. The O KLL transition in figure 5.8-a is not corrected for its relative sensitivity (factor ~ 2) compared to the Ni LMM transition. Obviously the O KLL Auger intensity (at 505 eV) is systematically lower compared with the nickel one (848 eV). The Ni peak intensity was obtained as described in chapter 3.

The thickness calibration was performed taking into account a layer-by-layer exponential decay for the Cu substrate, with λ = 10 Å. Surprisingly, we obtain a strong Ni over-stoichiometry (intensity 3 times larger than for oxygen) which stands in strong contradiction with the NiO nuggets evaporation at room temperature. Since the amount of oxygen partial pressure in the chamber during the evaporation (10^{-6} mbar) is much larger compared with the NiO nuggets evaporation (total pressure during evaporation of 10^{-9} mbar), we could intuitively expect the opposite behavior.

We will now compare the evolution of the relative Cu, Ni and O Auger intensities with those obtained in the case of NiO nuggets deposition at room temperature. To simplify the discussion, we will identify the “direct NiO nuggets deposition at room temperature” as “NiO(RT)” and the “Ni evaporation under O_2 atmosphere at 250°C” as “Ni+O_2”.

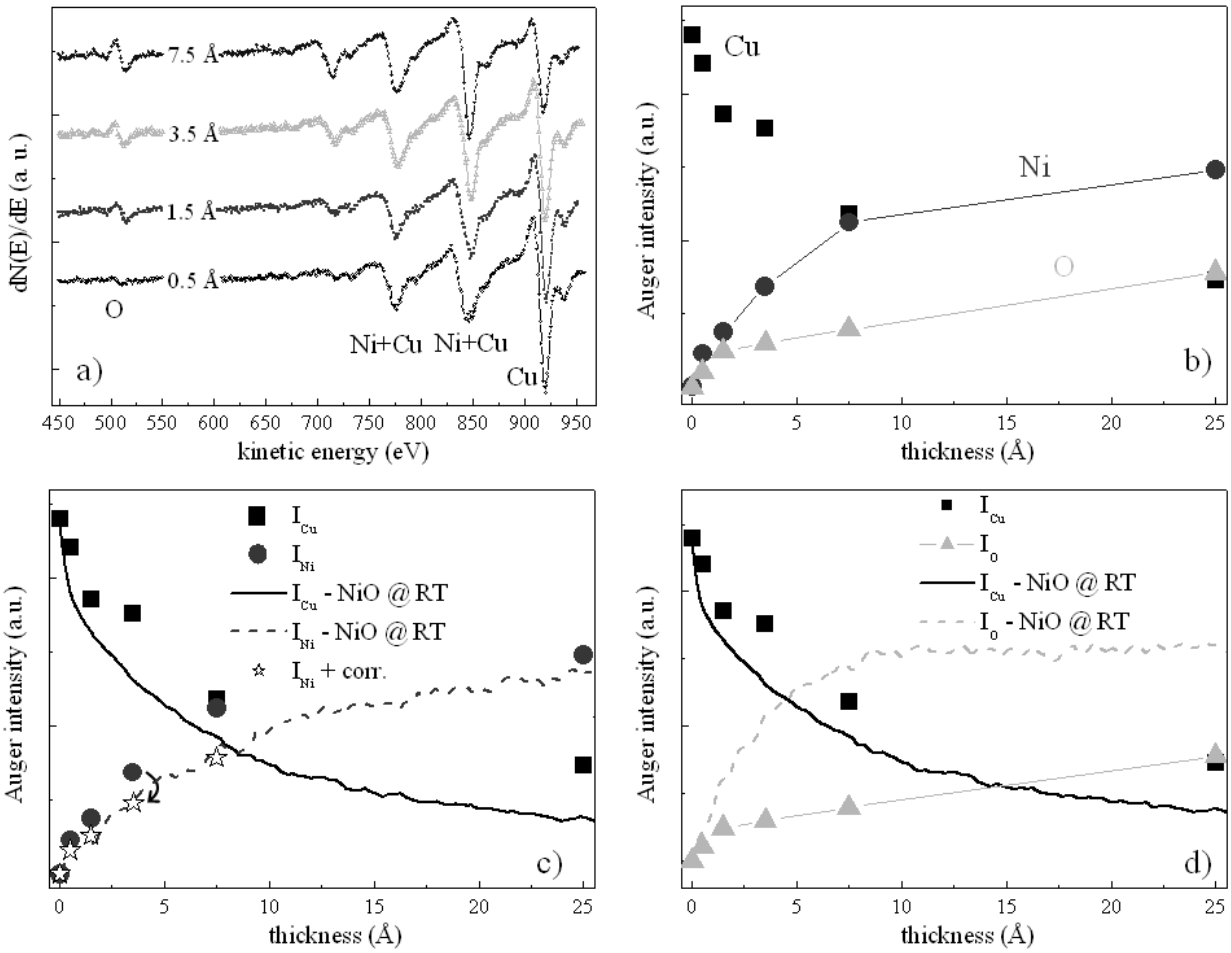

Figure 5.8: *Surface chemistry and stoichiometry:*
a) Evolution of the AES spectra for the NiO films elaborated by Ni deposition under 10^{-6} mbar O_2 at 250°C. The O KLL and Ni LMM transitions are shown for 0.5, 1.5, 3.5, and 7.5 Å.
b) Evolution of the Cu, Ni and O Auger peak-to-peak values as a function of the thickness. The intensities are corrected for their relative sensitivities.
c) Comparison of the Cu and Ni evolution with the case of direct NiO deposition at R.T. (§4.3) (continuous and dashed lines). With large star symbols we report the corrected Ni intensity, stemming from the open circles (factor ~0.75) taking into account an on-top oxygen atomic layer;
d) Comparative evolution of the Cu and O intensities. Symbols stand for the Ni evaporated under O_2 at 250°C and the lines for the direct NiO deposition.

In figure 5.8-c we can observe that the Cu Auger intensity evolution for Ni+O_2 is characterized by a smaller slope than the one corresponding to NiO(RT) (§4.3), whereas the Ni Auger peak intensity shows larger values. Thus, the growth modes are different, the Ni+O_2 being closer to a 3D growth, as will be shown in the next section. For the NiO(RT) case we explained the low Ni Auger intensities values by the oxygen atoms localized on the top of the metallic Ni (which is diffused in the topmost Cu(111) atomic layer), leading to a theoretically calculated attenuation factor of 0.75 in the first stages of the growth (0 – 6 Å). Therefore, in the Ni+O_2 case we can explain the higher Auger intensity values by the formation of metallic Ni at the surface (on-top or diffused in the first Cu(111) layer) which is not covered by oxygen atoms. Indeed, applying the 0.75 attenuation factor, the Ni Auger intensity values for

the Ni+O_2 follows perfectly the curve corresponding to NiO(RT) case (figure 5.8-c – star symbols). Another confirmation for the formation of metallic Ni at the surface is given by the small values of the O KLL Auger peak intensities (figure 5.8-b). Moreover, this behavior shows a poor oxidizing efficiency of molecular oxygen compared to the NiO(RT) case, where ionic O is most likely produced if the NiO molecule breaks off.

☑ *Contrary to the NiO nuggets (evaporated at room temperature), the NiO deposit shows a strong Ni overstoichiometry related with unoxidized Ni on the surface. Therefore, the stoichiometry of the Ni evaporated under 10^{-6} mbar O_2 at 250°C is strongly related with the oxidation efficiency of the molecular oxygen.*

In the following section we will examine the films surface by STM in order to detail the growth and the morphology.

5.2.2 Morphology of NiO/Cu(111) films

The STM study presented in the previous chapter revealed the original morphology of the NiO(RT) films. For comparison, the ultra-thin NiO films prepared by Ni evaporation under oxygen at 250°C were studied in the same thickness range, i.e. from 0 to 7.5 Å.

The results presented here were mainly obtained for negative bias, favoring therefore the STM contrast due to the oxygen atoms. Positive bias was also used, but the STM tip became very rapidly unstable, showing particular frequencies which make the images untreatable. In addition, the STM images performed with positive bias are characterized by several different contrasts during the scan, suggesting the rapid tip contamination.

Figure 5.9 shows the morphology evolution for different thicknesses between 0.8 and 7.5 Å. The evaporation of Ni under oxygen atmosphere results in a strong 3D growth. From 0.8 to 1.5 Å (figure 5.9-b and 5.9-c), mainly one or two monolayer high islands grow on the large terraces present on Cu(111), 0° miscut surface. Above 2.5 Å, large islands, of several hundreds of Å width and ~10 Å height, characterize the film morphology (figure 5.9-d). The thickest film, of 7.5 Å, shows even higher islands of about 20 Å. Since all these images were recorded with a negative polarization of the STM tip, assuming that the tip is tungsten-terminated, the “positive contrast” (protrusions in the STM image) corresponds to the electronic states over the oxygen sites on the surface. Regions with “negative contrast” (dark

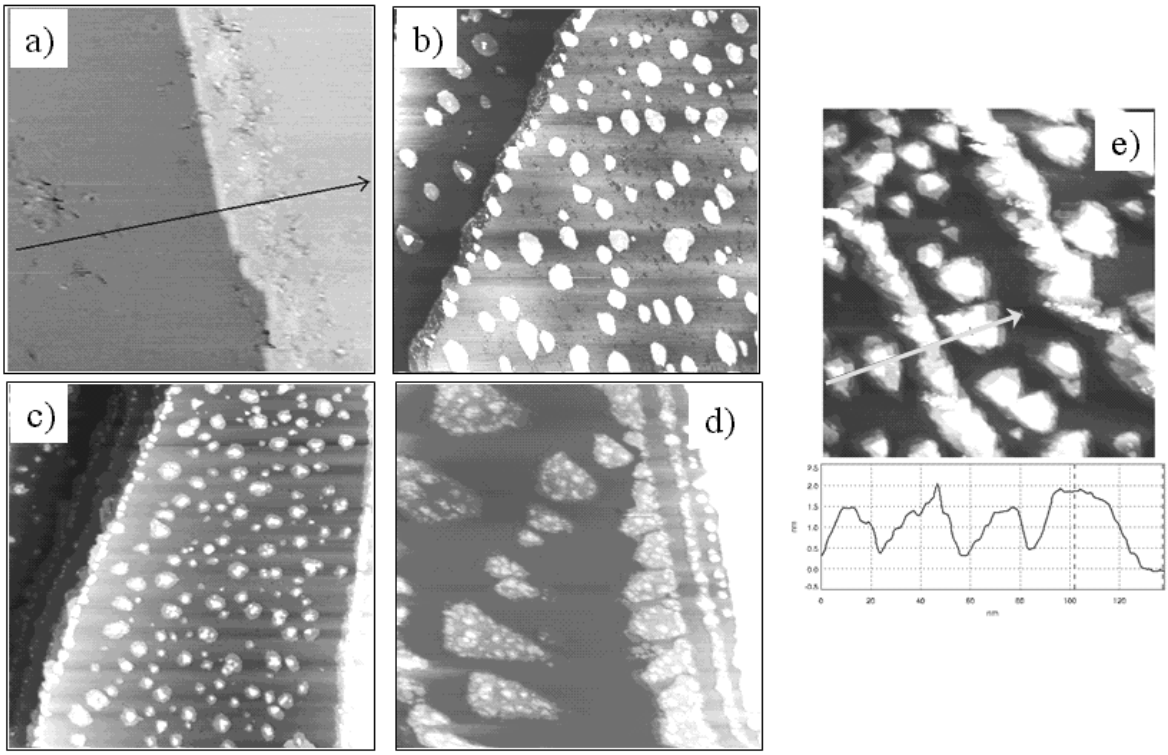

Figure 5.9: *morphology evolution of the NiO films elaborated by Ni evaporation under oxygen atmosphere, at 250°C:*
a) 0.8 Å NiO, U = -0.57 V, I = 0.14 nA (40×40 nm^2)
b) 1.2 Å NiO, U = -0.29 V, I = 0.13 nA (250×250 nm^2)
c) 1.5 Å NiO, U = -0.29 V, I = 0.16 nA (300×300 nm^2)
d) 2.5 Å NiO, U = -0.29 V, I = 0.13 nA (250×250 nm^2)
e) 7.5 Å NiO, U = -0.29 V, I = 0.12 nA (200×200 nm^2)

structures) also appear and, in agreement with the same convention, we attribute them to electronic states over Ni sites. This suggests a similar behavior as already observed in the case of the direct NiO evaporation at 250°C.

A particular morphology is observed for the very low thicknesses (0 – 0.8 Å) where no islands are formed (figure 5.9-a and 5.10). Similar features as in the case of the direct NiO deposition at 250°C are observed: disrupted surface, characterized by both positive and negative contrast (protrusions and respectively, holes). Interestingly, the disrupted zone is located at 20-30 Å away from the step edge. Zones with short-range surface ordering are also present in the STM images, marked by circle A in figure 5.10. Unfortunately, all attempts to zoom into this zone remained unsuccessful, due to STM tip instabilities. Note that even for this thickness the concentration of adsorbed molecular oxygen on the surface could favor the tip contamination.

The 3-D representation evidences the formation of mono-atomic stripes along the step edges, presenting a linear periodicity along the step of ~5.9 Å. This value corresponds well

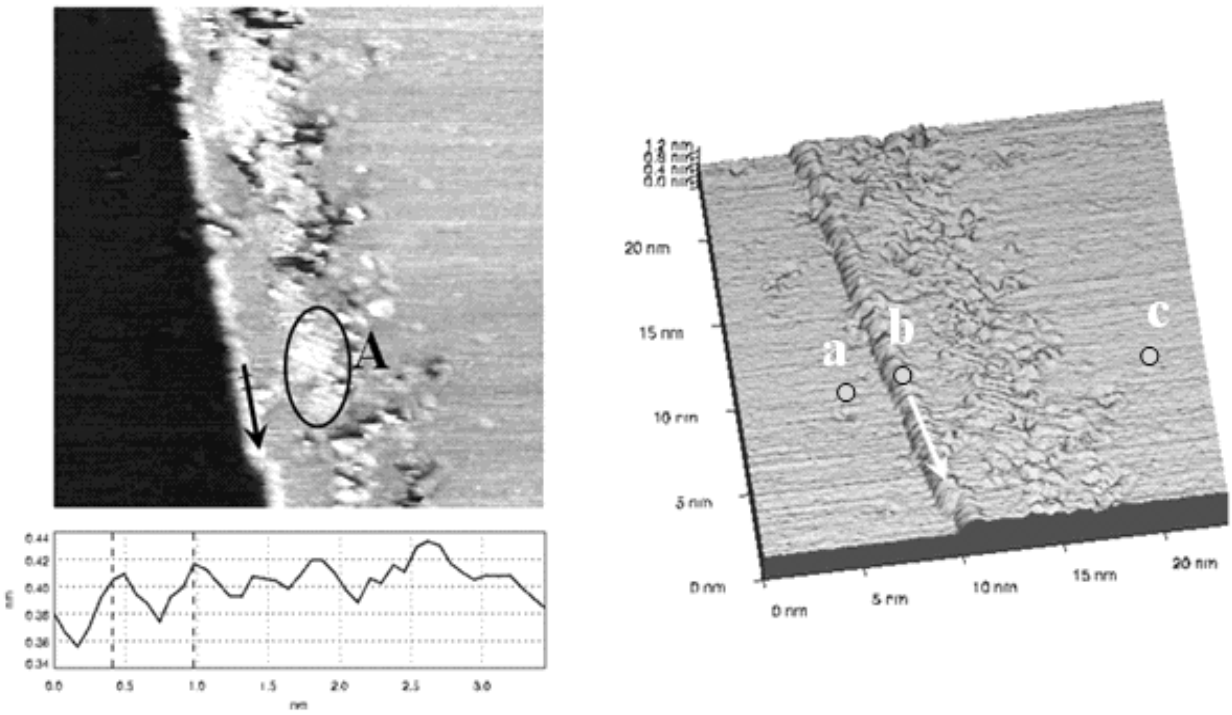

Figure 5.10: *morphology of the 0.8 Å NiO film elaborated at 250°C (23´23 nm^2):*
The scanning parameters are the same as those presented in figure 5.9. We remark the ~5.9 Å periodicity on the step edge, corresponding well with the NiO(111) p(2×2) lattice parameter (5.91 Å). The zone A stress the apparition of patterning effect (periodicity due probably to short-range surface order). The 3-D representation evidence better the periodicity along the step edge.

with the p(2×2) NiO(111) reconstruction (5.91 Å). Therefore we can assimilate it with the formation along the step edge of O-stripes. Moreover, following the z-contrast between the points labeled *a*, *b* and *c* (*a* – lower Cu terrace, *b* – the top of the O-stripe, and *c* – upper Cu terrace) in figure 5.10, we observe that $c - a \cong 2 \pm 0.1 \text{Å}$ and $b - c \cong 0.4 \pm 0.1 \text{Å}$. Since the typical Δz contrast for O atoms on top of the Cu(111) surface is higher than ~1 Å (see §4.4), we conclude that the O-stripe is formed on the lower Cu(111) terrace.

The fact that the disrupted part, characterizing the formation of NiO, is located at 20-30 Å away from the step edge deserves further discussions. The mechanism responsible for this behavior could be related to the Ni atoms diffusing into the step edge from the lower part over several angstroms, as was shown theoretically in the case of pure Ni deposited on the Cu(111) surface [Raek92], and favored by the oxygen surfactant effect in our case.

Contrarily to the calculations [Raek92, Pour99], we observe the disrupted part at tens angstroms away from the step edge and not buried into the Cu step on a distance of only few angstroms. Furthermore, the surfactant role of the oxygen is not obvious within this mechanism. As we have shown in §4.4, surfactant oxygen favors atomic exchange between

Ni and Cu atoms on the Cu(111) terraces[♣]. Since no islands are formed, it is obvious that the resulting Cu adatoms diffuse toward the step edge, giving rise to a new step front.

The formation of the O-stripe along the step edge, shows that there is a Ni fraction which diffuses into the copper step, or to be more precise, the Ni atoms are adsorbed on the lower part of the step edge. Even if the predominant mechanism is the same as in the case of the direct NiO nuggets deposition, Ni grown under oxygen atmosphere is not homogenous and grows preferentially near the step edges. Once more, the oxygen surfactant effect has to be considered to explain the experimental observations. There is a huge difference between the oxygen quantities present on the surface for NiO(RT) and Ni+O_2 evaporation, respectively. In the first case, the oxygen has only a local surfactant effect favoring a strongly localized direct exchange, while in the second case (10^{-6} mbar oxygen partial pressure), oxygen may affect the entire Cu(111) surface, enhancing the mobility of the deposited Ni atoms, promoting hence preferentially a step-flow growth. At the step edges, the Ni atoms undergo the direct exchange mechanism, as explained above.

In the following paragraph we detail the morphology in the 3D growth regime. Increasing the thickness yields in a typical island growth (figure 5.11). The height which characterize these islands has a mean value of ~2.4 Å, which corresponds well with the reticular distance between the successive atomic planes of same chemical species in the NiO(111) crystal, as shown in the schematic drawing in figure 5.11. For 1.2 Å, the mean width of the NiO(111) islands is of about 100 Å, but with a large lateral size distribution.

An obvious question rise up: if these islands are made of NiO(111), are they Ni- or O-terminated? Islands growing preferentially on defects and O and Ni having a large chemical affinity, we can reasonably assume that the observed islands (figure 5.11) grow on a Ni base (figure 5.12). For the 0.8 Å NiO film (figure 5.10) we saw that the O-stripe along the step edge is characterized by a STM contrast of 2.4 Å, relative to the lower Cu(111) terrace. Therefore, the STM contrast between the islands and the Cu(111) surface (2.4 Å) seems to be more likely due to *only one oxygen atomic layer lying on a Ni base buried in the topmost Cu atomic layer* (figure 5.12).

[♣] In the case of Ni deposited on Cu(111), atomic exchange can take place only at the step edges [Raek92].

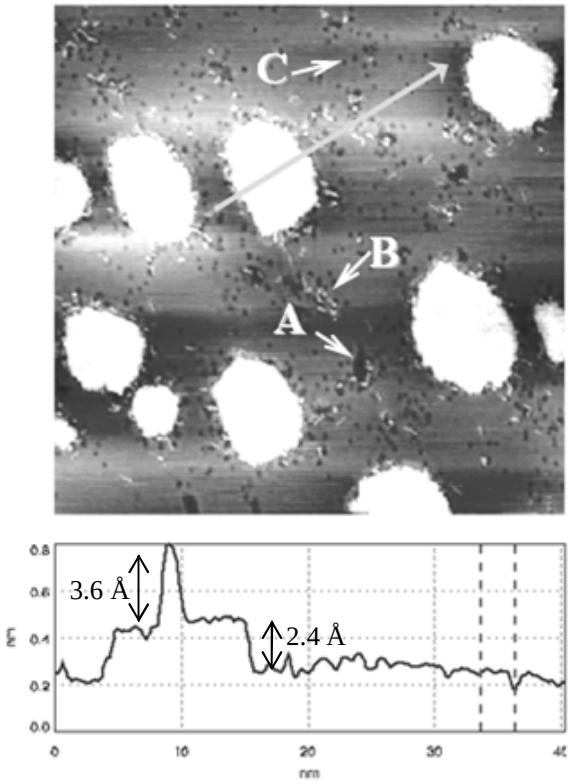

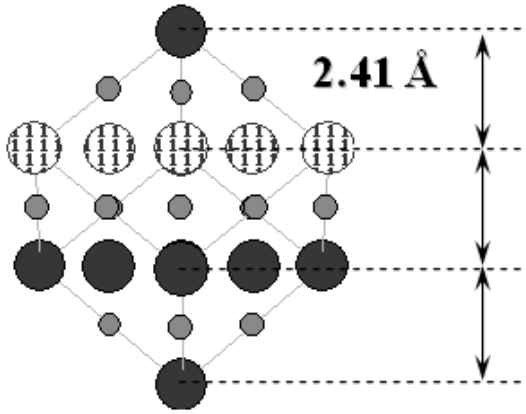

Figure 5.11: *1.2 Å NiO/Cu(111):*
75×75 nm^2, U = -0.29 V, I = 0.32 nA
Typical 3D growth by island formation. The line-profile reveals mono-atomic high islands. The schematic drawing shows the reticular distance (2.41 Å) between the NiO(111) atomic planes (small circles stand for Ni and the larger ones for the O atoms). Details about A, B and C is given in the text.

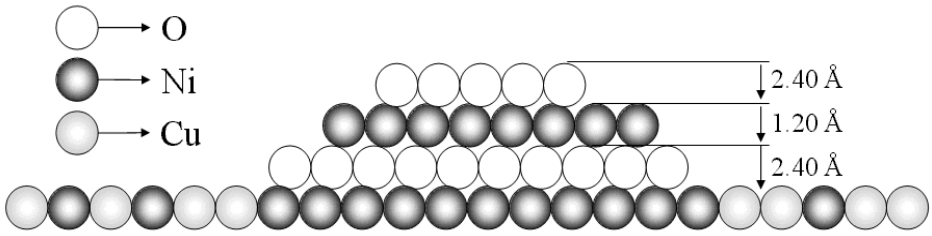

Figure 5.12: *schematic STM contrast for O-terminated island and with Ni base:*
Schematic drawing which corresponds to the line profile in figure 4.28, explaining the total 6 Å height of the island.

STM image line-profiles (figure 5.11) show a narrow peak in the middle of the mono-atomic island, with a total height of ~6 Å, corresponding to a second NiO level. From a structural point of view, the 6 Å value (measured from the island base to the top) can not be explained by measuring integers of the reticular distances. Taking into account the STM contrast between the adjacent metallic and oxide levels, we can imagine the situation presented schematically in figure 5.12. As observed for the mono-atomic island, the STM contrast O/Ni is of 2.40 Å. Therefore, assuming that the island is composed by 4 alternated layers O/Ni/O/Ni we measure experimentally 2.4 Å and 3.6 Å and deduce a resulting contrast for Ni/O of 1.20 Å. In this way, the 3rd level (without taking into account the Ni layer buried

in the Cu) is also an oxygen layer, obtaining once more an O-terminated island, in agreement with the observed STM contrast (oxygen protrusions for negative bias).

Let me now discuss some interesting particularities that can be observed on the STM image at 1.2 Å, labeled A, B and C in figure 5.11. In region **A** we observe topographic holes (depth ~ 2 Å), due to the vacancy of few Cu atoms. A second hole family can be observed in region **C**, with a STM contrast of about 0.5 Å. Already observed in the case of the direct NiO evaporation, these holes are attributed to Ni atoms (for negative STM tip bias) diffused in the topmost Cu atomic layer. Since we observed similar behaviors for the direct NiO nuggets evaporation at 250°C, *the disrupted surface shape is an intrinsic property of the NiO/Cu(111) system and does not depend on the evaporation method*.

In the first stages of the growth, the differences appearing from one evaporation method to another are dependent on the temperature, oxygen quantity and the oxygen chemical form (atomic or molecular). One of these differences is labeled **B** in figure 5.11, where we observe the presence of bright structures, with small sizes, corresponding to clusters of 2-3 atoms (dimers and trimers), sitting on top of the Cu(111) surface. Considering the STM contrast, these clusters should be composed mainly by oxygen atoms. Their spatial arrangement – agglomeration near the NiO islands - suggests that they could be *precursors* of the NiO islands. In other words, the 3D growth could be achieved by the diffusion and the aggregation of such clusters instead of the more classical atomic nucleation/aggregation process. There are several zones (e.g., in the zone pointed by **B**) in figure 5.11, where we can observe assemblies of such clusters, nucleating to form new islands. Moreover, the NiO islands are surrounded by the small holes associated with the Ni atoms, which present increased density in regions (e.g. **B**) where the clusters nucleate. Therefore, we conclude that *the NiO island growth is governed by the diffusion and the nucleation of O-like clusters in regions presenting a high density of Ni atoms*.

Figure 5.13 presents the morphology of a 1.5 Å thick NiO film. Figure 5.13-a shows a higher density of NiO islands compared with the 1.2 Å film. We remark that the NiO islands are disposed either at the step edges or at several tens of angstroms away from the step edge. In fact, we observe the same surprising behavior for the thinner NiO film (~0.8 Å) and we attribute this configuration to the direct exchange and step-front propagation processes. A closer look on the terraces (figure 5.13-b) reveals that the NiO islands have the same characteristics as observed for the 1.2 Å film: ~100 Å width and one or two-layer height (2.4 Å and 6 Å, respectively). The island shows a circular shape, without formation of

crystallographic facets, as was observed for the islands observed at 1.2 Å. This isotropic shape could be imposed by the island formation process, i.e. the clusters diffusion.

In the case of pure Ni deposited on the Cu(111) the islands grow *via* the atomic diffusion process with preferential diffusion along [100] directions, leading to triangular

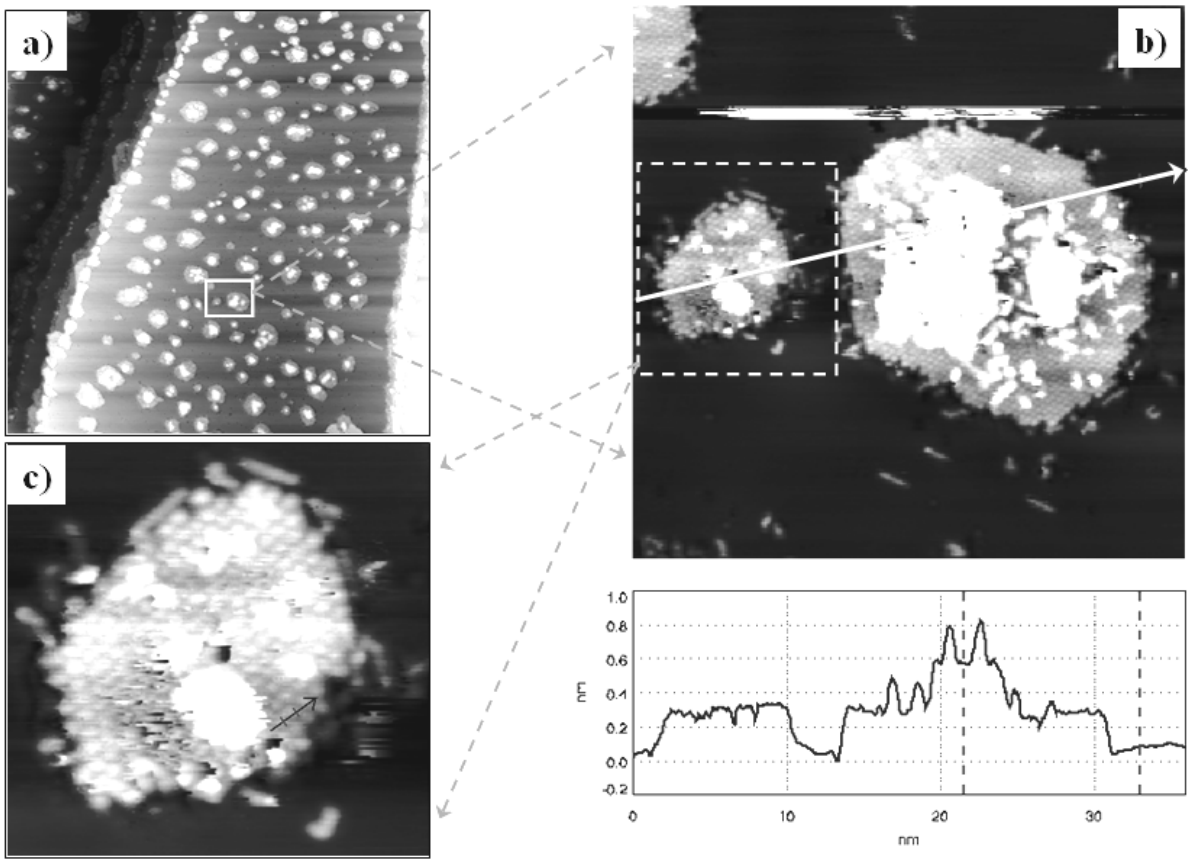

Figure 5.13: *STM images for 1.5 Å NiO film:*
a) 300×300 nm^2, U = -0.29 V, I = 0.16 nA; we remark the increased island density compared to the 1.2 Å situation (figure 5.11)
b) 35×35 nm^2 (zoom of (a)), U = -0.29 V, I = 0.53 nA
c) 12×12 nm^2 (zoom of (b)), U = -0.29 V, I = 0.53 nA; STM image with atomic resolution

shaped islands with (100) facets. Contrarily to the atomic diffusion process, the cluster diffusion and aggregation process leads to circular shaped islands. We note the high concentration of O-like clusters (figure 5.13-b) near the island and on the top of the island, surrounding the second NiO level.

Figure 5.13-c shows an atomic resolved STM image of a single-layer NiO island. The atomic resolution of this STM image evidences the insulator-like character of the NiO island, the surface electronic states being localized. This excludes the formation of metallic Ni islands. This figure clearly shows also the presence of the O-like clusters which surround the

NiO island. More details about the crystallographic order and quantitative values are given in the next section of this chapter, which treats the surface structure of the NiO films.

The evolution of the island morphologies during STM scans is evidenced in figure 5.14, showing 3 images of the same island, taken at different time intervals: at t = 0, 9 and 21

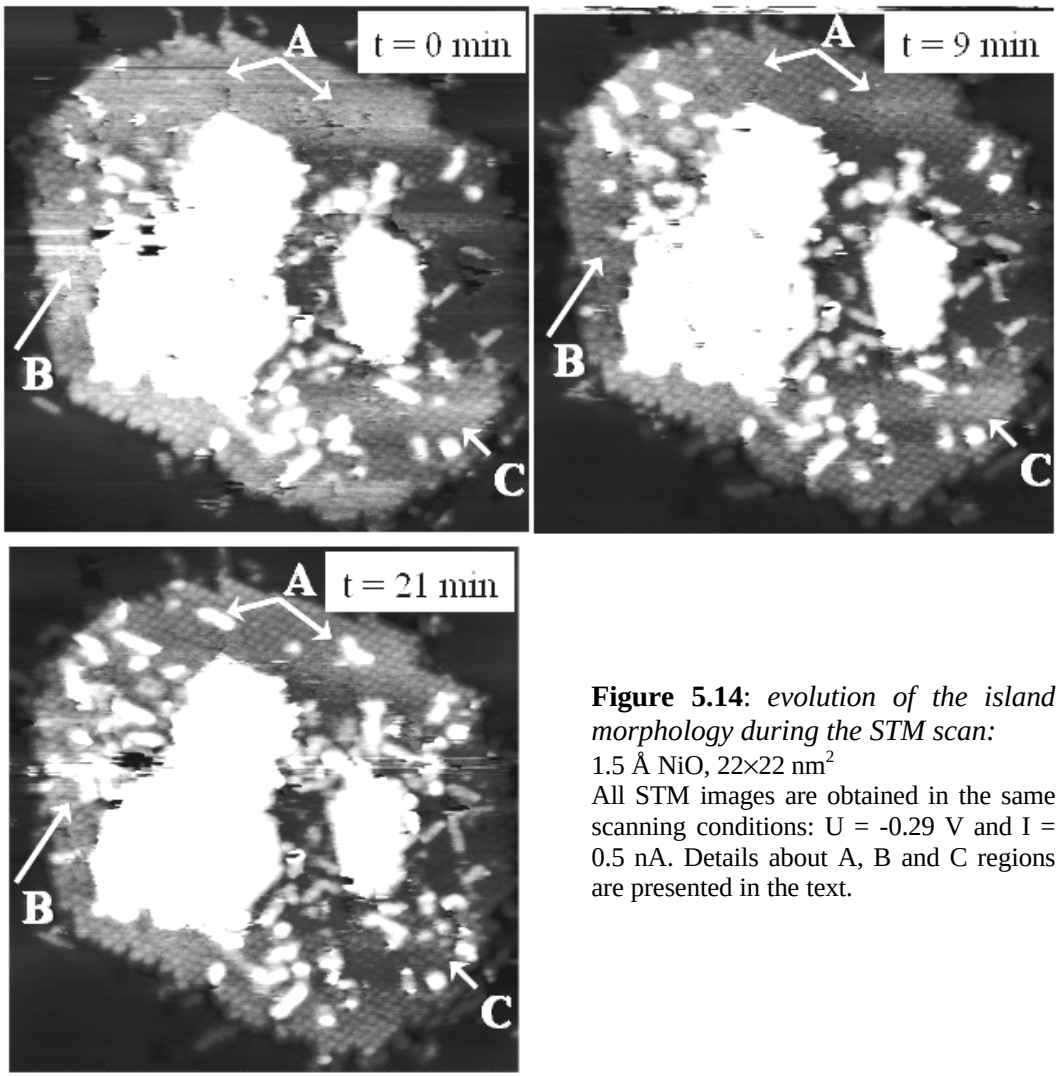

Figure 5.14: *evolution of the island morphology during the STM scan:*
1.5 Å NiO, 22×22 nm^2
All STM images are obtained in the same scanning conditions: U = -0.29 V and I = 0.5 nA. Details about A, B and C regions are presented in the text.

minutes, respectively. We directly observe that the number of clusters surrounding the second level of the island is increasing with time.

Three different regions of the island are labeled A, B and C. In region (A) we observe that after 9 minutes, two nuclei appear. After 21 minutes (3rd STM image), two additional clusters appear on the islands. Taking into account the shape and the size of these clusters, we can consider that they are made of three atoms (trimer), as the clusters observed already on wider STM images at 1.2 Å thickness (figure 5.11, B-zone). The notion of "trimer" defines the **in-plane** number of atoms. STM measurements reveal that the height of these clusters is of ~6 Å (measured with respect to the copper surface), similar with the height that

characterize the second level of the NiO island. Therefore we can define the **out-of-plane extent** of these clusters, corresponding to a Ni-O bound.

Regions B and C show also the agglomeration of new dimers and trimers, near the second level of the island. We note the dynamic of the second-level, with a shape changing continuously with the time. At t = 0, this part of the island seems to have a stabilized shape, presenting sharp facets. However, after 9 minutes, we remark some new clusters trapped on its edge, leading to the disrupted shape observed at t = 21 minutes.

The time evolution of the island morphology is a clear evidence of the high clusters mobility, leading to changes even after the evaporation stops. Therefore, the islands formation seems to be a bidirectional process: on one hand, the clusters aggregates together tending to create faceted shapes and, on the other hand, clusters are ejected from islands, possibly in order to preserve their faceted shape. We have to keep in mind that the STM tip can induce transformations in the morphology, especially for very low distance between the STM tip and the surface. In this case, the sample-tip interactions are characterized by instabilities and the STM image becomes fuzzy (the center of the first image in figure 5.14). For this reason we choose zones A, B and C, sufficiently far from the affected area.

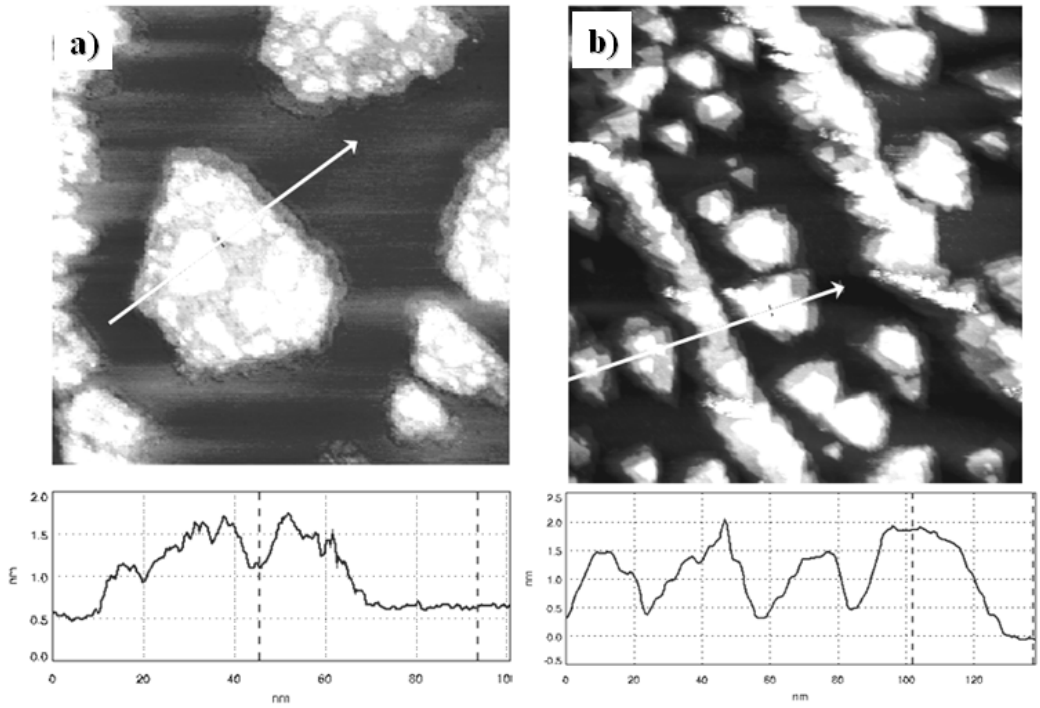

Figure 5.15: *2.5 Å NiO/Cu(111) a) and 7.5 Å NiO/Cu(111) b):*
a) 150×150 nm^2, U = -0.29 V, I = 0.18 nA
b) 200×200 nm^2, U = -0.29 V, I = 0.13 nA
Strongly 3D growth with huge islands of ~400 Å width and 10-20 Å height. We remark for high thickness the faceting of the NiO islands.

The STM images taken for higher thicknesses (figure 5.15) reveal a strong 3D growth with large islands presenting several atomic levels. At 2.5 Å, the islands have a mean height of about 6 Å (500 Å wide), the same as observed for the 1.5 Å NiO film. We distinguish also higher levels on the top of the islands, of about 13 Å. This value corresponds well with the expected STM contrast for an island presenting complete NiO(111) cell stacking (7 atomic planes, alternating pure Ni and O ionic planes).

The absence of O-like clusters and Ni-like holes is not necessarily real and could be caused by the large "up and down" values of the STM contrast (> 12 Å), hiding the smaller O and Ni contrast (< 2.5 Å). The NiO islands characterizing the thickest film, of 7.5 Å (figure 5.15-b), have the same mean width (~400 Å) as the ones observed at 2.5 Å, but their height increased strongly, presenting STM contrasts of about 20 Å. Taking into account the O-Ni and the Ni-O STM contrast, we estimate the height of these islands to 6 oxygen levels, always O-terminated. The step edge is completely covered by a NiO stripe, ~100-150 Å wide and with the same height as the NiO islands. The islands are faceted, presenting triangular shapes. Unfortunately, since we do not know the step orientation[♣], we can not distinguish between the $[1\bar{1}0]$, $[0\bar{1}1]$ and $[10\bar{1}]$ crystallographic directions.

☑ *In conclusion, the morphology shows strong 3D characteristics in the case of Ni evaporation under oxygen atmosphere at 250°C. The islands are formed by the nucleation/aggregation of O-like clusters on regions where Ni atoms diffused into the topmost copper substrate layer. Within some considerations, the islands height can be depicted in succession of O and Ni atomic planes with different STM contrast, always presenting O-terminated layers. While the low-thickness regime (< 2.5 Å) is characterized by isotropic-shaped islands, facets are formed for larger thicknesses (> 2.5 Å). We evidenced that the growth mechanism of the Ni evaporated under oxygen atmosphere at 250°C is governed by the molecular oxygen reactivity.*

♣ The Cu(111) single crystal used in this study is considered perfectly planar (0° miscut), so ideally there are no steps on the surface (no preferential direction for the crystal cut). Therefore, if steps appear, we can not know their crystallographic direction.

5.2.3 Structure of NiO/Cu(111) films

Due to the large ~15% misfit between NiO(111) and Cu(111), the NiO structure relaxation may be reached by complex structural changes (apparition of different oxide phases, surface reconstruction, multi-domain structures, etc.) compared to the fcc NiO(111) surface structure. In addition, since fcc NiO(111) presents a succession of pure Ni (anionic) and O (cationic) planes, only reconstructed NiO(111) surfaces (e.g. p(2×2) [Vent94, Barb00a, Mocu00a]) can be formed in order to overcome the electrostatic neutrality problem, discussed in §1.2.1.

Combined LEED, STM and GIXD measurements were used to resolve the structure of the nickel oxide films deposited by Ni evaporation under oxygen atmosphere at 250°C. I will present the results for each technique, discussing thereafter a possible model together with the limitations and the complementary measurements still needed in order to fully describe the structure.

The present structural analysis aims at determining the epitaxial conditions for the ultra-thin NiO films (~1 ML) deposited on Cu(111) and to compare them with the direct NiO

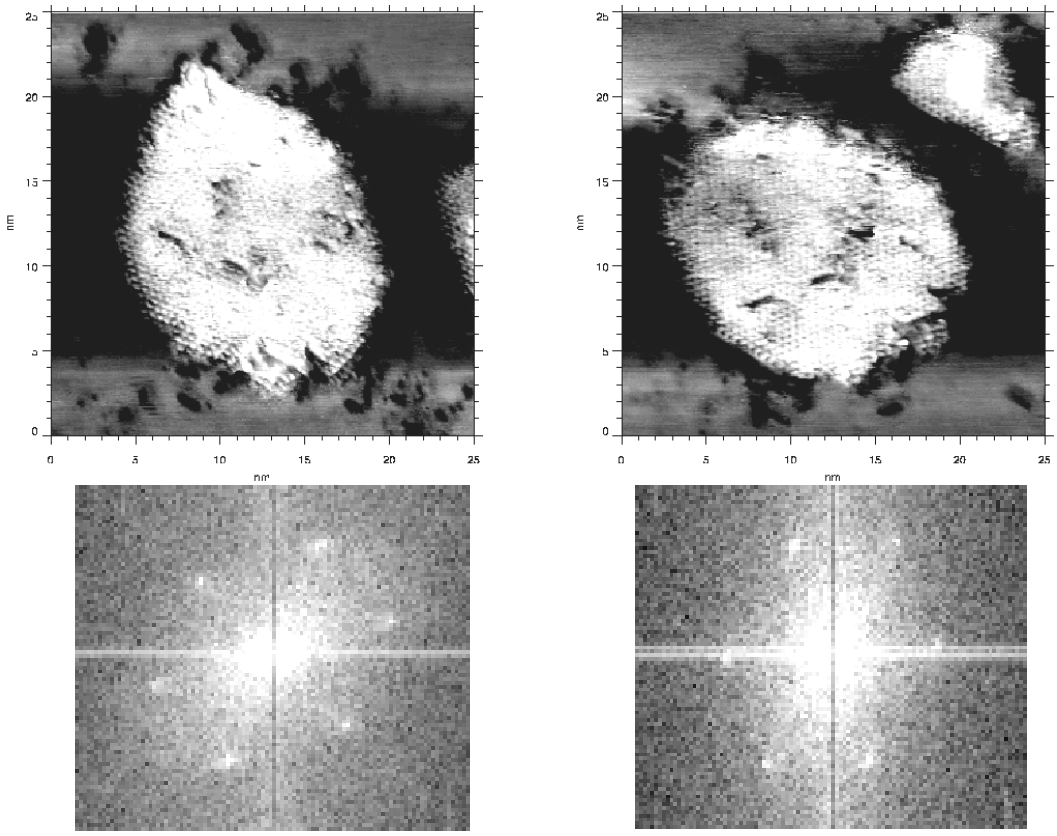

Figure 5.16: *surface symmetry through STM image Fourier transformation:*
1.5 Å NiO, U = -0.29V, I = 0.25 nA, (25×25 nm^2)
The STM image Fourier treatment reveals the six-fold symmetry of the surface islands. The same island is scanned in two directions to avoid the STM drift distortions.

nuggets evaporation at room temperature. The complex structure is not fully depicted and only the main aspects of the epitaxial growth of Ni evaporated under oxygen atmosphere will be described in this section.

Surface symmetry and in-plane structural measurements can be realized by STM thanks to the insulator-like character of the NiO islands, localizing the electronic states at the crystallographic sites. Already for very small thicknesses, ~1 Å, we observe the six-fold symmetry of the surface ordering (figure 5.16). These STM images show a clear periodicity (well defined frequencies), even if no atomic resolution is obtained. The Fourier processing of the STM images reveals the six-fold symmetry of the islands surface structure (figure 5.16 - below the STM images). Both scans were performed on the same island and in similar scanning conditions, using different scan angles, in order to avoid the distortions induced by the STM tip drift motion. A residual distortion appears however in the Fourier image. In the figure 5.17, the STM atomic resolution image shows that no such distortion appears on the

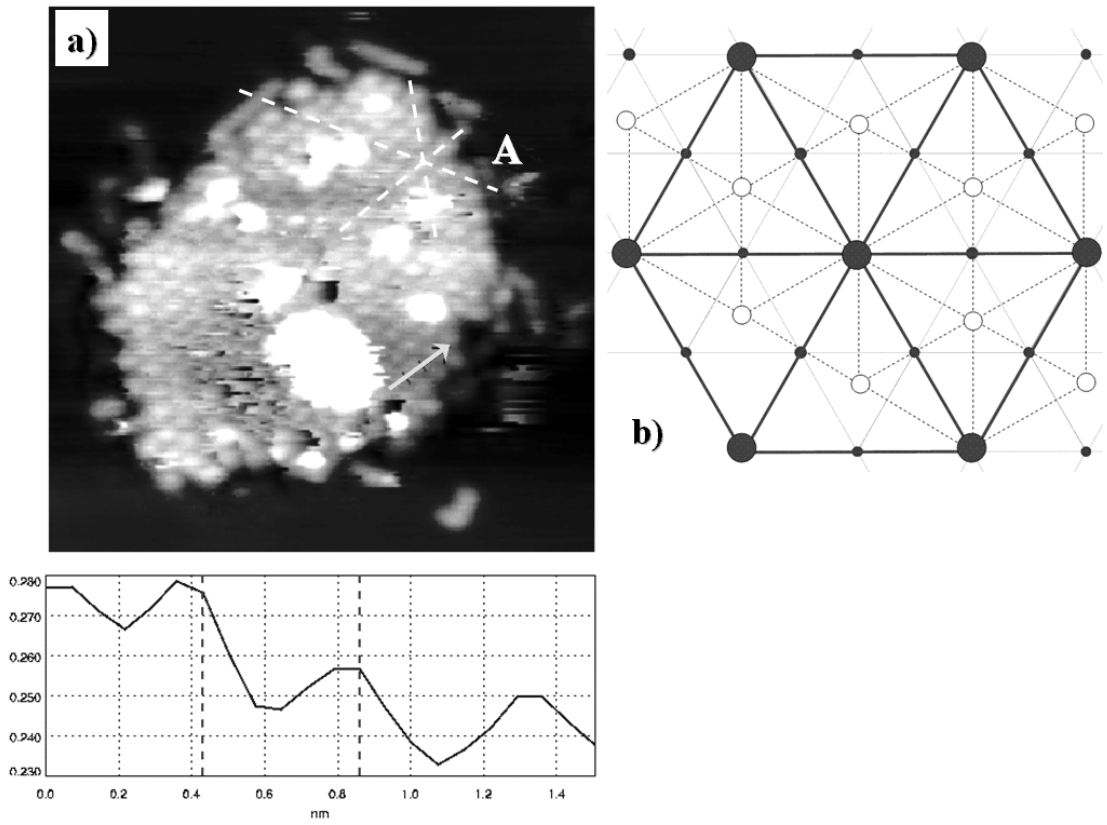

Figure 5.17:
a) STM estimation of the lattice parameter 1.2 Å NiO, U = -0.29V, I = 0.5 nA, (12×12 nm^2)
The estimated lattice parameter is 4.8±0.5 Å. This value is closest to the NiO($\sqrt{3}\times\sqrt{3}$)R30° structure.
b) Schematic drawing showing the geometrical construction of the NiO($\sqrt{3}\times\sqrt{3}$)R30° structure. The small black circles define the Cu(111) lattice and the open circles stand for the NiO(111) lattice rotated at 30° with respect to the Cu(111) lattice. The NiO($\sqrt{3}\times\sqrt{3}$)R30° structure, constructed on the NiO(111) lattice, is drawn with large black circles

lattice (image region A – the angle between the three crystallographic directions is 120°). Therefore, the slight distortion observed after the Fourier treatment is related with the island shape. Due to the island shape anisotropy, the Fourier numeric calculations will differently treat each direction. The "long"-axis of the hexagonal shape in the Fourier space is always parallel to the smallest direction of the island in the direct space. The apparent distortion of the hexagonal surface unit cell is thus an experimental artifact.

Once the surface symmetry established, we can estimate the lattice parameter of the fcc (hexagonal[♣]) NiO structure. In figure 5.17, we present the atomic details of a 10 nm NiO island. The line-profile evidences a periodicity of **4.8±0.5 Å**, far from the expected NiO(111) lattice parameter, of 2.95 Å. In fact the NiO(111) surface can not exist and we should expect reconstructed surface structures (e.g. NiO p(2×2)) which modify the stoichiometry of the topmost NiO atomic planes in order to achieve a surface with neutral electrostatic potential. The estimated value corresponds well with a NiO($\sqrt{3}\times\sqrt{3}$)R30° reconstructed structure, which has a lattice parameter of $2.95\times\sqrt{3} = 5.13$ Å. Indeed, as shown in the schematic construction in figure 5.17-b, the NiO($\sqrt{3}\times\sqrt{3}$)R30° structure has the most favorable lattice match with Cu(111) substrate (2×2.56 = **5.12 Å**). In this figure, the small black circles define the copper atoms and the large black circles stand for the atoms lying in the NiO($\sqrt{3}\times\sqrt{3}$)R30° structure. We show also the missing atoms from the NiO(111) structure, stressed by open circles. Using only STM arguments, we can not discern if the structure characterizes only the surface reconstruction or if the "bulk" island is formed following this epitaxy (Ni_xO_y phase different from the NiO one). We have to note that STM images with atomic resolution were obtained only for 1.2 Å and 1.5 Å NiO thicknesses. For higher thicknesses no atomic resolution could be obtained, due to the high values of the *z*-contrast/roughness (higher than 10 Å), the STM tip frequently showing strong instabilities.

[♣] The STM is sensitive only to the surface symmetry, without any information concerning the stacking of the atomic planes. Therefore we can not distinguish between an fcc or a hexagonal structure.

A complementary direct structural analysis has been performed using LEED in the thickness range 1 – 7.5 Å. Table 5.1 gives the evolution of the LEED patterns as a function of the NiO thickness and of the LEED electron energy. Calculated LEED patterns for each

	48±2 eV	**70±1 eV**	**95±2 eV**
1.5 Å	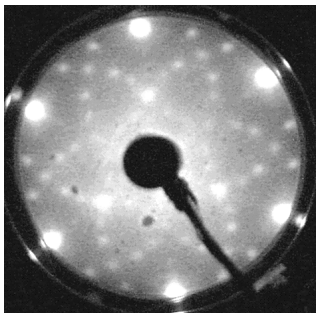	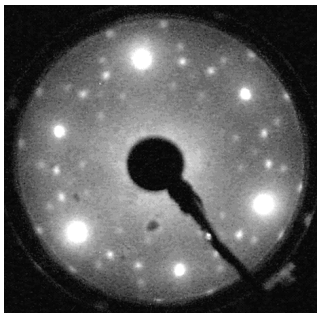	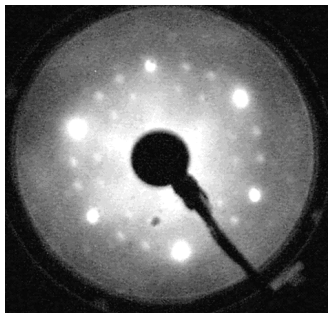
calculated LEED pattern	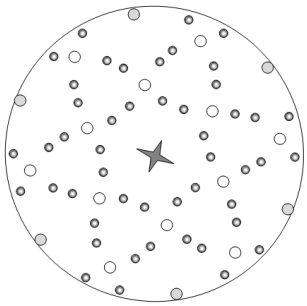	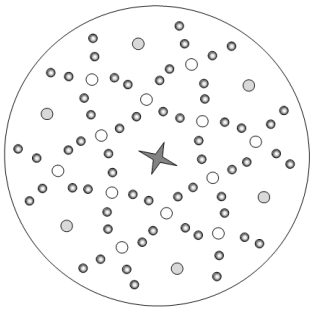	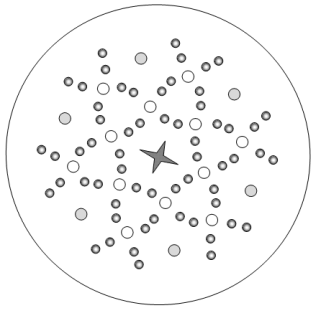
3.5 Å	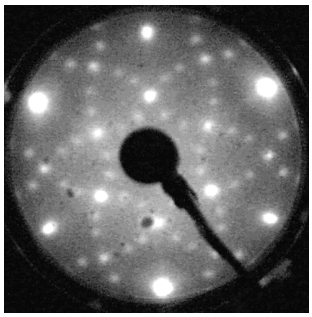	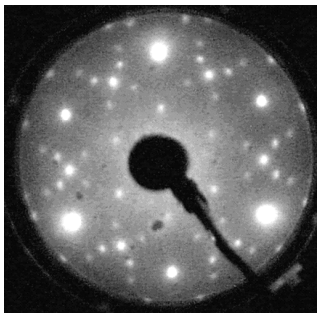	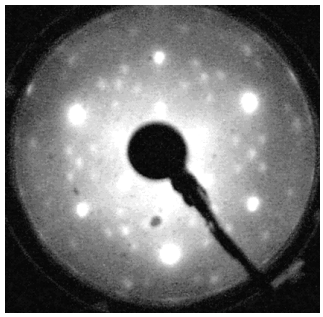
7.5 Å	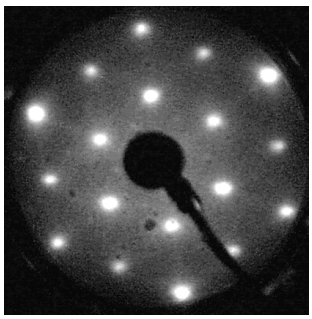	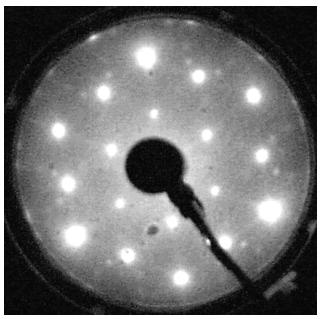	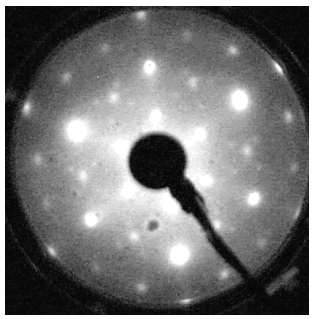

Table 5.1: *Experimental and calculated LEED patterns for different NiO thicknesses*:
LEED calculations show a "bulk" NiO($\sqrt{3}\times\sqrt{3}$)R30° structure with an additional surface reconstruction characterized by a lattice parameter of ~6.8 Å. For 95 eV, only the main reflections are reproduced for the sake of clarity. Large greyed circles correspond to Cu(111) reflections, open circles to the NiO($\sqrt{3}\times\sqrt{3}$)R30° structure and small greyed circles stand for the surface reconstruction.

energy are also shown. For the 1.5 Å NiO deposit, we recognize the strong spots characterizing the fcc Cu(111) and main spots aligned at $a_{Cu}\times 2$ = 5.12 Å on the LEED cliché. Several spots related with a reconstruction-like pattern also appear. At higher electron energies we observe the evolution of the strongest LEED spots which follow the characteristic extinction rules for an fcc lattice, with alternating intensity for the reflections situated at 120°. Above 100 eV the only spots which appear are related to the copper substrate. The absence of the higher diffraction orders (table 4.4, 1.5 Å and 95 eV) for high energy electrons characterize small diffracting domains, in good agreement with the size of the NiO islands observed by STM (~100 Å). Increasing the NiO thickness leads to a contrast increase of the LEED patterns, improving the observation of the same structures than for thinner NiO films. The "satellites" spots are also well defined with increasing NiO thickness, suggesting the stabilization of a possible surface reconstruction of the islands. At 7.5 Å, the LEED pattern presents bright spots at $a_{Cu}\times 2$, showing that the corresponding real space structure is bulk-like. Contrast effects have to be taken into account to explain the absence of the satellite spots for small electron energies. Indeed, for 70 eV, we observe that these "reconstruction" spots are present on the LEED cliché, at the same positions in the reciprocal space as observed for the thinner NiO films. Furthermore, for higher electron energies, we remark the apparition of higher diffraction orders, characterizing therefore larger diffracting domains (width increase of the NiO islands). Both Cu and "bulk" NiO($\sqrt{3}\times\sqrt{3}$)R30° LEED spots vary following the fcc stacking characteristic extinction rules. It is however difficult – due to the large number of spots present on the LEED cliché – to conclude on the nature (fcc or hexagonal) of the NiO islands.

The best calculated LEED patterns (table 5.1) are obtained considering a "bulk" NiO($\sqrt{3}\times\sqrt{3}$)R30° structure (**5.13** Å lattice parameter), which provides the main spots at $a_{Cu}\times 2$ (half of the distance between the Cu(111) reflections in the reciprocal space), in addition with a surface reconstruction characterized by a lattice parameter of ~**6.8 Å**, rotated by ±**18.4°**[♣] with respect to the Cu(111) lattice. This structure is compatible with the evolution of the LEED pattern as a function of the electron energy. Note that for the sake of clarity for the higher electron energy, of 95 eV, in the calculated LEED cliché we show only the same reflection orders as for lower electron energies. Unfortunately, the 6.8 Å value can be related

[♣] The ±18.4° rotation is equivalent with a rotation at +18.4° plus an additional axis of symmetry, i.e. a mirror. We can therefore consider that the reconstructed structure is rotated by 18.4° with respect to the NiO($\sqrt{3}\times\sqrt{3}$)R30° one and presents a macle along the epitaxial direction, i.e. the surface hexagonal [10] direction.

neither with Cu(111) nor with the NiO(111) lattice parameters values. In fact, the LEED pattern symmetry can be obtained for any pairs of lattices (vectors basis a_1 and a_2 respectively) with $a_2 \cong 1.3 \times a_1$, and with ±**18.4°** angular displacements. Therefore the proposed structural model is not necessarily unique. Note also the large size of the spots corresponding to the Cu(111) substrate, which may thus contain additional spots, e.g. NiO(111) (*a* = **2.95 Å**).

It is obvious that LEED measurements only can not fully describe the complex structure of our NiO films. Additional surface diffraction (GIXD) measurements were performed using synchrotron radiation at ESRF, on the BM32 (SUV) beam-line. Note that the diffraction measurements were performed maintaining the substrate at the evaporation temperature, i.e. 250°C, whereas the substrate was cooled down to RT for the other studies.

Figure 5.18 presents an overview of the in-plane structure evolution function of the Ni

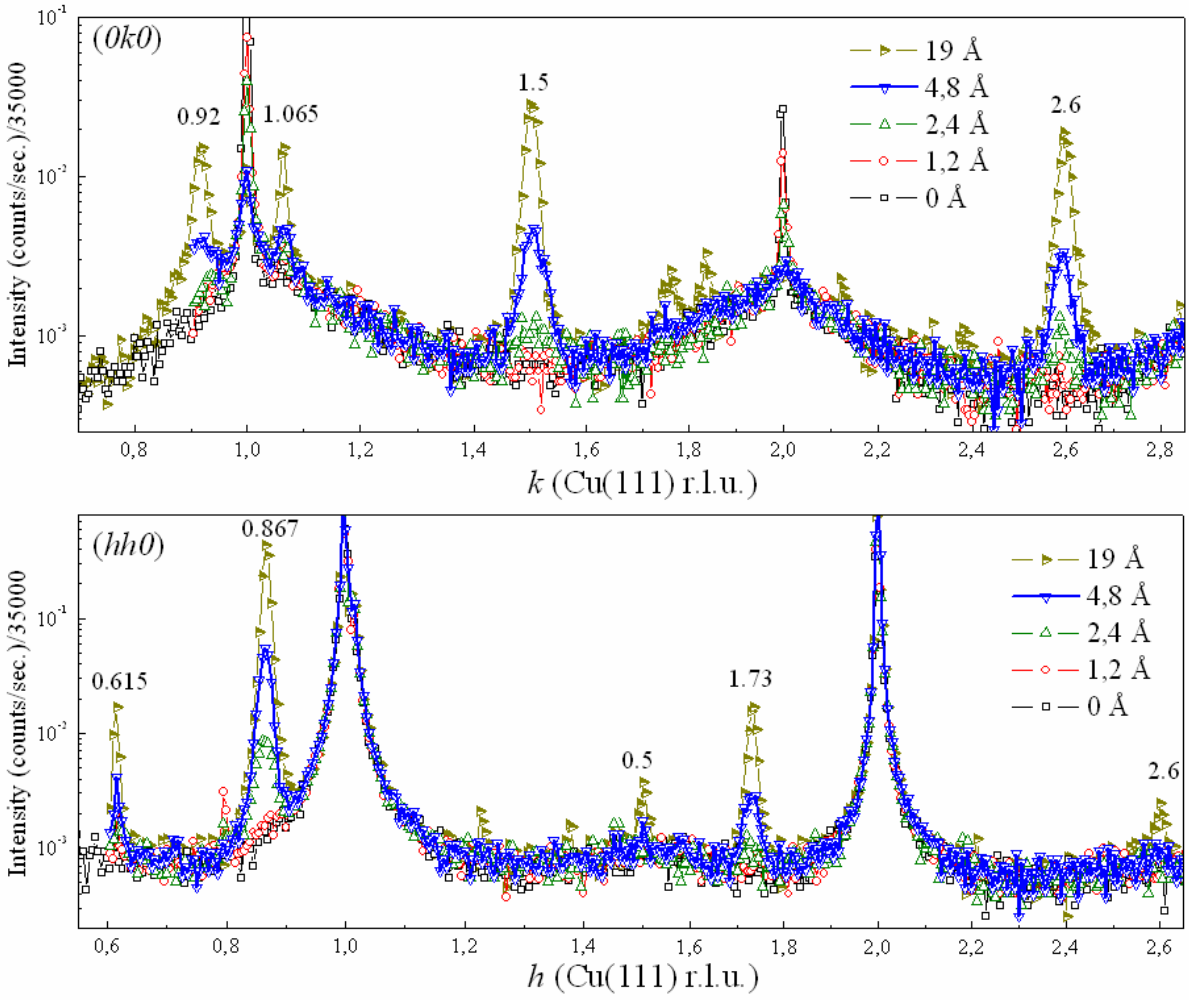

Figure 5.18: *Evolution of the in-plane scans along the (0k0) and (hh0) directions function of the thickness:*
Main reflections appear along the (0*k*0) at *k* = 1.5, 2.6 and *k* = 0.92, 1.065. Along the (*hh*0) directions new peaks appear at *h* = 0.615, 0.867, 1.5, 1.73, 2.6.

thickness deposited under 10^{-6} mbar oxygen. Two in-plane scan directions are shown: along (0*k*0) and (*hh*0). New diffraction positions appear at k = 0.92, 1.065, 1.5, and 2.6, and at h = 0.615, 0.867, 1.5, 1.73, and 2.6. All the values are given in function of the Cu(111) *reciprocal lattice units* (r.l.u.). The diffracted intensity at these new positions evolves differently one from another as a function of the thickness.

I will restrain the discussion to the main reciprocal lattice features, i.e. k = 1.5 and 2.6,

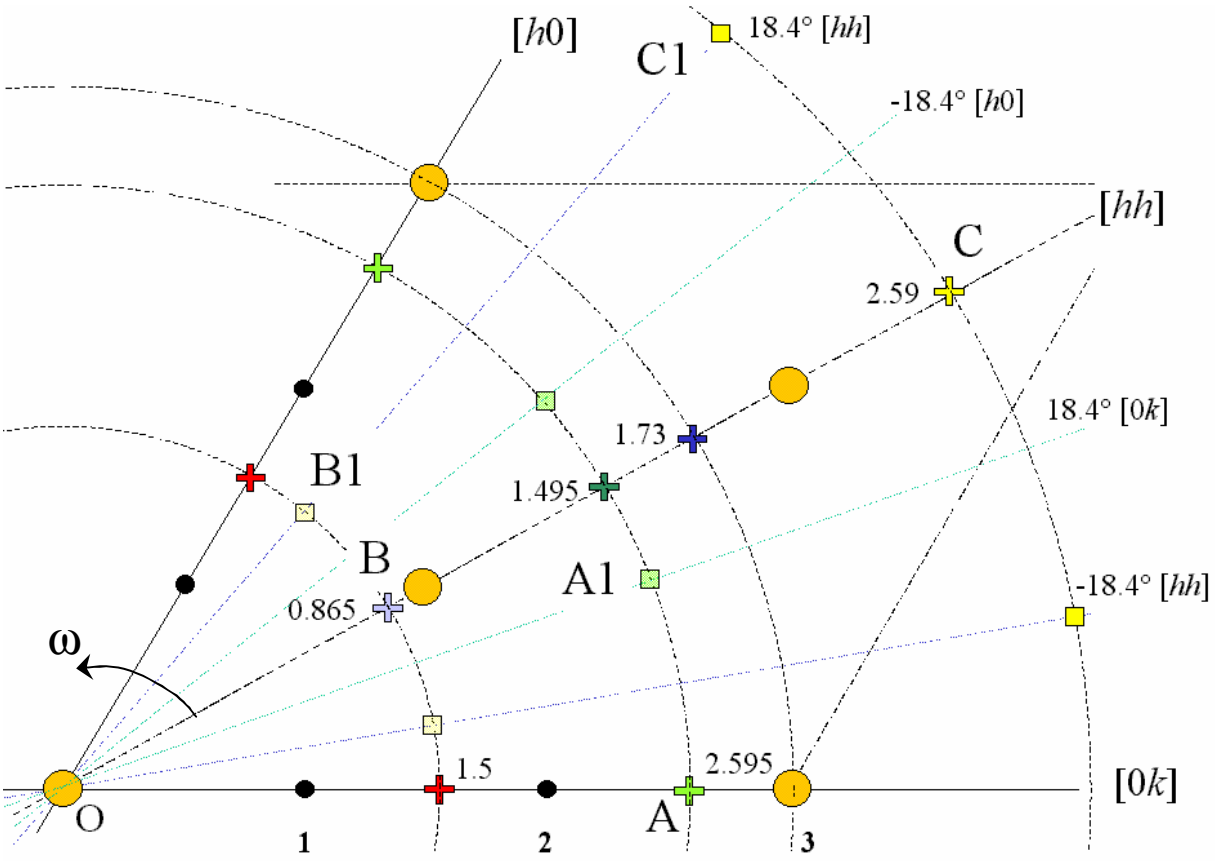

Figure 5.19: *NiO/Cu(111) reciprocal space in-plane cut-off:*
The large circles define the Cu(111) Bragg peaks in the reciprocal space and the small ones, the rods intersection with the (*hk*0) plane. The new peaks which appear along the Cu(111) in-plane directions are indexed with cross symbols and the squares stand for the peaks obtained by rocking scans (in-plane symmetry).

and h = 0.867 and 1.73. To establish the in-plane symmetry, rocking scans (rotations of the crystal around the axis normal at the surface, ω angle of the SUV four-circle goniometer) were recorded passing through all new positions. The angular positions of the peaks are schematically drawn in figure 5.19, which presents the in-plane cut-off of the NiO/Cu(111) reciprocal space.

Considering a perfect epitaxial relationship NiO[10]||Cu[10] between NiO(111) and Cu(111), in the Cu(111) reciprocal lattice units we expect new peak positions at:

$$\text{- along } [0k]_{Cu(111)} \rightarrow 0.86,\ 1.73,\ 2.59 \ldots = n \times \frac{1/2.95}{1/2.56}, \text{ with } n = 1, 2 \ldots$$

$$\text{- along } [hh]_{Cu(111)} \rightarrow 0.86,\ 1.73,\ 2.59 \ldots = n \times \frac{1/\sqrt{3} \times 2.95}{1/\sqrt{3} \times 2.56}, \text{ with } n = 1, 2 \ldots$$

In figure 5.19, along the [*hh*] directions all these peaks appear. On the contrary, along the [0*k*] direction, only the peak at $k = 2.59$ can be observed. Taking into account that all the peaks presented above are in fact Bragg peaks, the absence of the 0.86 and 1.73 positions along [0*k*], which are rods intersection with the (*hk*0) plane, can be understood taking into account the roughness of the NiO(111) film [Robi86, Robi91] and/or the very small amount of evaporated NiO.

The 1.5 position can be obtained considering the NiO[10]||Cu[11] or the NiO[11]||Cu[10]♣ epitaxial relationships:

$$\text{- along } [0k]_{Cu(111)} \rightarrow 0.5,\ 1,\ 1.5 \ldots = n \times \frac{1/\sqrt{3} \times 2.95}{1/2.56}, \text{ with } n = 1, 2 \ldots$$

$$\text{- along } [hh]_{Cu(111)} \rightarrow 1.5,\ 3,\ 4.5 \ldots = n \times \frac{1/2.95}{1/\sqrt{3} \times 2.56}, \text{ with } n = 1, 2 \ldots$$

In fact, this epitaxial relationship can also be expressed as rotations at ±30° of the NiO(111) lattice with respect to the Cu(111) lattice. The absence of the peaks at $k = 0.5$ and 2.5 is related also with the roughness of NiO films (3D growth, islands formation) and to the small amount of matter.

Scans along the direction normal to the surface (ℓ-scans) were also performed for all the new peaks observed along both in-plane directions. A value of 2.67 was found to characterize all these peaks and corresponds to a perpendicular lattice parameter of 7.02 Å. Compared with the expected value for NiO(111), of 7.23 Å, this value suggest a small compression of the $c_{NiO(111)}$-axis. The recorded ℓ-scans do not allow concluding on the fcc or hexagonal nature of the NiO lattice. However, the apparition of the peaks at positions characterizing the in-plane NiO(111) structure can be an argument for the fcc stacking (nearest neighbor in-plane distance related directly with the fcc structure).

♣ These two epitaxial relationships are equivalent in the surface plane: if we take the NiO[10] direction parallel to the Cu[11] one, it implies that the NiO[11] is parallel to the Cu[01] direction. But the Cu[10] and the Cu[01] directions are confounded due to the hexagonal symmetry (equivalent positions at 60°).

In this way we can explain the apparition of the main peaks along the in-plane Cu(111) crystallographic directions. The other peaks, outside these directions, can be obtained considering rotations of the NiO(111) lattice with ±18.4°, as shown in figure 5.19. For example, the +18.4° rotation (counterclockwise with respect to the [0*k*] and [*hh*] respectively, as specified in the figure) will produce the following transitions: A → A1, B → B1 and C → C1. The other peaks can be obtained in the same manner by a -18.4° rotation.

Summarizing, the GIXD results reveal strong intensities at positions which characterize the NiO[10]||Cu[10] epitaxy. Due to the strong lattice mismatch between the NiO(111) and Cu(111) lattices, of about 16%, the film relaxes mainly *via* rotations, i.e. ±30° and ±18.4°. However, there are parts of the reciprocal space which were not investigated, and further GIXD measurements are necessary to fully describe the structure. In addition, compared with the LEED results (table 5.1), the diffraction measurements show several differences. While LEED shows the formation of a "bulk" NiO($\sqrt{3}\times\sqrt{3}$)R30° structure, GIXD suggests the growth of well defined NiO(111) surface. Furthermore, the reconstruction-like structure observed by LEED was not found by GIXD. However, we note that the LEED and GIXD measurements were performed at different temperatures. While LEED was performed at room-temperature, the surface diffraction scans were recorded at T = 250°C, possibly favoring NiO phase transformations. It is known, for example, that the **Ni_2O_3** phase has a melting point of about 600°C (compared with 1960°C for NiO) and therefore varying the temperature toward 250°C may induce a phase transformation. On the other hand, we can attribute the differences between LEED and GIXD results to possible effects coming from structure distortions[♣] relative to the fcc NiO(111). Imagine, for example, that in the schematic drawing in figure 5.17-b (showing the NiO($\sqrt{3}\times\sqrt{3}$)R30° construction), all atoms in the NiO(111) structure are present, but they are not exactly in the same plane. More precisely, we can assume that in the former NiO(111) plane remain only the atoms disposed in the NiO($\sqrt{3}\times\sqrt{3}$)R30° structure, which is in perfect epitaxial relation with the copper substrate, all the others being slightly displaced in a superior atomic plane. In this case, the LEED patterns will be sensitive to the NiO($\sqrt{3}\times\sqrt{3}$)R30° structure, and the displaced atoms could be disposed in order to generate the reflections associated with the so-called "reconstruction". Increasing the temperature such strains could disappear and lead to the

[♣] We discuss here structure distortions (e.g. strains) which can not be assimilated with new Ni_xO_y phases.

expected NiO(111) structure measured by GIXD. As argument for this hypothesis is the rotational symmetry of ±18.4° observed by both LEED and GIXD, which seems to describe the same structure instead of two different phases. Double electron diffraction may be another possible explanation for the differences observed by LEED and GIXD, for this hypothesis too we lack experimental data allowing concluding.

A clearer interpretation would require additional measurements with respect to temperature by GIXD. The important points related to the comparison with the direct NiO deposition are however reached: an important crystallization, but a poor O_2 efficiency.

☑ *Combined STM, LEED and GIXD measurements evidence the structural ordering of the NiO films deposited at high temperatures. The complex structure of Ni deposited under oxygen atmosphere at 250°C is not yet completely solved. Complementary GIXD measurements are necessary at 250°C and room-temperature as well, to describe the structure of the NiO films. Nevertheless, it is obvious that this method of elaboration is favorable for obtaining well defined fcc NiO(111) films, although the growth becomes strongly 3D.*

5.3 NiO/FeNi/Cu(111) BILAYER GROWTH

Here we present the structure of the NiO films deposited by Ni evaporation under oxygen atmosphere at 150°C on a FeNi alloy, itself deposited on a vicinal (1.2° miscut) Cu(111) surface. A six-circle geometry was used to manage the vicinal surface of our sample. Therefore, in order to keep the crystallographic [111] direction parallel to the azimuthal rotation axis, two additional circles are required to compensate the sample miscut. This movement is controlled with two perpendicular cradles capable to create a tilt movement of the sample on any direction. In our particular case the cradles were aligned one along the $[1\bar{1}0]$ step direction and the other along the crystal cut direction (perpendicular to the steps), i.e. $[11\bar{2}]$. A second remark concerns the acquisition temperature, which was set to 150°C, same as the temperature used during the evaporation, for both FeNi and NiO, in order to limit the interdiffusion at the FeNi/Cu(111) interface.

The FeNi alloy grow in a pseudomorphic manner and the only evidence for the formation of ordered FeNi appears along the crystal truncation rods (figure 5.20), e.g. (10ℓ)

rod (figure 5.20-c), where supplementary Bragg peak appear. They are related with the formation of twinned FeNi structures. The apparition of these twinned structures is better evidenced by rocking scan at ℓ = 1, as shown in figure 5.21-a. In this way, we find at every 60° alternating Cu and FeNi peaks (angular distance between two Cu peaks of 120° and 60° for the twinned FeNi). The FeNi alloy shows pseudomorphic growth even for very thick films (> 60 Å). In figure 5.20-a and 5.20-b we show the in-plane scans for clean Cu(111), 7 Å FeNi/Cu(111) and NiO(7.5Å)/FeNi(7Å)/Cu(111). Only new Bragg peaks characterizing the

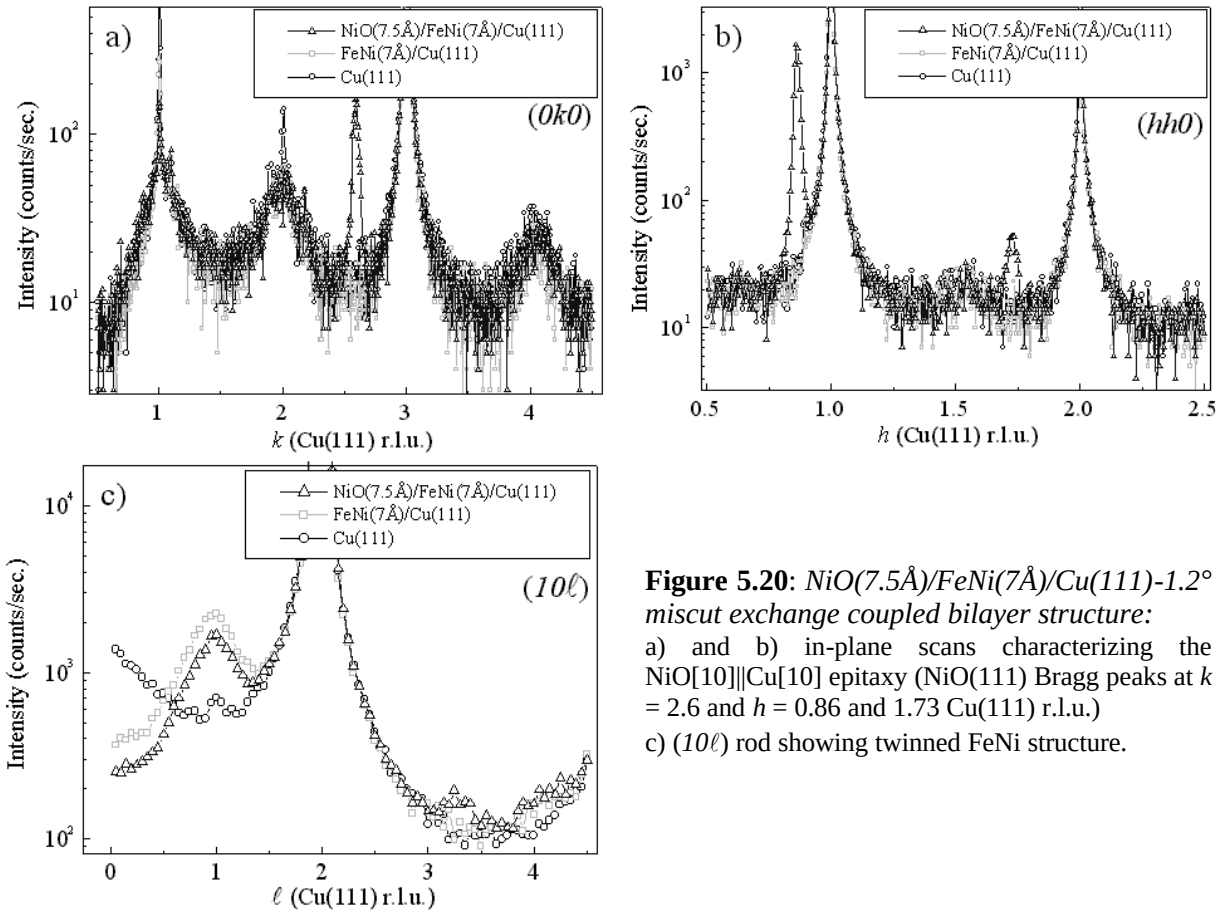

Figure 5.20: *NiO(7.5Å)/FeNi(7Å)/Cu(111)-1.2° miscut exchange coupled bilayer structure:*
a) and b) in-plane scans characterizing the NiO[10]||Cu[10] epitaxy (NiO(111) Bragg peaks at k = 2.6 and h = 0.86 and 1.73 Cu(111) r.l.u.)
c) (*10ℓ*) rod showing twinned FeNi structure.

NiO(111) structure appear. The Bragg peaks position along both in-plane directions (k = 2.6 and h = 0.86; 1.73) characterize a NiO[10]||Cu[10] epitaxial relationship.

A rocking scan characterizing the NiO(111) twins is shown in figure 5.21-b. From this figure we can affirm from a qualitative point of view that the faulted and unfaulted NiO(111) fractions are close to each other. Contrarily to the NiO/Cu(111), the ±30° and ±18.4° rotated NiO(111) structures have not been observed. The absence of rotated structures suggest that the NiO(111) epitaxy with a FeNi layer is better than the one obtained on Cu(111). Since FeNi grow in a pseudomorphic manner on the Cu(111) substrate and since the mismatch between NiO(111) and the FeNi is still ~16%, we should expect the apparition of variants as

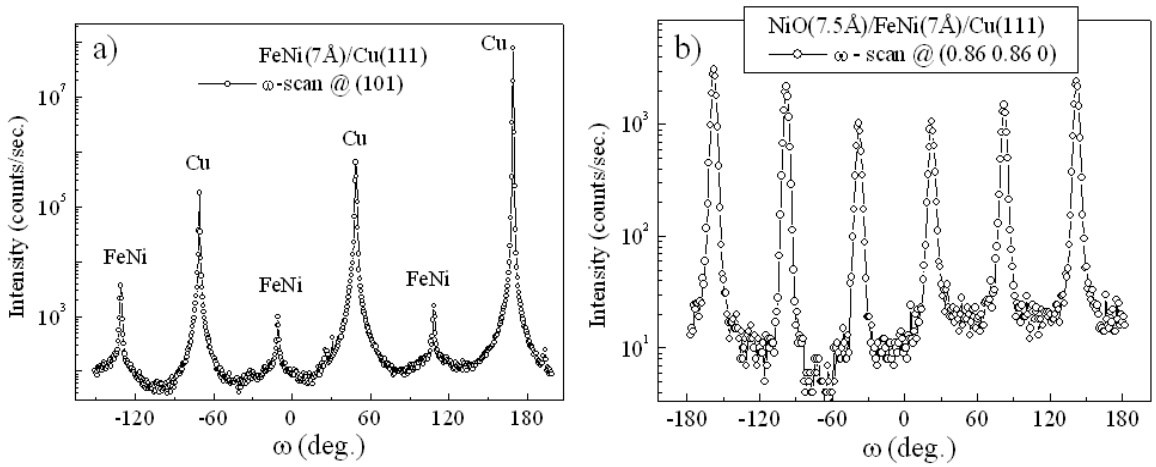

Figure 5.21: *in-plane NiO(7.5Å)/FeNi(7Å) bilayer symmetry:*
a) FeNi(7Å)/Cu(111) rocking scan (ω - scan) at $\ell = 1$, showing the FeNi twinned structure.
b) NiO(7.5Å)/FeNi(7Å)/Cu(111) rocking scan at the (0.86 0.86 0) position corresponding to the NiO(111), showing un-faulted and faulted stacking (twins).

in the case of the NiO/Cu(111). It is possible that the apparition of twins in the FeNi alloy favors the nickel oxide epitaxy. In addition, there might be slight interdiffusion at the NiO/FeNi interface which can accommodate the oxide lattice parameter. Only integrated intensity measurements along rods and chemical analysis can give details about the interface (formation of mixed Fe-Ni-O, spinel structure). An exhaustive study is in course at this time.

Several NiO films with thicknesses between 7.5 and 60 Å were grown on a thicker FeNi film (20 Å). The diffraction measurements show the same characteristics of the NiO(111) structure, i.e. formation of NiO(111) in good epitaxy including twinned NiO(111).

☑ *Preliminary structural studies of the NiO(111) grown at 150°C on ferromagnetic FeNi(111) alloys revealed a better epitaxy than the one characterizing the NiO/Cu(111) interface, i.e. the absence of rotated multi-domains. The FeNi alloys show a pseudomorphic growth even for very high thicknesses (~60 Å) with twin formation, possible at the origin of the good NiO(111)/FeNi(111) epitaxy. Nevertheless, additional chemical and structural analyses are required to characterize this complex interface.*

5.4 CONCLUSIONS

Using higher temperatures leads to improved structural ordering for both, NiO nuggets and metallic Ni deposition under oxygen atmosphere. Due to the increased mobility, the high temperature deposited NiO films exhibit different morphology compared to the room

temperature NiO films, i.e. the absence of the (monodispersed) 40 Å diameter holes. While increased temperature does not affect the chemistry for the NiO nuggets evaporation, the Ni evaporation in O_2 leads to drastic changes in the relative evolution of the Ni and O quantities. Strong Ni overstoichiometry is observed, related to the poor O_2 *oxidizing efficiency*. The NiO morphology, also differs from the homogenous aspect (~ layer-by-layer) which characterizes the NiO room temperature elaborated films. In the low coverage regime (0 – 2.5 Å), isotropic shaped islands characterize the NiO films, while for higher thicknesses faceted islands are formed. For thick NiO films (> 7.5 Å), we can thus conclude that better structural order is obtained in detriment of the Cu(111) wetting.

High-resolution STM images suggest a Ni-O *cluster nucleation/aggregation* mechanism, leading to this specific 3D morphology. Due to STM contrast considerations, we found that the NiO islands are always O-terminated. Structural ordering was evidenced using combined LEED and GIXD measurements, related with the increased temperature during the NiO films deposition and to the less disrupted Cu surface (absence of ~40 Å holes). The strong misfit between the metallic substrate and the oxide film (~15%) leads to formation of rotated multi-domains. However, additional structural measurements are required to fully describe the complex structure of the NiO films and to discriminate between the different possibilities (new Ni_xO_y phase, structural distortions, etc.). To the contrary, the NiO films deposited at high temperatures on FeNi alloys leads to formation of epitaxial NiO(111).

CONCLUSIONS AND PERSPECTIVES

CONCLUSIONS

The very first stages of the growth, of the finally fascinating and original but also quite complex NiO/Cu(111) interface, were successfully characterized on a microscopic scale including chemical, morphological, and structural aspects. For that purpose we used different elaboration procedures and we combined *in-situ* laboratory and synchrotron radiation techniques. Complete exchange coupled NiO/FeNi/Cu(111) bilayer system have also been investigated .

In a first step, the metallic Ni/Cu(111) interface has been studied (chapter 3), evidencing the close relationship between morphology, structure and magnetic properties. STM revealed step-decoration growth of Ni together with island formation on larger terraces on a vicinal Cu(111) substrate; the ability of Cu atoms to cap Ni islands has also been observed. Surface diffraction (GIXD) evidenced a pseudomorphic growth of the Ni layers on Cu(111) in the low coverage regime (0 – 1 ML). For higher thicknesses (> 1 ML) the Ni films are characterized by a *tetragonalized* fcc structure. Both, the Cu *capping* and the Ni *tetragonalization*, were used to explain the magnetic spin and orbital moments observed by XMCD. The reduced spin magnetic moments were correlated with the 3d hybridization at the Ni-Cu interface, for small thicknesses (< 1 ML) and with an increased hybridization effect due to the formation of a second Ni-Cu interface by Cu capping, for larger thicknesses (> 1 ML). The in-plane orbital moment anisotropy confirms that the easy axis of magnetization is in the plane for all measured thin nickel films.

Ultra-thin NiO films (0 – 30 Å), obtained through MBE evaporation of NiO nuggets, were grown at room temperature (chapter 4) and at high temperature (chapter 5). The comparison with the metallic Ni/Cu(111) interface highlighted the oxygen atoms *surfactant* effect enhancing the *direct exchange* mechanism between Ni and Cu. As a consequence, in the first growth stages, mainly metallic Ni is formed, diffused in the top copper layers. The chemical differences between the two evaporation methods (NiO nuggets and metallic Ni under partial oxygen pressure at 250°C), has been related with the *oxidizing efficiency* of oxygen with respect to its chemical state: ionic or molecular. Films with larger thicknesses (> 25 Å) show stoichiometric NiO. Therefore, the system can globally be described in terms of a spontaneous NiO/Ni/Cu(111) layering.

The room temperature elaborated NiO films exhibit an original morphology for very low coverages (0 – 2 Å): topographic holes (~40 Å diameter) that undergo *nucleation* and *multiplication* processes. Confirming the STM real-space observations, GISAXS experiments and calculations allowed to evidence the *self-organized* nature of the NiO islands, for the thicker NiO films (> 4 Å) obtained at room temperature. Although very homogenous (~ layer-by-layer), the NiO films do not show long-range structural ordering, related with the disrupted NiO/Cu(111) interface. Nevertheless, surface diffraction measurements allowed a quantitative estimation of the *differential diffusion* process, evidencing the formation of one equivalent metallic Ni layer at the interface. Both, increased temperature (250°C) growth for the NiO nuggets and post-annealing, lead to improvements of the crystalline quality.

Due to the poor oxidizing efficiency of the molecular oxygen, the NiO films deposited from metallic Ni at 250°C, exhibit several differences with respect to those obtained by NiO nuggets evaporation at room temperature. The morphology is characterized by 3D growth in the whole thickness range, closer to the metallic Ni/Cu(111) interface morphology than to the NiO nuggets one. Below ~2 Å, the NiO islands were atomically resolved by STM, and using the STM chemical contrast we concluded that only O-terminated islands forms on the Cu(111) surface. A *cluster nucleation/aggregation* mechanism was proposed, based on the STM observations. Formation of α-Ni_2O_3 hexagonal phase, or structural distortion of the NiO(111)($\sqrt{3}\times\sqrt{3}$)R30° structure could both explain the LEED and GIXD results.

First studies were performed on the exchange coupled NiO/FeNi/Cu(111) system, using both, NiO nuggets and metallic Ni in oxygen partial pressure evaporation. Interestingly, morphological studies revealed identical NiO islands sizes (~12 Å) as obtained by GISAXS calculations for the NiO/Cu(111) interface. This size seems thus to be an *intrinsic characteristic* of the NiO films. In addition, sharp NiO/FeNi interfaces were obtained, with textured NiO. Structural analysis of the NiO films, obtained from metallic Ni evaporation under oxygen partial pressure, deposited on FeNi/Cu(111) films, evidenced twinned NiO(111), in much better epitaxy than the oxides deposited on the Cu(111) substrate.

With respect to magnetically exchange coupled spin-valves, these results highlight the strong chemical reactivity between NiO and Cu. Hence the detrimental role of pin-holes may not only be limited to current shorts. Anyway, it is clear that this interface must be avoided to obtain a valuable device. Interestingly, when deposited on FeNi alloys, the NiO films do not

exhibit such reactivity. Improving spin valves leads thus to the improvement of the ferromagnetic FeNi films prior to NiO evaporation.

PERSPECTIVES

The complex structure and growth observed for NiO ultra-thin films evidences interesting parameters as temperature, deposition conditions favoring different characteristics as the wetting of the nanometer oxide film or the epitaxial growth and crystalline quality.

In the present study we could evidence the subtle role of the surface chemistry that may even lead to self organization on non patterned or reconstructed substrates. This result may open a new route to self-organization and certainly deserves further studies. Moreover the role of oxygen during oxidation appears as quite complex since its chemical state (molecular, ionic or atomic) obviously plays an important role as well as the partial pressure in the chamber favoring more or less surfactant effects. A clear understanding and description of the interplay between all these terms will also need further work.

REFERENCES

[Akta97] B. Aktas, *Thin Solid Films* **307**, 250 (1997)

[Alde96] D. Alders, F. C. Voogt, T. Hibma, G. A. Sawatzky, *Phys. Rev. B* **54**, 7716 (1996)

[Alde98] D. Alders, L. H. Tjeng, F. C. Voogt, T. Hibma, G. A. Sawatzky, C. T. Chen, J. Vogel, M. Sacchi, and S. Iacobucci, *Phys. Rev. B* **57**, 11623 (1998)

[Alta93] M. Altarelli, *Phys. Rev. B* **47**, 597 (1993)

[ana-rod] http://www.esrf.fr/computing/scientific/joint_projects/ANA-ROD/home.htm

[Ande97] J.F. Anderson, M. Kuhn, U. Diebold, K. Shaw, P. Stoyanov, D. Lind, *Phys. Rev. B* **56**, 9902 (1997)

[Ande98] J.F. Anderson, M. Kuhn, U. Diebold, *Surf. Sci. Spectra* **4**, 266 (1998)

[Andr85] S. R. Andrews and R. A. Cowley, *J. of Phy. C (Solid State Physics)* **18**, 6427 (1985)

[Aufr01] B. Aufray and C. Girardeaux, private communication

[Auge25] P. Auger, *J. Phys. Radium* **6**, 205 (1925)

[Auge26] P. Auger, *Ann. Phys. (Paris)* **6**, 183 (1926)

[Babo99] D. Babonneau, A. Naudon, D. Thiaudière and S. Lequien, *J. Appl. Cryst.* **32**, 226 (1999)

[Babo00] D. Babonneau, J. Briatico, F. Petroff, T. Cabioc'h and A. Naudon, *J. Appl. Phys.* **87**, 3432 (2000)

[Baib88] M. N. Baibich, J. M. Broto, A. Fert, F. Nguyen Van Dau, F. Petroff, P. Etienne, G. Creuzet, A. Friederich, J. Chazelas, *Phys. Rev. Lett.* **61** 2472 (1988)

[Band85] Y. Bando, T. Terashima, *Adv. Ceram.* **15**, 607 (1985)

[Barb99] A. Barbier, G. Renaud, C. Mocuta, et al., *Surf. Sci.* **433-435**, 761 (1999)

[Barb00a] A. Barbier, C. Mocuta, H. Kuhlenbeck, et al., *Phys. Rev. Lett.* **84**, 2897 (2000)

[Barb00b] A. Barbier, C. Mocuta, and G. Renaud, *Phys. Rev. B* **62**, 16056 (2000)

[Baud99] R. Baudoing-Savois, G. Renaud, M. De Santis, et al., *Nucl.Instrum.Methods **B** **149**, 213 (1999)

[BengPhD] O. Bengone, *PhD Thesis*, Université de Metz (2000)

[Berg92] A. Berger, U. Linke, and H. P. Oepen, *Phys. Rev. Lett.* **68**, 839 (1992)

[Bert96] Th. Bertrams and H. Neddermeyer, *J. Vac. Sci. Technol.*, B **14**, 1141 (1996)

[beyond2000] http://www.beyond2000.com/news/jun_01/story_1179.html

[Binn82a] G. Binnig, H. Rohrer, Ch. Gerber, and E. Weibel, *Phys. Rev. Lett.* **49**, 57 (1982)

[Binn82b] G. Binnig, H. Rohrer, *Hev. Phys. Acta* **55**, 726 (1982)

[Binn86] G. Binnig, H. Rohrer, *IBM J. Res. Develop*. **30**, 355-369 (1986)

[Bloe96] P.J.H. Bloemen, P.A.A. van der Heijden, R.M. Wolf, J. aan de Stegge, J.T. Kohlhepp, A. Reinders, R.M. Jungblut, P.J. van der Zaag, W.J.M. de Jonge, *Mater. Res. Soc. Symp. Proc.* **401**, 485 (1996)

[Boeg02] C. Boeglin, S. Stanescu, S. Cherifi, J.-P. Deville, P. Ohresser, A. Barbier, N. B. Brookes, *Surf. Sci.* **507-510**, 522 (2002)

[Bonn01] "*Scanning Probe Microscopy and Spectroscopy: Theory, Techniques, and Applications*", 2nd ed., D. Bonnell, (*Ed.*), Wiley-VCH, New York (2001)

[Borc95] W. Borchardt-Ott, "*Crystallography*", Second Edition, Springer, Berlin (1995)

[Brod93] A. Brodde, K. Dreps, J. Binder, et al., *Phys. Rev. B* **47**, 6609 (1993)

[Brun89] P. Bruno, *Phys. Rev. B* **39**, 865 (1989)

[Cai98] Y.Q. Cai, M. Ritter, W. Weiss, A.M. Bradshaw, *Phys. Rev. B* **58**, 5043 (1998)

[Cama98] J. Camarero, J. Ferron, V. Cros, et al., *Phys. Rev. Lett.* **81**, 850 (1998)

[Cama01a] J. Camarero, M. A. Nino, D. Farias, et al., *Surf. Sci.* **482**, 1077 (2001)

[Cama01b] J. Camarero, J. J. de Miguel, R. Miranda, et al., *Phys. Rev. B* **64**, 125406/1 (2001)

[Capp93] D. Cappus, C. Xu, D. Ehrlich, B. Dillmann, C. A. Ventrice, C. Al Shamery, H. Kuhlenbeck, H.-J. Freund, *Chem. Phys.* **177,** 533 (1993)

[Care92] M. J. Carey, A. E. Berkowitz, *Appl. Phys. Lett.* **60,** 3060 (1992)

[Carr90] B. Carrière, and G. Krill, Aussois Summer School course (1990)

[Carr93] P.Carra, B.T.Thole, M.Altarelli, X.Wang, *Phys. Rev. Lett.* **70,** 694 (1993)

[Cast97] M. R. Castell, P. L. Wincott, N. G. Condon, C. Muggelberg, G. Thornton, S. L. Dudarev, A. P. Sutton, and G. A. D. Briggs, *Phys. Rev. B* **55**, 7859 (1997)

[Cast99] M. R. Castell, S. L. Dudarev, G. A. D. Briggs, and A. P. Sutton, *Phys. Rev. B* **59**, 7342 (1999)

[Chai97] A.Chaiken, R.J.Wold, UXO Forum (1997)

[Cham77] B. Chamberland, *Crit. Rev. Solid State Sci.* **7** (1977)

[Cham98] S.A. Chambers, Y.J. Kim, Y. Gao, *Surf. Sci. Spectra* **5**, 219 (1998)

[Cham99a] S.A. Chambers, S.I. Yi, *Surf. Sci.* **439**, L785 (1999)

[Cham99b] S.A. Chambers, S.A. Joyce, *Surf. Sci.* **420**, 111 (1999)

[Cham00a] S. A. Chambers, *Surf. Sci. Rep.* **39**, 105 (2000)

[Cham00b] S.A. Chambers, S. Thevuthasan, S.A. Joyce, *Surf. Sci. Lett.* **450**, L273 (2000)

[Chen92] J. Chen and J. L. Erskine, *Phys. Rev. Lett.* **68**, 1212 (1992)

[Chen93] "*Introduction to Scanning Tunneling Microscopy*", C.J. Chen, Oxford University Press (1993)

[Chen95] C. T. Chen, Y. U. Idzerda, H.-J. Lin, et al., *Phys. Rev. Lett*. **75**, 152 (1995)

[Cher01a] S. Cherifi, S. Stanescu, C. Mocuta, et al., *Surf. Sci.* **482**, 1056 (2001)

[Cher01b] S. Cherifi, C. Boeglin, S. Stanescu, et al., *Phys. Rev. B* **64**, 184405/1 (2001)

[Cher97] G. Chern, C.L. Chang, Y.R. Chean, *Mater. Res. Soc. Symp. Proc.* **474**, 271 (1997)

[CherPhD] S. Cherifi, *PhD Thesis*, Université “Louis Pasteur”, Strasbourg (2001)

[Chie95] C. L. Chien, Magnetism and Giant Magneto-transport Properties in Granular Solids (1995) volume of *Annual Review of Materials Science*

[Chop00] H. D. Chopra, D. X. Yang, P. J. Chen, D. C. Parks, W. F. Egelhoff Jr, *Phys. Rev. B* **61**, 9642 (2000)

[Chop97] H. D. Chopra, B. J. Hockey, P. J. Chen, W. F. Egelhoff Jr, M. Wuttig; S. Z. Hua, *Phys. Rev. B* **55**, 8390 (1997)

[Citr78] P. H. Citrin, G. K. Wertheim, and Y. Baer, *Phys. Rev. Lett.* **41**, 1425 (1978)

[Comi02] E. Comini, M. Ferroni, V. Guidi, et al., *Sensors and Actuators B* **B84**, 26 (2002)

[Conn69] W.C. Connor, R.J. Kokes, *J. Phys. Chem.* **73**, 2436 (1969)

[Deby14] P. Debye, *Ann. der Physik* **43**, 49 (1914)

[DeSi00] W. J. DeSisto *et al*, *Appl. Phys. Lett.* **76** 3789 (2000)

[Dhes99] S. S. Dhesi, H. A. Durr, L. van der, et al., *Phys. Rev. B* **60**, 12852 (1999)

[Doni70] S. Doniach et M. Sunjic, *J. Phys. C* **3**, 285 (1970)

[Duda97] S. L. Dudarev, A. I. Liechtenstein, M. R. Castell, G. A. D. Briggs, and A. P. Sutton, *Phys. Rev. B* **56**, 4900 (1997)

[Durr96] H. A. Durr and G. van der Laan, *Phys. Rev. B* **54**, R760 (1996)

[Egel86] W. F. Egelhoff, Jr., *Surf. Sci. Rep.* **6**, 253 (1986)

[Eins05] A. Einstein, *Ann. Physik* **17**, 132 (1905)

[Eise93] S. Eisebitt, T. Boske, J.-E. Rubensson, W. Eberhardt, *Phys. Rev. B* **47,** 14103 (1993)

[Erde02] Z. Erdelyi, C. Girardeaux, Z. Tokei, et al., *Surf. Sci.* **496**, 129 (2002)

[Erdm00] N. Erdman, O. Warschkow, D. E. Ellis, et al., *Surf. Sci.* **470**, 1 (2000)

[Erik92] O. Eriksson, A. M. Boring, R. C. Albers, et al., *Phys. Rev. B* **45**, 2868 (1992)

[Ersk75] J. L. Erskine, E. A. Stern, *Phys. Rev. B* **12,** 5016 (1975)

[ESRF] http://www.esrf.fr

[Evan96] G. A. Evangelakis, N. I. Papanicolaou and G. C. Kallinteris, *Surf. Sci.* **369**, 185 (1996)

[Fan89] W.C.Fan, A.Ignatiev, H.Huang, S.Y.Tong, *Phys. Rev. Lett.* **62**, 1516 (1989)

[Feid89] R. Feidenhans'l, *Surf. Sci. Rep.* **10**, 105 (1989)

[Ferr00] J. Ferron, L. Gomez, J. M. Gallego, et al., *Surf. Sci.* **459**, 135 (2000)

[Figu93] J. de la Figuera, J. E. Prieto, C. Ocal, et al., *Phys. Rev. B* **47**, 13043 (1993)

[Figu94] J. de la Figuera, J. E. Prieto, C. Ocal, et al., *Surf. Sci.* **307**, 538 (1994)

[Fing80] L. W. Finger and R. M. Hazen, *J. Appl. Phys.* **51,** 5362 (1980)

[Font97] W.F.J. Fontijn, R.M. Wolf, R. Metselaar, P.J. van der Zaag, *Thin Solid Films* **292**, 270 (1997)

[Fran00] R. Franchy, *Surf. Sci. Rep*. **38**, 195 (2000)

[Freu02] H. J. Freund, *Surf. Sci.* **500**, 271 (2002)

[Freu93] H.-J. Freund, E. Umbach (Eds.), "*Adsorption on Ordered Surfaces of Ionic Solids and Thin Films*", Springer Series in Surface Sciences, vol. **33**, Springer, Heidelberg, (1993)

[Freu96] H. J. Freund, H. Kuhlenbeck, and V. Staemmlers, *Rep. Prog. Phys*. **59**, 283 (1996)

[Fuji90a] T. Fujii, M. Takano, R. Katano, Y. Bando, Y. Isozumi, *J. Cryst. Growth* **99**, 606 (1990)

[Fuji90b] T. Fujii, M. Takano, R. Katano, Y. Bando, Y. Isozumi, *J. Appl. Phys.* **68**, 1735 (1990)

[Fuji94a] T. Fujii, M. Takano, R. Kakano, Y. Isozumi, Y. Bando, *J. Magn. Magn. Mater.* **135**, 231 (1994)

[Fuji94b] T. Fujii, M. Takano, R. Katano, Y. Isozumi, Y. Bando, *J. Magn. Magn. Mater.* **130**, 267

[Fuji95a] R. Fujisawa and S. Tsujikawa,, edited by Murakami-T and Ewing-Rc "*Japan Scientific Basis for Nuclear Waste Management*" XVII Symposium. Mater. Res. Soc Pittsburgh PA USA (1995)

[Fuji96] T. Fujii, D. Alders, F.C. Voogt, T. Hibma, B.T. Thole, G.A. Sawatzky, *Surf. Sci.* **366**, 579 (1996)

[Fuji99] T. Fujii, F.M.F. de Groot, G.A. Sawatzky, F.C. Voogt, T. Hibma, K. Okada, *Phys. Rev. B* **59**, 3195 (1999)

[Gain97a] J.M. Gaines, P.J.H. Bloemen, J.T. Kohlhepp, C.W.T. Bulle-Lieuwma, R.M. Wolf, A. Reinders, R.M. Jungblut, P.A.A. van der Heijden, J.T.W.M. van Eemeren, J. aan de Stegge, W.J.M. de Jonge, *Surf. Sci.* **373**, 85 (1997)

[Gain97b] J.M. Gaines, J.T. Kohlhepp, J.T.W.M. Van Eemeren, R.J.G. Elfrink, F. Roozeboom, W.J.M. de Jonge, *Mater. Res. Soc. Symp. Proc*. **474**, 191 (1997)

[Gain97c] J.M. Gaines, J.T. Kohlhepp, P.J.H. Bloemen, R.M. Wolf, A. Reinders, R.M. Jungblut, *J. Magn. Magn. Mater.* **165**, 439 (1997)

[Gall93] H.C. Galloway, J.J. Benitez, M. Salmeron, *Surf. Sci.* **298**, 127 (1993)

[Gall94] H.C. Galloway, J.J. Benitez, M. Salmeron, *J. Vac. Sci. Technol. A* **12**, 2302 (1994)

[Gall96] H.C. Galloway, P. Sautet, M. Salmeron, *Phys. Rev. B* **54**, R11145 (1996)

[Galt99a] A. Galtayries, J. Grimblot, *J. Electron. Spectrosc. Related Phenom.* **98-99**, 267 (1999)

[Galt99b] A. Galtayries, E. Laksono, J.-M. Siffre, C. Argile and P. Marcus, *Surf. Interface Anal.* **30**, 140 (2000)

[Gao97a] Y. Gao, S.A. Chambers, *J. Cryst. Growth* **174**, 446 (1997)

[Gao97b] Y. Gao, Y.J. Kim, S.A. Chambers, G. Bai, *J. Vac. Sci. Technol. A* **15**, 332 (1997)

[Gao97c] Y. Gao, Y.J. Kim, S. Thevuthasan, S.A. Chambers, P. Lubitz, *J. Appl. Phys.* **81**, 3253 (1997)

[Gao98] Y. Gao, Y.J. Kim, S.A. Chambers, *J. Mater. Res.* **13**, 2003 (1998)

[Geun91] Geunseop Lee and S.-J. Oh, *Phys. Rev. B* **43**, 14674 (1991)

[Gidl89] D. W. Gidley, *Phys. Rev. Lett.* **62**, 811 (1989)

[Gome01] L. Gomez and J. Ferron, *Phys. Rev. B* **64**, 033409/1 (2001)

[Good96] D. W. Goodman, *J. Vac. Sci. Technol. A* **14**, 1526 (1996)

[Gota00] S. Gota, E. Guiot, M. Henriot, et al., *Surf. Sci.* **454**, 796 (2000)

[Gota01] S. Gota, M. Gautier Soyer, and M. Sacchi, *Phys. Rev. B* **64**, 224407/1 (2001)

[Gota99] S. Gota, E. Guiot, M. Henriot, et al., *Phys. Rev. B* **60**, 14387 (1999)

[Grad64] U. Gradmann, *Ann. Physik* **13**, 213 (1964)

[Grif90] J.E. Griffith, G. E. Kochanski, *Annu. Rev. Mater. Sci.* **20**, 219-244 (1990)

[Grüb93] G. Grubel, K. G. Huang, G. Doon, et al., *Phys. Rev. B* **48**, 18119 (1993)

[Guen93] "*Scanning Tunneling Microscopy*", Vol. I, II, and III, H.-J. Guentherodt, R. Wiesendanger (*Eds.*), Springer (1993, 1995, 1996)

[Guin94] A. Guinier, "*X-Ray Diffraction in Crystals, Imperfect Crystals, and Amorphous Bodies*", Dover Publications, New-York (1994)

[Guio98] E. Guiot, S. Gota, M. Henriot, M. Gautier-Soyer, S. Lefebvre, *Mater. Res. Soc. Symp. Proc.* **524**, 101 (1998)

[Guo98] Q. Guo, C. Xu, and D. W. Goodman, *Langmuir* **14**, 1371 (1998)

[Hags64] S. B. M. Hagström, C. Nordling, and K. Siegbahn, *Z. Physik* **178**, 433 (1964)

[Hara92] T. Harada, M.Asano and Y.Mizumati, *J. Cryst. Growth* **116**, 243 (1992)

[Harr68] L. A. Harris, *J. Appl. Phys.* **39**, 1419 (1968)

[Heij95] P.A.A. van der Heijden, J.J. Hammink, P.J.H. Bloemen, R.M. Wolf, M.G. van Opstal, P.J. van der Zaag, W.J.M. de Jonge, *Mater. Res. Soc. Symp. Proc.* **384**, 27 (1995)

[Heij98] P.A.A. van der Heijden, M.G. van Opstal, C.H.W. Swuste, P.H.J. Bloemen, J.M. Gaines, W.J.M. de Jonge, *J. Magn. Magn. Mater.* **182**, 71 (1998)

[Henr94] V.E. Henrich, P.A. Cox, "*The Surface Science of Metal Oxides*", Cambridge University Press, Cambridge, (1994)

[Hibm99] T. Hibma, F.C. Voogt, L. Niesen, P.A.A. van der Heijden, W.J.M. de Jonge, J.J.T.M. Donkers, P.J. van der Zaag, *J. Appl. Phys.* **85**, 5291 (1999)

[Hjor96] O. Hjortstam, J. Trygg, J. M. Wills, et al., *Phys. Rev. B* **53**, 9204 (1996)

[Hope97] S. Hope, J. Lee, P. Rosenbusch, et al., *Phys. Rev. B* **55**, 11422 (1997)

[Hove77] M.A.Van Hove, S.Y.Tong, M.H.Elconin, *Surf. Sci.* **64**, 85 (1977)

[Hove79] M.A.Van Hove, S.Y.Tong, "*Surface Crystallography by LEED: Theory, Computation and Structural Results*" **2**, Springer Verlag, Springer Series in Chem.Phys. (1979)

[Hove85] M.A.Van Hove S.Y.Tong editors, "*The Structure of Surfaces*" **2**, Springer Verlag, Springer Series in Surf.Sci. (1985)

[Hove86] M.A.Van Hove, W.H.Weinberg, C.M.Chan, "*LEED: Experiment, Theory and Surface Structure Determination*" **6**, Springer Verlag, Springer Series in Surf.Sci. (1986)

[Huan88] H.Huang, S.Y.Tong, W.E.Packard, G.Glander, M.B.Webb, *Phys. Lett A* **130**, 166 (1988)

[Huan90a] HHuang, S.Y.Tong, J.Quinn, F.Jona, *Phys. Rev. B* **41**, 3276 (1990)

[Huan90b] H.Huang, S.Y.Tong, W.S.Yang, H.D.Shih, F.Jona, *Phys. Rev. B* **42**, 7483 (1990)

[Hüfn94] S. Hüfner, *Advances in Physics* **43**, 183 (1994)

[IBMa] http://www.storage.ibm.com/

[IBMb] http://www.almaden.ibm.com/st/projects/magneto/mram/, http://researchweb.watson.ibm.com/resources/news/20001207_mramimages.shtml

[Imad95] S. Imaduddin, A.M. Davidson, R.J. Lad, *Mater. Res. Soc. Proc.* **357**, 177 (1995)

[Imad96] S. Imaduddin, R.J. Lad, *Mater. Res. Soc. Proc.* **401**, 507 (1996)

[Jame65] R.W. James, "*The Optical Principles of the Diffraction of X-Rays*", Cornell University Press, Ithaca, NY (1965)

[Jenn96] H. Jenniches, M. Klaua, H. Hoche, et al., *Appl. Phys. Lett.* **69**, 3339 (1996)

[Jesu96] Juan Carlos de Jesus, Pedro Pereira, José Carrazza, Francisco Zaera, *Surf. Sci.* **369**, 217 (1996)

[Jona78] F. Jona, *J. Phys. C* **11**, 4271 (1978)

[Jona82] F. Jona, J.A. Strozier, W.S. Yang, *Rep. Prog. Phys.* **45**, 527 (1982)

[Jull75] M. Jullière, *Phys. Lett.* A **54** 225 (1975)

[Kake02] Y. Kakehi, S. Nakao, K. Satoh, et al., *J. of Crys. Growth* **237-239**, 591 (2002)

[Kall96] G. C. Kallinteris, G. A. Evangelakis, and N. I. Papanicolaou, *Surf. Sci.* **369**, 185 (1996)

[Kapl54] J. I. Kaplan, *J. Chem. Phys.* **22,** 1709 (1954)

[Keff57] F. Keffer, W. O'Sullivan, *Phys. Rev.* **108,** 637 (1957)

[Kief93] M. T. Kief and W. F. Egelhoff, Jr., *Phys. Rev. B* **47**, 10785 (1993)

[Kim97a] Y.J. Kim, Y. Gao, S.A. Chambers, *Appl. Surf. Sci.* **120**, 250 (1997)

[Kim97b] Y.J. Kim, Y. Gao, S.A. Chambers, *Surf. Sci.* **371**, 358 (1997)

[Kim98] Y.J. Kim, C. Westphal, R.X. Ynzunza, Z. Wang, H.C. Galloway, M. Salmeron, M.A. Van Hove, C.S. Fadley, *Surf. Sci.* **416**, 68 (1998)

[Kita96] O. Kitakami, H. Takashima, Y. Shimada, J. *Magn. Magn. Mater.* **164,** 43 (1996)

[Kita98a] N. Kitakatsu, V. Maurice, P. Marcus, *Surf. Sci.* **411**, 215 (1998)

[Kita98b] N. Kitakatsu, V. Maurice, C. Hinnen, P. Marcus, *Surf. Sci.* **407**, 36 (1998)

[Kool96] J.C.S.Kools, *IEEE Trans. Magn.* **32,** 3165 (1996)

[Kota] A. Kotani, "*Inner shell photoelectron process in solids*", chapter 9, 613-660

[Kuch00] W. Kuch, J. Gilles, S. S. Kang, et al., *Phys. Rev. B* **62**, 3824 (2000)

[Kuch98] W. Kuch, A. Dittschar, M. Salvietti, et al., *Phys. Rev. B* **57**, 5340 (1998)

[Kuhl97] H. Kuhlenbeck, H.-J. Freund, in: D.A. King, D.P. Woodruff (Eds.), "*Growth and Properties of Ultrathin Epitaxial Layers, The Chemical Physics of Solid Surfaces*", Elsevier, New York, 1997 (Chapter 9).

[Laan86] G. van der Laan, J. Zaanen, G. A. Sawatzky, R. Karnatak and J.-M. Esteva, *Phys. Rev. B* **33**, 4253 (1986)

[Laan98] G. Van der Laan, *J. Phys. C* **10**, 3239 (1998)

[Lee97] J. Lee, G. Lauhoff, M. Tselepi, et al., *Phys. Rev. B* **55**, 15 103 (1997)

[Leem92] L.E.C. van de Leemput, H. van Kempen, *Rep. Prog. Phys.* **55**, 1165-1240 (1992)

[Levi89] J.R. Levine, J.B. Cohen, Y.W. Chung and P. Georgopoulos, *J. Appl. Cryst*. **22**, 528 (1989)

[Levi91] J.R. Levine, J.B. Cohen and Y.W. Chung, *Surf. Sci.* **248**, 215 (1991)

[Li01] L. Li, A. Kida, M. Ohnishi, et al., *Materials Transactions* **42**, 1056 (2001)

[Li99a] X. W. Li, A. Gupta, and G. Xiao, *Appl. Phys. Lett.* **75** 713 (1999)

[Li99b] X. W. Li *et al*, *J. Appl. Phys.* **85** 5585 (1999)

[Lind91] D.M. Lind, S.D. Berry, G. Chern, H. Mathias, L.R. Testardi, *J. Appl. Phys.* **70**, 6218 (1991)

[Lind92] D.M. Lind, S.D. Berry, G. Chern, H. Mathias, L.R. Testardi, *Phys. Rev. B* **45**, 1838 (1992)

[Ling01] W. L. Ling, Z. Q. Qiu, O. Takeuchi, et al., *Phys. Rev. B* **63**, 024408/1 (2001)

[Luch01] P. Luches, S. Altieri, C. Giovanardi, et al., *Thin Solid Films* **400**, 139 (2001)

[Lund96] I. Lundstroem, *Sens. Actuators A* **56,** 75 (1996)

[Maek82] S. Maekawa, U. Gäfvert, *IEEE Trans. Magn.* **18**, 707 (1982)

[Marc82] P.M.Marcus, F.Jona, "*Determination of Surface Structure by LEED*", Plenum Press, The IBM Research Symposia Series (1984)

[Marg96] D.T. Margulies, F.T. Parker, F.E. Spada, R.S. Goldman, J. Li, R. Sinclair, A.E. Berkowitz, *Phys. Rev. B* **53**, 9175 (1996)

[Marg97] D.T. Margulies, F.T. Parker, M.L. Rudee, F.E. Spada, J.N. Chapman, P.R. Aitchison, A.E. Berkowitz, *Phys. Rev. Lett.* **79**, 5162 (1997)

[Meye02] H. L. Meyerheim, R. Popescu, N. Jedrecy, M. Vedpathak, M. Sauvage-Simkin, R. Pinchaux, B. Heinrich, and J. Kirschner, *Phys. Rev. B* **65**, 144433 (2002)

[Meze82] L. Z. Mezey and J. Giber, *Surf. Sci.* **117**, 220 (1982)

[Mich93] T. Michely, M. Hohage, M. Bott, et al., *Phys. Rev. Lett.* **70**, 3943 (1993)

[Mocu00a] C. Mocuta, A. Barbier, G. Renaud, et al., *J. Magn. Mater. Magn.* **211**, 283 (2000)

[Mocu00b] C. Mocuta, A. Barbier, S. Lafaye, et al., Proceedings of Spring 2000 Materials Research Society Meeting, (2000)

[MocuPhD] C. Mocuta, *PhD Thesis*, Université "Joseph Fourier", Grenoble (2000)

[Motorola] http://www.motorola.com

[Mull00] F. Muller, R. de Masi, P. Steiner, D. Reinicke, M. Stadtfeld, S. Hufner, *Surf. Sci.* **459**, 161 (2000)

[Mull01] S. Muller, J. E. Prieto, C. Rath, et al., *J. Phys. C* **13**, 1793 (2001), and S. Muller, J. E. Prieto, T. Kramer, et al., *J. Phys. C* **13**, 9897 (2001)

[Naka99] R. Nakajima, J. Stöhr, and Y. U. Idzerda, *Phys. Rev. B* **59**, 6421 (1999)

[Naud97] A. Naudon and D. Thiaudière, *J. Appl. Cryst*. **30**, 822 (1997)

[Naud98] A. Naudon, D. Babonneau, F. Petroff and A. Vaurès, *Thin Solid Films* **319**, 81 (1998)

[Noak01] T. C. Q. Noakes and P. Bailey, *Thin Solid Films* **394**, 16 (2001)

[Nogu99] J.Nogués, I.K.Schuller, *J. Magn. Magn. Mater*. **192,** 203 (1999)

[Öfne97] Helmut Öfner and Francisco Zaera, *J. Phys. Chem. B* **101**, 9069 (1997)

[Ohld01] H. Ohldag, A. Scholl, F. Nolting, S. Anders, F. U. Hillebrecht, and J. Stohr, *Phys. Rev. Lett.* **86**, 2878 (2001)

[Oshi96] N. Oshima, M. Nakada, Y. Tsukamoto, *Jpn. J. Appl. Phys*. **33,** L1585 (1996)

[Pass00] M. C. G. Passeggi, Jr., J. E. Prieto, R. Miranda, et al., *Surf. Sci.* **462**, 45 (2000)

[Peac94] S. D. Peacor and T. Hibma, *Surf. Sci.* **301**, 11 (1994)

[Pede97] M. O. Pedersen, I. A. Bonicke, E. Laegsgaard, et al., *Surf. Sci.* **387**, 86 (1997)

[Pend74] J.B. Pendry, "*LEED: The Theory and its Application to Determination of Surface Structure*" **2**, Academic Press, Techniques of Physics (1974)

[Pend80] J.B Pendry, *J. Phys. C* **13**, 937 (1980)

[Plat99] W. Platow, U. Bovensiepen, P. Poulopoulos, et al., *Phys. Rev. B* **59**, 12641 (1999)

[Pons01] S. Pons, P. Mallet, and J. Y. Veuillen, *Phys. Rev. B* **64**, 193408/1 (2001)

[Poro82] G. Porod, "*Small Angle X-ray Scattering*" edited by Academic Press (1982), pp. 37

[Port01] M. Portalupi, L. Duo, G. Isella, et al., *Phys. Rev. B* **64**, 165402/1 (2001)

[Pour99] L. V. Pourovskii, N. V. Skorodumova, Y. Vekilov, et al., *Surf. Sci.* **439**, 111 (1999)

[Prut75] M.Prutton, "*Surface Physics*" **8**, Clarendon Press, 1975, Oxford Physics Series (1975)

[Raek92] T. J. Raeker and A. E. DePristo, *J. Vac. Sci. Tech. A* **10**, 2396 (1992)

[Read] http://www.readrite.com

[Rega01] T. J. Regan, H. Ohldag, C. Stamm, et al., *Phys. Rev. B* **64**, 214422/1 (2001)

[Rena98] G. Renaud, *Surf. Sci. Rep.* **32,** 1 (1998)

[Rena99] G. Renaud, M. Noblet, A. Barbier, C. Revenant, O. Ulrich, Y. Borensztein, R. Lazzari, J. Jupille , C.Henry, To be published -, - (1999)

[Rena00] G. Renaud, M. Noblet, A. Barbier, J.P. Deville, O. Fruchart and F. Scheurer, Unpublished results - (2000)

[Ritt97] M. Ritter, H. Over, W. Weiss, *Surf. Sci.* **371**, 245 (1997)

[Roba00] O.Robach, Y.Garreau, K.Aïd, M.B.Véron-Jolliot, *J. Appl. Cryst.* **33,** 1006 (2000)

[Robb98] P.S. Robbert, H. Geisler, C.A. Ventrice Jr., J. van Ek, S. Chaturvedi, J.A. Rodriguez, M. Kuhn, U. Diebold, *J. Vac. Sci. Technol. A* **16**, 990

[Robi86] I. K. Robinson, *Phys. Rev. B* **33**, 3830 (1986)

[Robi91] I.K. Robinson, "*Surface crystallography*," edited by Elsevier, Amsterdam & New-York, Vol. **3**, pp. 221-266 (1991)

[Robi92] I.K.Robinson, D.J.Tweet, *Rep. Prog. Phys.* **55**, 599 (1992) and references therein

[Rohr94] F. Rohr, K. Wirth, J. Libuda, D. Cappus, M. Bäumer, and H. J. Freund, *Surf. Sci*. **315**, L977 (1994).

[Roth58a] W. L. Roth, *Phys. Rev.* **110,** 1333 (1958)

[Roth58b] W. L. Roth, *Phys. Rev.* **111,** 772 (1958)

[Ruan93] L. Ruan, F. Besenbacher, I. Stensgaard, et al., *Phys. Rev. Lett.* **70**, 4079 (1993)

[Russ91] T.P. Russel, "*Small-angle scattering*" edited by Elsevier, Amsterdam & New-York, Vol. **3**, pp. 379-470 (1991)

[Saik89] R. S. Saiki, A. P. Kaduwela, J. Osterwalder, C. S. Fadley and C. R. Brundle, *Phys. Rev. B* **40**, 1586 (1989)

[Saku90] T. Sakurai et al., *Progr. Surf. Sci.* **33**, 3-89 (1990)

[Sanc00] M. Sanchez-Agudo, F. Yubero, G. G. Fuentes, A. Gutiérrez, M. Sacchi, L. Soriano and J. M. Sanz, *Surf. Interface Anal*. **30**, 396-400 (2000)

[Scha93a] C.Schamper, H.L.Meyerheim, W.Moritz, *J. Appl. Cryst*. **26,** 687 (1993)

[Scha93b] C. Scharfschwerdt, T. Liedtke, M. Neumann, T. Straub and P. Steiner, *Phys. Rev. B* **48**, 6919 (1993)

[Sche98] F. Schedin, L. Hewitt, P. Morrall, V.N. Petrov, G. Thornton, S. Case, M.F. Thomas, V.M. Uzdin, *Phys. Rev. B* **58**, R11861 (1998)

[Schm99] M. Schmidbauer, T. Wiebach, H. Raidt, M. Hanke, R. Köhler, H. Wawra, *J. Phys. D : Appl. Phys.* **32**, A230 (1999)

[Schw86] K.-H. Schwarz, *J. Phys. F: Met. Phys.* **16** L211 (1986)

[Seag] http://www.seagate.com

[Seba99] I. Sebastian, T. Bertrams, K. Meinel, et al., *Faraday Discussions* **114**, 129 (1999)

[S-EF90] Proceedings of the International School of Physics "Enrico Fermi", Elsevier Science Publisher B.V. North Holland (1990)

[Shai99a] S.K. Shaikhutdinov, W. Weiss, *Surf. Sci.* **432**, L627 (1999)

[Shai99b] S.K. Shaikhutdinov, M. Ritter, X.G. Wang, H. Over, W. Weiss, *Phys. Rev. B* **60**, 11062 (1999)

[Shar83] M. Sharon, B.M. Prasad, *Sol. Energy Mater*. **8,** 457 (1983)

[Shi88] A.-C. Shi, M. Wortis, *Phys. Rev. B* **37,** 7793 (1988)

[Shir72] D. A. Shirley, *Chem. Phys. Lett.* **17**, 312 (1972)

[Slau02] J. M. Slaughter, R. W. Dave, M. DeHerrera, et al., *Journal of Superconductivity* **15**, 19 (2002)

[Soey93] S. Soeya, S. Tadokoro, T. Imagawa, M. Fuyama, *J. Appl. Phys.* **74,** 6297 (1993)

[Soey97] S. Soeya, M H. Hoshiya, K. Meguro, H. Fukui, *Appl. Phys. Lett.* **71,** 3424 (1997)

[Span85] D. Spanjaard, C. Guillot, M. C. Desjonquères, G. Tréglia, and J. Lecante, *Surf. Sci. Rep.* **5**, 1 (1985)

[Span98] D. Spanke, V. Solinus, D. Knabben, F. U. Hillebrecht, F. Ciccacci, L. Gregoratti and M. Marsi, *Phys. Rev. B* **58**, 5201 (1998))

[Spic58] W. E. Spicer, *Phys. Rev.* **112**, 114 (1958)

[Spin00] L. Spinu *et al*, *Phys. Rev.* B **62** 8931 (2000)

[Sriv98] P. Srivastava, F. Wilhelm, A. Ney, et al., *Phys. Rev. B* **58**, 5701 (1998)

[Stan00] B. Stanka, W. Hebenstreit, U. Diebold, S.A. Chambers, *Surf. Sci.* **448**, 49 (2000)

[Stöh95] J. Stohr and H. Konig, *Phys. Rev. Lett.* **75**, 3748 (1995)

[Stoh98] J.Stöhr, H.A.Padmore, S.anders, T.Stammler, M.R.Scheinfen, *Surf. Rev. Lett.* **5,** 1297 (1998)

[Stro93] "*Scanning Tunneling Microscopy*", J. Stroscio, W.J. Kaiser (*Eds.*), Academic Press (1993)

[Suez87] Y. Suezawa, Y. Gondo, in: Proceedings of the International Symposium on Physics of Magnetic Materials, Vol. MAG-18, Sendai, p. 303 (1987)

[Suez92] Y. Suezawa, F. Takahashi, Y. Gondo, *Jpn. J. Appl. Phys.* **31,** L1415 (1992)

[Taka97] K. Takano, R. H. Kodama, A. E. Berkowitz, et al., *Phys. Rev. Lett.* **79**, 1130 (1997)

[Taka98] K. Takano, "*Exchange Anisotropy in Thin Film Bilayers of Nickel Cobalt Monoxide and Various Ferromagnetic Materials*", Ph.D. Report (1998) University of California, San Diego

[Task79] P. W. Tasker, *Philos. Mag.* **39**, 119 (1979)

[Tayl99] M. B. Taylor, C. E. Sims, G. D. Barrera, N. L. Allan, W. C. Mackrodt, *Phys. Rev. B* **59**, 6742 (1999)

[Tear82] S. P. Tear and K. Roll, *J. Phys. C* **15**, 5521 (1982)

[Ters82] J. Tersoff and L. M. Falicov, *Phys. Rev. B* **26**, 6186 (1982)

[Tham57] B. J. Thamer, R. M. Douglass, and E. Staritzky, *J. Am. Chem. Soc.* **79,** 547 (1957)

[Thev99] S. Thevuthasan, Y.J. Kim, S.I. Yi, S.A. Chambers, J. Morais, R. Denecke, C.S. Fadley, P. Liu, T. Kendelewicz, G.E. Brown Jr., *Surf. Sci.* **425**, 276 (1999)

[ThiaPhD] D. Thiaudière, *PhD Thesis*, Université de Poitiers (1996)

[Thol92] B. T. Thole, P. Carra, F. Sette, G. Van der Laan, *Phys. Rev. Lett.* **68,** 1943 (1992)

[Tiet89] L.A. Tietz, S.R. Summerfelt, G.R. English, C.B. Carter, *Appl. Phys. Lett.* **55**, 1202 (1989)

[Tone93] M.F.Toney, D.G.Wiesler, *Acta Cryst*. A **49,** 624 (1993)

[Tong88] S.Y.Tong, H.Huang, C.M.Wei, W.E.Packard, F.K.Men, G.Glander, M.B.Webb, *J. Vac. Sci. Tech.* **A6**, 615 (1988)

[Tong91] S.Y.Tong, M.A.Van Hove, K.Takayanagi, X.D.Xie editors, "*The Structure of Surfaces*" III **24**, Springer Verlag, Springer Series in Surf. Sci. (1991)

[Ulme97] H. Ulmer, J. Mitrovics, G. Noetzel, U. Weimar, W. Goepel, *Sens. Actuators B* **43,** 24 (1997).

[Veen88] J.F.van der Veen, M.A.Van Hove editors, "*The Structure of Surfaces*" II **11**, Springer Verlag, Springer Series in Surf. Sci. (1988)

[Veen93] M. A. van Veenedaal and G. A. Sawatzky, *Phys. Rev. Lett.* **70**, 2459 (1993)

[Veen96] M. van Veenendaal, J. B. Goedkoop, and B. T. Thole, *Phys. Rev. Lett.* **77**, 1508 (1996)

[Vent94] C.A. Ventrice, T. Bertrams, H. Hannemann, A. Brodde, N. Neddermeyer, *Phys. Rev. B* **49**, 5773 (1994)

[Vlie97] E. Vlieg, *J. Appl. Cryst*. **30**, 532 (1997)

[Vlie98] E.Vlieg, *J. Appl. Cryst*. **31,** 198 (1998)

[Voge94a] J.Vogel, M.Sacchi, *Phys. Rev. B* **49,** 3230 (1994)

[Voge94b] J. Vogel, G. Panaccione, and M. Sacchi, *Phys. Rev. B* **50**, 7157 (1994)

[Voog95] F.C. Voogt, T. Hibma, G.L. Zhang, M. Hoefman, L. Niesen, *Surf. Sci.* **331-333**, 1508 (1995)

[Voog97a] F.C. Voogt, T. Hibma, P.J.M. Smulders, L. Niesen, T. Fujii, *Mater. Res. Soc. Symp. Proc.* **474**, 211 (1997)

[Voog97b] F.C. Voogt, T. Hibma, P.J.M. Smulders, L. Niesen, T. Fujii, P.A.A. van der Heijden, R.J.M. van der Veerdonk, P.J. van der Zaag, *J. Phys. IV* **7**, C1/601 (1997)

[Voog98] F.C. Voogt, T.T.M. Palstra, L. Niesen, O.C. Rogojanu, M.A. James, T. Hibma, *Phys. Rev. B* **57**, R8107 (1998)

[Voog99] F.C. Voogt, T. Fujii, P.J.M. Smulders, L. Niesen, M.A. James, T. Hibma, *Phys. Rev. B* **60**, 11193 (1999)

[Vure88] G.H. Vurens, M. Salmeron, G.A. Somorjai, *Surf. Sci.* **201**, 129 (1988)

[Wang98] X.-G. Wang, W. Weiss, S.K. Shaikhutdinov, M. Ritter, M. Peterson, F. Wagner, R. Schlogl, M. SchefØer, *Phys. Rev. Lett.* **81**, 1038 (1998)

[Ware69] B.E. Waren, "*X-Ray Diffraction*" Addison-Wesley, Reading, MA (1969)

[Waro01] B. Warot, E. Snoeck, P. Baules, et al., *J. of Cryst. Growth* **224**, 309 (2001), and B. Warot, E. Snoeck, P. Baules, et al., *Appl. Surf. Sci.* **177**, 287 (2001)

[Waro02] B. Warot, E. Snoeck, J. C. Ousset, et al., *Appl. Surf. Sci.* **188**, 151 (2002)

[Webe96] W. Weber, A. Bischof, R. Allenspach, et al., *Phys. Rev. B* **54**, 4075 (1996)

[Weis02] W. Weiss, W. Ranke, *Prog. Surf. Sci.* **70**, 1 (2002)

[Weis93] W. Weiss, G.A. Somorjai, *J. Vac. Sci. Technol. A* **11**, 2138 (1993)

[Weis97] W. Weiss, *Surf. Sci.* **377-379**, 943 (1997)

[Weis99] W. Weiss, M. Ritter, *Phys. Rev. B* **59**, 5201 (1999)

[Well95] D. Weller, J. Stohr, R. Nakajima, et al., *Phys. Rev. Lett.* **75**, 3752 (1995)

[Wies98] "*Scanning Probe Microscopy and Spectroscopy: Methods and Applications*", R. Wiesendanger, Cambridge University Press (1998)

[Will80] R. H. Williams, G. P. Srivastava, and I. T. McGovern, *Rep. Prog. Phys.* **43**, 1357 (1980)

[Wolf92] D.Wolf, *Phys. Rev. Lett.* **68,** 3315 (1992)

[Woll01] J. Wollschlager, D. Erdos, H. Goldbach, et al., *Thin Solid Films* **400**, 1 (2001)

[Wood86] D.P.Woodruff, T.A.Delchar, "*Modern Techniques of Surface Science*" **10**, Cambridge, University Press, Cambridge Solid State Science Series (1986)

[Wool70] M.M. Woolfson, "*An introduction to X-Ray crystallography*" Cambridge University Press, Cambridge, UK (1970)

[Wulf98] W. Wulfhekel, I. Beckmann, G. Rosenfeld, et al., *Surf. Sci.* 395, 168 (1998)

[www-nobel] http://www.nobel.se/physics/laureates/1986/

[xps_nist] http://srdata.nist.gov/xps/

[Yama66] T. Yamada, *J. Phys. Soc. Jpn.* **21,** 650 (1966); **21,** 664 (1966)

[Yang01] F. Y. Yang *et al*, *Phys. Rev.* B **63** 092403 (2001)

[Ydze94] Y.Ydzerda et al, Nucl.Instrum.Meth. *Phys. Res. A* **347**, 134 (1994)

[Yeh85] J. J. Yeh and I. Lindau, *Atomic Data and Nuclear Data Tables* **32**, 1 (1985)

[Yerm75] Y. Yermakov, V. Zakharov, *Adv. Catal.* **173** (1975)

[Yi99] S.I. Yi, Y. Liang, S.A. Chambers, *Surf. Sci.* **443**, 212 (1999)

[Youn71] R. Young, J. Ward, R. Scire, *Phys. Rev. Lett.* **27**, 922 (1971)

[Youn72] R. Young, J. Ward, R. Scire, *Rev. Sci. Instrum.* **43**, 999 (1972)

[Zana77] E.Zanazzi, F.Jona, *Surf. Sci.* **62**, 61 (1977)

[Zang88] A.Zangwill, "*Physics at Surfaces*", Cambridge University Press (1988)

[Zhan93] J. Zhang, Z. L. Han, S. Varma, et al., *Surf. Sci.* **298**, 351 (1993)

[Zhan97a] L. Zhang, M. Kuhn, U. Diebold, *J. Vac. Sci. Technol. A* **15**, 1576 (1997)

[Zhan97b] L. Zhang, M. Kuhn, U. Diebold, *Surf. Sci.* **375**, 1 (1997)